STRATEGIES TO ENHANCE SEISMIC PERFORMANCE OF REINFORCED MASONRY SHEAR WALLS

STRATEGIES TO ENHANCE SEISMIC PERFORMANCE OF REINFORCED MASONRY SHEAR WALLS

By

MARWAN MOHAMED TAREK SHEDID
B.Sc., M.A. Sc.

A Thesis

Submitted to the School of Graduate Studies

in Partial Fulfillment of the Requirements

for the Degree

Doctor of Philosophy

McMaster University

November 2009

DOCTOR OF PHILOSOPHY (2009) McMaster University

(Civil Engineering) Hamilton, Ontario

TITLE: Strategies to Enhance Seismic Performance of Reinforced Masonry Shear Walls

AUTHOR: Marwan Mohamed Tarek Shédid,
B.Sc. (Ain Shams University)
M.A.Sc (McMaster University)

ADVISORS: Dr. Robert Drysdale
Dr. Wael El-Dakhakhni

NUNMBER OF PAGES: xvi, 225.

ABSTRACT

Better understanding of the structural behaviour of concrete and masonry structures is facilitated through experimental testing. Although some experimental testing of reinforced masonry (RM) rectangular walls is reported in literature, little experimental data is available on RM walls with flanges or with boundary element. Unlike those pertaining to rectangular walls, seismic design provisions of flanged and end-confined masonry walls are not available in North American masonry design codes.

In the current study, the response of seven half scale fully grouted RM shear walls, all with the same length but different end configurations and aspect ratios is investigated. The goal of the study was to evaluate and document the enhanced ductile behaviour of rectangular RM shear walls when flanges and boundary elements are structurally connected at the wall ends. Another goal was to extract specific seismic performance parameters of reinforced concrete-block rectangular, flanged and end-confined shear walls based on quasi-static experimental results. Finally, nonlinear dynamic analysis was conducted on the test walls to quantify seismic force modification factors used in seismic design.

High levels of ductility accompanied by relatively small strength degradation were observed in all walls in general with a significant increase in ductility and displacement capabilities for the flanged and end-confined walls compared to the rectangular ones. The drift levels attained at 20% strength degradation by the rectangular, the flanged, and the end-confined walls were 1.0%, 1.5%, and 2.2%, respectively. The ductility values of the flanged and end-confined walls were, respectively, 1.5 and 2.0 times that of their rectangular wall counterparts. In addition to the enhanced ductility, a saving of more than 40% in the amount of vertical reinforcement was achieved using the proposed alternative strategies while maintain the lateral resistance. The relationship between the energy dissipation and the ratio of the post-yield to the yield displacement was found to be almost linear for the test walls. Wall stiffnesses degraded rapidly to about 60% of their gross stiffness at very

low drift levels (0.1% drift). Measured compressive strain at the wall toes were almost double those specified in both North American codes. Extent of plasticity over the wall height was about 75% of the wall length. Equivalent plastic hinge lengths, needed in wall displacement predictions, using theoretical curvatures and experimental displacement ductilities varied between 17% and 40% of the wall length at ultimate load for all the tested walls. The test results indicated that higher seismic force modification factors should be assigned to the flanged and end-confined RM shear walls compared to values currently assigned to rectangular walls.

The data presented in this study is expected to facilitate better understanding of RM wall behaviour under in-plane load to researchers, practicing engineers, and code developers. This study aimed at presenting the flanged and end-confined categories as cost-effective alternatives to enhance the seismic performance of mid-rise RM construction in North America.

DEDICATIONS

To my Mother & Father,

To my Brother,

To my Wife & Daughter.

ACKNOWLEDGMENTS

All praise and gratitude be to
ALLAH the Most Gracious, the Most Compassionate and the Most Merciful
with the blessings of Whom the good deeds are fulfilled.

I wish to express my deep gratitude to my advisor Dr. Robert Drysdale for his interest and insight throughout this research especially during the experimental study. Sincere thanks and gratitude are also due to my co-advisor Dr. Wael El-Dakhakhni for his encouragement, support, advices, and innovative ideas. I am especially grateful for our long evening discussions that significantly impacted the quality of the dissertation.

Special thanks are due to my supervisory committee members, Dr. John Wilson and Dr. Peidong Wu for their valuable advice and suggestions. Their helpful comments and discussions during our meetings are greatly appreciated.

A word of thanks is due to the Applied Dynamic Laboratory technicians Mr. David Perrett and Mr. Kent Wheeler for their unwavering help. I would also like to thank all of my friends and colleagues, Ahmed Mostafa, Amr Nasr, Badr Abou Zeid, Bennett Banting, Joe Wizbeski, Kevin Hughes, and Tom Kasparik for their help and useful discussions during all stages of my experimental and analytical studies.

The financial supports of the Ontario Research and Development Challenge Fund (ORDCF) of the Ministry of Research and Innovation and the McMaster University Centre for Effective Design of Structures are gratefully acknowledged. Provision of mason time by Ontario Masonry Contractors Association and Canada Masonry Design Centre is appreciated. The supply of the half scale blocks by the Canadian Concrete Masonry Producers Association (CCMPA) and the supply of the horizontal wires by Laurel-Lec-Steel is gratefully acknowledged.

At last but by no means the least, I would like to say that no words can express my sincere gratitude to my parents, Maha and Tarek and to my brother, Mostafa, for their patience, care, support and for everything they did, and are still doing for me.

Without their continuous support, love, prayer and encouragement throughout my life I would have never been the one I am now. Many thanks to my grandmother, Nan, for her care and support since I arrived to Canada. Special thanks are due to my wife, Yasmine, for her patience, understanding, and unwavering encouragement and support throughout the tough and the good times at McMaster. She has happily supported me far beyond her fair share. I would also like to acknowledge my daughter, Yasmina, for her innocent and kind smile that eased the long nights of work.

TABLE OF CONTENTS

LIST OF TABLES

LIST OF FIGURES

LIST OF SYMBOLS AND ACRONYMS

The following subscripts are used with the notations:
y = yield, u = ultimate, 0.8u = at 20% degradation in strength, 1% = 1% drift, e= elastic, d= design, g = gross, in = inelastic, ex = experimental

The following superscripts are used with the notations:
ep = elastic-plastic, I= simplified elastic-plastic idealization

A_e = Effective shear area;
A_s' = Compression reinforcement;
c = Depth of the compression zone under factored load;
C_d = Deflection amplification factor specified in the ASCE-7 (2008);
dt = Time step for the earthquake record;
E_d = Dissipated energy;
E_m = Masonry modulus of elasticity;
E_s = Elastic energy;
f'_m = Average compressive strengths of four-course masonry prisms;
G_m = Masonry shear modulus;
h_{gauge} = Segment height over the wall height used to measure strains and curvatures;
h_w = Wall height;
I_e = Effective cross section inertia (CSA A23.3-05);
I_g = Gross cross section inertia;
k = Shear shape factor;
k_e = Average yield stiffness;
K_i = Wall stiffness (Q/Δ);
l_p = Equivalent plastic hinge length;
L_p = Extent of plasticity zone;
l_w = Wall length;
m = Equivalent mass of the single degree of freedom system;
P = Axial compression applied on the wall;
Q = Wall lateral resistance;
R = Force reduction factor used in ASCE-7 (2008);
R_d = Ductility-related force modification factor in CSA S034.1-04;
R_o = Overstrength-related force modification factor in CSA S034.1-04;
t = Wall thickness;
T_d = Period corresponding to elastic stiffness;
$T_{initial}$ = Period corresponding to the gross stiffness;
T_{norm} = Normalized period ratio;
V^*_m = Shear force carried by the masonry inside the plastic hinge region;
V_m = Shear force carried by the masonry;
V_s = Shear force carried by the horizontal reinforcement;
V_u^s = Maximum shear strength of the wall;

V_u^{s*} = Maximum shear strength of the wall inside the plastic hinge region;
z = Length of the compression zone based on elastic analysis;
γ_w = Wall overstrength factor equal to the ratio of the load corresponding to nominal moment resistance of the wall to the factored load on the wall;
Δ = Lateral top wall displacement;
Δ_{Ci} = Net measured compression displacement over h_{gauge};
Δ_f = Displacement due to flexure;
Δ_F = Deflection of the top of the wall due to factored loads;
Δ_s = Displacement due to shear;
Δ_{sl} = Displacement due to sliding;
Δ_t = Time step in nonlinear dynamic analysis;
Δ_{Ti} = Net measured elongation displacement over h_{gauge};
ε_0 = Masonry strain corresponding to maximum stress;
ε_{cu} = Ultimate concrete compressive strain;
θ_i = Rotation over segment along the wall height;
θ_{ic} = Inelastic rotational capacity of the wall;
θ_{id} = Inelastic rotational demand of the wall;
μ_Δ = Multiples of yield displacement (Δ/Δ_y);
μ_φ = Curvature ductility;
ξ_{hyst} = Hysteresis damping;
ρ_h = Ratio of steel reinforcement in horizontal direction;
ρ_v = Ratio of steel reinforcement in vertical direction;
σ = Axial compressive stress applied on the walls;
φ = Curvature;
Ω_0 = Overstrength specified in the ASCCE-7 (2008);
HBD = Ductility-related hysteresis parameter (IDARC-5, 2002);
HBE = Strength-related hysteresis parameter (IDARC-5, 2002);
HC = Stiffness degradation parameter (IDARC-5, 2002);
HS = Slip parameter (IDARC-5, 2002);
PGA = Peak ground acceleration; and
PGV = Peal ground velocity.

Chapter One

Introduction

CHAPTER 1
INTRODUCTION

1.1 General

Recent examples of building damage due to earthquake loading have led to the adoption of more stringent seismic design requirements in North America. These requirements have significantly affected the design of masonry buildings which are perceived to be less ductile and thus more vulnerable to seismic loading. The common perception that reinforced masonry (RM) cannot provide high ductility compared to reinforced concrete (RC) may be in part attributed to the poor performance of unreinforced masonry (URM) during a series of earthquakes in the 19th and the 20th century such as Imperial Valley (1892), San Fernando (1906), Long Beach (1933), San Fernando (1971) and Northridge (1994) earthquakes that illustrated the seismic vulnerability of URM structures.

The need for a more ductile and earthquake-resistant form of masonry construction resulted in the development of RM systems. Nevertheless, it seems that seismic design of RM structures still adopts a high level of conservatism in the National Building Code of Canada (NBCC 2005). Recent experimental investigations (Shing et al. 1990, Seible et al. 1993, Eikanas 2003, and Shedid et al. 2008) concluded that high levels of ductility and small strength degradation, at large drift levels, can be achieved from RM shear walls failing in flexure. However, there is still a need for applied research with detailed documentation to support the proposal that RM walls are indeed ductile. Moreover, fundamental research focusing on enhancing the ductility and energy dissipation qualities of masonry structures is required to facilitate quantification of seismic design parameters.

As a first step in research to enhance the behaviour of masonry under in-plane loading, the differences between typical RM construction practice and the detailing of ductile RC shear walls should be identified. A significant difference between RM and RC walls is the presence of closed ties and two layers of vertical reinforcement in RC walls which provide a reinforcing cage to confine the compression zone. In comparison, due to practical limitations associated with concrete block wall cross sections, single horizontal ties and a single layer of vertical reinforcement are typically used in RM and, therefore, no confinement is provided at the wall ends. In this regards, it is thought that the reinforcing arrangement in RM may lead to instability of the compression zone under high inelastic strains in the vertical bars during cyclic loading. The instability could consist of out-of-plane displacement of the wall and bar buckling in the compression zone (Paulay and Priestley 1993).

An objective of this thesis is to study the performance of RM walls with boundary elements or flanges. The presence of boundary elements at the end zone of the walls allows the use of more than one layer of vertical bars that can be confined within closed ties. Moreover, structurally connecting a rectangular wall to a small flange (or an intersecting wall) or to a boundary element could limit the damage at the wall ends and increase out-of-plane stability. Also, the increased thickness at the wall ends can significantly decrease the required length of the compression zone leading to increased curvature at maximum load. Consequently, the increased curvature ductility should lead to a corresponding increase in the displacement ductility of the wall. In this regard, it is noted that the response of rectangular RC walls has been shown to be greatly enhanced when boundary elements were added at their ends or when walls are structurally connected to intersecting walls (Paulay and Priestley 1992). Surprisingly, very little research has been carried out on the lateral loading performance characteristics of flanged RM walls and RM walls with boundary elements.

The seismic design philosophy of current North American codes allows most structures to undergo inelastic deformation under strong ground motion. To account for ductility and energy dissipation in actual structures, seismic response modification factors are used in these force-based design codes to reduce the seismic forces from those that would develop if the structures remain elastic. These factors are influenced by engineering judgment and observation of the performance of various structural systems in previous strong earthquakes (Uang 1991). Little information is available to justify the use of current values and furthermore, as stated in the ATC-63 (2008) document, "*Original R factors were based largely on judgement and qualitative comparisons with the known capabilities of relatively few-seismic-force-resisting systems in widespread use at the time. The most recent edition of the NEHRP published as FEMA 450 (2004) includes more than 75 individual systems, each having a somewhat arbitrarily R factor and many of these individual systems have never been subjected to any significant level of earthquake ground shaking*".

Although, seismic force modification factors are given in North American codes for rectangular RM shear walls, no values are provided for flanged and end-confined walls. In fact, there are no guidelines or provisions included to enable advantage to be taken of new systems developed to achieve improved seismic performance. It would seem that the reduction values specified and the methodology used should be based on a sufficiently sound fundamental approach that existing and new systems could be evaluated in a consistent, open, and fair manner.

1.2 Scope of the research

The aim of this study is to experimentally evaluate and document the ductile behaviour of RM shear walls having flanges or boundary elements structurally connected at the wall ends. The experimental results are to be analysed to quantify seismic performance parameters of the proposed alternative construction techniques. It is intended to propose values of the force modification factors to be used for the seismic design of the identified alternative types of construction. The corresponding factors for the existing rectangular wall configurations currently covered in the Canadian and the American codes will also be reviewed.

In the current study, seven half-scale fully-grouted RM shear walls were designed with the same length but with different end configurations and aspect ratios to provide new data. The rectangular, flanged, and end-confined (walls with boundary elements) RM shear walls are to be subjected to fully-reversed displacement-controlled quasi-static cyclic loading. It is intended that cyclic loading be continued up to a 50% degradation in strength in order to obtain information on their post-peak behaviour.

The planned analytical part of this study involves modeling the test walls using nonlinear dynamic analysis software to capture the overall wall response under actual earthquake records. In this regard, it is anticipated that the wall models should be subjected to a wide variety of ground motions to simulate different dynamic responses. This will help in determining seismic response modification factors for the proposed wall construction categories.

1.3 Objectives of the dissertation

The research reported in this dissertation is a part of major ongoing experimental and analytical investigations at McMaster University of the response of reinforced masonry shear walls having various end configurations and aspect ratios and subjected to various levels of axial compressive stress. The objectives of this dissertation are to:

- Evaluate the effect of flanges on increasing the curvature ductility and ultimate displacement for RM shear walls.
- Propose a new boundary-element construction technique for RM shear wall construction. This is expected to result in a new seismic force resisting system category in the next editions of CSA S304.1 and the National Building Code of Canada (NBCC).
- Establish the difference between specimen behaviour with and without inclusion of floor slabs, in terms of crack pattern and the relative contributions of shear and flexural deformations.

- Provide data related to wall stiffness and its degradation as the main factor controlling the base shear attracted by a building during seismic events. This data is expected to give a clearer picture regarding change in the period with increased deformation. Longer period of vibration should result in significant reductions of seismic demand for masonry buildings especially if displacement-based seismic design approach is considered.
- Provide estimates for the plastic hinge length to better predict wall displacements and displacement ductilities at different performance levels.
- Quantify and present the variation of hysteresis damping of the proposed wall construction, which is needed for both force-based and displacement-based seismic design approaches.
- Determine the contributions of shear and flexural deformations for the proposed wall constructions. This will facilitate better prediction of the overall building displacement and interstorey drift.
- Establish ductilities of RM shear walls when flanges or boundary elements are structurally connected at the ends of the walls.
- Propose seismic response modification factors for the Canadian and American codes to be used with the proposed wall construction categories.

1.4 Organization of the dissertation

This dissertation describes a combination of experimental and analytical research used to investigate and document the seismic performance of rectangular, flanged and end-confined RM shear walls. This information is used to propose seismic response modification factors following the philosophies of the Canadian and the American codes. The content is as follows:

- The scope and objectives of the dissertation as well as background information pertaining to RM shear walls are presented in Chapter 1.
- Chapter 2 contains a description of the experimental program, test matrix, test setup and instrumentation, and provides information about the properties of the materials used in wall construction.

- The details of the hysteresis behaviour, test observations, and failure modes of the test walls as well as comparison of the load-displacement responses and ductilities of the different wall types tested are presented in Chapter 3.
- Analysis of the test results and elastic and inelastic characteristics of the walls are then presented in Chapter 4.
- Seismic performance parameters and plastic hinging of the test walls, as well as evaluation of the seismic response modification factors following the design philosophies of both the Canadian and American codes are presented in Chapter 5.
- The thesis summary, major conclusions and recommendation for future research are presented in Chapter 6.
- Seismic performance parameters of full scale RM shear walls tested by Shedid (2006) are quantified in Appendix A. This analytical work, done as part of the dissertation research, is used as the basis for comparison for the half-scale RM shear walls tested in this study.

1.5 Literature review

The literature review presented in the following section focuses on the performance of rectangular, flanged, and end-confined RC and RM wall under cyclic loading. It also contains a discussion of the basis for ductility calculations and background pertaining to the calculation of seismic response modification factors.

1.5.1 Introduction

The increase use of masonry shear wall systems was accompanied by experimental investigations; a significant portion of the masonry research conducted to date has been dedicated to studying the in-plane behaviour of masonry under different combinations of axial load and lateral shear force (Priestley 1977; Paulay 1980; Paulay et al. 1982; Sveinsson et al. 1985; Tomazevic et al. 1986; Shing et al.

1989a; Seible et al. 1993; Voon and Ingham 2004; Miller et al. 2005; Shedid et al. 2008). These studies identified flexural and shear failures as the main failure mechanisms. Shear failure was characterized by either diagonal tension cracking across the length of the wall or shear slip along mortar bed joints. Walls failing in a predominantly brittle shear failure mode exhibited rapid strength degradation after the ultimate strength was reached. Flexural failure was characterized by yielding of the vertical reinforcement, formation of a plastic hinge zone at the bottom of the wall and, eventually, crushing of the masonry at the critical wall region. This mechanism is generally considered to be a more favourable failure mode, compared to shear failure, because of its ductile nature and its effectiveness in dissipating energy by yielding of the vertical reinforcement.

Most of the research conducted on masonry shear walls (Shing et al. 1990; Brunner and Shing 1996; Ibrahim and Suter 1999; Miller at al. 2005; Voon and Ingham 2006) focused on evaluating the shear failure mechanism and the behaviour of walls failing in shear rather than walls failing in flexure. This might be attributed to the complexity of predicting the capacity of walls failing in shear compared to walls failing in flexure or perhaps it was because the flexural behaviour of RM shear walls is well understood. The flexural capacity was shown to be easily calculated with a reasonable degree of accuracy (Priestley 1986; Shing et al. 1989b). However, the ductility supply and energy dissipation capabilities of such walls are not well quantified, despite being the main factor needed to predict the structural performance under earthquake excitation. To better predict wall displacements at ultimate loads, wall ductility and plastic hinge length, l_p, need to be accurately determined.

1.5.2 Plastic hinge length

The flexural lateral displacement of cantilever walls can be easily predicted based on the approach described by Paulay and Priestley (1992) and illustrated in Fig. 1.1. Inelastic rotations of cantilever masonry walls, failing in flexure, tend to be concentrated at the base of the wall within what is called the plastic hinge zone.

Within this zone, large curvatures, compared to the curvature at yield stage, occur and significantly contribute to the top lateral displacement of the wall. Although, the moment varies linearly over the height, h_w, of a cantilever wall as a result of the concentrated force at the top, the actual curvature profile over the wall height is not linear and large inelastic curvatures occur at the base.

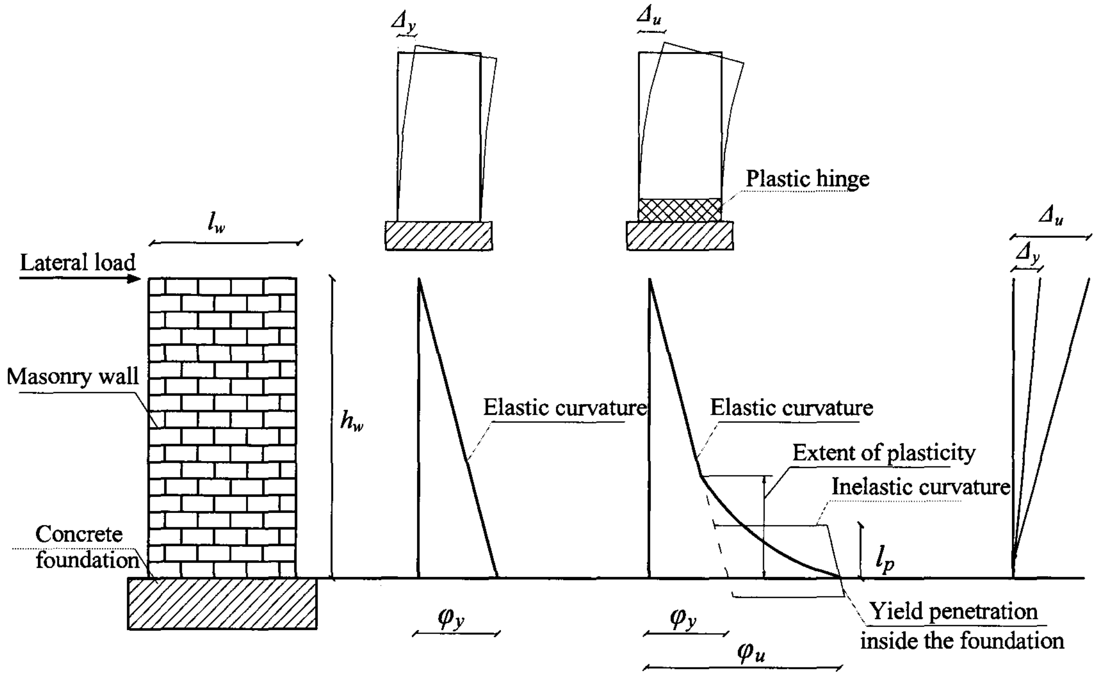

Fig. 1.1: Elastic and inelastic deformation

In order to idealize the actual curvature profile, Paulay and Priestley (1992) suggested representing it by an elastic region and a plastic region (within a length of l_p as the plastic hinge) to facilitate rotation calculation. The plastic rotation in this approach is assumed to act at mid-height of the equivalent plastic hinge length. The following equation, relating curvature ductility, displacement ductility, and equivalent plastic hinge length was proposed by Paulay and Priestley (1992) to predict lateral displacement of walls at ultimate load.

$$\mu_\Delta = 1 + 3 \times (\mu_\varphi - 1) \times \frac{l_p}{h_w} \times \left(1 - 0.5 \times \frac{l_p}{h_w}\right) \qquad \text{Eq. 1.1}$$

In the above expression, the curvature ductility, $\mu_\varphi = \varphi_u / \varphi_y$, is the ratio between the curvature at ultimate load, φ_u, and the curvature at yield, φ_y. The displacement ductility, μ_Δ, is the ratio between the displacement at maximum load, Δ_u, and the displacement at yield, Δ_y, assuming an elastic-plastic load-displacement relationship for the wall. If the equivalent plastic hinge length is assumed to be constant, an increase in the curvature ductility in this equation will result in an increase in the displacement ductility, μ_Δ. As will be explained later, this is related to the force modification factor used in design.

Plastic hinge length (or more correctly, equivalent plastic hinge length) is an important factor in modelling the inelastic response of shear walls subjected to earthquake loading since it influences the displacement at maximum load, Δ_u, and, consequently, affects the curvature ductility, μ_φ, required to attain a target displacement ductility, μ_Δ.

Flexural plastic hinging of masonry shear walls is not well quantified (Paulay and Priestley 1992; Drysdale and Hamid 2005; and Drysdale and Hamid 2008) where the scarcity of data related to this subject is evident from the widely differing, arbitrary, and changing expectations regarding the plastic hinge length. For this critical feature of seismic response, Paulay and Priestley (1992) reported equivalent plastic hinge lengths, l_p, between 30% to 80% of the wall length, l_w, whereas the USA Masonry Standard Joint Committee code (MSJC 2008) specifies that l_p is to be taken equal to l_w. The Canadian Standard Association in CSA S304.1 (CSA 2004) *"Design of Masonry Structures"* recommends the use of the smaller of $l_p = l_w/2$ or $h_w/6$ for walls with limited ductility but up to l_w for shear walls with moderate ductility, where h_w is the wall height. The Federal Emergency Management Agency document (FEMA-273/274, 1997) sets l_p equal to half the flexural depth of the wall cross section with an upper limit of one storey height. These ambiguities in estimating a parameter as fundamental as the equivalent plastic hinge length lead to inaccurate prediction of the wall displacement ductility, which is a major factor in determining the wall seismic demand (design force).

1.5.3 Intersecting walls

Despite the common occurrence of intersecting structural walls in buildings (see Fig. 1.2), little research has been carried out on the lateral load-displacement characteristics of flanged RM walls. For both RM and RC shear walls, the responses of I, T, L-shape walls are significantly different than that of rectangular walls (Priestley and Limin 1990; Thomsen and Wallace 2004; Orakcal and Wallace 2006).

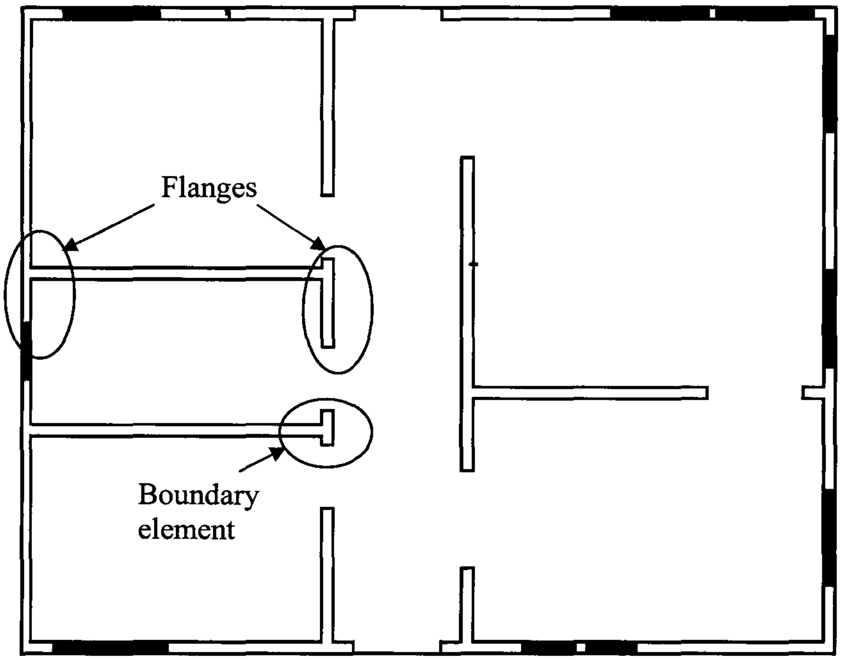

Fig. 1.2: Plan of a wall bearing building

Compared to rectangular walls, shear walls with flanges are characterized by a smaller compression zone which results in a significant increase in curvatures at ultimate load. The presence of flanges not only increases the curvature at ultimate load, but also reduces the curvature at the onset of yield of the vertical reinforcement. This can have a significant impact on the curvature ductility and subsequently on the displacement ductility. The flanges also increase the overall wall stability against out-of-plane buckling, and delay the occurrence of reinforcement buckling at the outermost end of the wall under compression.

Orakcal and Wallace (2006) indicated that the plane sections remaining plane assumption, which assumes that the entire flange is effective in compression, is appropriate. Alternatively, the measured tensile strains followed a nonlinear distribution across the width of the flanges. This is also consistent with the observations by Thomsen and Wallace (2004). The latter observation indicated that peak moment strength of walls with the flange in tension did not develop until high drift levels were reached. This is due to gradual yielding of the tension reinforcement within the flange, with reinforcement closest to the web–flange intersection yielding first. Subsequently, yielding of bars away from the web–flange intersection progressed as lateral drift levels increased. This observation implies that the assumption of a constant strain along the flange in tension is not correct and would lead to overestimation of the tensile strains of the reinforcing bars in the flanges resulting in overestimation of the lateral load capacity of the wall when the flange is in tension. In contrast, the measured compressive strains along the flange were nearly uniform for all drift levels. Orakcal and Wallace (2006) also indicated that the measured tensile strains in concrete tend to decrease suddenly at the web-flange intersection due to the abrupt change in cross section geometry.

1.5.4 Effect of detailing and bar buckling

Poor detailing of the connection between the web and the flange and lack of proper understanding of the role of the web and the flange can, however, results in an inferior response of walls with flanges as opposed to rectangular walls. Because of the reduced compression zone, flanged walls failing in shear can be more seriously affected by sliding shear than rectangular walls (Paulay et al. 1982). Sliding shear displacements can seriously affect the integrity of the flanges for shear walls responding beyond the elastic stage, as indicated by Paulay and Priestley (1992), due to increased crack size and reduced shear resistance. However in the elastic range, they concluded that as long as the cracks remain small, the shear strength is primarily due to aggregate interlock action which will be in excess of the diagonal tension or compression load-carrying capacity.

Observations of the responses of masonry shear walls indicated that the lateral load capacity of RM walls can be maintained for high drift levels well beyond the levels corresponding to maximum load (Shedid 2006). Almost no degradation of the lateral load capacity was observed even though toe crushing and spalling of the face shells of the end blocks occurred and minor cracks in the outermost grout columns were observed. Shedid et al. (2008) reported that it was only when splitting of the outermost grout column and buckling of the end reinforcing bars occurred that strength degradation became significant. The strength degradation was mainly due to damage in the masonry compression zone as well as the reduction of the strength due to buckling of the vertical bars in compression.

Based on experimental results, Bae et al. (2005) indicated that the post-buckling strength of a reinforcing bar can be as low as 20% of the yield strength and was associated with high lateral displacement of the bar. Moreover, the increase in the lateral displacement of the vertical bars accelerated the deterioration of the masonry compression zone with additional crumbling of the grout columns and the blocks observed.

Due to cyclic loading of flexural walls, high inelastic tensile strains occur in the vertical bars and result in wide horizontal cracks. During wall unloading (corresponding to changing the direction of load), tensile stresses in the bars reduce to zero, while the crack width remains large, as a result of plastic tensile strains that had been developed in the bars. As shown in Fig. 1.3, until the cracks close, the internal compression force, *C*, within the wall section, *b*, must be resisted solely by the vertical reinforcement. Paulay and Priestley (1993) indicated that even for RC walls with two layers of reinforcement as shown in Fig. 1.4 (a), the compression force, not being aligned with the centroid of the two vertical bars, would cause higher stresses on one bar compared to the other until closure of the horizontal crack occurs. In the case of RM walls (see Fig. 1.4 (b)), with a single layer of reinforcement, the situation is more extreme as there is no apparent stability provided by the reinforcement until the crack closes on one side of the wall, which leads to out-of-plane displacement of the wall. The use of flanges (by connecting intersecting walls) or enlarged boundary elements to stabilize masonry walls by preventing the out-of-plane displacement is, therefore, very beneficial for wall performance.

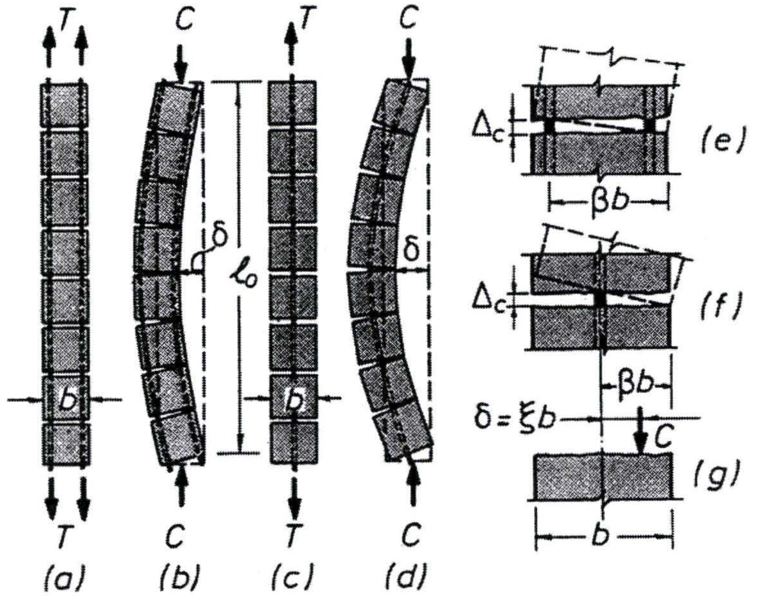

Fig. 1.3: Curvature and buckling of masonry walls (Paulay and Priestley 1993)

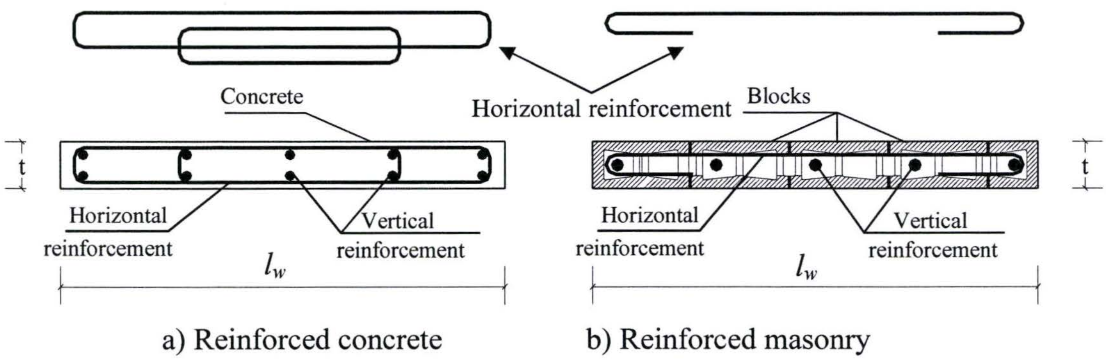

Fig. 1.4: Cross section of typical shear wall in a building

1.5.5 Walls with boundary elements

Walls with boundary element are rectangular walls with an enlarged thickness at the ends (see Fig. 1.2). Boundary elements for masonry walls, can be in the form of pilasters (or columns) at the ends of the walls. A pilaster can be constructed using additional blocks at the wall end or by using a pilaster unit.

Walls with boundary elements have the same previously discussed benefits of flanged walls. The behaviour is characterised by a small compression zone which decreases curvatures at the onset of yield of the vertical reinforcement and increases curvatures at ultimate conditions. This dual action, as explained earlier, will increase the curvature ductility and subsequently enhances the displacement ductility. Also, the enlarged wall end delays buckling of vertical bars, increases the stability of the compression zone and preserves the flexural strength of the wall. This further increases the ductility of the walls which in turn, increases the ductility modification factor of the wall which reduces the earthquake design load and thus achieves more economical masonry buildings.

In addition to all the aforementioned benefits, the use of a boundary element allows forming a closed tie instead of the typical 180° hook formed by the horizontal shear reinforcement in a RM wall. This accommodates more than one layer of vertical bars to provide a reinforcing cage to confine the region subjected to the high compressive stresses at failure, and prevent the buckling of the vertical wall reinforcement. The confinement provided by the transverse reinforcement can also increase the maximum compressive strain and strength of masonry and thus result in a more ductile behaviour, as will be explained in the following section.

1.5.6 Confining effect of transverse reinforcement

The available research on the confining effects of transverse reinforcement has been conducted on RC walls and columns. Lack of similar research on RM elements may be due to the typical use of rectangular RM walls having a single layer of reinforcement as opposed to walls with boundary elements. Since the general responses of RM and RC elements are similar, somewhat similar performances of RM and RC walls with attached boundary element would be expected.

In RC shear walls, the existence of more than one layer of vertical steel and closed transverse reinforcement in the form of rectangular ties provides confinement for the concrete and enhances the buckling resistance of the vertical reinforcement. Closely-spaced transverse reinforcement in conjunction with longitudinal reinforcement also restrains the lateral expansion of concrete inside the reinforcing cage. This enables higher compressive stresses and, more importantly, higher compressive strains to be sustained by the compression zone before failure occurs as opposed to unconfined concrete under uniaxial compressive stresses. A secondary purpose of closely-spaced closed transverse reinforcement is to delay the buckling of the vertical reinforcement in walls or columns and to enable the compression reinforcement to remain effective after the concrete cover has spalled. In the case of RM walls, almost no confinement of the zones under compression is achieved by having a single layer of vertical reinforcement and a single leg of horizontal reinforcement. Thus the common perception is that, compared to the confined concrete, the ultimate compressive strain of the unconfined masonry may be inadequate to allow the wall to achieve high levels of ductility without extensive spalling and deterioration of masonry units and grout columns.

When unconfined concrete is subjected to compressive stress levels approaching the crushing strength, high lateral tensile strains develop and result in the formation of longitudinal microcracks at peak-stress (see Fig. 1.5). The propagation of these cracks beyond peak stress results in instability of the compression zone, and eventually leads to failure. However, despite this eventual behaviour, for design purposes, strain at failure is not represented by the strain at peak-stress as relatively high compressive stresses can be maintained at much larger strains.

Since the early work by King (1946) on the effect of transverse reinforcement on RC columns, the amount of lateral confinement has been well recognized as an important factor affecting ductility of RC columns. Several research programs [Ozcebe and Saatcioglu 1987; Sakai and Sheikh 1989; Saatcioglu 1991; Wehbe et al. 1999; Sittipunt et al. 2001; Lam el al. 2003] were conducted later to investigate the effect of the amount, configuration, shape, and anchorage of transverse reinforcement on the response of RC column under axial load. Data from these programs indicated that confinement of the concrete core significantly improves column deformability and that longitudinal bars, if not enclosed by a corner of a hoop or a hook of a cross-tie, were incapable of providing sufficient confinement to enhance the deformability of plastic hinge regions.

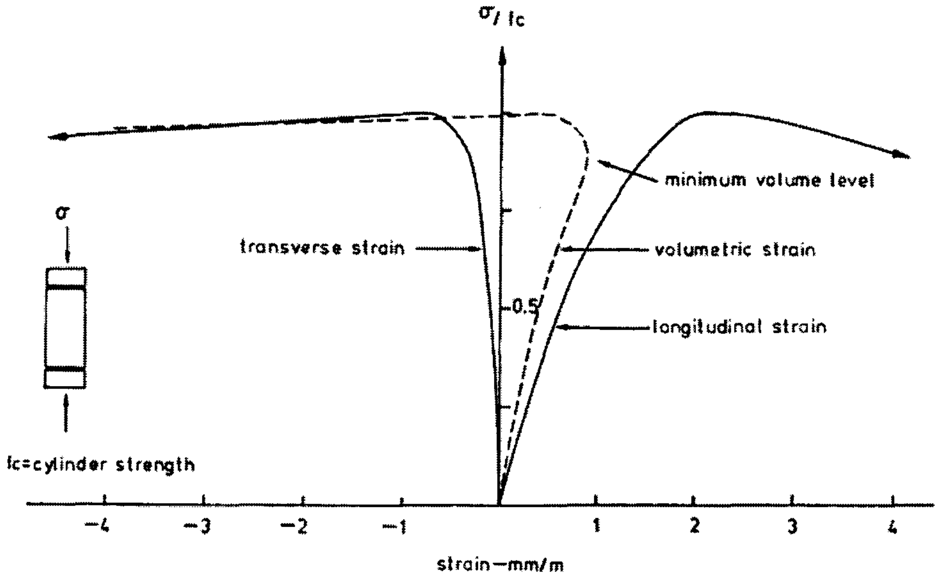

Fig. 1.5: Typical stress-strain curves of concrete cylinders tested under uniaxial compression (Park and Paulay 1975)

Confining transverse reinforcement may only be required in the highly stresses zones since the need to confine the entire section of a wall or a column would rarely arise. For the confinement to be effective, the vertical spacing of hoops should be limited to delay buckling of the longitudinal bars. During construction, the longitudinal reinforcement must be placed tightly against the transverse steel because the transverse steel provides confining reactions to the longitudinal bars. When movement of the longitudinal bars is necessary to bring them into effective contact with the transverse steel, the efficiency of the confinement is reduced.

1.5.7 Behaviour of confined and unconfined concrete

Prior to reaching the peak-stress for a uniaxilly loaded RC column, the stress-strain relationship is almost identical to a uniaxially loaded plain concrete column after excluding the increased capacity due to the compression reinforcement. However, at strains beyond the peak-stress, the response is quite different. For a uniaxially loaded plain concrete column, the most significant feature of the behaviour is the larger increase of lateral expansion that the specimen undergoes when the vertical strain exceeds the strain at the peak load, as seen in Fig. 1.5. In the absence of confining elements, this lateral expansion leads to rapid failure. This behaviour is quite different from that of an axially loaded confined RC column as several variables influence the descending curve, as explained by Park and Paulay (1975). Confinement restrains lateral dilatation (volume increase) of the concrete beyond peak-stress. Triaxial compression loading of plain concrete illustrates this effect. In the case of reinforced concrete elements confining reinforcement achieves some confinement (Lefas et al. 1990).

Based on tests of 25 RC columns, Scott et al. (1982) found that the appearance of vertical cracks in the concrete cover was always the first sign of distress in a columns and that these cracks spread rapidly as compression failure of the concrete cover caused it to spall. However, after the concrete cover spalled, a higher load could be achieved as the concrete core became confined by the hoops and longitudinal bars. Failure of the columns was associated with fracture of the hoops and buckling of the longitudinal bars at much higher strains. As the hoops failed, the now unconfined core concrete in their near vicinity was reduced to rubble.

The concrete strength, and the amount, spacing, yield strength, and size of transverse reinforcement have significant influences on the response of the specimen during the post-peak loading stage. Low strength concrete produces a more ductile behaviour than high-strength concrete, as the former is characterized by a less steep descending branch allowing for larger strains associated with a more sustained capacity (Park and Paulay 1975). A larger amount of transverse steel will produce an increase in lateral force to confine the concrete core. Reducing the spacing between the transverse steel hoops leads to more effective confinement of the concrete by reducing the total volume of unconfined concrete per hoop. As seen in Fig. 1.6, more closely spaced hoops also provide more uniform confinement and reduce the size of the less confined concrete between hoops.

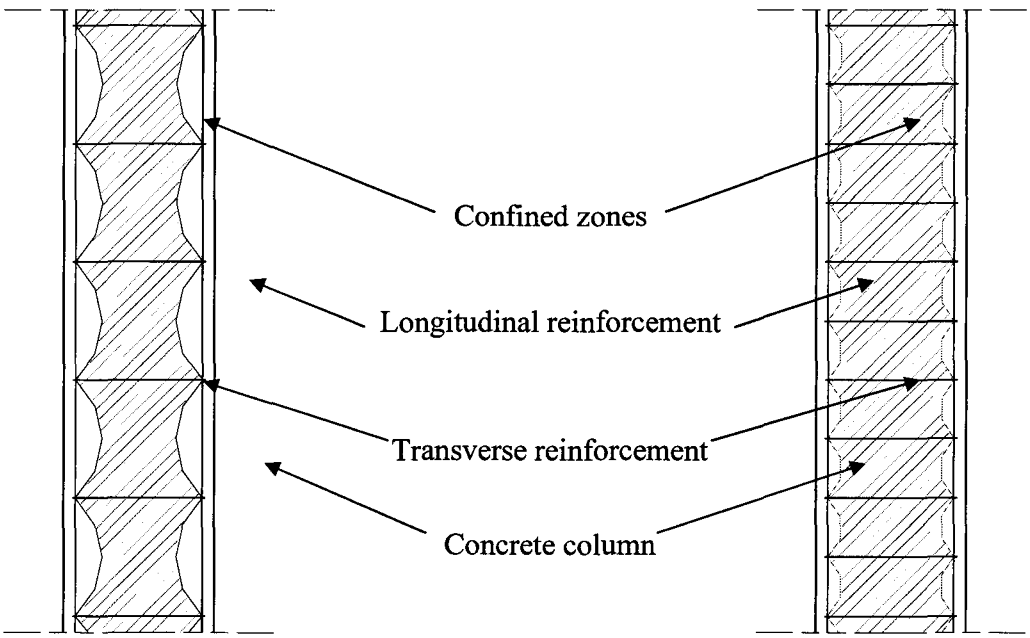

Fig. 1.6: Effect of spacing of transverse reinforcement on the confinement efficiency (redrawn from Park and Paulay 1975)

The yield strength of the transverse reinforcement determines the upper limit of the confining pressure on the core. As recommended by Priestley and Park (1987), the usable concrete compressive strain corresponds to the strain in the concrete when the transverse confining steel first fractures. In the case of rectangular stirrups or hoops, higher ratios of the diameter of the transverse bar to its unsupported length between the corners of the hoops lead to more effective confinement. Transverse bars of small diameter have low flexural stiffness and typically bow outward reducing the confined zone.

It is worth noting that axially loaded concrete cylinders or masonry prisms, having longitudinal reinforcement and widely spaced transverse reinforcement or no transverse reinforcement, can experience a steeper descending curve with less strain during the post-peak stage as opposed to unreinforced concrete cylinders or masonry prisms. This finding is explained by Priestley and Elder (1983) based on testing masonry prism with longitudinal reinforcement. They indicated that, if the reinforcement has yielded in compression when vertical splitting of the masonry face shells begins, the assemblage may be unable to restrain the steel from buckling laterally. This situation would create additional instability of the cracked assemblage and result in a more brittle failure. They also indicated that initiation of failure for prisms with longitudinal reinforcement was similar to unreinforced prisms; both failures resulted from vertical splitting of the face shells. The subsequent loss of lateral stability of the bars yielding in compression resulted in their tendency to buckle at high strains, causing more apparent damage to the prisms at the end of test than to prisms without reinforcement. On the other hand, significantly less damage and less steep descending branches are expected when closely spaced ties are provided to confine the vertical reinforcement and concrete core for RC elements.

1.5.8 Displacement ductility

For members and structures that exhibit near ideal elastic-plastic load-deflection behaviour as shown in Fig. 1.7 (a), it is generally agreed that calculation of displacement ductility, $\mu_\Delta = \Delta_u / \Delta_y$, can be carried out with little error either by using the actual yield displacement or by defining an effective yield displacement, Δ_y^{ep}, at the point where the elastic portion intersects the plastic portion of the load-displacement curve. However, for walls containing several reinforcement layers, load-displacement curves typically have yielding of the outermost tension bar at loads well below ultimate load, as illustrated in Fig. 1.7 (b).

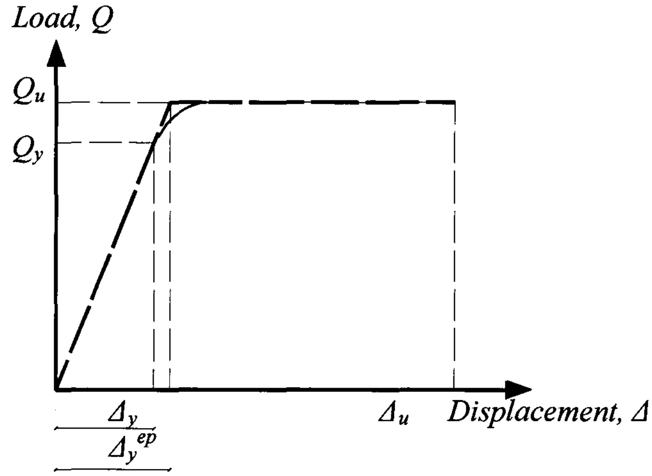

(a) Idealized elastic-plastic behaviour

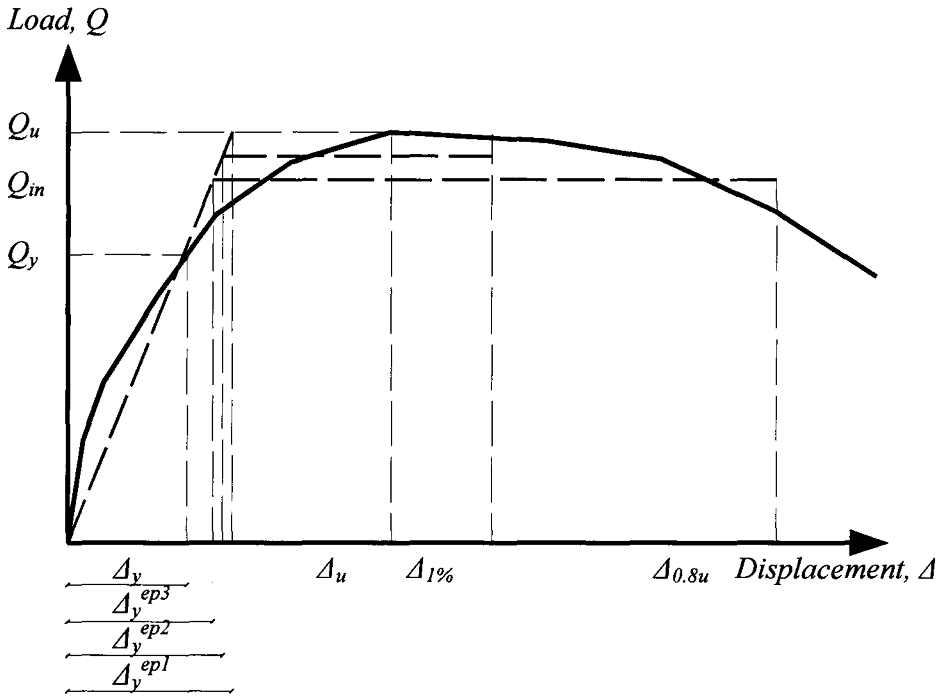

(b) Alternative definitions of displacement ductility

Fig. 1.7: Displacement ductility definitions

There are several useful discussions in the literature regarding the appropriate definition of displacement ductility (Park and Paulay 1975; Shing et al. 1989a; Paulay and Priestley 1992; Priestley et al. 1996; Tomazevic 1998), but there is no general consensus at this time. Therefore, some of the alternatives subsequently used to calculate ductility values from the test results are briefly discussed here.

Option 1. This option ignores the part of the load-displacement curve above yield strength and any post-peak capacity and uses an elastic-plastic idealization intersecting at the yield point, $\mu_{\Delta u} = \Delta_u / \Delta_y$.

Option 2. A very conservative alternative to Option 1 would be to define an effective yield displacement, $\Delta_y^{ep1} = \Delta_y (Q_u / Q_y)$ corresponding with the point where extension of the elastic line through the yield point reaches the maximum load, Q_u.

Option 3. A somewhat less conservative value of displacement ductility is to locate and define effective yield displacement so that the idealized curve has the same total energy under the curve as the actual data up to the displacement at maximum load.

Option 4. Displacement ductility can be related to a specific limit on displacement where it can be argued that additional ductility beyond that point cannot be taken advantage of. For example, if 1% drift is the stipulated limit, a simple approach is to use the yield displacement, Δ_y, with this definition of ultimate displacement $\Delta_{1\%}$ to give $\mu_{\Delta 1\%}$.

Option 5. This option is similar to Option 4 except that an effective yield displacement, Δ_y^{ep2}, is defined to provide equal energy under the curve up to the limiting displacement.

Option 6. It has been argued by some that there is considerable benefit of ductility that exists even when there is some degradation of capacity. A reasonable limit to strength degradation under such circumstance may be taken as 80% of Q_u and, simplistically, the displacement ductility $\mu_{\Delta 0.8u} = \Delta_{0.8u} / \Delta_y$ may be calculated.

Option 7. An alternative to Option 6 is to redefine an effective yield displacement, Δ_y^{ep3}, as the value that produces equal areas under the curves up to the displacement $\Delta_{0.8u}$.

In summary, there are several discussions in the literature regarding the appropriate definition of displacement ductility for behaviours that are not *ideally* elastic-plastic. However, as highlighted by Priestley (2000) and Priestley et al. (2007), there is no general consensus or a unified definition for the yield and the ultimate displacements. Shedid et al. (2010) showed that, for RM shear walls failing in flexure, the average wall capacity based on an elastic-plastic idealizations of the actual load-displacement responses using an the equal area approach was 97% of the measured capacities. Therefore setting the plastic strength of the idealized bilinear load-displacement relationship to be equal to the ultimate wall strength would simplify the evaluation of ductility and result in a slightly conservative approximation.

1.5.9 Seismic response modification factor

To account for the effects of ductility and energy dissipation through inelastic behaviour, seismic design can be carried out using prescriptive requirements that allow for a reduction in seismic design forces that were calculated based on elastic behaviour. In the USA, the calculated elastic force is divided by a force reduction factor, R, (ASCE-7, 2008), whereas, in the National Building Code of Canada (NBCC 2005), the elastic force is divided by the product of the ductility-related force modification factor, R_d, and the overstrength-related force modification factor, R_o. To determine the inelastic displacements based on the elastic design displacement, in the NBCC (2005) the elastic displacements are amplified by the product $R_d \times R_o$, whereas, in ASCE-7 (2008) the elastic displacements are amplified by a deflection amplification factor, C_d. In the ASCE-7 (2008), an R value of 5.0 is assigned to *Special reinforced concrete* shear wall buildings and to *Special reinforced masonry* shear wall buildings. However, in the NBCC (2005), reinforced masonry shear wall construction is considered to be relatively brittle compared to reinforced concrete shear walls. The Canadian code assigns a maximum reduction factor $R_d \times R_o$ of $2.0 \times 1.5 = 3.0$ for what is considered the most ductile system: *Moderately ductile reinforced masonry* shear wall buildings, whereas, for *Ductile reinforced concrete* shear wall buildings, the maximum assigned reduction factor $R_d \times R_o$ of $3.5 \times 1.6 = 5.6$. Therefore, based on the Canadian code, the seismic demand for reinforced masonry shear wall buildings will result in significantly higher design forces (87% higher) compared to similar reinforced concrete shear wall buildings. This preferential treatment of RC is not found in the American code provisions (ASCE-7, 2008).

The response modification factors were generally based on engineering judgment and on observation of the performance of different structural systems in previous strong earthquakes (Uang 1991). That study also suggested that it is difficult to justify the relative values of the factors R and C_d proposed in the American code, and that the factor R should be smaller than the factor C_d for various structural systems. Similarly, as stated in the ATC-63 (2008), little information is available to justify the use of these values and, furthermore, somewhat arbitrarily R factors were assigned to individual systems that have never been subjected to any significant level of earthquake ground shaking.

Many studies [Newmark and Hall 1973; Riddell and Newmark 1979; Elghadamsi and Mohraz 1987; Riddell et al. 1989; Nassar and Krawinkler 1991; Paulay and Priestley 1992; Vidic et al. 1992; Miranda 1993; Chopra 2000; and Drysdale and Hamid 2005] were conducted to quantify the effect of the structure's parameters on the ductility modification factor, R_μ. In general, for rigid structures having very short periods, the system will behave essentially elastically and thus $R_\mu = \mu_\Delta = 1$ (i.e., no modification), [Paulay and Priestley (1992), Chopra (2000), Drysdale and Hamid (2008)].

For structural systems having a long period of vibration, elastic and inelastic systems will have approximately the same displacement wherein the *equal displacement principle* (Fig. 1.8 (a)) is used to determine the relationship between μ_Δ and R_μ as $R_\mu = \mu_\Delta > 1$. For structures with short or moderate vibration periods, the *principle of equal energy* can be used in which case the energy under the load-displacement diagram of the elastic system up to the maximum displacement is equated to that of the elastic-perfectly plastic system subjected to the same excitation which will yield $R_\mu = \sqrt{(2\,\mu_\Delta\ -1}$ (see Fig. 1.8 (b)).

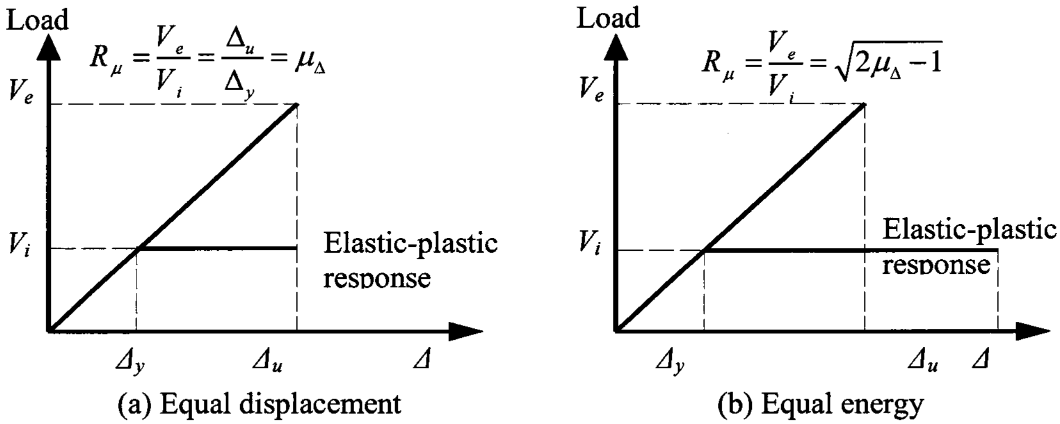

Fig. 1.8: Equal displacement and equal energy principles for calculation of response modification factors

1.6 Summary and conclusions

The literature survey showed that limited experimental data are available for flanged RM shear walls and almost no data related to RM shear walls with boundary element (end-confined walls) was found.

The values of equivalent plastic hinge length, l_p, found in the literature were quite scatter and were associated with rectangular walls. No separate guidelines available for flanged and end-confined shear walls were found. Previous work conducted on reinforced masonry shear walls indicate that ductile behaviour was achieved when rectangular shear walls were properly designed and detailed. However, ductilities of flanged and end-confined walls need to be quantified and compared to rectangular walls. Seismic performance parameters associated with this type of construction are also needed.

Values of seismic reduction factors in North American seismic codes were found to be, in many cases, based on previous experience or judgement. There is a great need to follow a more rational method to determine these values in order to provide uniform safety in design and equitable conditions for competing structural systems.

Chapter Two

Experimental Program

CHAPTER 2
EXPERIMENTAL PROGRAM

This chapter contains a detailed description of the experimental program and the wall test matrix used in this study. Material properties, specimen design and construction, reinforcement detailing, and predicted capacities and displacements were presented and discussed in detail. In addition, descriptions of the test setup and instrumentation are provided. The wall test matrix was based on two phases of testing. The first phase was comprised of three walls, W1, W2, and W3 *(Rectangular, Flanged, and End-confined)* tested under reversed cyclic loading, and the second phase of testing was comprised of four walls, W4, W5, W6, and W7, *(Rectangular, Flanged, and two variations of End-confined)* designed and constructed taking into account the observations and results from the walls tested in the first phase.

2.1 Introduction

Better understanding of the structural behaviour of concrete and masonry structures can be obtained through experimental testing. As discussed in the previous chapter, although some experimental testing of reinforced masonry rectangular walls is reported in the literature, little experimental data is available on reinforced masonry walls with flanges or with boundary elements.

The experimental program adopted in this study was designed to investigate the cyclic flexural response of reinforced concrete masonry rectangular walls, walls with flanges, and walls with boundary elements. The test matrix was developed to allow direct comparisons to evaluate the expected enhancement of wall ductility when flanges or boundary elements were added. An associated criterion was to investigate the influence of adding flanges or boundary elements on the stability of the compression zone. It was intended that all the test walls would be subjected to fully reversed displacement-controlled quasi-static cyclic loading with loading continued up to 50% degradation in strength in order to obtain information on the post-peak behaviour. Monitoring the propagation of damage and plastic deformation into the base was also an objective to assess the impact of this behaviour on overall wall ductility (Paulay and Priestley 1992). The effects of the various test parameters on the extent of plastic deformation over the wall height were also of interest.

Sections 2.2 to 2.5 describe the criteria for wall design, wall construction, reinforcement details, and wall design, respectively. The results of auxiliary tests on masonry assemblage and constituent materials are presented in Section 2.6. This is followed by details of the test setup and instrumentations in Sections 2.7 and 2.8. The chapter concludes with documentation of the test procedure and final comments.

2.2 Criteria for wall design

2.2.1 Selection of shear wall dimensions

For a typical mid-rise (e.g. 5 storeys) masonry building, wall lengths can vary between 2 m to 8 m resulting in an aspect ratio of at least 1.5, and an axial compressive stress ranging, on average, from 1 MPa to 2 MPa (i.e., 0.2 to 0.4 MPa per floor).

Laboratory testing of full scale masonry walls can be impractical due to space limitations, construction and testing constraints, and financial restrictions. Even with the 10 m head room and the strong structural floor in McMaster University's Applied Dynamics Laboratory (ADL), testing of full scale structures is limited. An alternative solution is to model full scale elements using reduced scale masonry units. Half scale versions of reinforced concrete masonry shear walls failing in flexure were tested by Long (2006) and compared well with the full scale versions tested by Shedid (2006), in terms of strength and displacement.

The idea of testing a wall having a compression zone depth greater than one block long was an important criterion in wall dimension selection in order to ensure that compressive strength and damage to the compression zone would have significant effects. Similarly, it was important to have the whole area of the boundary elements and the flanges and possibly even several layers of reinforcement under compression. In addition, to realistically represent shear wall behaviour when governed by flexure, a reasonable aspect ratio was also a controlling condition in the selection of the wall dimensions. Since squat or near squat walls (h_w/l_w=1.0) are special case for behaviour, an aspect ratio above this was desired.

Due to test facility limitation in the ADL, a reasonable height limit for testing, that does not raise concerns with regard to safety or require a complicated procedure to stiffen the reaction frame, is about 5.6 m. Based on this value, it was desirable to limit the height of the test specimen in Phase I to be about 4.0 m. This dimension along with the wall foundation (400 mm), the base slab (600 mm), and the top loading beam (200 mm), resulted in the highest point of the test specimen being close to the 5.6 m height.

Using half scale blocks, a reasonable number of storeys to model was 3, assuming a floor height of about 1.2 m (2.4 m in full scale construction). Based on both the compression zone and aspect ratio consideration, the wall length was selected to be 1.8 m (representing a 3.6 m long wall) containing 19 cells which allowed for several possible uniform arrangements of vertical reinforcement (e.g., every cell, every other cell, and every third cell). Therefore, in Phase I, the aspect ratio of the test walls was h_w/l_w= 2.2. However, based on the test results in Phase I, discussed in Chapter 3, it was observed that the third storeys sustained almost no cracking and, based on the analysis of strains and curvatures, it was found that the third storeys of the walls behaved in a linear elastic manner. Therefore, it was decided that, in Phase II, the wall cross sections would be kept the same as those of Phase I but two storey high walls with aspect ratio of 1.5 would be tested. This change of the wall height would also facilitate investigating the effect of the wall aspect ratio on the extent of the plastic hinge zone.

2.2.2 Blocks used and wall cross-section

The standard 2-cell hollow 20 cm concrete block (190×190×390 mm) widely used in Canada was scaled to 50 percent and used for construction of the test walls [Note that the actual scale was 47.2 percent due to using a 90 mm height corresponding to the height of a full scale units]. Full scale and half scale block dimensions were presented in Fig. 2.1. The pilaster units, shown in Fig. 2.1, were used in one of the end-confined walls constructed in Phase II.

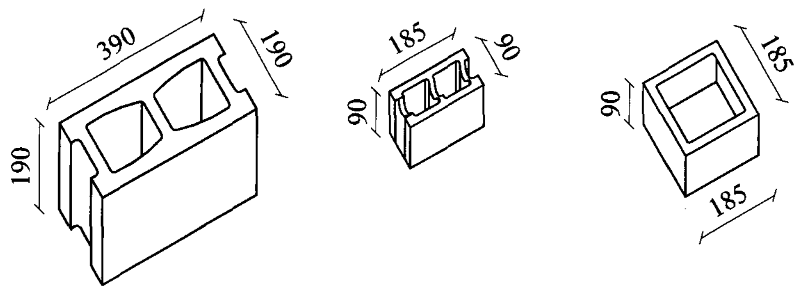

a) Full scale b) Half scale c) Half scale pilaster block

Fig. 2.1: Overall dimensions of block (all dimensions in mm)

To achieve the selected wall length (1.8 m), each course of the rectangular walls (W1 and W4, in Table 2.1) was constructed using nine and one half blocks, as shown in Fig. 2.2. The flanged walls (W2 and W5) had the same total length as the rectangular walls and were constructed using eight and one half blocks along the web and one and one half blocks (282 mm) placed perpendicular to the web (90 mm) at each wall end, as shown in Fig. 2.2. The end-confined walls (W3, W6, and W7) had the same overall length as the rectangular and the flanged walls, and were constructed using seven and one half blocks along the web. The boundary elements for Walls 3 and 6 were composed of two blocks (185 mm × 90 mm each) placed adjacent to each other and rotated 90° in successive courses. For Wall 7, a pilaster unit (185 mm × 185 mm) was used.

Steel D4 deformed wires (25.4 mm^2) were used as horizontal reinforcement and were fitted within the existing 30 mm notch in the webs of the half scale blocks. In the flanged and end-confined walls, the face shells of the blocks located in the boundary element units were saw cut to a depth of 20 mm to accommodate the shear reinforcement. This construction detail formed a continuous horizontal cell that accommodated the shear reinforcement along the entire length of the wall and provided full embedment of the horizontal wires in the grout.

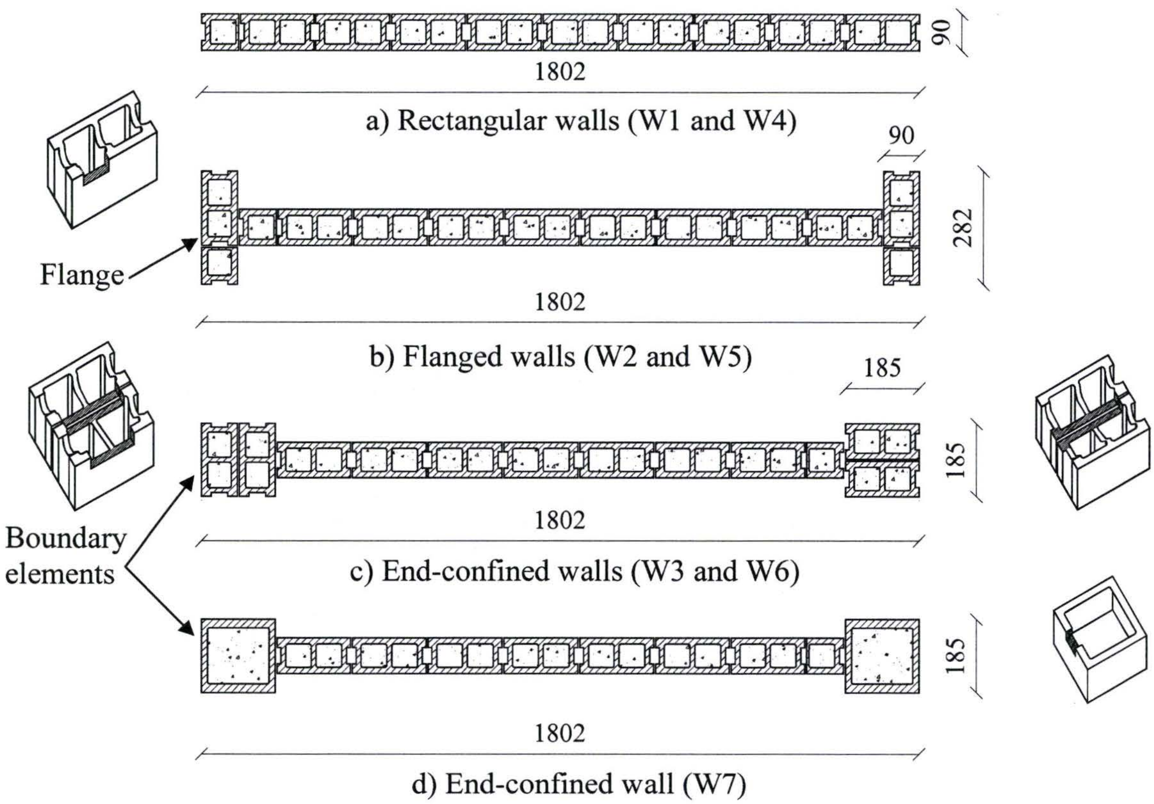

Fig. 2.2: Cross-section of the test walls (all dimensions in mm)

2.3 Shear wall construction

The construction of the test walls up to the first storey was divided into four stages starting with pouring the reinforced concrete foundation, then building the walls up to the storey height, followed by grouting the walls solid, and finally by the construction of the reinforced concrete slab portion representing the storey floor. For the remaining storeys, a similar procedure was followed.

2.3.1 Wall foundation construction

Reinforced concrete foundations were designed to provide fixed end conditions at the bottom of the walls. These foundations were designed to remain uncracked during testing and had dimensions of 2,300 mm long × 500 mm wide × 400 mm deep. As shown in Fig. 2.3, to provide a fixed end condition at the base of a wall, the vertical reinforcement was anchored in the reinforced concrete foundation, based on the requirements specified in CSA A23.3 (2005). Additional longitudinal and web reinforcement were provided in the foundation as a precaution in the event that cracking occurred

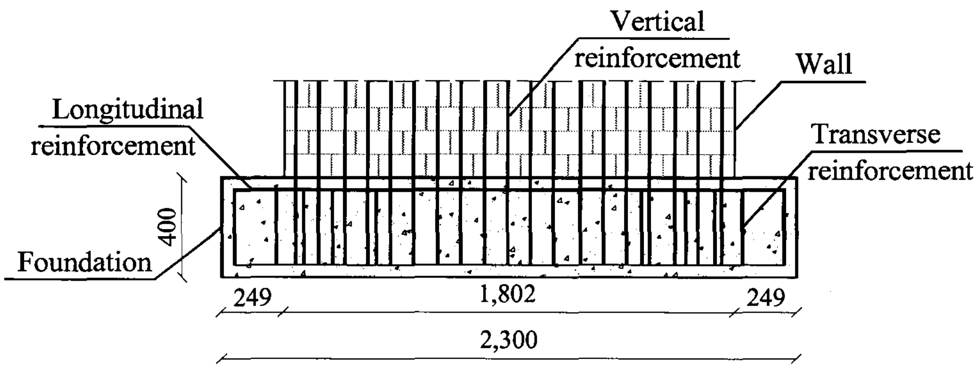

Fig. 2.3: Details of wall reinforcement in the foundation (all dimensions in mm)

In Phase I, the concrete was poured in the forms with the vertical reinforcement for the walls extending up to about 2.0 m above the foundation (mid-height of the wall). After the construction of the first half of the second storey was completed, 2.4 m long bars were welded to the existing vertical reinforcement using an extra 90 mm splice bar on each side of the spliced bar. For the 2.6 m high walls in Phase II, the reinforcement extended to the entire height of the walls. Although it caused some complications in construction due to threading the blocks over the reinforcement, this method of reinforcing was required to avoid lap splices in the expected plastic hinge region which would complicate interpretation of the test results. [Existence of splice lengths in reinforcement in the plastic hinge region is outside the scope of this research.] As the photograph in Fig. 2.4 shows, a temporary wooden frame was constructed to hold the vertical steel bars in place during placing of the concrete in the foundations.

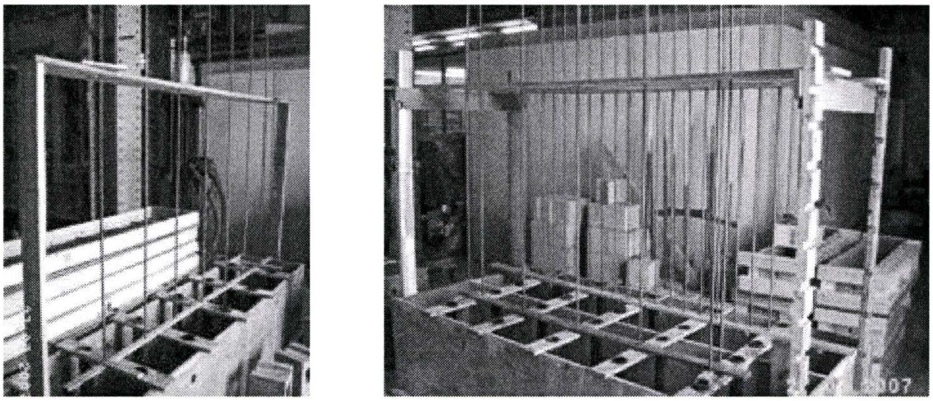

Fig. 2.4: Temporary support of vertical steel during concreting of the foundations

Ten plastic tubes (50 mm outer diameter) were placed vertically in each foundation to create openings in the foundation to accommodate the post-tensioning rods. These rods were used to fasten the foundation of the wall specimen onto a reusable concrete floor slab used in testing. Figure 2.5 contains the details of the wall locations on the reinforced concrete foundations as well as locations of the holes for post-tensioning. All tubes were carefully secured inside the wooden forms prior to concrete pouring in order to accurately maintain their locations and prevent filling the tubes with concrete.

2.3.2 Wall construction

An experienced mason constructed all wall specimens in a running bond pattern with face shell mortar bedding using half scale (5 mm) mortar joints. The properties of the mortar were controlled by drying the sand and preparing the mortar batches using proportions by weight including the water. Flow tests on each mortar batch provided a measure of the workability and served as an indicator of any differences in mix proportions. During construction, the concrete blocks were threaded over the vertical reinforcing bars extending over 2.0 m above the foundation.

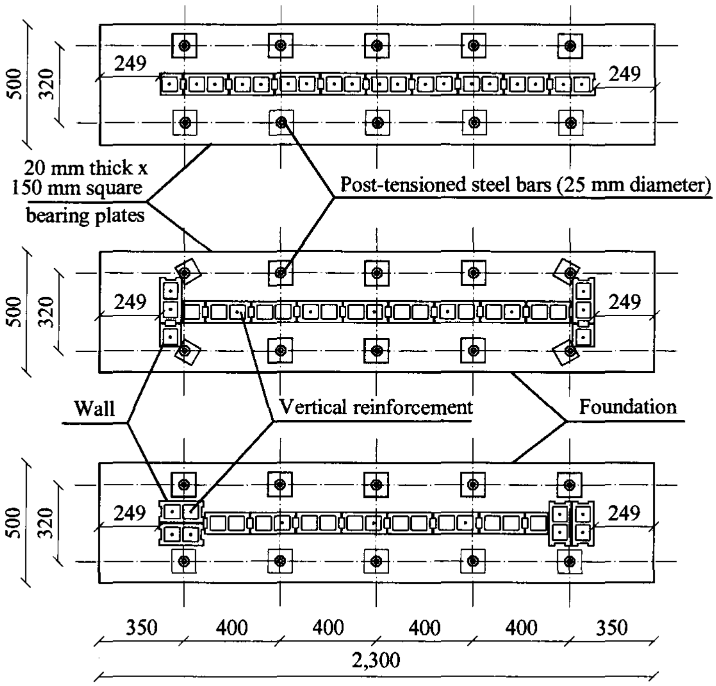

Fig. 2.5: Details of the foundation and location of wall (all dimensions in mm)

The height of the walls in Phase I consisted of 39 block courses (13 courses per storey) and 3 reinforced concrete slabs (100 mm each), and in Phase II consisted of 26 block courses and 2 reinforced concrete slabs. The walls were constructed in single wythe construction, except at the end zones for the flanged and end-confined walls. All specimens were fully grouted and the vertical and horizontal reinforcement were uniformly distributed over the walls.

The horizontal reinforcement in the rectangular walls formed 180° hooks around the outermost vertical reinforcement. As shown in Fig. 2.6 (a), the 200 mm return leg of the hook extended to the third last cell to provide adequate development length. For the flanged wall in Phase I, the horizontal reinforcement along the web was bent 90° in the flanges and an additional length of bar was added along the width of the flanges. Based on the observed failure mode of the flanged wall during Phase I, the horizontal reinforcement in Phase II, was bent 90° in the flange and then 180° around the outermost reinforcement in the flange, as shown in Fig. 2.6 (b).

For the end-confined walls, the horizontal reinforcement along the web was developed inside the boundary zone using a 90° bend around one of the outermost vertical bars. For the boundary elements composed of half scale blocks in the end-confined walls, closed ties were provided around the 4 end bars as shown in Fig. 2.6 (c), whereas, 6 mm spiral reinforcement (Fig. 2.6 (d)), having a 30 mm pitch, was used within the pilaster units.

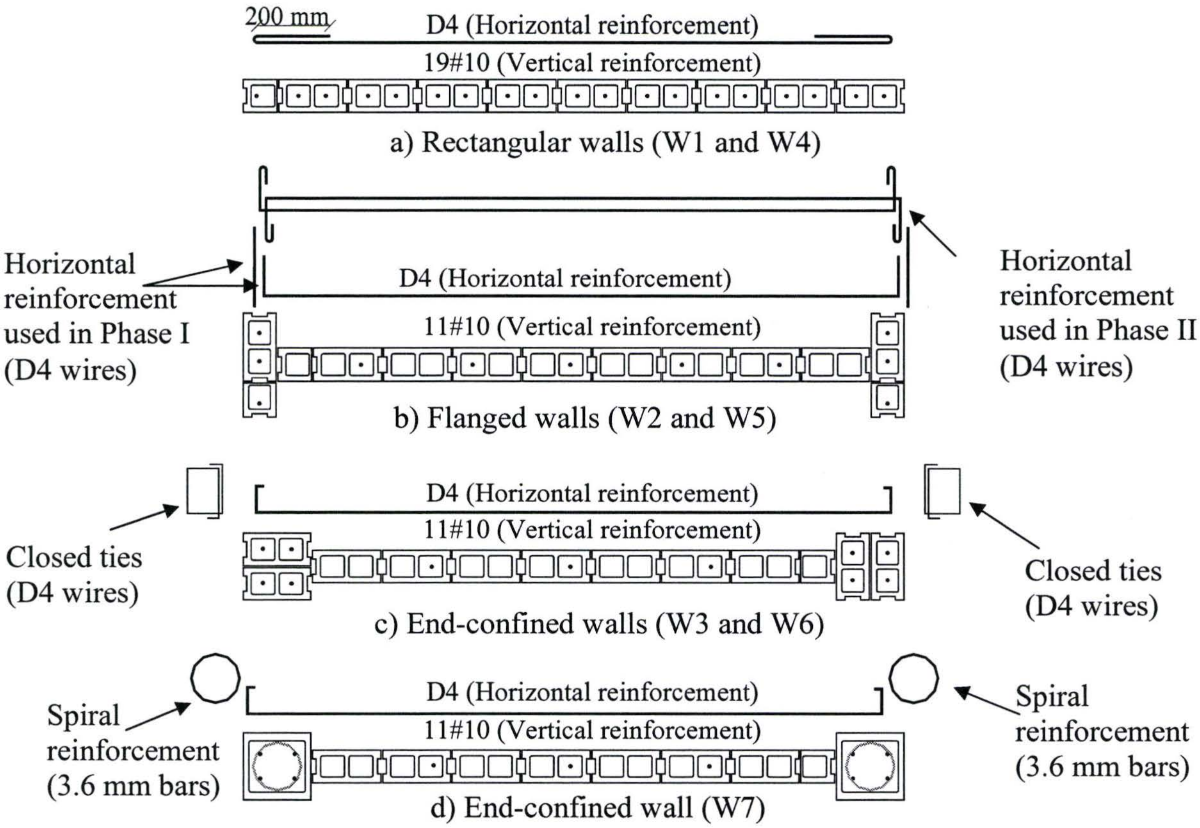

Fig. 2.6: Details of horizontal and vertical reinforcement in the test walls

2.3.3 Grouting of the walls

Grouting of the walls was accomplished using fine grout having, on average, 280 mm slump. The grout was mixed in the laboratory and grouting for each storey was conducted in two stages to ensure complete filling of the cells (construction and grouting of the first 7 courses in stage 1 followed by construction and grouting of the remaining six courses in stage 2). Rodding of the hollow cells before grouting was important to clear the path for the grout from any small amount of hardened mortar obstructions created during construction. The high workability of the grout as well as the vibration of the vertical reinforcement (No. 10 bars) of the wall was employed to ensure grout filling of the cells. For the cells not containing vertical bars, a No. 10 bar was used to rod the grout and was also vibrated to insure consistency; it was gradually removed as grouting progressed.

2.3.4 Floor slabs

Reinforced concrete slabs were cast at the specified wall heights to represent the floor at each storey. The slabs were 100 mm thick (200 mm in full scale construction) and extended the whole length of the wall with an overhanging width of 150 mm on each side of the wall. The floor slabs were also used to anchor the out-of-plane bracing as will be discussed in Section 2.7. The slabs were reinforced using 2 No. 10 bars in the longitudinal direction and No. 10 bars spaced at 300 mm in the transverse direction. Once the construction and grouting of the wall representing each storey was completed, formwork for the slab was constructed and the slab reinforcement was placed (See Fig. 2.7). Then the concrete was cast.

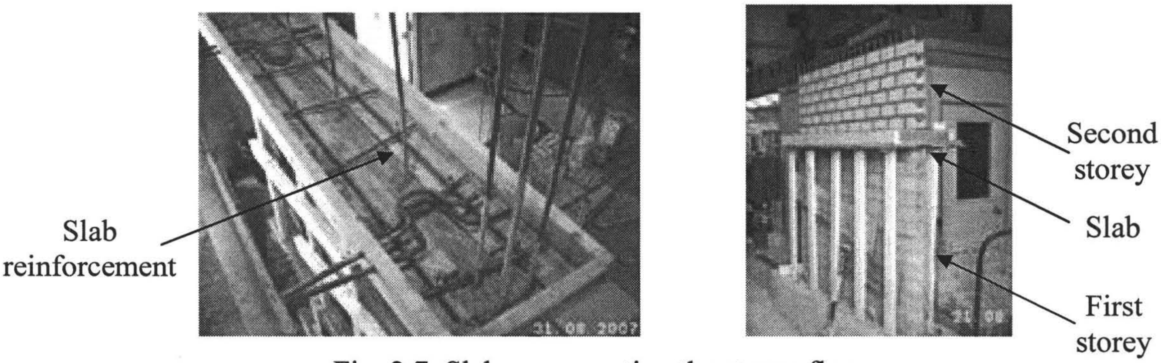

Fig. 2.7: Slabs representing the storey floors

2.4 Details of shear wall test specimen

This section provides details of each test specimen regarding wall dimensions and reinforcement. The predicted flexural and shear strengths and top deflections of all walls are presented in the next section. As closely as was practical, the walls in each phase were designed to have nearly the same flexural capacity under constant axial load.

Details of the reinforcement for the walls are shown in Fig. 2.8. All walls in Phase I were 3,990 mm high × 1,802 mm long resulting in an aspect ratio of 2.2, whereas, all walls in Phase II were 2,660 mm high × 1,802 mm long resulting in an aspect ratio of 1.5.

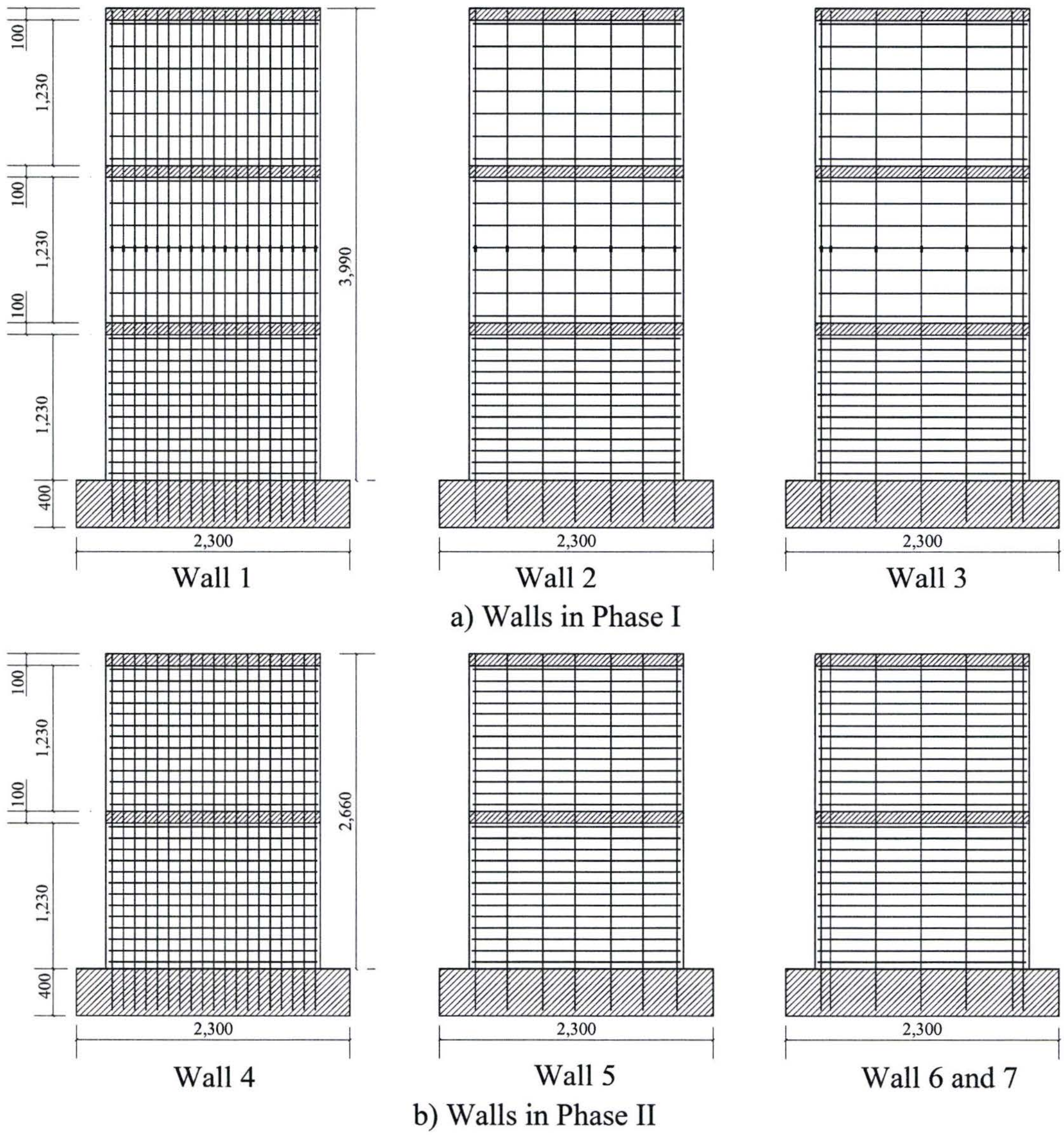

Fig. 2.8: Reinforcement details for the test specimens

The test wall reinforcement ratios, numbers of bars, and levels of applied axial stress are listed in Table 2.1. The areas of the vertical and horizontal reinforcement are also described as percentages of the gross areas of the horizontal and vertical masonry cross section, respectively. The horizontal reinforcement indicated in Table 2.1 was reduced to half over the upper storeys for Walls W1, W2, and W3 in Phase I, as will be explained later. Two D4 wires were used in every course for Walls W4, W5, W6, and W7 in Phase II compared to using a single D4 wire for the walls in Phase I.

Table 2.1: Matrix for test walls

	Specimen designation	Wall dimensions	Vertical reinforcement		Horizontal reinforcement		Axial stress (MPa)
			Number and size of bars	ρ_v (%)	No. D4 @ spacing (mm)	ρ_h (%)*	
Phase I	W1	1,802 mm ×3,990 mm (Length × Height)	19 No. 10	1.17	1 @95	0.30	1.07
	W2		11 No.10	0.55	1 @95	0.30	0.89
	W3		11 No.10	0.55	1 @95	0.30	0.89
Phase II	W4	1,802 mm ×2,660 mm (Length × Height)	19 No.10	1.17	2 @95	0.60	1.07
	W5		11 No.10	0.55	2 @95	0.60	0.89
	W6, W7		11 No.10	0.55	2 @ 95	0.60	0.89

* As shown in Fig. 2.8, the spacing of horizontal reinforcement was increased in the upper storeys of walls in Phase I.

The rectangular walls (W1 and W4), flanged walls (W2 and W5), and the end-confined walls (W3, W6, and W7) had vertical steel ratios of 1.17%, 0.55% and 0.55%, respectively. The total axial compressive stresses including self weight were 1.09 MPa, 0.89 MPa, and 0.89 MPa, at the base of the three storey walls corresponding to the rectangular, flanged, and end-confined walls, respectively.

All walls in each phase were designed to resist almost the same lateral load at 0.003 ultimate masonry compressive strain while subjected to the same magnitude of axial compressive load (160 kN), resulting from the same tributary area. This was the design criterion selected to illustrate the effect on the cyclic behaviour, ductility, and post-peak response of adding flanges or boundary elements onto rectangular walls

2.5 Design of test specimen

The methods used in the flexural and the shear design of the test specimen, and the basis for the top wall deflection predictions are presented in this section. All walls were designed to fail in flexure with a reasonable safe margin for shear capacity.

2.5.1 Design for flexure

All walls were designed to exhibit ductile failure but, particularly for the rectangular walls, a relatively large amount of reinforcement was used. Walls with large amounts of reinforcement tend to be less ductile than is the case for low (0.2%) or moderate (0.5%) amounts. The amount of reinforcement was calculated for the walls to result in the same ultimate capacity based on the requirements of CSA S304.1 (2004) but excluding the material resistance factors. In these standards, the equivalent rectangular stress block uses a stress of 0.85 f'_m, a depth of rectangular stress block equal to 80% of the distance to the neutral axis, and a limiting extreme fibre compressive strain of 0.003. Predictions of strength were done twice; first, the influence of compression reinforcement, A_s', was neglected and then the compression reinforcement was included in the calculation. All calculations were based on yield strength of 495 MPa (idealized elastic-plastic curve), and 515 MPa for the vertical reinforcement and the horizontal wires, respectively, and masonry compressive strength, f'_m, of 13.5 MPa.

Table 2.2 contains the amount and the percentage of vertical reinforcement, the load at calculated flexural capacity, Q_u, the external applied axial compression load, P, and the axial compressive stress, σ, at the base of the wall (P + self weight). For ease of reference, the axial compression stress, σ, also was expressed as a percentage of the masonry compressive strength, f'_m.

Table 2.2: Predicted flexural strength

	W1	W2	W3	W4	W5	W6	W7
Vertical reinforcement	19 # 10	11 # 10	11 # 10	19 # 10	11 # 10	11 # 10	11 # 10
ρ_v	1.17	0.55	0.55	1.17	0.55	0.55	0.55
P (kN)	160	160	160	160	160	160	160
σ (MPa)	1.07	0.89	0.89	1.07	0.89	0.89	0.89
σ (%f'_m)	7.9	6.6	6.6	7.9	6.6	6.6	6.6
Q_u (kN) (without A_s')	138	142	141	207	213	212	212
Q_u (kN) (with A_s')	160	156	154	240	234	231	231

2.5.2 Design for shear

Walls in Phase I were designed to have about 22% higher shear capacities than the shear forces (within the plastic hinge region) corresponding to the predicted flexural strengths discussed in the previous section. The shear equations specified in CSA S304.1 (2004) were used to calculate the amount of horizontal reinforcement needed in walls to achieve a safe margin against shear failure. Factors that account for variability in construction and in response were removed for these calculations, and only the total length of the wall and the thickness of the wall webs were used in the calculation. Table 2.3 contains the calculated shear strengths provided by the horizontal reinforcement, V_s, and by the masonry, V_m, as well as the shear capacity of the walls, V_u^s.

Based on the shear demand for walls in Phase I, horizontal reinforcement was provided every other course (i.e., spaced @ 190 mm) to ensure adequate shear capacity outside the expected plastic hinge region (second and third storeys). In the CSA S304.1 (2004), only half of the contribution of the masonry was accounted for in the shear strength, V^*_m, calculation inside the plastic hinge zone. The shear strength of the wall inside the plastic hinge zone, V_u^{s*}, based on spacing of 190 mm for the horizontal reinforcement, will not ensure a flexural failure as represented by the lateral loads listed in Table 2.2. Therefore, the horizontal reinforcement in the expected plastic hinge zone, assumed at this stage to extend over the first storey only, should be provided every course (95 mm). The increase in the amount of shear reinforcement in the first storey will increase the shear strength of the walls, V_u^{s*}, to more than 193 kN, assuming the calculation is conducted in the plastic hinge region.

Table 2.3: Predicted shear strength

Wall	Compressive stress (MPa)	V_s (kN)	V_m (kN)	V_u^s (kN)	V^*_m (kN)	V_u^{s*} (kN)
W1	1.07	134	126	260	63	197
W2 & W 3	0.89	134	118	252	59	193
W4	1.07	268	126	394	63	331
W5, W6 & W7	0.89	268	118	386	59	327

V_s is the shear force carried by the horizontal reinforcement

V_m is the shear force carried by the masonry

V^*_m is the masonry shear strength inside the plastic hinge region

V_u^s is the maximum shear strength of the wall

V_u^{s*} is the maximum shear strength inside the plastic hinge region

A limitation of the maximum possible shear capacity of a masonry wall is specified in CSA S304.1 (2004). Based on the wall dimensions and the masonry compressive strength, it was equal to 215 kN. This limiting shear capacity would, therefore, imply that the two storey walls constructed in Phase II would unavoidably fail in shear. However, based on the experimental results presented by Miller et al. (2005), the upper limiting values specified in CSA S304.1 (2004) and the MSJC code (2008) were considered to be very conservative. Therefore, in the design of the walls in Phase II, this limiting value was ignored.

In order to use the same type of shear reinforcement for of all the test walls, the same D4 wires, used in Phase I, were used for walls in Phase II. Due to the limitation in the spacing between the horizontal reinforcement (multiples of course height (95 mm)) and the need to use the D4 wires, the shear capacity of the walls in Phase II was significantly higher than the flexural capacity.

2.5.3 Prediction of deflection at the top of the walls

When designing the walls, flexural deflections at initial yielding of the outermost tension reinforcement and at ultimate conditions were predicted using beam theory and assuming that plane sections remaining plane after cracking. The equivalent plastic hinge length, l_p, was assumed to be equal to half of the wall length for all specimens (l_p = 900 mm) for prediction of deflection at ultimate load. It was expected that the experimental lateral deflections of the walls would significantly exceed the predictions due to the additional contributions of shear and sliding deflections not accounted for in the predictions. It could be expected that the shear deflections would be about 30 percent of the total deflection for the rectangular concrete masonry shear walls with an aspect ratio of 2.0, as demonstrated by Shedid et al. (2009).

Table 2.4 contains the predicted values of lateral deflections of the walls at the onset of yield of the outermost vertical reinforcement, Δ_y, and at maximum load, Δ_u, corresponding to a maximum specified masonry compressive strain. The predicted lateral deflections were calculated based on the theoretical curvatures, φ_y and φ_u, at the base of the wall at the onset of yield of the outermost vertical reinforcement and at maximum load, respectively. Deflection predictions were initially done by neglecting the influence of the compression reinforcement and then by including the compression reinforcement, as was the case in the strength calculation. All calculations were based on steel yield strength of 495 MPa (based on an elastic-plastic stress-strain curve), masonry compressive strength, f'_m, of 13.5 MPa, and a maximum specified masonry compressive strain of 0.0025, as recommended by CSA S304.1 (2004) for ductility calculations.

Table 2.4: Predicted flexural deflections

Wall	Without A_s'						With A_s'					
	Z^* (mm)	$\varphi_y \times 10^{-6}$ (rad/mm)	Δ_y (mm)	c^{**} (mm)	$\varphi_u \times 10^{-6}$ (rad/mm)	Δ_u (mm)	Z^* (mm)	$\varphi_y \times 10^{-6}$ (rad/mm)	Δ_y (mm)	c^{**} (mm)	$\varphi_u \times 10^{-6}$ (rad/mm)	Δ_u (mm)
W 1	496	1.96	10.5	606	4.13	17.3	469	1.92	10.2	534	5.60	19.0
W 2	428	1.86	9.9	280	10.70	38.1	465	1.84	9.7	202	12.38	43.3
W3	467	1.90	10.0	279	10.71	38.2	419	1.85	9.8	209	12.51	42.1
W4	496	1.96	4.6	606	4.13	8.9	469	1.92	4.5	534	5.60	10.0
W 5	428	1.86	4.4	280	10.70	22.0	465	1.84	4.3	202	12.38	25.3
W 6	467	1.90	6.5	279	10.71	22.1	419	1.85	4.4	209	12.51	24.5
W 7	467	1.90	6.5	279	10.71	22.1	419	1.85	4.4	209	12.51	24.5

* Length of the compression zone based on linear elastic analysis.

** Length of the compression zone at ultimate conditions.

2.6 Material properties

2.6.1 Steel properties

Tension tests were conducted on the reinforcement to determine the yield strengths for the steel used in wall construction. Five 600 mm long tensile specimens for each of the No.10 bar, D4 wires, and smooth bars, representing the vertical, horizontal, and spiral reinforcement, respectively, were tested to determine the stress-strain characteristics. The results of the tensile tests were summarized in Table 2.5. All of the reinforcement was ordered at the same time and it was specified to be supplied from the same batch and have the same heat number to eliminate larger variations in steel properties.

Stress-strain curves for the No. 10 reinforcement, presented in Fig. 2.9, indicated that there is no well defined yield point or yield plateau for the vertical reinforcement used in the walls. The yield strength of the bars, f_y, was then determined using three different methods, the 0.002 strain offset method, the

ASTM A1035/A1035 M Standard 0.005 strain method (ASTM 2007), and a bilinear elastic and strain hardening stress-strain relationship, as shown in Fig. 2.9.

Table 2.5: Steel properties

	Yield strength (MPa)						
Specimen	1	2	3	4	5	Average	*c.o.v.* %
No.10 (93 mm^2)	501	506	479	495	498	495	1.99%
D4 wires (25.4 mm^2)	546	540	537	523	525	534	1.85%
Smooth bars (10.1 mm^2)	695	690	701	702	699	698	0.71%

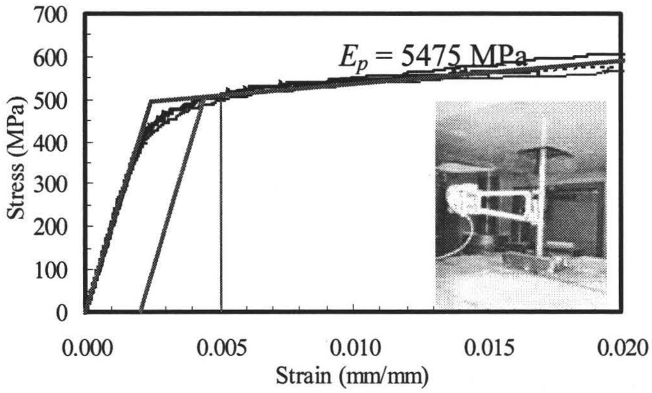

Fig. 2.9: Stress-strain curves for No. 10 bars

For the No. 10 bars, the offset method defines the yield strength as 497 MPa (*c.o.v* = 2.29%) corresponding to the intersection of the line starting at 0.2% strain with a slope equal to the Young's modulus of steel and the actual stress-strain relationship of the tested reinforcement. The ASTM A1035/A1035 M Standard (ASTM 2007) defines the yield strength as 498 MPa (*c.o.v* =1.72%) corresponding to the 0.005 strain level. The third method, which was used in this study to define the characteristics of reinforcement for predicting the wall capacities and in analyzing the test wall, was based on idealizing the actual stress-strain to a bilinear elastic-strain hardening relationship and resulted in average yield strength of 495 MPa (*c.o.v.* =1.99%), using an average young's modulus of 200.6 GPa (*c.o.v.* =2.15%). The strain-hardening modulus was taken equal to 5,475 MPa.

2.6.2 Properties of concrete in the foundation

Five standard 152 mm diameter × 300 mm high cylinders were tested to determine the properties of the concrete used in the foundations for the walls. The average compressive strength after 2 months for the cylinders was 27.3 MPa (*c.o.v.*= 2.8% for Phase I, and 27.0 MPa (*c.o.v.* =2.4%) for Phase II. For completeness, splitting tests conducted on 3 concrete cylinders resulted in an average splitting tensile strength of 2.4 MPa (*c.o.v.* =2.0%).

2.6.3 Properties of the concrete in the floor slabs

The concrete used in the slabs representing each floor was mixed in the laboratory. For the 100 mm thick concrete slabs, the maximum crushed limestone aggregate size was 10 mm. The mix proportions were presented in Table 2.6. The compressive strengths of the slab concrete, presented in Table 2.7, were determined by testing 3 concrete cylinders per floor. The average strength of the concrete used in all floor slabs was 34.6 MPa (*c.o.v.* =9.8%).

Table 2.6: Concrete mix proportions

Constituent material	Cement	Coarse aggregate	Concrete sand (dry)	Water	Total
kg/ batch	30 kg	82 kg	41 kg	19 kg	172 kg
Parts by weight	1.00	2.73	1.36	0.63	5.73

Table 2.7: Concrete strength

Cylinder	Concrete strength (MPa)				
	Phase I			Phase II	
	1^{st} storey	2^{nd} storey	3^{rd} storey	1^{st} storey	2^{nd} storey
1	38.5	33.9	32.9	37.6	30.8
2	40.2	36.5	32.4	34.3	29.8
3	38.0	36.0	35.6	35.6	28.3
Average	38.9	35.4	33.6	35.8	29.6
c.o.v. %	2.9%	3.8%	5.1%	4.6%	4.4%

2.6.4 Mortar properties

To achieve consistency during the construction process, a target mortar flow of 120% mm was selected. The mix proportions employed to attain this value were presented in Table 2.8. Compressive tests were conducted on mortar cubes in order to evaluate their strength and consistency during construction. Fourteen batches, weighting 42.8 kg each, were prepared during the construction of all walls. Although standards specify a damp condition for sand for site use, dry sand was used in the mixes prepared in the laboratory for better quality control. Flow tests resulted in an average mortar flow of 130%. Twenty randomly chosen 51 mm mortar cubes were tested in compression according to ASTM C109 (2002) and resulted in an average compressive strength of 26.4 MPa (*c.o.v.* =13.2 %).

Table 2.8: Mortar mix proportions

Constituent materials	Cement	Lime	Masonry sand (dry)	Water	Total
kg/ batch	7.6 kg	1.5 kg	27.0 kg	6.7 kg	42.8 kg
Parts by weight	1.00	0.20	3.55	0.88	5.58

2.6.5 Grout properties

Fine grout mixed in the laboratory was used for grouting the walls. The mix proportions used for the grout are presented in Table 2.9. The high workability of the grout, having 280 mm average slump, resulted in the filling of almost all of the cells in the walls based on the observed wet surface of the walls after grouting was completed, as shown in Fig. 2.10.

Table 2.9: Grout mix proportions

Constituent materials	Cement	Lime	Concrete sand (dry)	Water	Total
kg/ batch	41 kg	1.6 kg	160 kg	35 kg	237.6 kg
Parts by weight	1.00	0.20	3.53	0.85	6.49

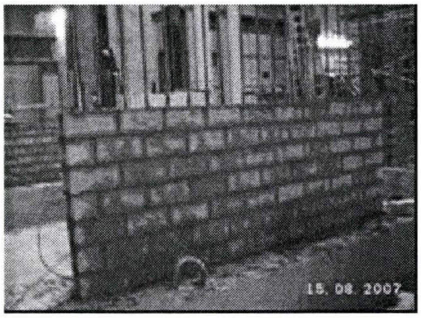

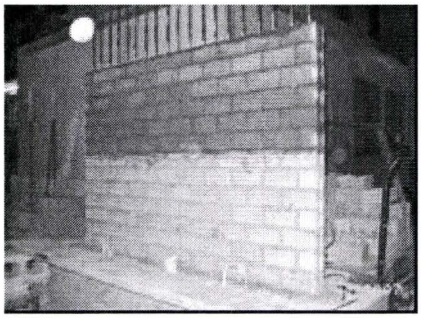

Fig. 2.10: Walls becoming wet from absorbed water after grouting

Eighteen block moulded grout prisms were constructed to determine the grout properties. Three of the grout prisms were block-moulded with dimensions of 65 mm×65 mm×130 mm and the others were poured inside the cells (2 blocks high×1 cell area) of the same type of blocks used in the walls as shown in Fig. 2.11. The grout was air cured in the block moulds similar to the curing of the walls and then the blocks were saw cut to extract the grout prisms. Compression tests conducted on the block moulded grout prisms and on grout cylinders, prepared in Phase I, resulted in average compressive strengths of 29.1 MPa, (*c.o.v.*=18.9%) and 21.8 MPa (*c.o.v.*=16.2%), respectively. In Phase II, the average compressive strength of the grout cylinders was 24.8 MPa (*c.o.v.* = 11.2%).

a) Molding between blocks

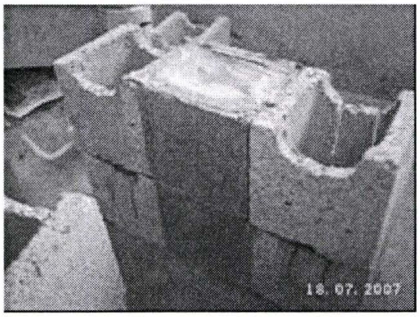

b) Molding in cells of block

Fig. 2.11: Block moulded grout prisms

2.6.6 Block properties

Compression tests were conducted on three half scale hollow concrete masonry units in accordance with the CSA A165.1 (CSA 2004) using hard capping and 120 mm thick bearing plates. Average compressive strength, based on net area, was 27.2 MPa (*c.o.v.* = 7.1%). Complete details of the half scale blocks properties including density, absorption, and splitting tensile strength can be found elsewhere (Long 2006).

2.6.7 Prism properties

Three grouted block prisms were constructed during each grouting stage and were tested to determine the compressive strength of the masonry assemblage as well as the ultimate compressive strain under axial load. Compression tests were conducted in accordance with CSA S304.1 (CSA 2004) which is similar to ASTM C1314 (ASTM 2003) in terms of the test methods. Hydrostone capping was implemented for the prisms and the upper steel platen of the testing machine's spherical head covered the full prism area and the bottom of the prism sat on the steel base of the test machine.

The prisms were four blocks high by one block long (375 mm high ×185 mm long × 90 mm thick) and were constructed and grouted at the same time as the walls. The grout was rodded during grouting to ensure complete filling of all cells. The configuration of prisms that were tested during Phase I was shown in Fig. 2.12(a). The prisms were constructed in running bond, using the ¼ - ¾ end block pattern. This block arrangement, as discussed by Halucha (2002), eliminated the problem of filling the frogged ends of the block with grout and provided the same strength as that of the whole and one half unit arrangements in the actual construction.

Vertical wood boards were attached to the ends of the prisms before grouting to allow filling of the open ends of block cells. It was decided to change the prism configuration in Phase II to the traditional full block and half block configuration shown in Fig. 2.12 (b). Photographs of the tested prisms with highlighted cracks were presented in Fig. 2.13.

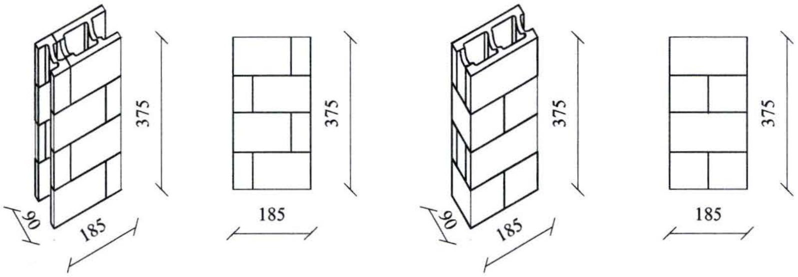

a) ¼ - ¾ end block pattern b) Full and half-block pattern

Fig. 2.12: Prism configurations (all dimensions in mm)

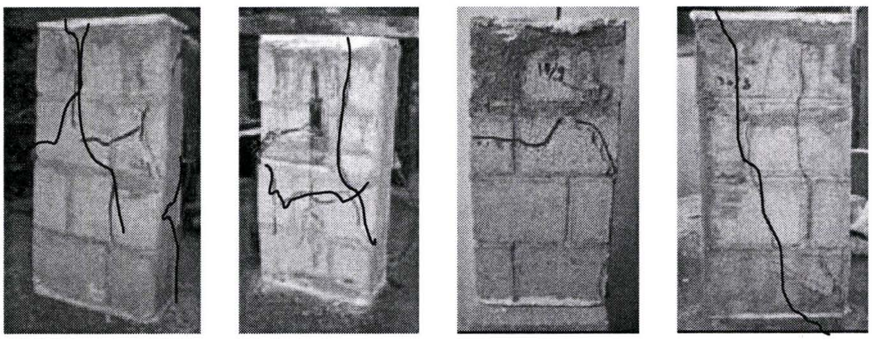

Fig. 2.13: Failure mode for masonry prisms

Strains were measured during prism testing using two potentiometers, placed on opposite faces of the prism over a gauge length equal to the prism height. Typical stress-strain curves for each type of prism were presented in Fig. 2.14. Prism compressive strengths, f'_m, strains at maximum strength, ε_0, and modulus of elasticity, E_m, were reported in Table 2.10.

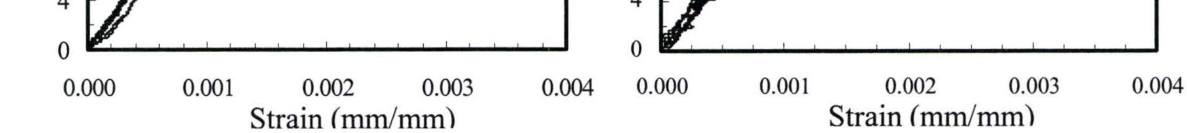

a) Phase I tests b) Phase II tests

Fig. 2.14: Stress-strain relationship for block prisms (see Table 2.10)

Table 2.10: Prisms test results

Prism location			f'_m (MPa)	Avg. f'_m (MPa) *c.o.v.* (%)	ε_0* (mm/mm)	Avg. ε_0 *c.o.v.* (%)	E_m/f'_m	Avg. E_m/f'_m *c.o.v.* (%)
Phase I	1st Storey	1st Half	20.4	19.4 (*N.A.*)	0.0024	0.00207 (*N.A.*)	652	675 (*N.A.*)
			14.9**		0.0021		695	
			18.4		0.0017		698	
		2nd Half	13.6**	19.9 (*N.A.*)	0.0010	0.00220 (*N.A.*)	645	675 (*N.A.*)
			19.0		0.0025		651	
			20.7		0.0019		698	
	2nd Storey	1st Half	14.3	13.7 (4.1%)	0.0019	0.00173 (12.0%)	998	920 (17.0%)
			13.5		0.0018		740	
			13.2		0.0015		1021	
		2nd Half	13.1	15.2 (13.6%)	0.0015	0.00157 (13.3%)	933	985 (4.8%)
			15.2		0.0014		995	
			17.2		0.0018		1026	
	3rd Storey	1st Half	16.5	15.6 (*N.A.*)	0.0017	0.00165 (*N.A.*)	634	804 (*N.A.*)
			14.7		0.0016		974	
			10.4***		0.0016		989	
		2nd Half	16.4	16.1 (4.0%)	0.0019	0.00187 (8.2%)	653	746 (15.3%)
			15.3		0.0020		712	
			16.5		0.0017		873	
Phase II	1st Storey	1st Half	15.5	16.1 (4.1%)	0.0016	0.00157 (16.1%)	786	878 (25.4%)
			16.8		0.0018		715	
			16.0		0.0013		1132	
		2nd Half	15.3	16.1 (5.0%)	0.0015	0.00167 (9.2%)	787	896 (11.5%)
			16.9		0.0017		991	
			16.4		0.0018		911	
	2nd Storey	1st Half	16.3	14.7 (10.0%)	0.0015	0.001576 (3.7%)	811	857 (5.9%)
			14.4		0.0016		911	
			13.4		0.0016		850	
		2nd Half	17.1	15.5 (9.2%)	0.0017	0.00163 (12.7%)	678	879 (30.1%)
			15.1		0.0018		780	
			14.3		0.0014		1178	
Average (c.o.v%)			16.0 (12.5%)	NA	0.0017 (17.5%)	NA	837 (18.9%)	NA

* Strain at maximum stress, f'_m.

** Misalignment of the prism resulted in reduced capacity. The result was ignored.

*** Poorly grouted prism. The result was ignored

2.6.8 Boundary element prisms

Corresponding to Walls W3 and W6, 3 sets of prisms (two blocks thick and four blocks high) were constructed as shown in Fig. 2.15 (a) and tested under uniaxial compression in order to determine the stress-strain relationship for the boundary element of the end-confined walls. The first set of prisms (G1) was simply filled with grout whereas the second set (G2) had four No. 10 vertical bars placed as in Walls W3 and W6. The third set (G3) included the ties along with the vertical reinforcement. The latter two sets were constructed to evaluate the effect of the presence of the vertical reinforcement and the horizontal ties on the behaviour of the assemblage. In addition, two sets of three prisms (G4 and G5) were constructed using four courses of pilaster units to determine the characteristics of the compression zone for the Wall W7, in Phase II. The three unreinforced prisms (G4) and three vertically reinforced prisms confined with spiral reinforcement (G5) were also tested under uniaxial compression to investigate the effect of confinement on the masonry compressive strains. Prism compressive strengths, $f'_m = P/A_{total}$, and strains at maximum strength, ε_0, were reported in Table 2.11.

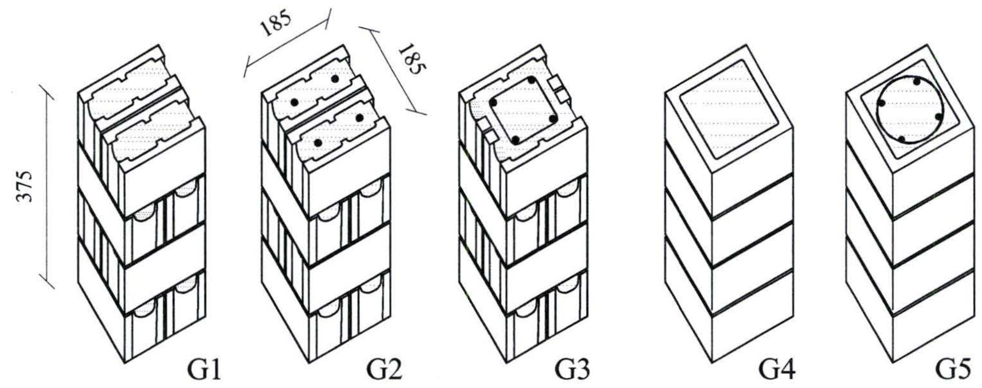

a) Phase I tests b) Phase II tests

Fig. 2.15: Boundary element prisms

The construction of the reinforced prisms was preceded by welding the vertical reinforcement to a 10 mm thick base steel plate over which the prisms were constructed. After construction and grouting were completed, the vertical reinforcement was welded to a similar top steel plate where the bars were fitted through predrilled holes in the plates. These plates were bedded on a thin layer of hydrostone to position it prior to welding. The steel plates, to which the reinforcement was welded, were used to create a uniform loading plane for the masonry and the steel.

Table 2.11: Results of boundary element prism tests

Group	At maximum load			At 30% strength degradation	
	Stress (MPa)	Strain (mm/mm)	Steel contribution	Stress (MPa)	Strain (mm/mm)
G1	13.8	0.0019	N.A.	9.5	0.0031
	12.9	0.0013	N.A.	9.3	0.0020
	11.3	0.0020	N.A.	7.9	0.0028
G2	21.0	0.0019	19.8%	14.8	0.0037
	20.5	0.0018	19.0%	15.8	0.0027
	18.1	---(*)	----(*)	----(*)	----(*)
G3	25.4	0.0017	14.6%	17.9	0.0042
	22.1	0.0016	15.8%	18.9	0.0031
	19.1	0.0015	17.3%	13.4	0.0046
G4	24.8	0.00222	N.A.	10.8	0.0051
	22.1	0.0030	N.A.	18.9	0.0046
G5	30.3	0.0021	15.3%	20.3	0.0048
	29.1	0.0020	18.7%	20.7	0.0054
	29.0	0.0019	14.3%	20.8	0.0067

(*) Erronous reading from the two potentiometers

The contributions of the vertical reinforcement to the load carrying capacity, calculated using strains corresponding to the maximum load, were presented in Table 2.11 as a percentage of the total compressive strength of the tested prisms.

Only vertical cracks were observed after reaching the maximum loads for the unreinforced prisms (G1) and this was followed by spalling of the face shells and end webs. The vertically reinforced prisms (G2) suffered less damage compared to the unreinforced prisms after maximum load was reached. When the vertical bars buckled, the damage propagated rapidly and strength degraded at a faster rate. For the tied G3 prisms, vertical cracks were also observed at maximum load and spalling of face shells occurred but buckling of the reinforcement was not observed and damage was limited to the unconfined masonry outside the confining ties.

Damage conditions at the end of the test for all prisms were presented in Fig. 2.16. The G3 prisms reached, on average, 12% higher strength compared to the G2 prisms as a result of the confining effect of the horizontal ties. In addition, it was found that the contribution of the vertical reinforcement to axial load carrying capacity at maximum load in the G3 prisms was slightly less than in the G2 prisms. This can be attributed to the triaxial compressive stresses on the confined masonry core resulting in a higher compressive strength at lower strain. The descending branches of the stress-strain relationships presented in Fig. 2.17 indicated slower strength degradation when reinforcement and confined reinforcement were included. On average, the strain at 30% strength degradation were 52%, 72%, and 149% higher than the strain at maximum load for the unreinforced (G1), reinforced (G2), and confined (G3) prisms, respectively.

G1 G2 G3 G4 G5

Fig. 2.16: Failure modes

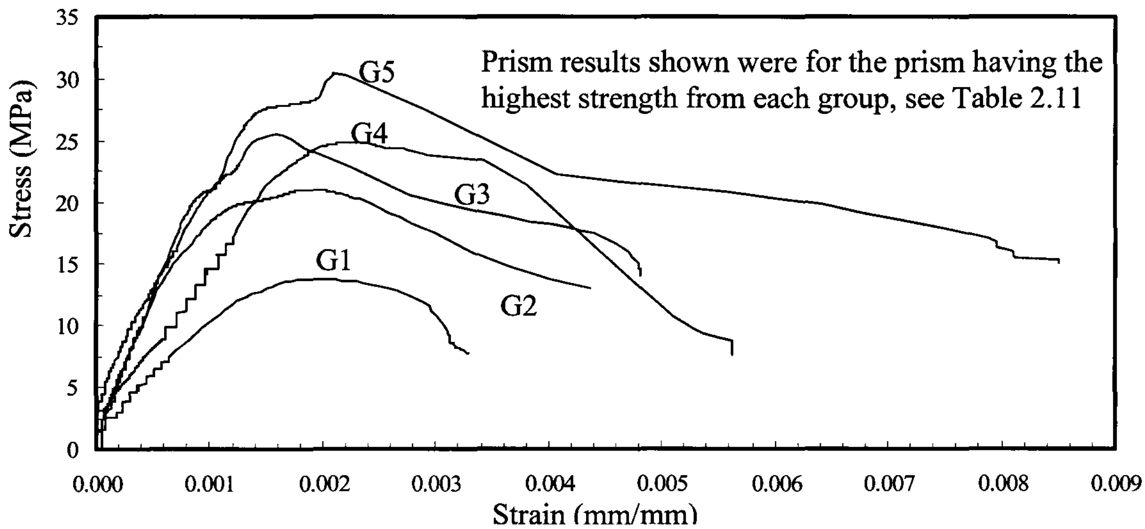

Fig. 2.17: Stress-strain relationships for boundary element prisms

2.7 Shear wall test setup

The test rig, shown in Fig. 2.18, was designed to test shear walls of up to three meters length under cyclic loading. It consisted of a 4,200 mm long × 1,100 mm wide × 600 mm deep reusable concrete floor slab that was prestressed to the laboratory strong floor with the aid of ten, 63 mm diameter, post-tensioned steel bolts spaced at 920 mm in both the longitudinal and the transverse directions. Sixteen 25.4 mm diameter prestressing steel bars were anchored in the reusable floor slab and, after positioning the test wall, were post-tensioned to clamp the wall foundation to the reusable floor slab in order to provide a fixed end condition during testing. These prestressing bars were spaced at 400 mm in the longitudinal direction and at 320 mm in the transverse direction.

Lateral in-plane cyclic load was applied using a hydraulic actuator with a maximum capacity of 500 kN and a maximum stroke of ± 250 mm. The lateral load applied to the wall was positioned to coincide with the top level of the wall in order to create a zero moment condition at the wall top. The actuator was attached to the stiff steel loading beam on the top of the walls to which the vertical reinforcing bars of the wall were welded. In addition to the vertical reinforcement, vertical steel dowels were inserted during the grouting of the second half of the top storeys in the cells that did not contain vertical reinforcement. These dowels extended from the upper two masonry courses to a height of 200 mm above the top courses. Along with the vertical reinforcement, these dowels were welded to the top loading beam to simulate the transmission of the earthquake load along the length of the shear wall to represent the action of a horizontal diaphragm instead of applying point loads at the top corners of the wall.

An out-of-plane bracing system was used to represent the stabilizing influence of rigid diaphragm floors and consisted of two box steel members pinned to a steel frame at each floor level. These were connected to the reinforced concrete slabs, as illustrated in Fig. 2.18 (b). The length of these box members was 1.1 m and was calculated to limit out-of-plane deflection of the walls to 4.5 mm at 100 mm in-plane top deflection. The box sections were attached to the out-of-plane bracing columns and to the reinforced concrete slab at each storey with 25 mm diameter vertical high-strength steel threaded rods to create pinned end connections. The two link members (box sections) at each storey were designed to offer minimal resistance to the in-plane displacement of the loading beam and to prevent significant out-of-plane movement of the wall at all floor levels during the test.

The top bracing differed from the bracing at the first and second storeys to limit out-of-plane deflection during high lateral in-plane displacement. Rollers were attached to two fixed in place box section bracing members and fitted within the vertical channel sections of the loading beam. The rollers guided the top loading beam and offered minimal resistance to the in-plane movement while preventing out-of-plane movement at the top of the wall.

For the two storey walls in Phase II, it was expected that the lateral displacement at the top of the walls would be smaller than that of the three storey walls. Therefore, the same out-of-plane system as used in Phase I for the first and second storeys was used.

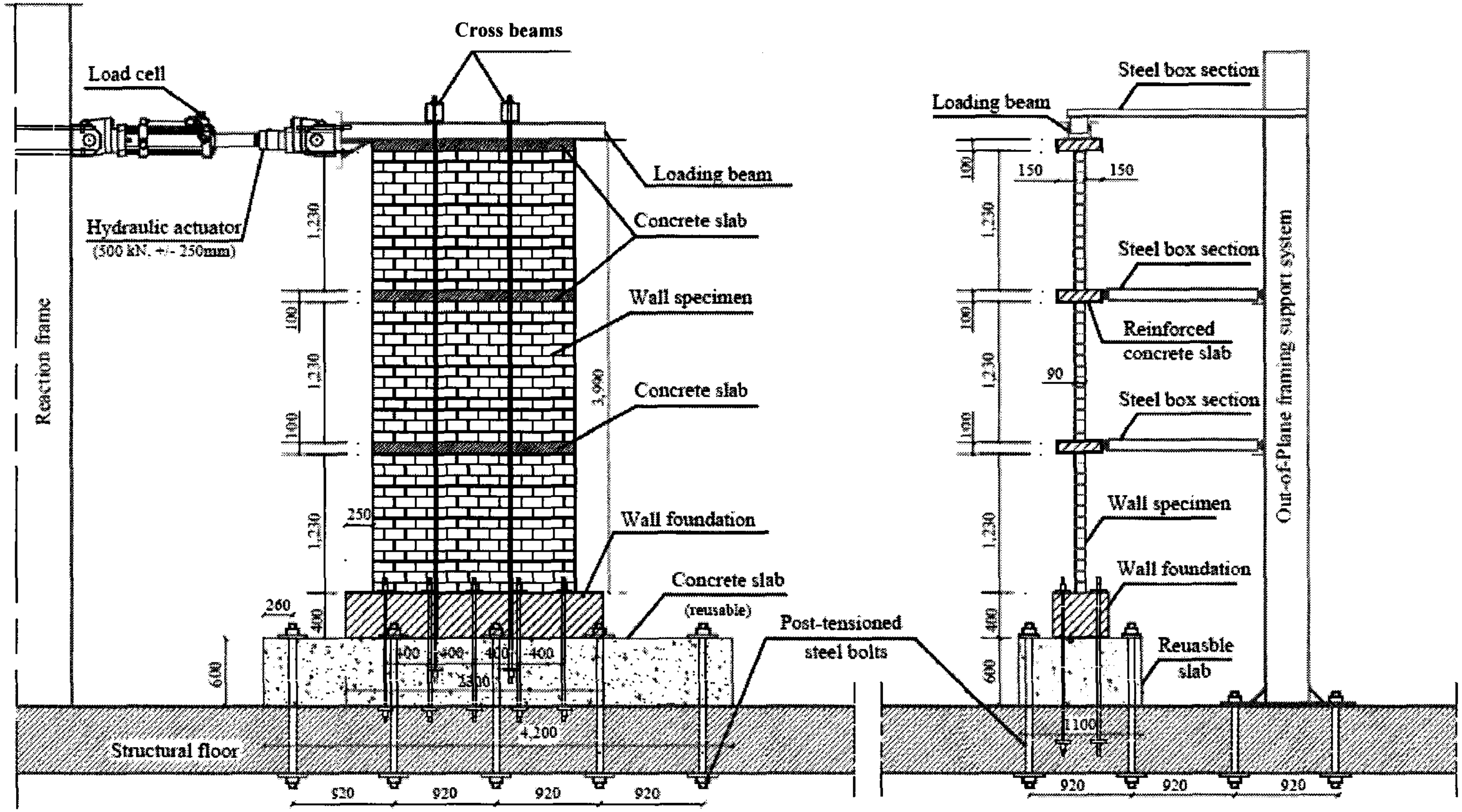

a) Elevation b) Side view

Fig. 2. 18: Test setup and out-of-plane bracing system (all dimensions in mm)

Axial load was applied at the top of the wall by the means of 2 pairs of 13 mm diameter high strength prestressing rods anchored at the bottom to a 102 mm × 102 mm × 4.8 mm steel beam that was attached to the reusable concrete slab, as shown in Fig. 2.19. Each pair of bars was attached to a cross beam pivoted on a roller oriented along the length of the wall. This ensured equal force in the 2 rods. Load was applied by a manually operated hydraulic jack on one side of each pair of the prestressing rods and the load was monitored using a load cell at the top of one of the rods.

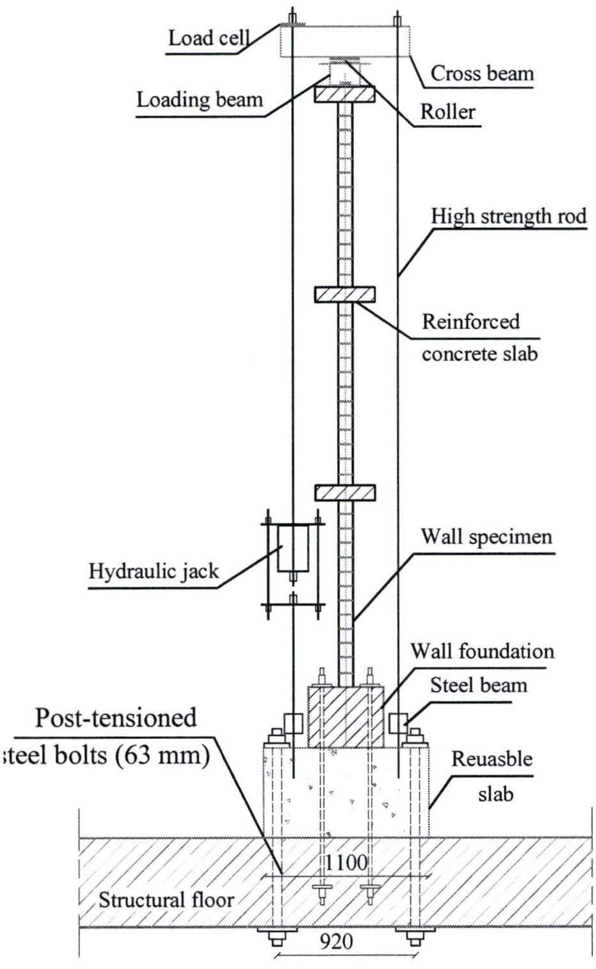

Fig. 2.19: Axial load setup

2.8 Measurements

During testing, loads, deflections and strains were measured to monitor the behaviour of the test walls. A 60-channel PC data acquisition system was used to record the readings every 2 seconds. The following sections contain details of the instrumentation.

2.8.1 External instrumentation

Throughout testing, displacement measurements at key points on the wall specimens were continuously recorded. The displacement potentiometer at the top of the wall was used to control the cyclic loading, instead of the displacement of the jack, to avoid error arising from displacement of the reaction frame supporting the hydraulic actuator. As shown in Fig. 2.20 (a), thirty-six potentiometers were used to monitor the lateral deflection, vertical deformation, diagonal deformation, sliding along the base, and wall uplift.

The vertical displacements of the walls were monitored by the twenty-two potentiometers (L1 to L22) installed vertically along the two wall ends. These potentiometers measured the vertical movements of the storeys relative to the concrete slabs and were used to calculate average curvature over various segments of the wall height. The configuration of displacement measurements using the diagonally oriented potentiometers (L24 to L29) along with the vertical potentiometers attached to the concrete foundation and to the concrete slab at each storey created strain rosettes which were required to distinguish between shear and flexural deformations.

The in-plane lateral displacements of the walls at different heights were measured using seven horizontally positioned potentiometers (L30 to L36). One additional potentiometer (L23) was mounted horizontally at the base of the wall to measure any horizontal slip that might occur between the wall and the concrete foundation. However, since no relative movement was observed between the wall foundation and the floor slab at any stage of testing, no corrections to the lateral deflection were required to account for wall sliding on the concrete slab. The anchors holding the strings of all the potentiometers were located in the concrete slabs in order not to lose all readings due to damage associated with toe crushing of the wall. For the test walls in Phase II, the same configuration was used for the first two storeys.

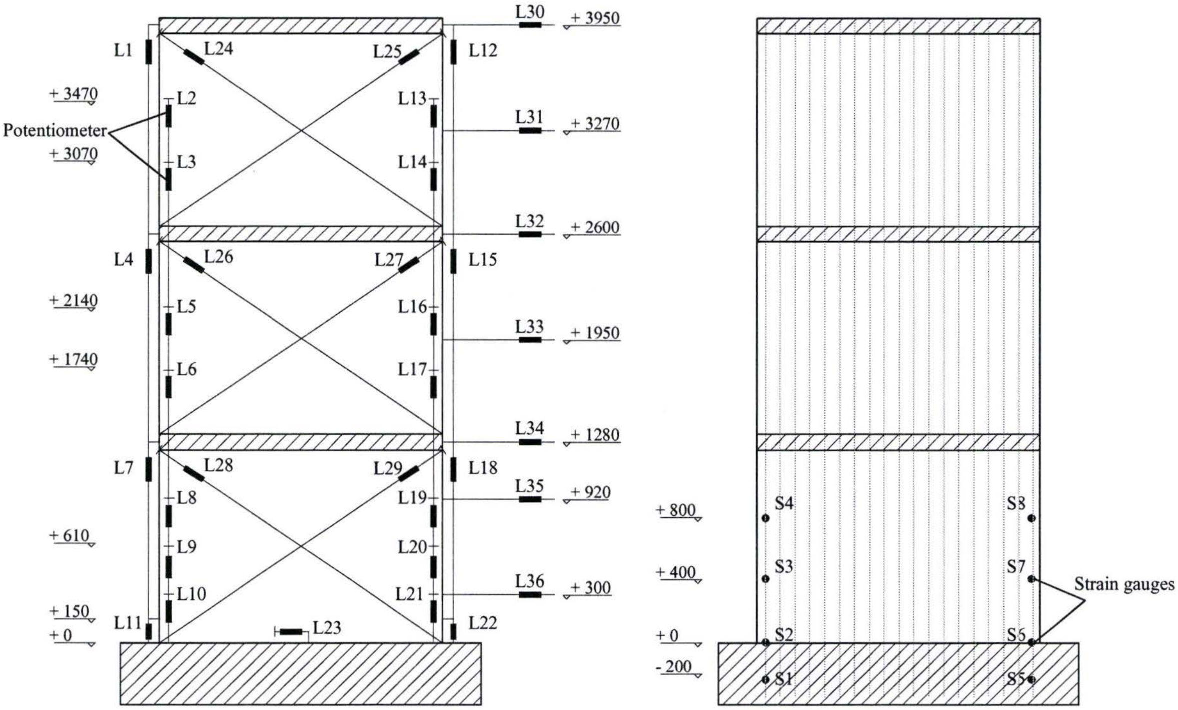

a) Displacement potentiometers b) Strain gauges

Fig. 2.20: Wall instrumentation

2.8.2 Internal instrumentation

In addition to the displacement potentiometers used externally on the masonry, electric strain gauges were epoxied onto some reinforcing steel bars prior to wall construction. Surface preparation of the reinforcing steel required removing bar ribs with an electric grinder prior to strain gauge bonding. This resulted in a slight reduction of the area of the bar. The foil gauges were protected with a clean sealer coating for waterproofing. A butyl sealer and electrician tape were added for protection from physical damage during the grouting process as well as during wall construction.

As shown in Fig. 2.20 (b), the gauges were located within the most highly stressed region to monitor initial yielding, extent of yielding over the wall height, and penetration of bar yielding inside the wall foundation. Eight strain gauges were used in the rectangular walls (W1 and W4) and sixteen gauges were used in the walls with flanges (W2 and W5) and the walls with boundary elements (W3, W6, and W7).

The strain gauges were located at the same heights for all walls. Strain gauges S1 to S8 (used in the rectangular walls) were attached on the outermost vertical reinforcement. Each bar was fitted with four strain gauges distributed along the height of the bar according to a defined scheme. One strain gauge was installed at the interface between the wall and the foundation to detect the initial yielding. One strain gauge was attached on the steel bar inside the concrete foundation at a depth of 200 mm (level -200 mm). The other two gauges were installed at heights of 400 mm (level +400 mm) and 800 mm (level +800 mm) above the wall base, located at 1/3 and 2/3 of the height of the first storey. Because more than one bar existed at the end zone of the flanged and end-confined walls, it was decided to use the same strain gauge scheme for two of the outermost bars.

2.8.3 Loading

The lateral cyclic load was applied using a hydraulic actuator that contained a built-in load cell used for monitoring the horizontal force and an internal LVDT for monitoring its horizontal displacement. However, as mentioned earlier, because the actuator LVDT measurement also included displacement of the loading frame, independently measured top displacements of the wall were used to control the cyclic loading.

Applied axial loads were measured from the load cell at the top of the prestressing rods. The axial load on each specimen was held constant during testing by constantly adjusting the pressure in the hydraulic jacks depending on the elongation or shortening of the wall end next to each load cell.

2.9 Test procedure

All wall specimens were tested under displacement control with a prescribed lateral displacement plan after yielding occurred. At each new displacement level, two full loading cycles were applied with readings being taken during the loading and unloading phases in each direction, where each loading cycle started in the +(ve) (push) direction. Prior to reaching yielding of the outermost reinforcement, the loading scheme used was based on the calculated yield strength of each wall. A displacement-controlled procedure was used to reach different target loads until initial yielding of the outermost bar occurred. For the walls tested during Phase I, four complete cycles were performed corresponding to loads 20%, 40%, 60%, and 80% of the theoretical yield resistance of the wall. The fifth cycle was continued until yielding occurred as described above. For walls tested in Phase II, it was decided to reduce the number of cycles before yielding to three instead of five for all walls and to reduce the number of cycles after yielding to avoid failing the vertical reinforcement due successive bar bending and low cyclic fatigue.

The yield displacement was determined based on the reading of the strain gauge attached to the outermost bar at the interface between the wall and its foundation. After this cycle, loading was based on reaching multiples of the measured displacement at the first yield of the outermost bar, Δ_y. The sequence was repeated until the specimen had lost about 50% of its maximum lateral load resistance which was considered the failure criterion in this study.

2.10 Closure

The design of the test walls and the criteria used in developing the test matrix were presented in this chapter. Construction of the shear wall specimens, including the concrete foundations and floor slabs was described. The details of reinforcement in the shear walls in this study ensured flexurally dominated behaviour with a sufficiently safe margin against shear failure. All auxiliary tests for the masonry assemblage and their constituent materials were reported in this chapter. Details of the setup and procedure used for testing the shear walls as well as the instrumentation were presented.

The following chapter contains the test result for the wall specimens. Wall behaviour and the effects of the test parameters on the responses of the walls are discussed.

Chapter Three

Test Results

CHAPTER 3
TEST RESULTS

3.1 Introduction

The test results for all wall specimens are presented in this chapter. For each specimen, observations pertaining to cracking and progress of failure during the test are described. Load-displacement responses and the effects of the test parameters on the ductility and post-peak behaviour of the tested walls are discussed. Bilinear idealizations of the load-displacement relationships are described and displacement ductilities based on this idealization are discussed.

At the beginning of the discussion pertaining to each wall, the main characteristics of the specimen were listed and, for ease of reference, were summarized in the lower right corner of the figure containing the hysteresis response of the wall. Data on displacement and lateral load resistance for both the (+) ve and (-) ve cycles corresponding to initial yield of tension reinforcement, wall capacity, and 20% strength degradation are summarized in the upper left corner of the figures containing the hysteresis loops. For each wall, several photographs and detailed descriptions were provided to document cracking stages and progressive deterioration of the compression zones with respect to wall deflections.

Prior to initial yielding, each wall was cycled using displacement control to reach target lateral load resistances based on percentages of the predicted yield resistance. The wall was subjected to two complete cycles at displacement corresponding to target loads equal to 20%, 40%, 60%, and 80% of the expected yield resistance of the walls in Phase I and to 33% and 66% for the walls in Phase II. The loading following the 80% cycle for walls in Phase I and the 66% in Phase II was based on the reading from the strain gauge located on the outermost reinforcing bar at the interface between the wall and the foundation. When the strain gauge indicated tensile strain equal to the yield strain of the vertical reinforcement, the loading in that direction was stopped and then reversed to reach yield strain in the outermost reinforcing bar located at the other end of the wall. The yield displacement of the wall was then determined as the top wall displacement recorded for each direction of loading. After yielding, the loading was based on a target displacement level (as multiples of yield displacement) until wall capacity had degraded by about 50% or when vertical reinforcement broke.

For each wall, unless otherwise indicated, the deflection corresponding to initial yielding of the outermost tension bar was obtained using the electric strain gauges on the reinforcement at the level of the foundation. The average of the deflection for both directions of loading was then used as the reference yield value, Δ_y, upon which subsequent cycles of deflections are based. Predicted yield load was also used to confirm that readings were near the correct value.

3.2 Wall 1

3.2.1 Details of Wall 1

Wall 1 was a 3 storey rectangular wall with dimensions of 1,802 mm length, 3,990 mm height and 90 mm thickness. The wall was reinforced with a No. 10 vertical bar in every cell ($\rho_v = 1.17\%$) and D4 deformed wires in every course over the first storey ($\rho_h = 0.30\%$) and in every other course over the second and third storeys ($\rho_h = 0.15\%$) as was presented in Section 2.4. The wall was subjected to a compressive axial load equal to 160 kN in addition to its self weight which resulted in an axial compressive stress equal to 1.07 MPa at the wall base. The hysteresis loops of Wall 1 were presented in Fig. 3.1.

3.2.2 General observations

Horizontal bed joint cracks were first observed during the fourth loading level corresponding to 80 kN lateral load and about 5 mm top lateral displacement. The cracks formed in the mortar joints between the second and the eighth courses in the first storey and extended, on average, about 500 mm along the length of the wall. During the next load level cycle, which corresponded to yielding of the outermost vertical reinforcement at about 8.5 mm top lateral displacement, horizontal cracks were visible along all bed joints in the first storey and extended about 700 mm along the length of the wall from both ends as shown in Fig. 3.2. In addition, horizontal cracks were observed along the first and second bed joints in the second storey at the same loading stage.

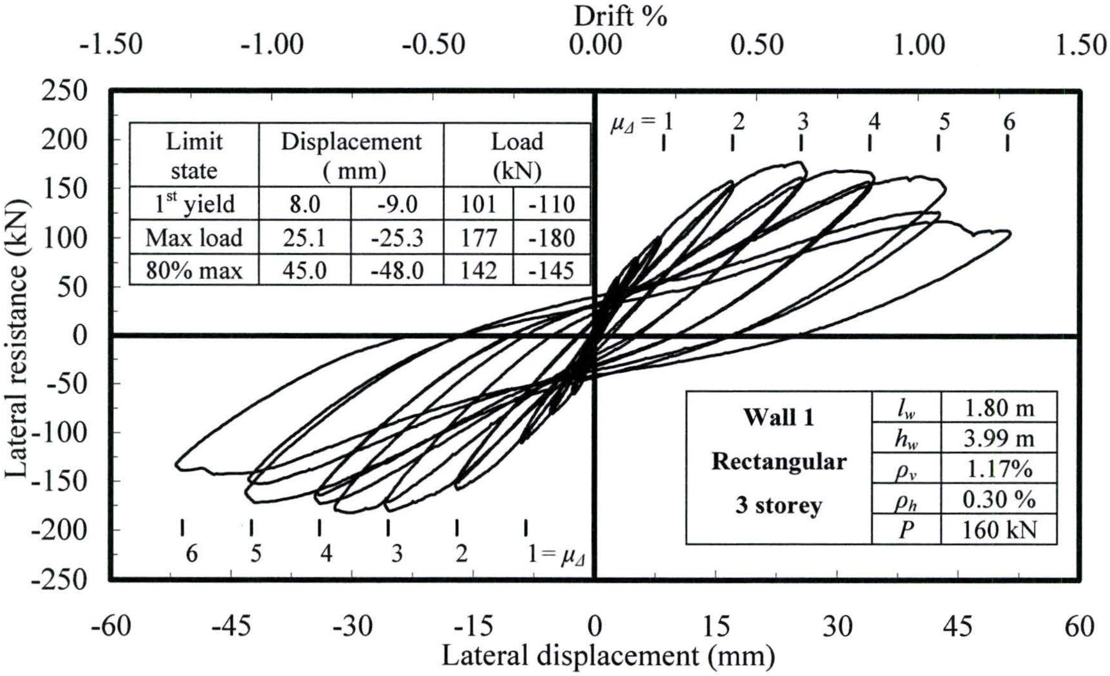

Fig. 3.1: Hysteresis loops (Wall 1)

During the loading cycle at 17 mm top displacement, corresponding to two times the yield displacement, Δ_y, horizontal cracks were observed to extend along most of the length of the wall over the entire first storey and up to mid-height of the second storey, whereas, no cracks were seen in the third storey. Vertical cracks up to the third course were seen in the right wall toe during the 25.5 mm loading cycle ($3\times\Delta_y$) as shown in Fig. 3.3 (a). The left toe crushed, as shown in Fig. 3.3 (b), during the second loading cycle at a displacement level of about 27 mm top displacement due to an accidental increase of loading beyond 25.5 mm in the (-) ve direction. During the same cycle, crushing occurred in the bottom right corner half block just above the foundation and inclined cracking developed thought the face shells of the block, as shown in Fig. 3.3 (c).

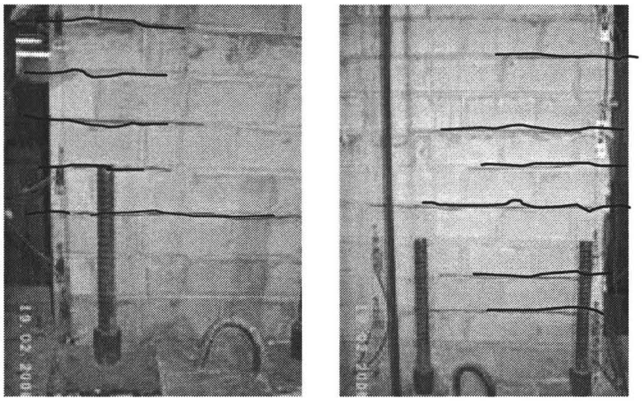

a) Left end b) Right end

Fig. 3.2: Horizontal cracks at Δ_y (Wall 1)

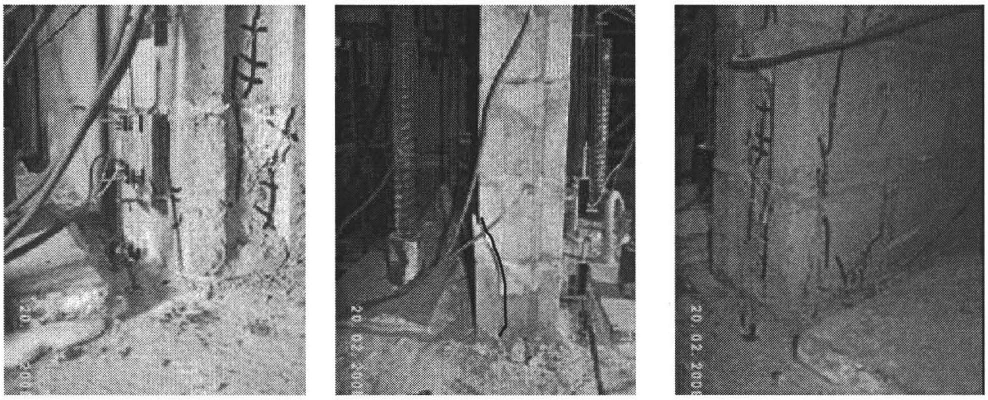

a) Cracking at right toe b) Crushing at left toe c) Crushing of right toe

Fig. 3.3: Vertical cracks and toe crushing at $3\times\Delta_y$ (Wall 1)

Diagonal cracks were seen over the height of the first storey across the middle third of the wall length during the 25.5 mm loading cycle, as shown in Fig. 3.4 (a). Diagonal cracks extended to the second storey but were concentrated over the lower six courses above the concrete slab during the first cycle and extended to the tenth course during the second loading cycle, as shown in Fig. 3.4 (b). These cracks extended through the concrete slab and joined with the diagonal cracks that had developed in the first storey.

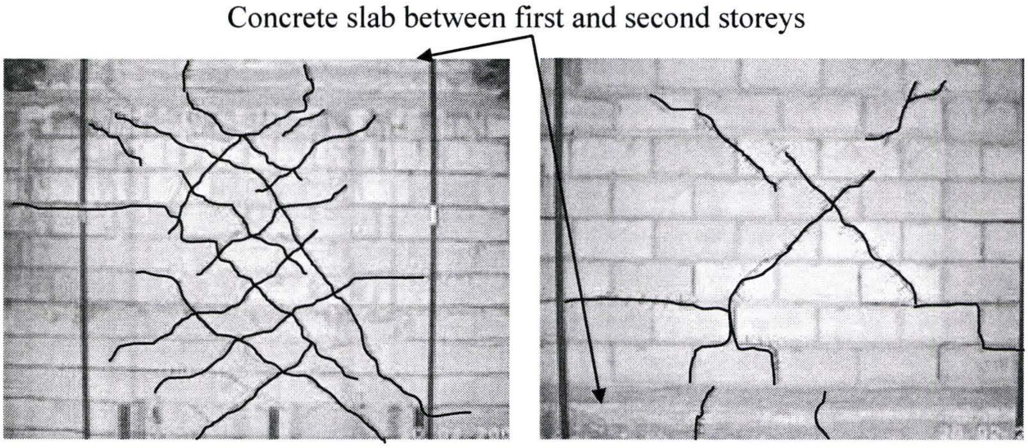

a) Cracking in the first storey b) Cracking in the second storey

Fig. 3.4: Diagonal cracks at 3 $\times \Delta_y$ (Wall 1)

Extensive cracking was observed at both toes which led to their spalling during the 34 mm loading cycle ($4\times\Delta_y$). Spalling extended to the second course at the right end of the wall and cracking of the second course at the left end of the wall occurred during the same cycle, as shown in Fig. 3.5. Diagonal cracking extended during this loading cycle to the full height of the second storey, and vertical cracks were seen at the first course above the base at a distance equal to about 210 mm from the each end of the wall.

Separation of the block end web at the left end of the wall over the lower two courses was seen during the 42.5 mm loading cycle ($5\times\Delta_y$) leading to some spalling, as shown in Fig. 3.6 (a), whereas, the spalling at the right end of the wall extended over the entire end block over the lower three courses. During the second loading cycle, the vertical cracks seen at about 210 mm from the right end of the wall became wider and separation of the face shell occurred at this location, as shown in Fig. 3.6 (b). These cracks coincided with the end of the 180° hook of the horizontal reinforcement. In addition, the outermost right reinforcing bar buckled between the first and the fourth courses coinciding with splitting of the outermost grout column and significant spalling and crumbling of the grout and the blocks at the right end of the wall up to the fourth course, as shown in Fig. 3.6 (c). At the left toe of the wall and during the same loading cycle, the outermost vertical reinforcement buckled between the first and the second courses and grout crumbling was localized over the bottom two courses, as seen in Fig. 3.7 (a). At the right toe at the end of the cycle, spalling of the face shells up to the end of the wall occurred as shown in Fig. 3.7 (b).

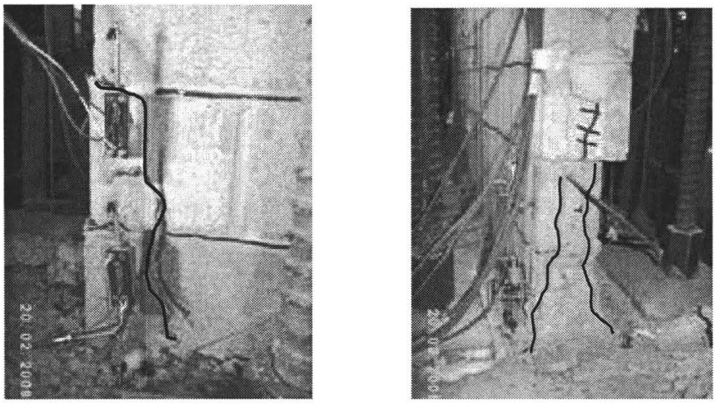

a) Left toe b) Right toe

Fig. 3.5: Cracking and spalling of both toes at 4 $\times\Delta_y$ (Wall 1)

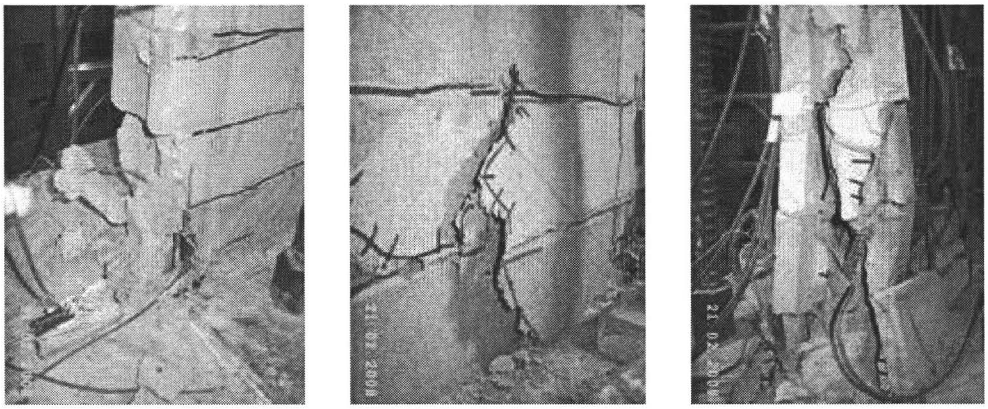

a) Spalling at left toe b) Cracking at right end c) Bar buckling at right end

Fig. 3.6: Spalling, cracking, and bar buckling at $5\times\Delta_y$ (Wall 1)

At the end of the test corresponding to the 51 mm loading cycle ($6\times\Delta_y$), the damage at the right end of the wall included buckling of the three outermost vertical bars with spalling of the masonry blocks and crumbling of the grout columns over the lower four courses and up to a distance equal to two block length along the length of the wall. The extent of damage at the left end of the wall included buckling of the outermost vertical bar between the first and the second courses and spalling of the masonry blocks over the lower two courses up to a distance equal to one block length along the length of the wall. The extent of damage at the end of the test for the wall, presented in Fig. 3.8, shows that most of the damage was limited to the lower three courses of the first storey, and that the cracks over the upper 10 courses of the storey were significant. Cracking in the second storey was much less than in the first storey. The third storey (not shown in the figure) exhibited barely any cracking.

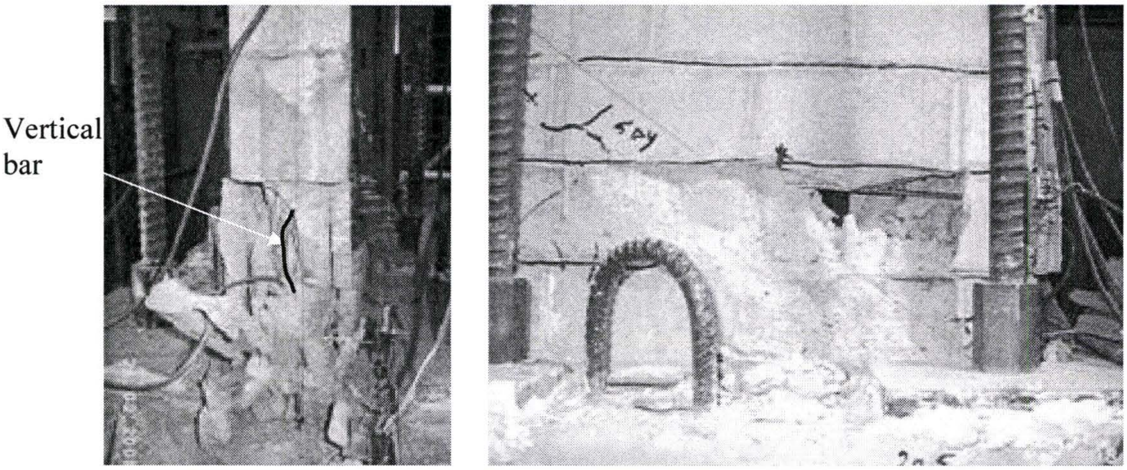

a) Bar buckling at left toe b) Spalling of the lower two courses at right toe

Fig. 3.7: Damage during the second cycle at 5 $\times\Delta_y$ (Wall 1)

3.2.3 Load-displacement response

The hysteresis loops for Wall 1, shown in Fig. 3.1, indicate a symmetric response for loading in both directions. The slopes of the loops decreased gradually with increases in lateral top displacement indicating loss of stiffness. The wall response was almost linear elastic, characterized by thin hysteresis loops generating low energy dissipation, up to the first yield of the outermost reinforcement at the base of the wall. At higher displacement levels, bigger loops generating higher amounts of energy dissipation and increases in plastic deformations were evident. The wall maintained almost the same capacity (within 5% less) when subjected to the second loading cycle of the same target displacement level until reaching about 158 kN, corresponding to a top displacement of about 17 mm ($2\times\Delta_y$). However, cycling the wall at higher displacement levels resulted in larger lateral resistance differences (more than 5%) between the two cycles (see envelope of cyclic loading in Fig. 3.9).

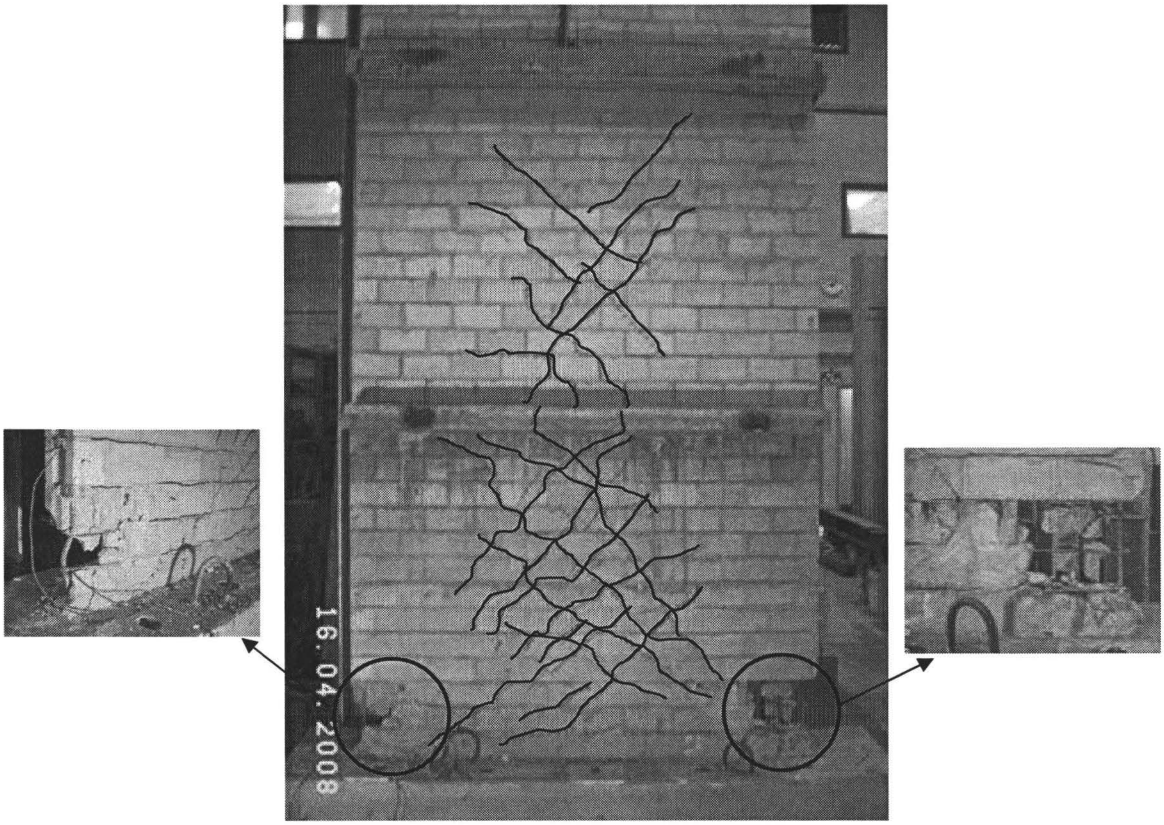

Fig. 3.8: Extent of damage at the end of the test (Wall 1)

Wall 1 reached a maximum lateral load capacity of 177 kN at 25.1 mm top lateral displacement ($3\times\Delta_y$) during loading in the (+) ve direction. The wall had lost almost 7% and 10% of its maximum lateral capacity at 34 mm and 42.5 mm top lateral displacement ($4\times\Delta_y$ and $5\times\Delta_y$), respectively. During the second loading cycle corresponding to $5\times\Delta_y$ top lateral displacement, the wall had lost about 29% of its maximum lateral capacity, which coincided with splitting of the outermost grout column and buckling of the outermost reinforcement bar. When displaced to $6\times\Delta_y$ in the (+) ve direction, the wall capacity had decreased to 60% of its maximum capacity, and at this level, buckling of the outermost three vertical reinforcement was observed and was associated with crumbling of the grout columns encasing these bars.

During loading in the (-) ve direction, Wall 1 reached a maximum lateral load capacity of 180 kN at 25.3 mm top lateral displacement ($3\times\Delta_y$). The wall had lost about 5% of its maximum lateral capacity at 42.5 mm top lateral displacement ($5\times\Delta_y$). During the second loading cycle corresponding to $5\times\Delta_y$ top lateral displacement, the wall had lost about 17% of its maximum lateral capacity, which coincided with splitting of the outermost grout column and buckling of the outermost reinforcement. When displaced to $6\times\Delta_y$ in the (-) ve direction, the wall had lost a total of about 24% of its maximum capacity and, at this level, buckling of the outermost vertical reinforcement was observed and was associated with crumbling of the grout columns encasing this bar.

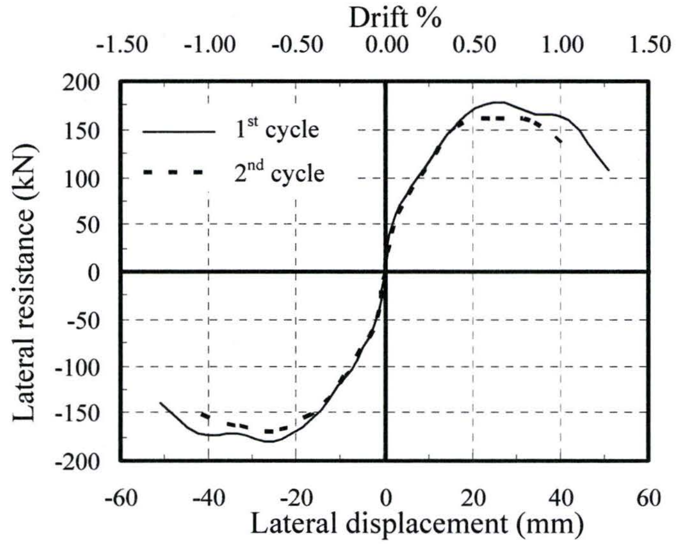

Fig. 3.9: Envelopes of load-displacement relationships (Wall 1)

3.3 Wall 2

3.3.1 Details of Wall 2

Wall 2 was a three storey flanged wall, with overall dimensions of 1,802 mm length and 3,990 mm height. The wall web was 90 mm thick and the flanges were constructed using an additional half block on each side of the wall web at both ends. Thus the flange length was 282 mm with a thickness of 90 mm (1 block width compared to 90 mm web thickness). The wall was reinforced with 5 No. 10 vertical reinforcing bars along the web and 3 No. 10 bars in each flange (ρ_v = 0.55%). Horizontal reinforcement consisted of D4 deformed wires in every course over the first storey (ρ_h = 0.30%) and at every other course over the second and third storeys (ρ_h = 0.15%). The wall was subjected to an axial compressive axial load equal to 160 kN in addition to its self weight which resulted in an axial compressive stress equal to 0.89 MPa at the wall base. The hysteresis loops of Wall 2 were presented in Fig. 3.10.

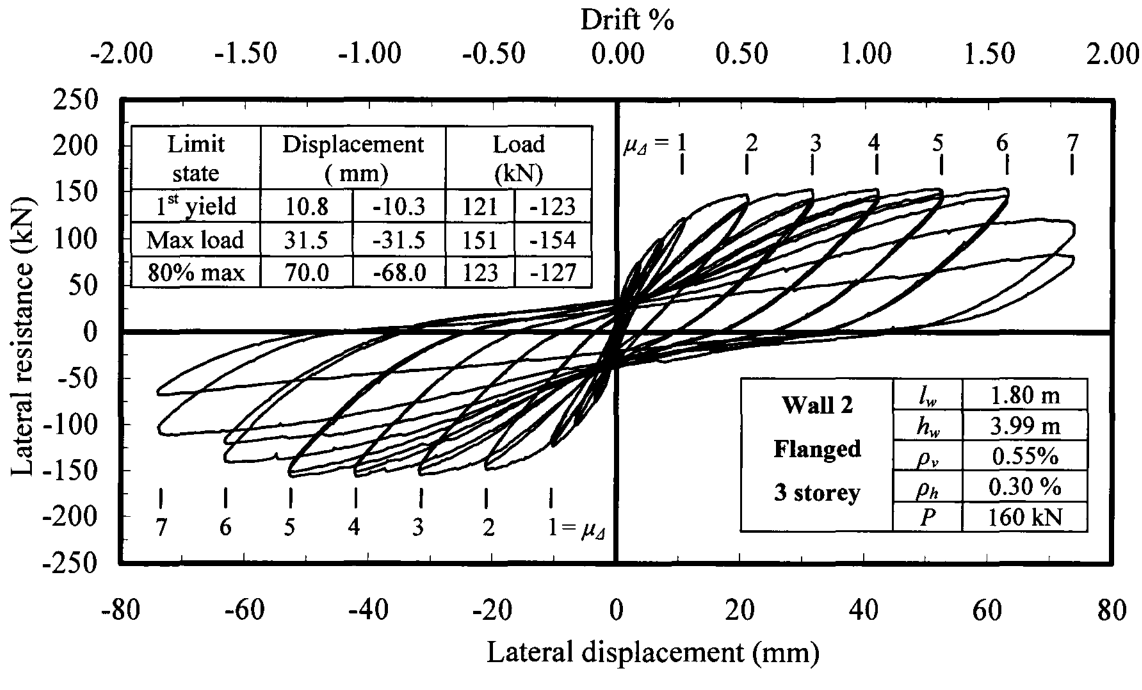

Fig. 3.10: Hysteresis loops (Wall 2)

3.3.2 General observations

Using the predicted yield resistance of about 125 kN for Wall 2, the cyclic loading scheme for Wall 2 prior to yielding was similar to Wall 1. Horizontal bed joint cracks were first observed during the loading cycle corresponding to 75 kN and about 3.5 mm top lateral displacement. The cracks occurred in the mortar joints between the second and the fifth courses in the first storey and were only observed in the flange for both directions of loading. During the loading cycle corresponding to 100 kN, horizontal cracks were seen up to the eleventh course above the base and extended to the third block along the wall length beyond the flange (about 600 mm). During the following loading cycle which corresponded to yielding the outermost vertical reinforcement at about 10.5 mm top lateral displacement, horizontal cracks were observed along all bed joints in the first storey and extended to about mid-length of the wall from both ends. In addition, horizontal cracks were seen between the second and the sixth courses in the second storey at the same loading stage.

During the loading cycle corresponding to 21 mm top displacement ($2\times\Delta_y$), stepped and diagonal cracks were observed in the first and second storeys, whereas, similar to Wall 1, no cracks were seen in the third storey. During the 31.5 mm loading cycle ($3\times\Delta_y$), horizontal cracks were seen in the masonry blocks in the left flange at the second and fifth courses and vertical and horizontal cracks were seen in the left toe, as shown in Fig. 3.11 (a). Vertical cracks in the right toe were also seen during the same loading cycle as shown in Fig. 3.11 (b). Also, increases in diagonal cracking in the first storey and cracking through the concrete slab of the first storey had occurred. During loading in both directions, the horizontal crack between the wall and the foundation extended along almost the entire wall length except the end 280 mm (one block length past the flange of the wall).

Additional vertical cracks extended to the second course in both toes of the wall, as shown in Fig. 3.12. Propagation of the diagonal cracks over the lower storey were observed during the 42 mm loading cycle ($4\times\Delta_y$). During the first loading cycle at 52.5 mm ($5\times\Delta_y$), additional vertical cracks in both toes of the wall as well as diagonal cracks over the first storey were seen. During the second loading cycle, major cracking of the flange and separation of part of the face shell and end web occurred at both wall ends, as shown in Fig. 3.13. Wide horizontal cracks were seen at this level of displacement especially at the joint located in the first storey between the seventh and the eighth courses, where wall construction had been stopped for grouting (A lower tensile strength would be expected at the intersection between successive lifts of grout).

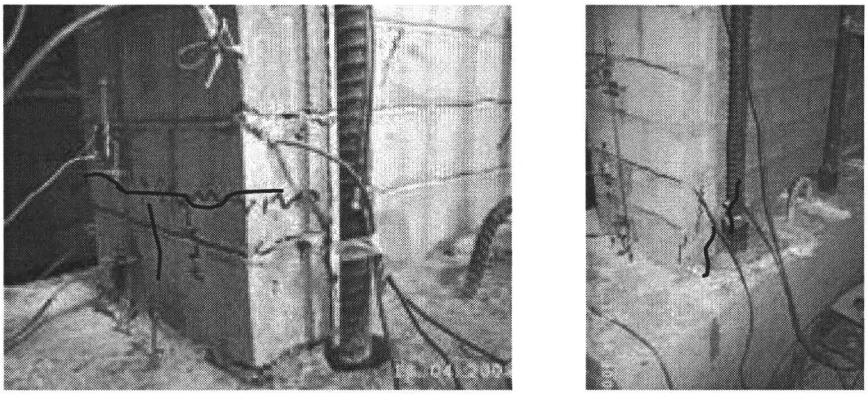

a) Left toe b) Right toe

Fig. 3.11: Horizontal and vertical cracks at $3\times\Delta_y$ (Wall 2)

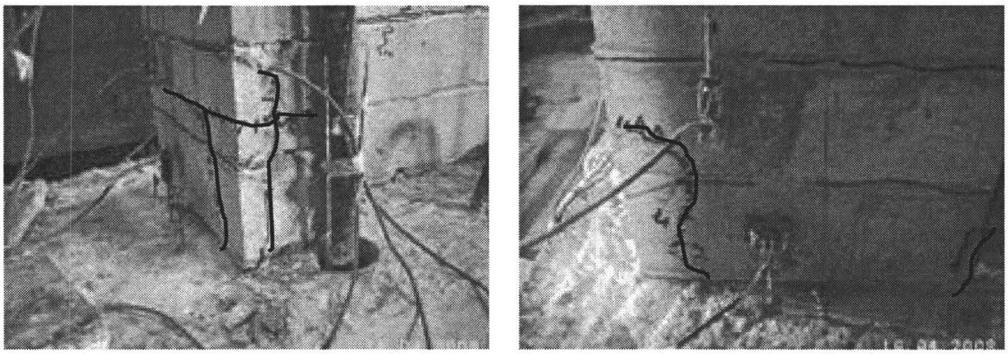

a) Left toe b) Right toe

Fig. 3.12: Cracks at toes at $4\times\Delta_y$ (wall 2)

Vertical cracking extended to the fourth course above the foundation at the right end of the wall during the first loading cycle at 63 mm ($6\times\Delta_y$) (see Fig. 3.14 (c)), whereas spalling of the face shells and end webs of the flange blocks occurred on both sides of the wall at the left end. This was associated with visible buckling of the vertical bar and splitting of the grout column encasing the bar up to the third course on one side only, as shown in Figs. 3.14 (a) and (b). During the second loading cycle, no additional cracking or spalling occurred at the right end of the wall. However, at the left end of the wall, the vertical reinforcement on one side of the wall buckled between the first and the fourth courses and on the other side of the wall, bar buckling was observed between the first and second courses and was associated with spalling of the blocks and crumbling of the grout column, as shown in Fig. 3.15.

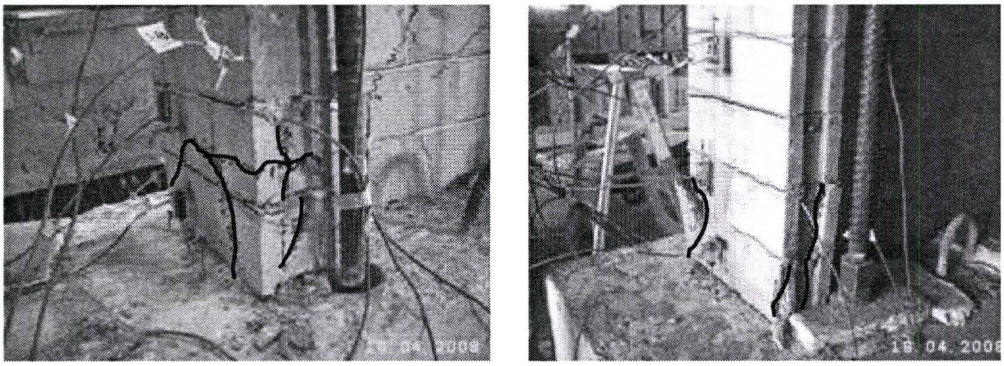

a) Left toe b) Right toe

Fig. 3.13: Separation of end face shells at $5 \times \Delta_y$ (Wall 2)

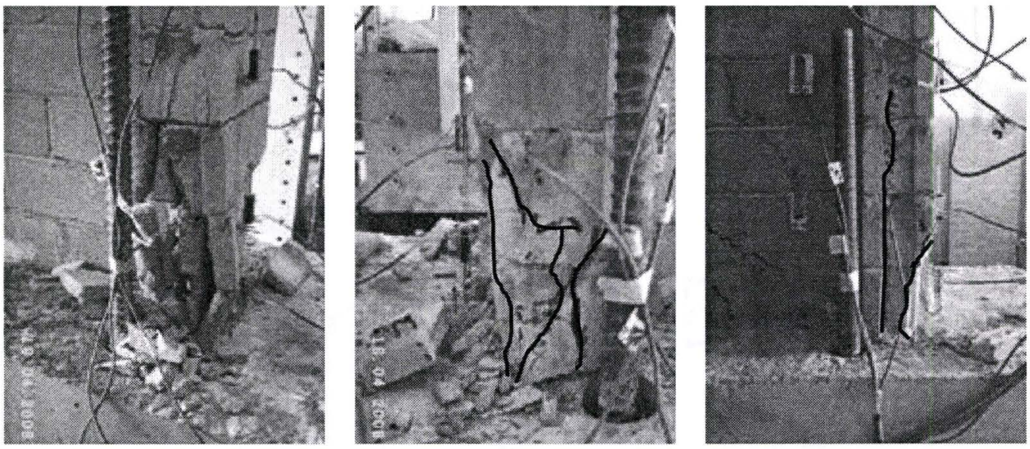

a) Grout splitting (left toe) b) Face shell spalling (left toe) c) Cracking (right toe)

Fig. 3.14: Splitting of grout, spalling and cracking of face shell at $6 \times \Delta_y$ (Wall 2)

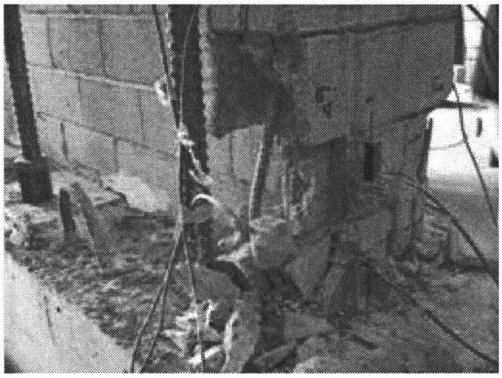

a) Bar buckling at one side

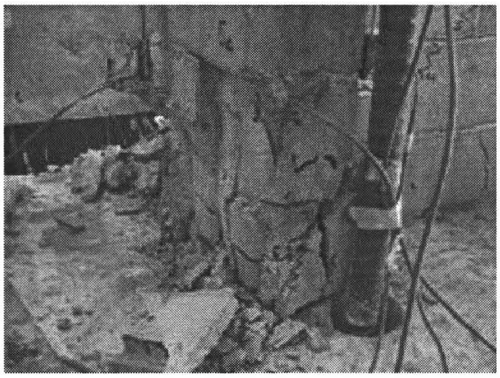

b) Crumbling of grout of the other side

Fig. 3.15: Damage at the left toe during the second loading cycle at $6 \times \Delta_y$ (Wall 2)

During loading to a target top displacement of 73.5 mm ($7 \times \Delta_y$), spalling of the right toe occurred on both ends of the flange, as shown in Fig. 3.16 (a) and was associated with splitting of the grout columns over the lower 2 courses and buckling of the vertical reinforcement in the flanges. As shown in Fig. 3.16 (b), the middle vertical bar in the flange did not buckle at this stage perhaps as the result of more effective tying by the horizontal reinforcement in the wall web. At the same displacement level, the vertical reinforcement in the left flange buckled between the first and the sixth courses on one end of the flange and between the first and the third courses on the other end of the flange associated with crumbling of the grout column around the buckling bars.

a) Splitting of gout column

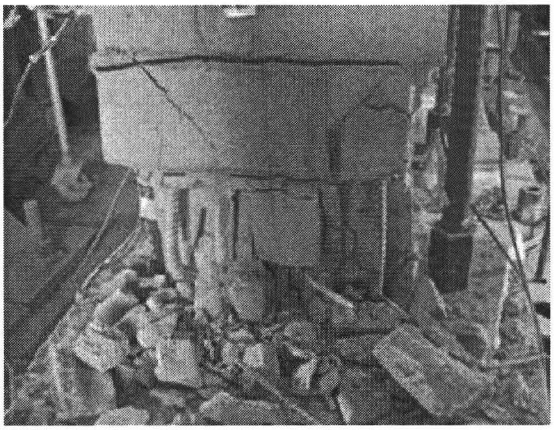

b) Spalling of face shells and bar buckling

Fig. 3.16: Damage at the right flange at $7 \times \Delta_y$ (Wall 2)

During the second loading cycle at 73.5 mm displacement, spalling of the face shells and crumbling of the grout column extended at the right flange up to the fourth course along the whole length of the flange, whereas, the left flange was damaged around the outer reinforcement only as shown in Fig. 3.17. At this stage, the test was terminated as a result of having lost about 50% of the lateral load resisting capacity. The vertical load had been maintained at a constant level throughout the test.

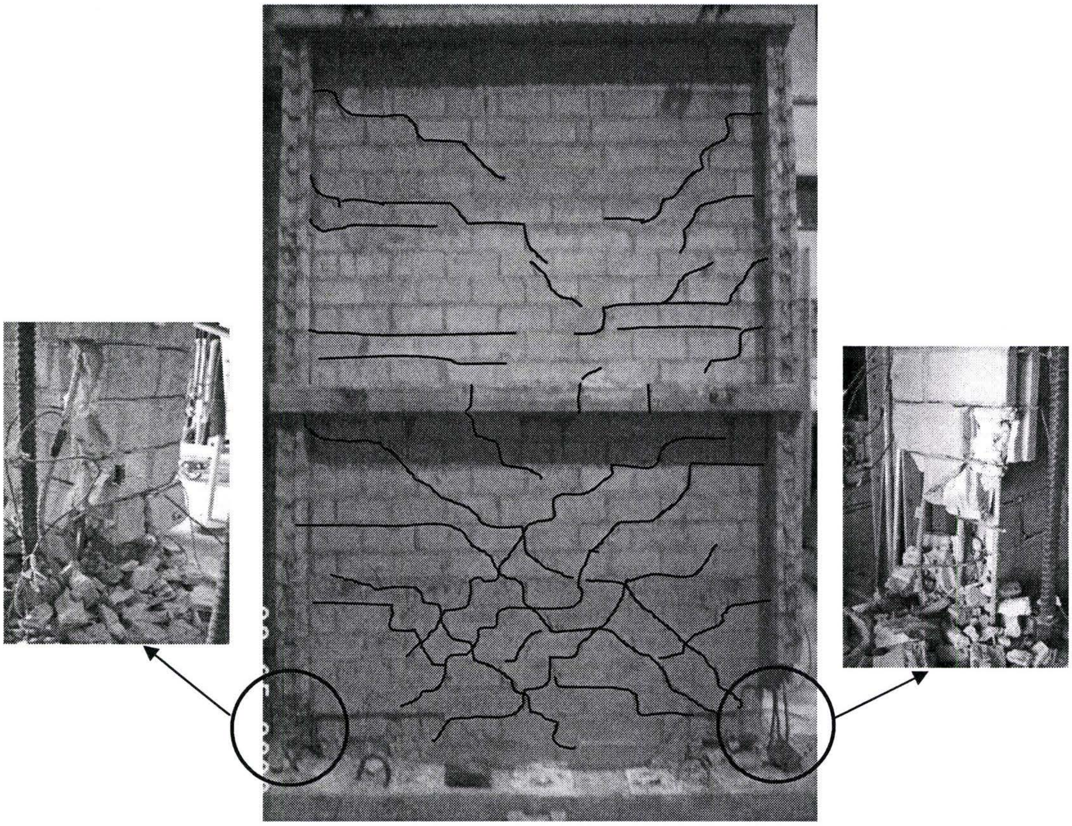

Fig. 3.17: Extent of damage in Wall 2 at the end of the test (Wall 2)

3.3.3 Load-displacement response

The hysteresis loops for Wall 2, shown in Fig. 3.10, indicate a symmetric response for loading in both directions. The slopes of the loops decreased gradually with increases in lateral top displacement indicating loss of stiffness. The wall response was almost linear elastic, characterized by thin hysteresis loops generating low energy dissipation, up to first yield of the outermost reinforcement at the base of the wall. At higher displacement levels, larger loops generating higher amounts of energy dissipation and increased plastic deformations (corresponding to zero load) were evident similar to Wall 1.

The wall maintained almost the same capacity (within 5%) when subjected to the second loading cycle at the same target displacement level until reaching about 154 kN load, corresponding to a top displacement of about 52 mm ($5 \times \Delta_y$). However, cycling the wall to higher displacement levels resulted in greater differences in lateral resistance (more than 5%) between the two cycles, as shown in Fig. 3.18.

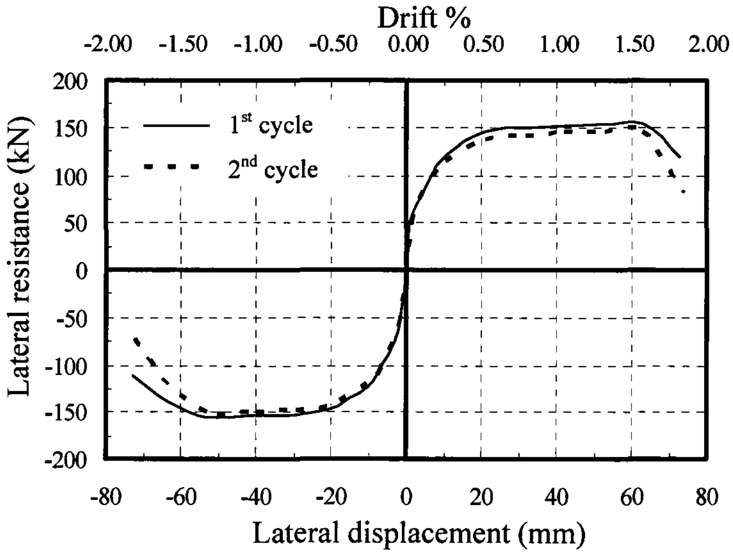

Fig. 3.18: Envelopes of load-displacement relationship (Wall 2)

Wall 2 reached a maximum lateral load capacity of 151 kN at 31.5 mm top lateral displacement ($3 \times \Delta_y$) during loading in the (+) ve direction. The wall did not loose any significant amount of its lateral load capacity until the 63 mm top lateral displacement ($6 \times \Delta_y$) cycle. The wall had lost about 20% and 50% of its maximum lateral capacity during the first and second cycles at 73.5 mm top lateral displacement ($7 \times \Delta_y$), respectively. The significant loss in strength coincided with splitting of the outermost grout columns encasing the three vertical bars in the flange and buckling of the outermost reinforcement.

During loading in the (-) ve direction, Wall 2 reached a maximum lateral load capacity of 154 kN at 31.5 mm top lateral displacement ($3\times\Delta_y$). The wall had lost about 10% of its maximum lateral capacity at 63 mm top lateral displacement ($6\times\Delta_y$). During the second loading cycle corresponding to $6\times\Delta_y$ top lateral displacement, the wall had lost about 22% of its maximum lateral capacity, which coincided with splitting of the outermost grout column and buckling of the outermost reinforcement. At $7\times\Delta_y$ displacement in the (-) ve direction, the wall had lost about 30% of its maximum capacity and, at this level, buckling of two vertical reinforcing bars in the flange was observed and was associated with crumbling of the grout columns encasing these bars.

3.4 Wall 3

3.4.1 Details of Wall 3

Wall 3 was a 3 storey end-confined wall (wall with boundary elements), with overall dimensions of 1,802 mm length and 3,990 mm height. The wall web was 90 mm thick and the boundary elements were constructed using an additional block at each end of the wall. The boundary element was square in shape with length and thickness equal to 185 mm. The wall was reinforced with 3 No. 10 vertical bars along the web and 4 No. 10 bars in each boundary element (ρ_v = 0.55%). For the horizontal reinforcement, D4 deformed wires were used in every course over the first storey (ρ_h = 0.30%) and at every other course over the second and third storeys (ρ_h = 0.15%). A closed tie was placed in each boundary element at each course. The wall was subjected to an axial compressive axial load of 160 kN in addition to its self weight which resulted in an axial compressive stress equal to 0.89 MPa at the base of the wall. The hysteresis loops for Wall 3 were presented in Fig. 3.19.

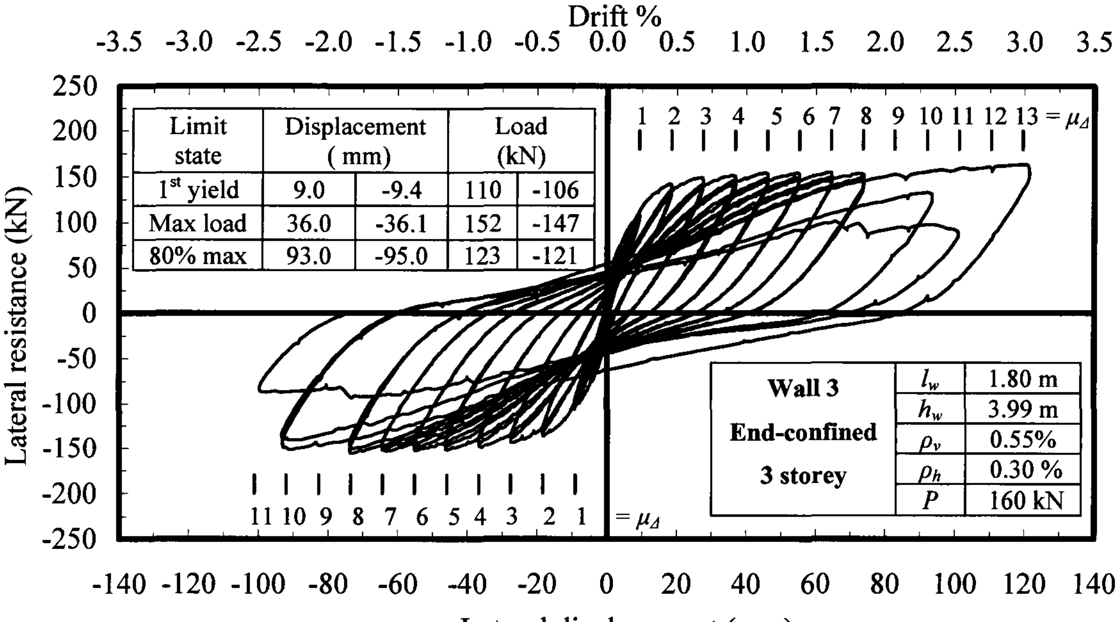

Fig. 3.19: Hysteresis loops (Wall 3)

3.4.2 General observations

Before yielding, the wall was cycled in displacement control to reach target lateral load resistances based on the predicted yield resistance of the wall of 120 kN. Horizontal bed joint cracks were first observed during the third loading cycle corresponding to 75 kN at about 3.9 mm top lateral displacement. The cracks formed in the mortar joint between the second and the seventh courses in the first storey. During the fourth loading cycle corresponding to 100 kN, horizontal cracks were observed up to the tenth course in the first storey. During the following loading cycle which corresponded to yielding of the outermost vertical reinforcement at about 9.2 mm top lateral displacement, horizontal cracks were observed along all of the bed joints in the first storey and some cracks extended to about mid-length of the wall from both ends. In addition, some horizontal cracks were seen in the second storey during the same loading cycle.

During the 18.4 mm top displacement ($2\times\Delta_y$) loading cycle, stepped and diagonal cracks were observed in the first and second storeys whereas, similar to the previous walls, no cracks were observed in the third storey. A horizontal crack between the seventh and the eighth courses in the second storey (where construction was interrupted for grouting) and a crack in the concrete slab in the first storey were seen during the same loading cycle.

During the 27.6 mm loading cycle ($3\times\Delta_y$), a horizontal crack was seen in the masonry blocks at the right end of the wall at the second course, as shown in Fig. 3.20 (a). During the 36.8 mm loading cycle ($4\times\Delta_y$), the horizontal cracks between the wall and the foundation and between the seventh and the eighth courses in the first storey (where construction was interrupted for grouting) became larger and were clearly visible. Also, increased diagonal cracking occurred in the first storey and additional cracking was observed through the concrete slab of the first storey. Propagation of the diagonal cracks over the lower storey, extending almost to the whole diagonal length of the storey, and wider opening of the horizontal cracks were observed during the 46.0 mm loading cycle ($5\times\Delta_y$), as shown in Fig. 3.20 (b).

During the loading cycle at 55.2 mm ($6\times\Delta_y$) displacement, vertical and horizontal cracks were observed at both toes of the wall and at 64.4 mm ($7\times\Delta_y$), cracks at both toes were observed over the lower two courses, as shown in Fig. 3.21. During the second loading cycle, spalling of the end webs occurred.

Similar increased damage at both toe occurred during the 73.6 mm ($8\times\Delta_y$) loading cycle. Spalling of the end face shells and webs of the lower two courses occurred at both toes and the grout columns were visible over half the length of the boundary zone with some minor vertical cracks. During the second loading cycle, the unconfined grout, encasing the vertical reinforcement and the ties in the boundary elements, crushed over the lower two courses, as shown in Fig. 3.22.

Due to a problem with the potentiometer controlling the wall displacement, the wall was accidentally displaced to 124 mm ($13.5\times\Delta_y$) in the (+) ve direction of loading. At this displacement level, crumbling of part of the confined grout column (encased within the ties) occurred over the lower course and the vertical reinforcement buckled between the foundation and the first confining tie located at

80 mm from the foundation. After correcting the problem with the top potentiometer, it was decided to complete the cycle corresponding to a top displacement of 92 mm (10 $\times\Delta_y$). Similar spalling of the face shells, crumbling of grout columns, and buckling of the vertical bars occurred during loading in the (–) ve direction.

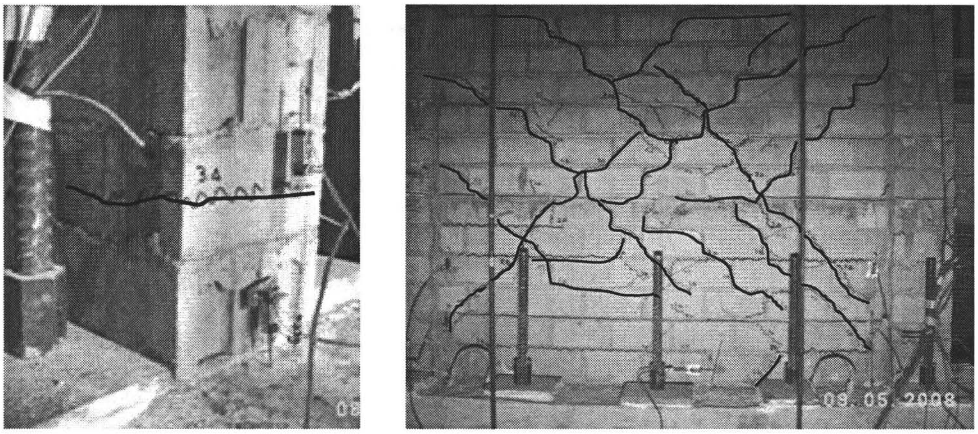

a) Cracks at right toe ($3\times\Delta_y$) b) Cracking of the first storey at $5\times\Delta_y$

Fig. 3.20: Horizontal and diagonal cracks in first storey (Wall 3)

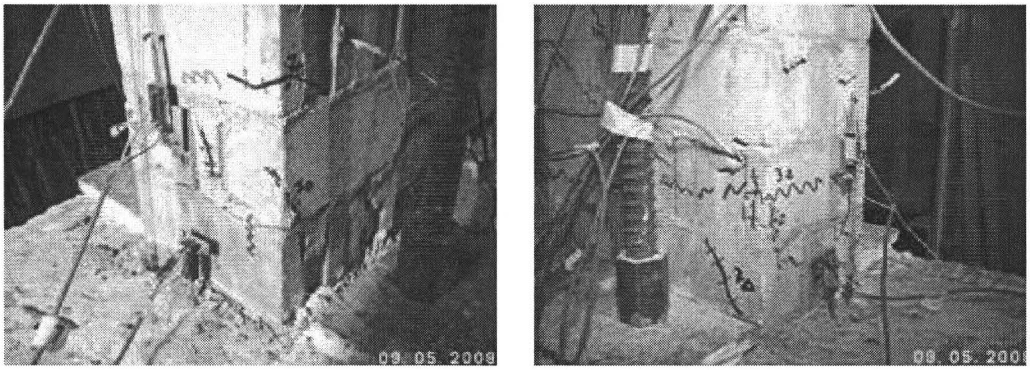

a) Left toe b) Right toe

Fig. 3.21: Cracking at both toes at $7\times\Delta_y$ (Wall 3)

During the loading cycle at 101.2 mm ($11\times\Delta_y$), the outermost two vertical reinforcing bars broke at both ends of the wall, which may be in part attributed to low cyclic fatigue. At this stage, the test was terminated due to the loss of about 50% of the wall lateral load capacity. The extent of damage at the end of the test was confined to the outer half of the boundary elements at both ends of the wall and over the lower 2 courses, as shown in Fig. 3.23.

a) Spalling of face shells b) Crumbling of the unconfined zone

Fig. 3.22: Right toe at $8\times\Delta_y$ (Wall 3)

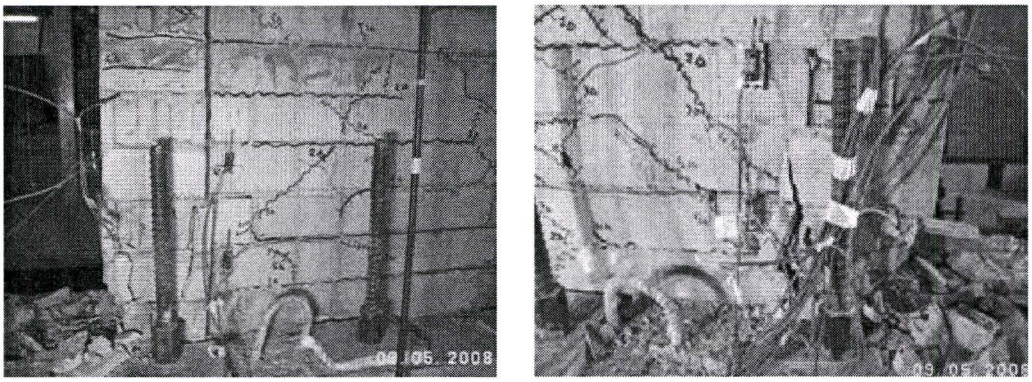

a) Left end of the wall b) Right end of the wall

Fig. 3.23: Extent of damage at the end of the test (Wall 3)

3.4.3 Load-displacement response

The hysteresis loops for Wall 3, shown in Fig. 3.19, indicate a symmetric response for loading in both directions. The slopes of the loops decreased gradually with increases in lateral top displacement indicating loss of stiffness. The response of the wall was almost linear elastic, characterized by thin hysteresis loops generating low energy dissipation, up to the first yield of the outermost reinforcement at the base of the wall. At higher displacement levels, larger loops generating higher amounts of energy dissipation and increases in plastic deformations were evident. The wall maintained almost the same capacity (within 5%) when subjected to the second loading cycle at displacement up to 73 mm ($8\times\Delta_y$) at about 153 kN load. However, cycling the wall to higher displacement levels resulted in increasing lateral resistance differences between the two cycles as shown in Fig. 3.24.

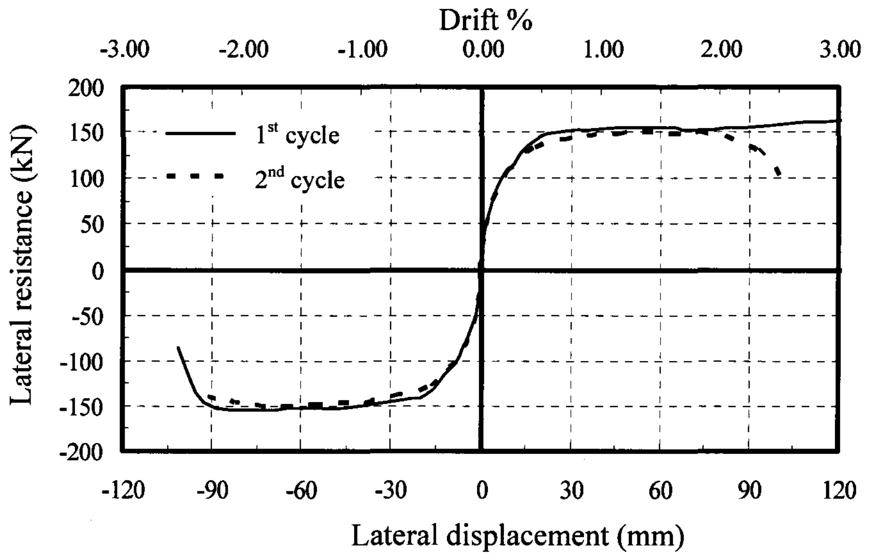

Fig. 3.24: Envelopes of load-displacement relationship (Wall 3)

Wall 3 reached a maximum lateral load capacity of 152 kN at 36.0 mm top lateral displacement ($4\times\Delta_y$) during loading in the (+) ve direction. The wall did not loose any significant amount of lateral capacity until the 92 mm top lateral displacement ($10\times\Delta_y$) cycle. During the second 92 mm loading cycle, the wall lost about 15% of its maximum lateral capacity but this large loss may have been due to the significant damage at the toe resulting from the accidental loading to 124 mm top displacement instead of 92 mm at the beginning of the cycle.

During loading in the (–) ve direction, Wall 3 reached a maximum lateral load capacity of 147 kN at 36.1 mm top lateral displacement ($4\times\Delta_y$). The wall did not loose any significant amount of lateral capacity until the 92 mm top lateral displacement cycle and had lost about 40% of its maximum capacity at 101.2 mm top lateral displacement ($11\times\Delta_y$).

The significant loss in strength occurred due to the failure of the vertical reinforcement which may be due to the relatively large number (>20) of post-yielding cycles of loading. The accidental loading to a top displacement of 124 mm indicates that the wall could have provided higher ductility capabilities if the reinforcement had not failed due to fatigue.

3.5 Wall 4

3.5.1 Details of Wall 4

Wall 4 was a 2 storey rectangular wall with dimensions of 1,802 mm length, 2,660 mm height, and 90 mm thickness. The wall was reinforced with No. 10 vertical bars in every cell (ρ_v = 1.17%) and two D4 deformed wires placed horizontally in every course over the wall height (ρ_h = 0.60%) as was described in Section 2.4. The wall was subjected to an axial compressive axial load of 160 kN which, with the addition to its self weight, resulted in an axial compressive stress equal to 1.07 MPa at the wall base. The hysteresis loops for Wall 4 were presented in Fig. 3.25.

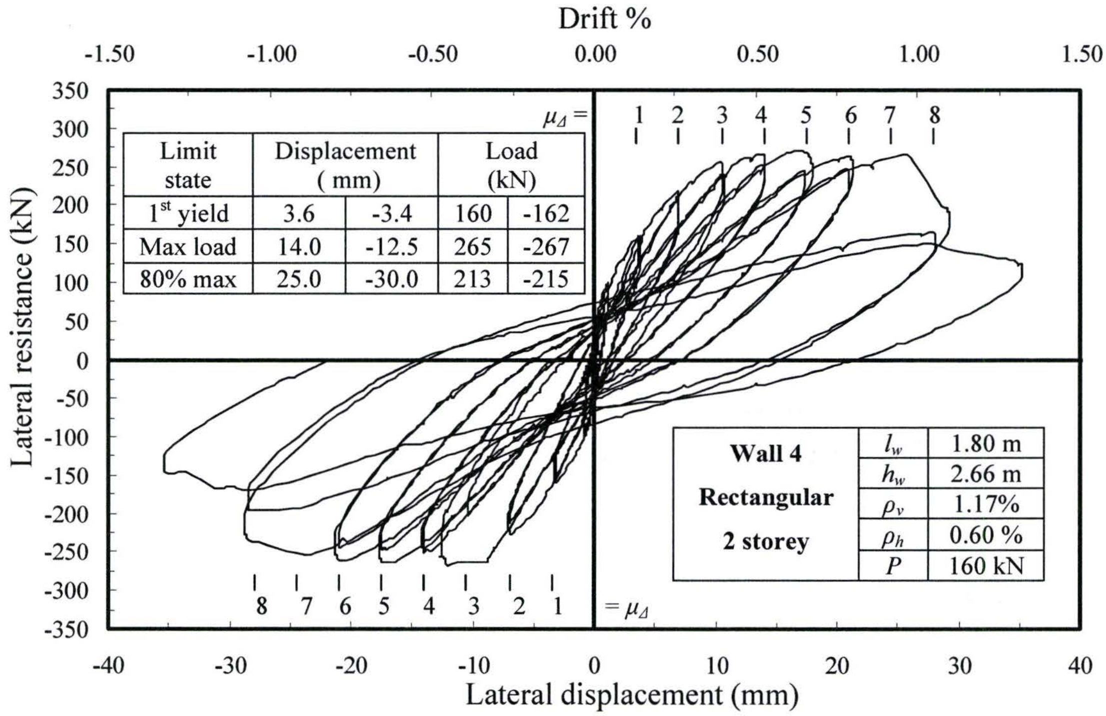

Limit state	Displacement (mm)		Load (kN)	
1st yield	3.6	-3.4	160	-162
Max load	14.0	-12.5	265	-267
80% max	25.0	-30.0	213	-215

Fig. 3.25: Hysteresis loops (Wall 4)

3.5.2 General observations

Before yielding, the wall was cycled in displacement control to reach a target lateral load resistance based on the predicted yield resistance of about 160 kN. As was discussed in Section 2.9, it was decided to reduce the number of before yielding cycles for walls in Phase II. The wall was subjected to two complete cycles at target loads equal to about 33% and 66% of the expected yield resistance of the wall.

Horizontal bed joint cracks were observed during the loading cycle corresponding to yielding of the vertical reinforcement at 160 kN lateral load and about 3.5 mm top lateral displacement. During the loading cycle corresponding to 7.0 mm ($2\times\Delta_y$), horizontal bed joint cracks were observed over the full height of the first storey in addition to diagonal cracks starting to form at the eighth and the tenth courses. No cracking was observed in the second storey at this displacement level.

During the loading cycle corresponding to 10.5 mm top displacement ($3\times\Delta_y$), diagonal cracks were observed over the first storey at the third course and up to the slab at the first storey. They were concentrated over the middle third along the length of the wall, as shown in Fig. 3.26 (a). Diagonal cracks over the lower four courses in the second storey and a vertical crack through the concrete slab were observed at the same cycle, as shown in Fig. 3.26 (b).

During the 14 mm loading cycle ($4\times\Delta_y$), vertical cracks were observed at both toes along with some crushing, as shown in Fig. 3.27. Additional diagonal cracks over the first and second storeys and a new vertical crack in the floor slab were observed at the same loading cycle. Vertical cracks at the toes during the second loading cycle reached the third course above the foundation.

Separation of face shells at both toes was observed during the loading cycle corresponding to 17.5 mm ($5\times\Delta_y$) as well as some increase in the amount of diagonal cracking over the wall. At 21 mm top lateral displacement ($6\times\Delta_y$), spalling of the block end webs occurred at both toes and increases in diagonal cracking were observed over the first 6 courses above the foundation.

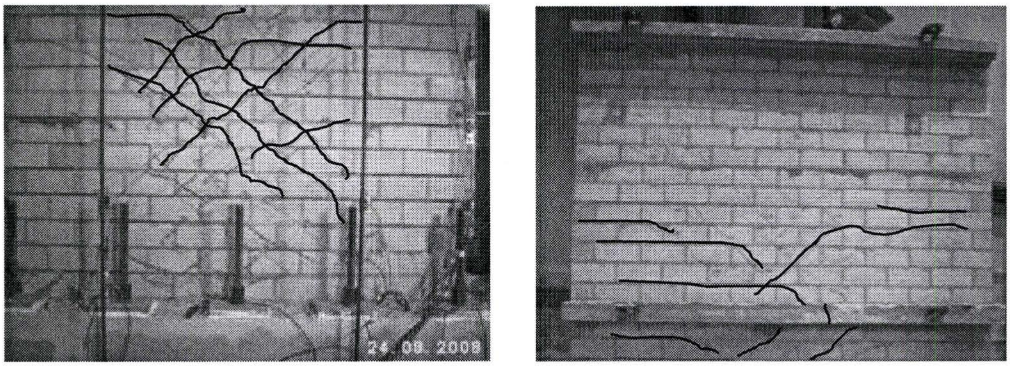

a) First story b) Second storey and floor slab

Fig. 3.26: Cracking at $3\times\Delta_y$ (Wall 4)

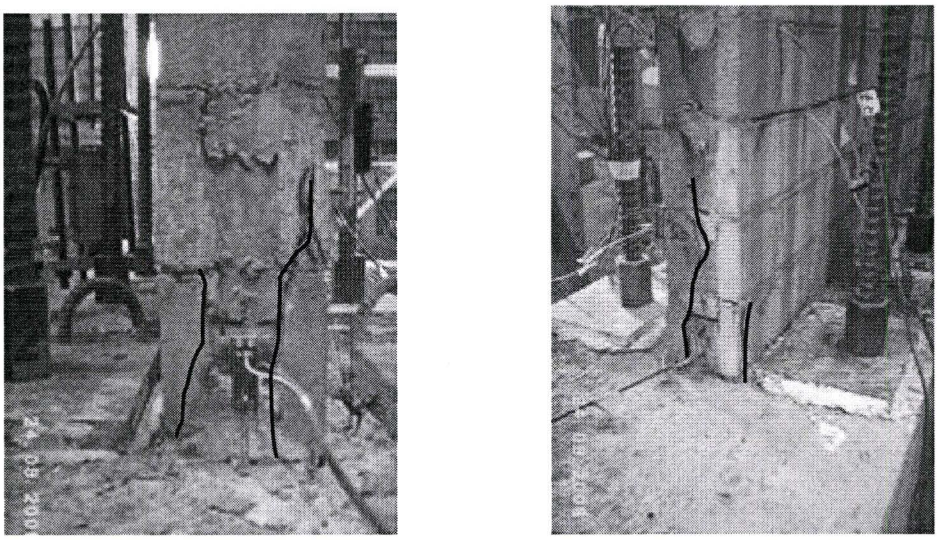

a) Left toe b) Right toe

Fig. 3.27: Cracking at both toes at $4\times\Delta_y$ (Wall 4)

It was decided to omit the $7\times\Delta_y$ displacement cycle to reduce the number of cycles after yielding in an attempt to avoid premature fatigue failure of the vertical reinforcement at the wall ends. During loading to 28 mm top displacement ($8\times\Delta_y$), a wide vertical crack was observed at the right toe (under compression during loading in the (+) ve direction) and extended to the third course above the foundation. Splitting of the end webs, cracking of the grout column, and spalling of the face shells in the first course over the length of the end block occurred as shown in Fig. 3.28. The load dropped during loading in the (+) ve direction from 260 kN at 26 mm displacement to about 190 kN when 28 mm was reached. A less dramatic change in load carrying capacity occurred during loading in the (-) ve direction as the load only dropped from 255 kN at 24 mm to about 222 kN when 28 mm was reached. Spalling of the face shells at the left toe occurred in the first course over the end half block during the first loading cycle.

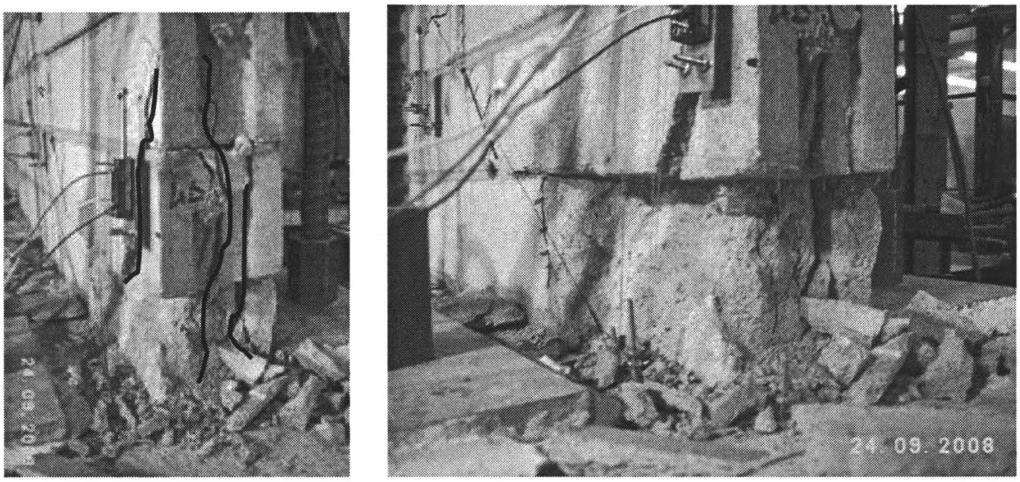

a) Vertical cracks b) Spalling of the of face shells of the end block

Fig. 3.28: Spalling and cracking at the right toe at $8 \times \Delta_y$ (Wall 4)

During the second loading cycle at $8 \times \Delta_y$ (28 mm), out-of-plane buckling of the vertical reinforcement at the right toe occurred and spalling of the face shells extended to about a 2 block lengths at the second course above the foundation. The displacement of the outermost bar was followed by the out-of-plane displacements of the second and third vertical bars at the right toe as well as the horizontal reinforcement and the end of the wall, as shown in Fig. 3.29 (a). During the same loading cycle, the left toe crushed, vertical cracks at the end of the wall extended to the third course above the foundation, the outermost grout column split, and buckling of the vertical bars were observed, as shown in Figs. 3.29 (b) and (c).

At the end of the test and during the 35 mm loading cycle ($10 \times \Delta_y$), the damage at the right end of the wall included buckling of the outermost four vertical bars, spalling of the masonry blocks, and crumbling of the grout columns over the lower three courses and up to a distance equal to three block lengths along the length of the wall. The extent of damage at the left end of the wall included buckling of the outermost two vertical bars between the first and the second courses and spalling of the masonry blocks over the lower two courses and up to a distance equal to two block lengths along the length of the wall. The extent of damage at the end of the test for the wall is shown in Fig. 3.30. It can be seen that most of the damage was limited to the lower three courses of the first storey, and that cracking was significant over the first storey but insignificant in the second storey.

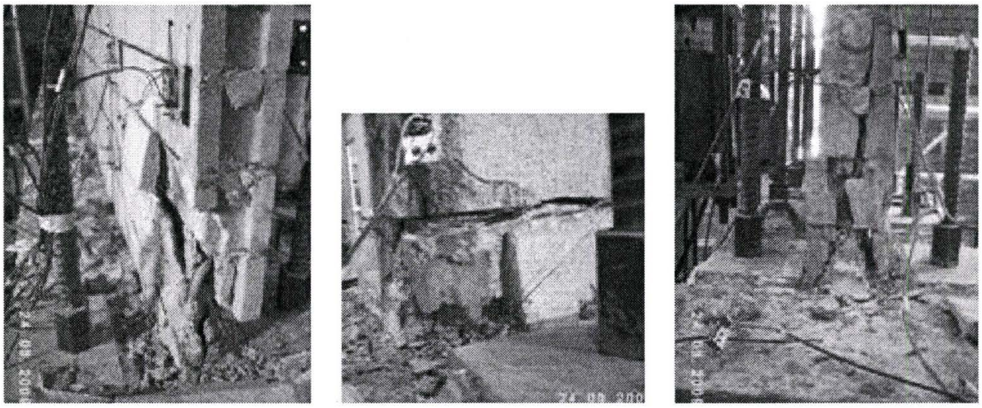

a) Right toe damage b) Crushing at left toe c) Splitting at the left toe

Fig. 3.29: Damage at the second cycle of the $8\times\Delta_y$ displacement cycle (Wall 4)

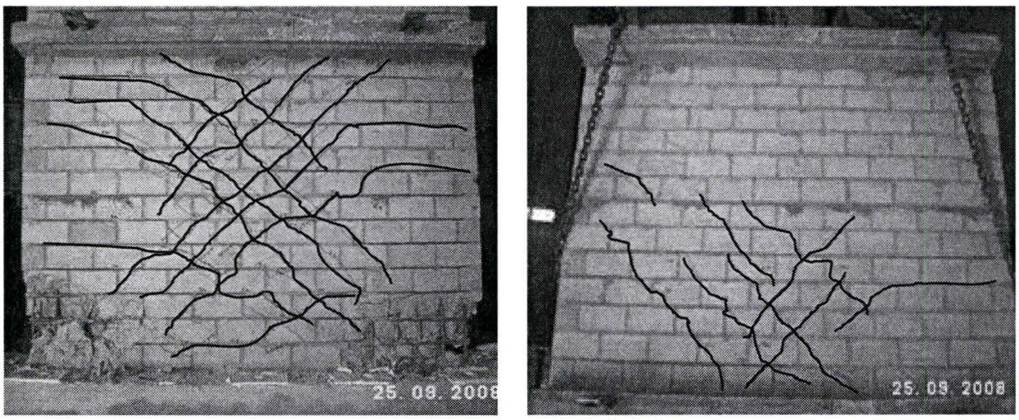

a) First storey b) Second storey

Fig. 3.30: Extent of damage at the end of the test (Wall 4)

3.5.3 Load-displacement response

The hysteresis loops for Wall 4, shown in Fig. 3.25, indicate a symmetric response for loading in both directions. The slopes of the loops decreased gradually with increases in lateral top displacement indicating loss of stiffness. The wall response was almost linear elastic, characterized by thin hysteresis loops generating low energy dissipation, up to the first yield of the outermost reinforcement at the base of the wall. At higher displacement levels, larger loops generating higher amounts of energy dissipation and increases in plastic deformations (corresponding to zero load) were evident. The wall exhibited almost the same capacity (within 5%) when subjected to the second loading cycle of the same displacement level until reaching about 261 kN lateral load, corresponding to a top displacement of about 14 mm ($4 \times \Delta_y$). However, at higher displacement levels the lateral load resistance differences between the two cycles increased as shown in Fig. 3.31.

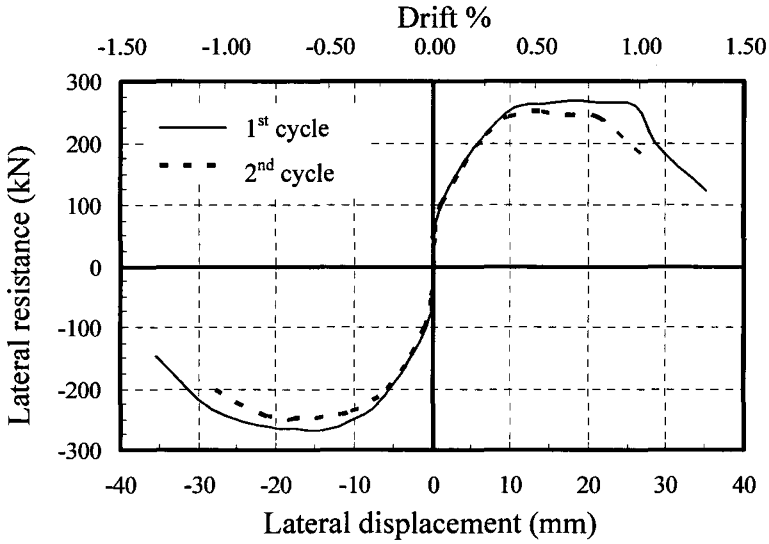

Fig. 3.31: Envelopes of load-displacement relationship (Wall 4)

Wall 4 reached a maximum lateral load capacity of 265 kN at 14.0 mm top lateral displacement ($4 \times \Delta_y$) during loading in the (+) ve direction. The wall maintained its capacity up to 26 mm top displacement ($7.5 \times \Delta_y$) but at 28 mm top lateral displacement ($8 \times \Delta_y$) had lost 25% of its maximum lateral load capacity. This significant loss in strength coincided with splitting of the outermost grout column and buckling of the outermost reinforcing bar.

During loading in the (-) ve direction, Wall 4 reached a maximum lateral load capacity of 267 kN at 12.5 mm top lateral displacement ($3.6\times\Delta_y$). The wall lost 12% and 25% of its maximum lateral capacity during the first and second cycles at 28 mm top lateral displacement ($8\times\Delta_y$), respectively. This significant loss in lateral resistance was observed after the lower block at the toe of the wall crushed, the outermost grout columns split and the vertical reinforcement buckled.

3.6 Wall 5

3.6.1 Details of Wall 5

Wall 5 was a two storey flanged wall, with overall dimensions of 1,802 mm length and 2,660 mm height. The wall cross section dimension and vertical reinforcement arrangement were similar to Wall 2. The wall was reinforced horizontally with two D4 deformed wires in every course over the entire wall height (ρ_h = 0.60%). The wall was subjected to an axial compressive axial load of 160 kN which in addition to its self weight resulted in an axial compressive stress of 0.89 MPa at the wall base. The hysteresis loops of Wall 5 were presented in Fig. 3.32.

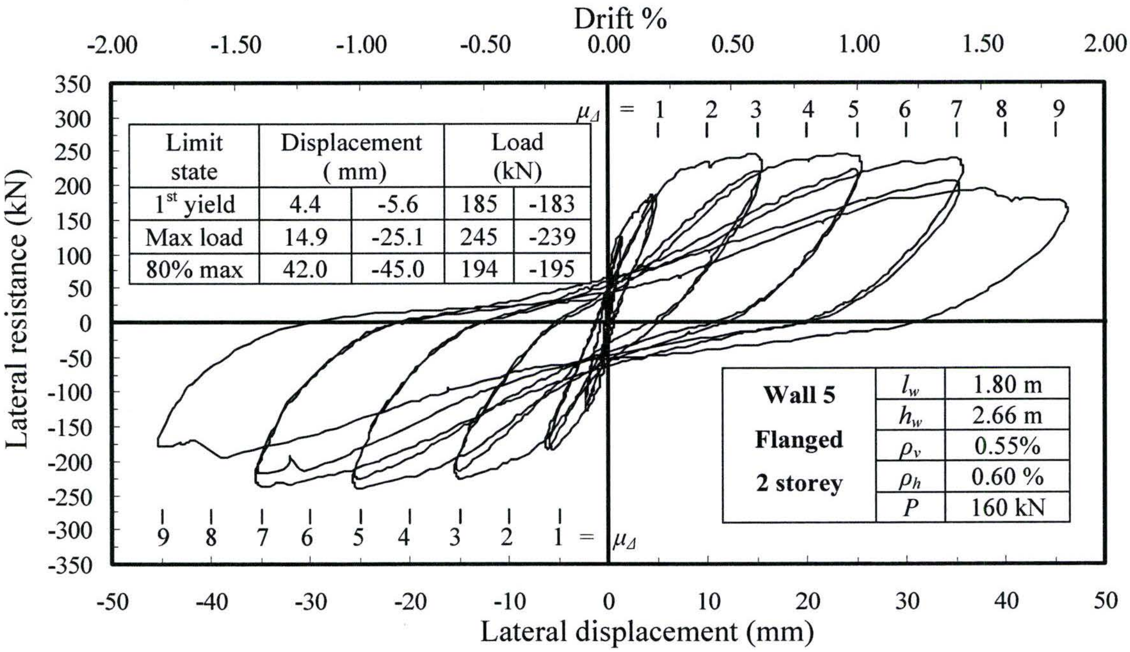

Limit state	Displacement (mm)		Load (kN)	
1st yield	4.4	-5.6	185	-183
Max load	14.9	-25.1	245	-239
80% max	42.0	-45.0	194	-195

Wall 5	l_w	1.80 m
Flanged	h_w	2.66 m
	ρ_v	0.55%
2 storey	ρ_h	0.60 %
	P	160 kN

Fig. 3.32: Hysteresis loops (Wall 5)

3.6.2 General observations

Before yielding, the wall was cycled in displacement control to reach target lateral load resistances based on the predicted 185 kN yield resistance of the wall. The loading scheme up to yielding was similar to Wall 4. However, after yielding, it was decided to cycle the wall using increments of $2\times\Delta_y$ to reduce the number of loading cycles.

No cracks were observed during the loading cycles before yielding. At yielding of the outermost reinforcement, horizontal cracks were observed over almost all of the bed joints in the first storey. Some diagonal cracks were also observed in the first storey between the sixth and the ninth courses above the foundation. No cracks were observed in the second storey at this displacement level.

During the 15 mm ($3\times\Delta_y$) loading cycle, diagonal cracks were observed between the second and eleventh courses above the foundation, as shown in Fig. 3.33 (a). Also, horizontal cracks were observed in the face shell in the left flange at the fourth course and at the first course in the right flange. In the second storey, diagonal and horizontal cracks were observed over the six courses above the slab, as shown in Fig. 3.33 (b).

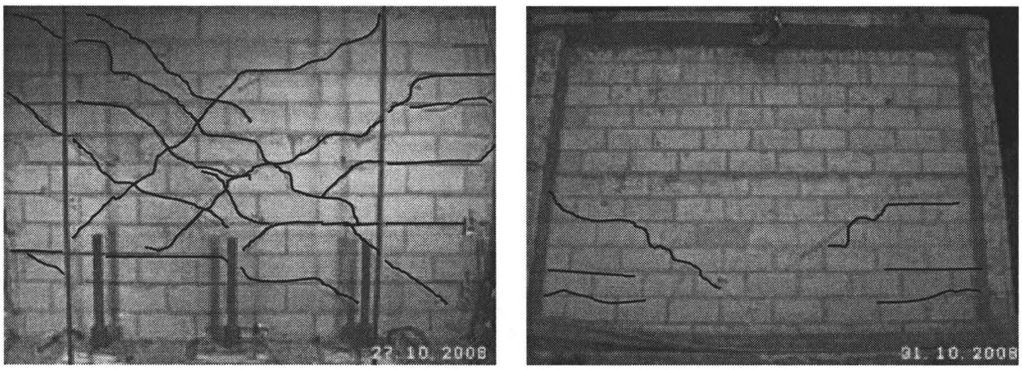

a) First storey b) Second storey

Fig. 3.33: Diagonal cracks at $3\times\Delta_y$ (Wall 5)

During the 25 mm ($5\times\Delta_y$) loading cycle, vertical cracks were observed in both toes up to the third course above the foundation, as shown in Fig. 3.34 (a) for the left flange. Diagonal cracks over the first storey extended from the first course up to the concrete slab at the floor level, as shown in Fig. 3.34 (b), and vertical cracks were also observed in the concrete slab at the first storey. Diagonal cracks, originally observed in the second storey at $3\times\Delta_y$, increased slightly in length.

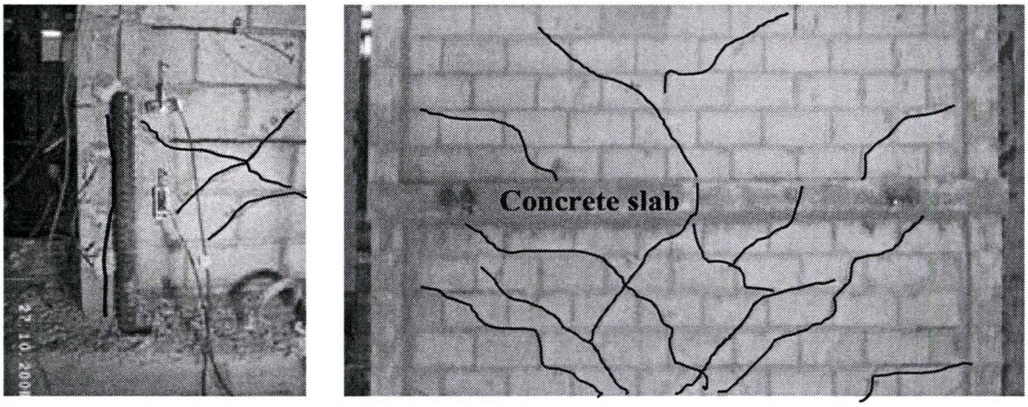

a) Cracking at left toe b) Cracks between first and second storeys

Fig. 3.34: Cracking at toe level and in the floor slab at $5\times\Delta_y$ (Wall 5)

During the first loading cycle at 35 mm ($7\times\Delta_y$), widening of the vertical cracks at the right toe and separation of the face shells were observed, as shown in Fig. 3.35 (a). During the second loading cycle, splitting of the grout column of each side of the wall web at the right flange, crushing of the first course, and spalling of the end face shells occurred, as shown in Figs. 3.35 (b) and (c). No significant damage was observed at the left toe, with formation of new vertical cracks at the first course above the foundation seen as the only visible change.

During the loading cycle at 45 mm ($9\times\Delta_y$), buckling of the reinforcement in the right flange on each side of the wall web occurred and spalling of the face shells and crumbling of the grout column extended up to the third course along the entire length of the flange, as shown in Fig. 3.36 (a). The damage at the end of the test extended into the wall web but the reinforcement in the middle of the flange (aligned with the web) had not buckled, as shown in Fig. 3.36 (b). During loading in the (–) ve direction at the same displacement level, the middle bar in the right flange broke at about $8\times\Delta_y$. The extent of damage at the left end of the wall was similar to the right end. Spalling of the face shells, crumbling of the grout columns, and buckling of the reinforcement occurred at both ends of the left flange. The damage was concentrated in the lower 3 courses above the foundation and in the flange, as shown in Fig. 3.37. At this stage the test was terminated due to the loss of about 50% of the lateral load capacity.

a) Widening of cracks b) Grout column splitting c) Spalling of face shells

Fig. 3.35: Damage at the right toe at $7\times\Delta_y$ (Wall 5)

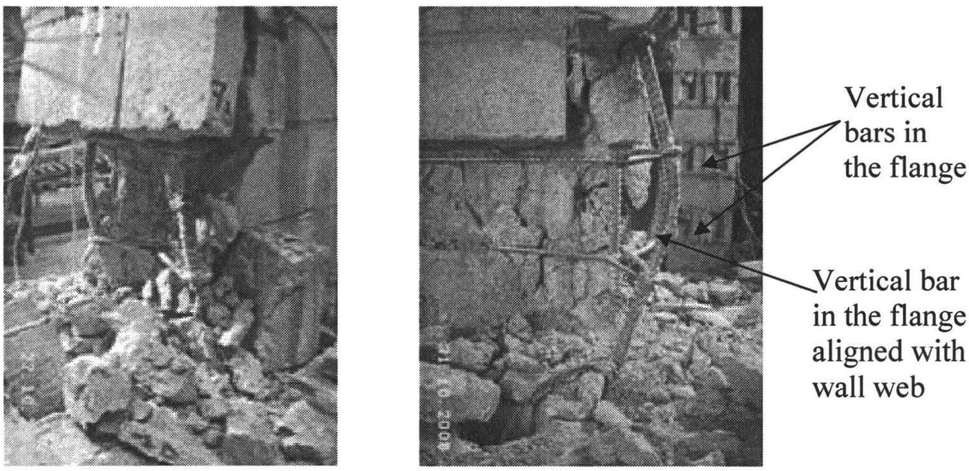

a) Buckling of reinforcement b) Extent of damage

Fig. 3.36: Damage at the right toe at $9\times\Delta_y$ (Wall 5)

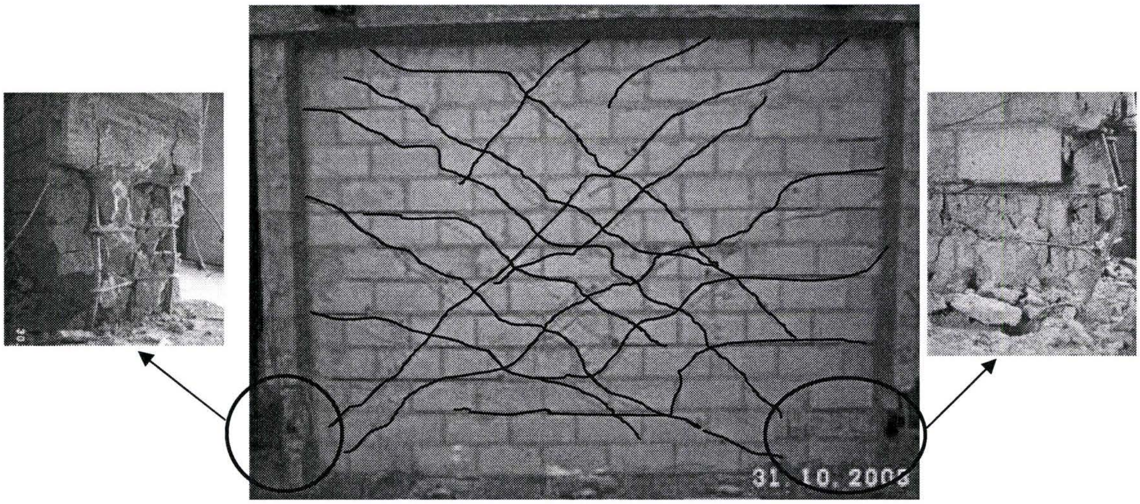

Fig. 3.37: Damage at the end of the test (Wall 5)

3.6.3 Load-displacement response

The hysteresis loops for Wall 5, shown in Fig. 3.32, indicate a symmetric response for loading in both directions. The slopes of the loops decreased gradually with increases in lateral top displacement indicating loss of stiffness similar to previous walls. The wall response was almost linear elastic, characterized by thin hysteresis loops generating low energy dissipation, up to the first yield of the outermost reinforcement at the base of the wall. At higher displacement levels, larger loops generated higher amounts of energy dissipation resulting from increases in plastic deformation.

The wall maintained almost the same capacity (within 5% less) when subjected to the second loading cycle at the same target displacement level until reaching about 220 kN, corresponding to a top displacement of about 10 mm ($2\times\Delta_y$) in both directions of loading. However, cycling the wall to higher displacement levels resulted in changes in lateral load resistance of more than 5% between the two cycles, as shown in Fig. 3.38.

Wall 5 reached a maximum lateral load capacity of 245 kN at 14.9 mm top lateral displacement ($3\times\Delta_y$) during loading in the (+) ve direction. The wall did not loose any significant amount of its lateral capacity until the first cycle at 35 mm top lateral displacement ($7\times\Delta_y$) but lost about 16 % of its resistance during the second loading cycle. The wall had lost about 30% of its maximum lateral capacity during the 45 mm top lateral displacement ($9\times\Delta_y$). The significant loss in strength coincided with splitting of the outermost grout columns encasing the three vertical bars in the flange and buckling of the outermost reinforcement similar to Wall 2.

During loading in the (-) ve direction, Wall 5 reached a maximum lateral load capacity of 239 kN at 25.1 mm top lateral displacement ($5\times\Delta_y$). The wall lost about 10% of its maximum lateral capacity during the second loading cycle at 35 mm top lateral displacement ($7\times\Delta_y$). During the loading cycle corresponding to $9\times\Delta_y$ top lateral displacement, the wall lost about 25% of its maximum lateral capacity, which coincided with fracture of the outermost reinforcement.

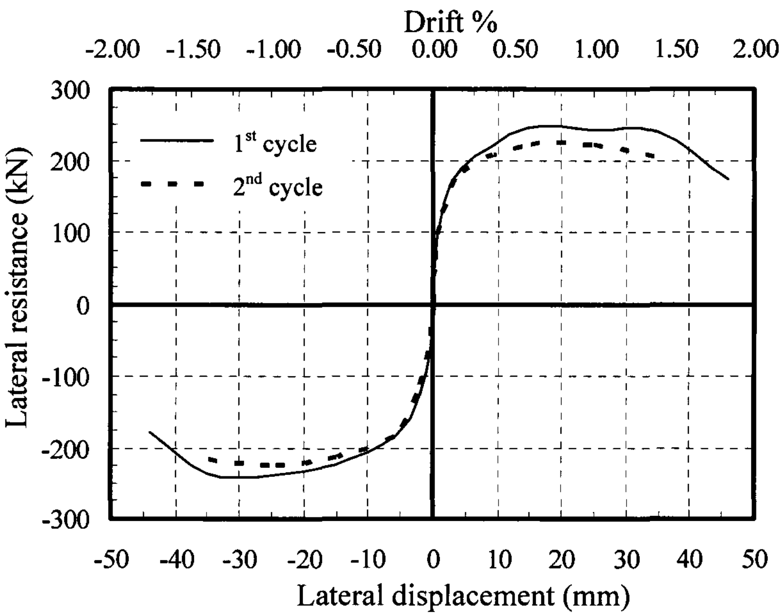

Fig. 3.38: Envelopes of load-displacement relationships (Wall 5)

3.7 Wall 6

3.7.1 Details of Wall 6

Wall 6 was a 2 storey end-confined wall (wall with boundary elements), with overall dimensions of 1,802 mm length and 2,660 mm height. The wall cross section dimensions and vertical reinforcement arrangement were similar to Wall 3. The wall was reinforced horizontally with two D4 deformed wires in every course over the wall height ($\rho_h = 0.60\%$). The wall was subjected to an axial compressive load equal to 160 kN which with the addition to its self weight, resulted in an axial compressive stress of 0.89 MPa at the wall base. The hysteresis loops for Wall 6 were presented in Fig. 3.39.

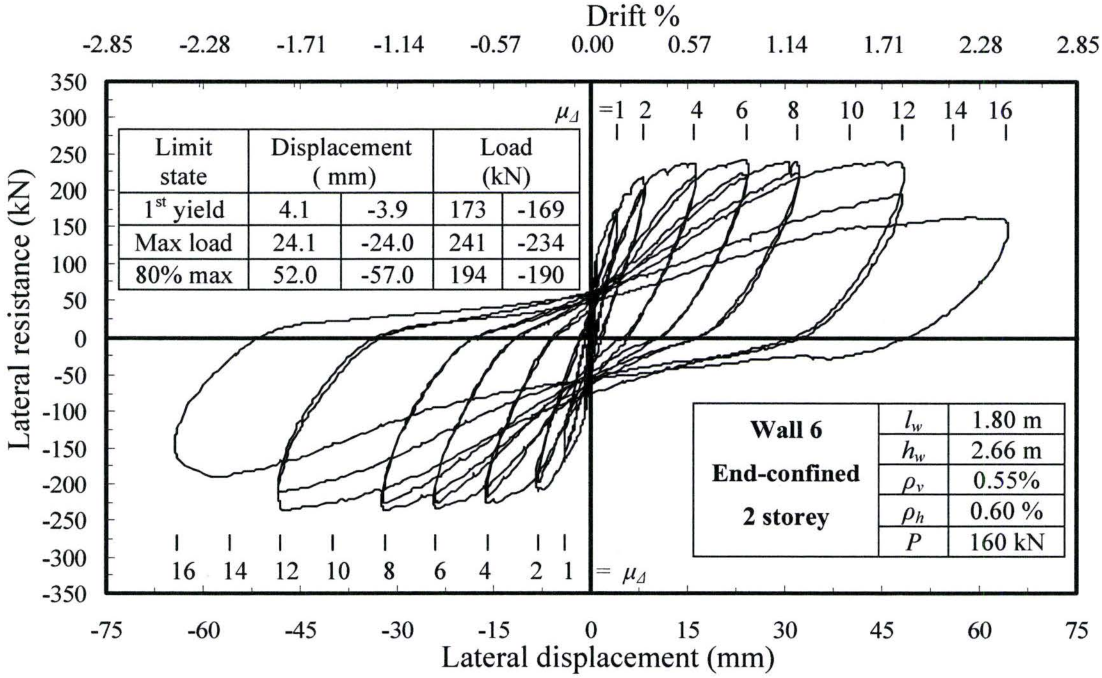

Fig. 3.39: Hysteresis loops (Wall 6)

3.7.2 General observations

Before yielding, the wall was cycled in displacement control to reach a target lateral load resistance based on the predicted yield resistance of about 175 kN. The loading scheme up to yielding was similar to Wall 5.

No cracks were observed during the loading cycles before yielding. At yielding of the outermost reinforcement, horizontal cracks were observed in almost all of the bed joints in the first storey. Some diagonal cracks were also observed in the first storey between the third and the tenth courses above the foundation. No cracks were observed in the second storey at this displacement level.

During the loading cycle corresponding to 8 mm displacement ($2\times\Delta_y$), diagonal cracks were observed at the second course above the foundation and up to the concrete slab at the top of the first storey. In the following loading cycle corresponding to 16 mm ($4\times\Delta_y$), diagonal cracks in the first storey extended to the boundary element at each end of the wall, as shown in Fig. 3.40 (a). Diagonal cracks in the second storey over the lower six courses and vertical cracks in the concrete slab were observed during this loading cycle, as shown in Fig. 3.40 (b).

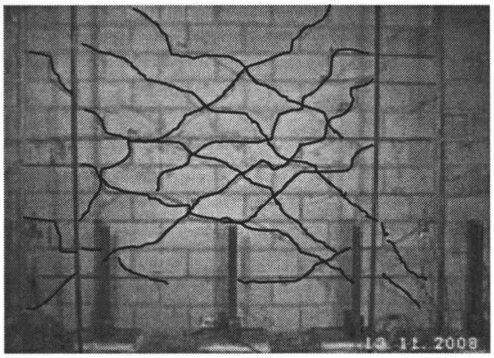

a) First storey

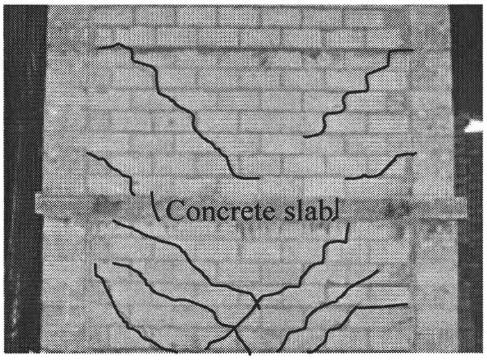

b) Second storey

Fig. 3.40: Cracks at $4\times\Delta_y$ (Wall 6)

To limit the number of loading cycles beyond yielding to reduce the possibility of fatigue failure of the reinforcement as seen in previous wall tests, the cyclic testing proceeded with increments of $2\times\Delta_y$. During the loading cycle at 24 mm ($6\times\Delta_y$), no new cracks were observed. However, slight propagation of diagonal cracks and widening of horizontal cracks occurred. During the loading cycle at 32 mm ($8\times\Delta_y$), horizontal cracks were observed at the first and the third courses in the right boundary element as shown in Fig. 3.41 (a) and widening of cracks between the wall and the foundation was significant, as shown in Fig. 3.41 (b).

During the first loading cycle at 48 mm ($12\times\Delta_y$), vertical and inclined cracks at the right toe and inclined cracks at the left toe were observed during loading in the (+) ve direction, as shown in Fig. 3.42. During loading in the (–) ve direction, vertical and inclined cracks at the left toe and wide opening of the horizontal cracks between the first and the second courses above the foundation at the right toe were observed, as shown in Fig. 3.43.

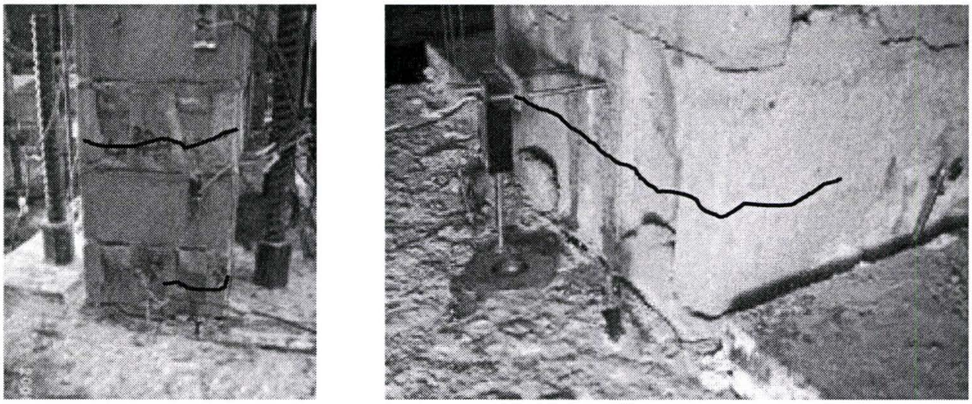

a) Right toe b) Left toe

Fig. 3.41: Horizontal cracks at both toes at $8\times\Delta_y$ (Wall 6)

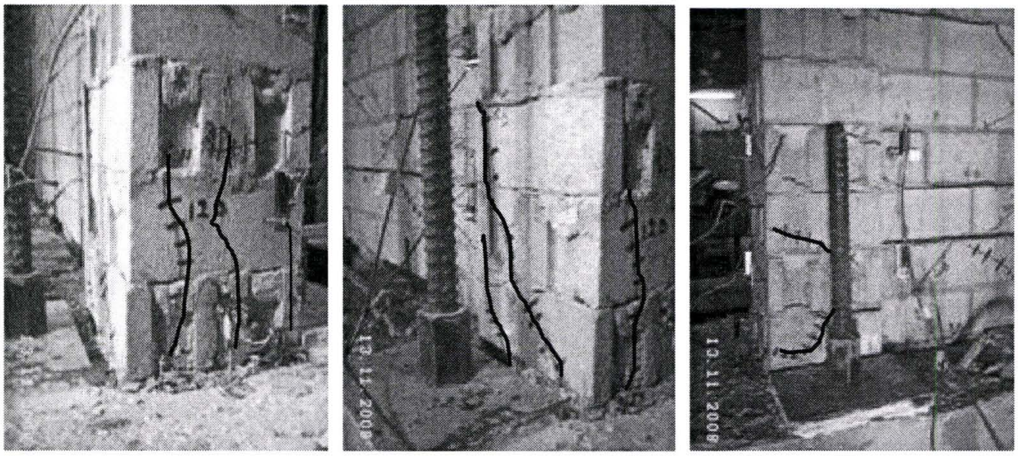

a) Vertical cracks (right) b) Inclined cracks (right) c) Inclined cracks (left)

Fig. 3.42: Toe cracking during loading in the +(ve) direction at $12\times\Delta_y$ (Wall 6)

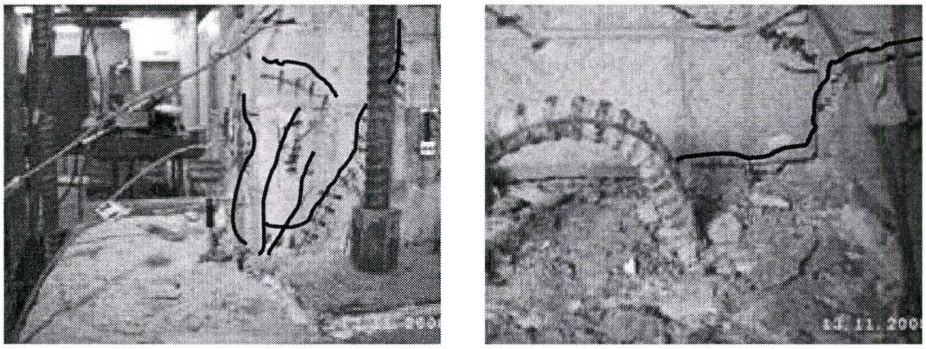

a) Left toe b) Right toe

Fig. 3.43: Toe cracking during loading in the -(ve) direction at $12\times\Delta_y$ (Wall 6)

During the second loading cycle at 48 mm (12×Δ_y), crushing of both toes, spalling of the end face shells, and crumbling of the grout between the foundation and the first horizontal tie in the boundary elements were observed, as shown in Fig. 3.44. Buckling of the outermost vertical reinforcement at the left toe occurred between the foundation and the first horizontal tie in the boundary element.

a) Left toe

b) Right toe

Fig. 3.44: Damage during the second loading cycle at 12×Δ_y (Wall 6)

When the wall was displaced to 64 mm (16×Δ_y), buckling of the outermost bars occurred at the right end of the wall and lateral out-of-plane displacement was observed at the level of the first course, as shown in Fig. 3.45 (a). This lateral displacement resulted in propagation of damage towards the web of the wall and spalling of the face shells along the web occurred, as shown in Fig. 3.45 (b). During loading in the (–) ve direction, buckling of all of the reinforcement in the boundary element at the left end of the wall was observed between the foundation and the horizontal ties at the first and the second courses, as shown in Fig. 3.45 (c). The wall lost a significant amount of its lateral resistance as a result of the lateral displacement at the right toe and during the second loading cycle, its lateral resistance had decreased to about 80 kN (about one third of the maximum resistance) at 64 mm top lateral displacement. At this displacement level, buckling of reinforcement in the web was observed and deterioration of the second course occurred due to the lateral displacement of the horizontal reinforcement, as shown in Fig. 3.45 (d). The test was terminated at this point.

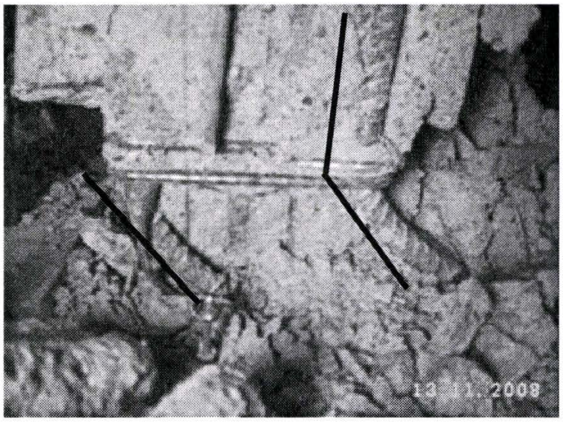

a) Buckling of bar at the right toe

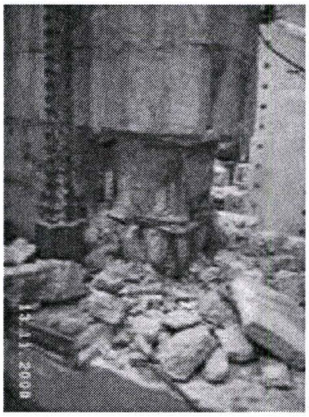

b) Spalling at the left toe

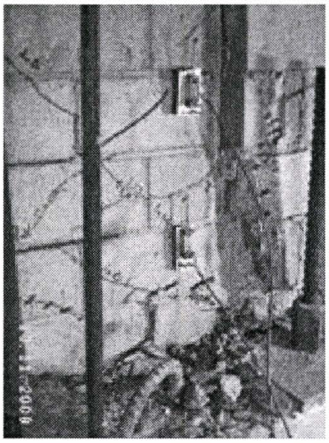

c) Spalling along the web

d) Deterioration of the second course

Fig. 3.45: Damage at the end of the test at $16\times\Delta_y$ (Wall 6)

3.7.3 Load-displacement response

The hysteresis loops for Wall 6, shown in Fig. 3.39, indicate a symmetric response for loading in both directions. The slopes of the loops decreased gradually with increases in lateral top displacement indicating loss of stiffness similar to previous wall tests. The wall response was almost linear elastic, characterized by thin hysteresis loops generating low energy dissipation, up to first yield of the outermost reinforcement at the base of the wall. At higher displacement levels, larger loops generated higher amounts of energy dissipation coinciding with increases in plastic deformation.

The wall maintained almost the same capacity (within 5%) when subjected to the second loading cycle at 16 mm ($4\times\Delta_y$) in the (+) ve direction of loading at about 223 kN. In the (–) ve direction of loading, the wall maintained its capacity until reaching about 236 kN, corresponding to a top displacement of about 32 mm ($8\times\Delta_y$). However, cycling of the wall to higher displacement levels resulted in differences in lateral resistance (more than 5%) between the two cycles, as shown in Fig. 3.46.

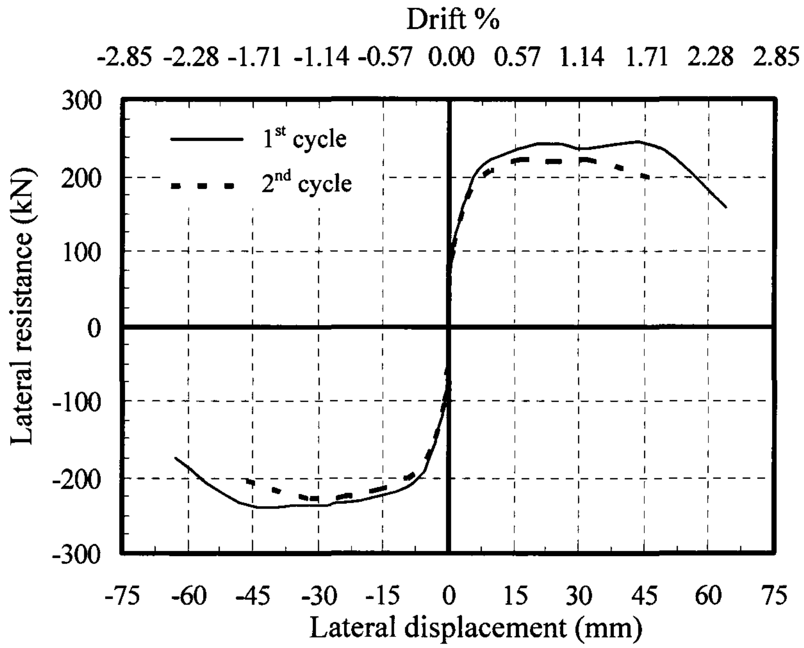

Fig. 3.46: Envelopes of load-displacement relationships (Wall 6)

Wall 6 reached a maximum lateral load capacity of 241 kN at 24.1 mm top lateral displacement ($6\times\Delta_y$) during loading in the (+) ve direction. The wall did not loose any significant amount of its lateral capacity up to the first cycle at 48 mm top lateral displacement ($12\times\Delta_y$) but lost about 20 % of its capacity during the second loading cycle at this displacement. The significant loss in strength coincided with spalling of the face shells and crumbling of the grout encasing the outermost bars in the boundary element.

During loading in the (-) ve direction, Wall 6 reached a maximum lateral load capacity of 234 kN at 24.0 mm top lateral displacement ($6\times\Delta_y$). The wall lost about

14% of its maximum lateral load capacity during the second loading cycle at 48 mm top lateral displacement ($12\times\Delta_y$). During the loading cycle corresponding to $14\times\Delta_y$ top lateral displacement, the wall had lost about 25% of its maximum lateral load capacity, which coincided with almost the same type of damage that had occurred at the right end of the wall.

3.8 Wall 7

3.8.1 Details of Wall 7

Wall 7 was a 2 storey end-confined wall (wall with boundary elements, as show in Figs. 2.2 and 2.15), with overall dimensions of 1,802 mm length and 2,660 mm height. The wall web was 90 mm thick and the boundary elements are constructed using a pilaster unit at each end of the wall. The vertical and horizontal reinforcement were similar to that in Wall 6 but spiral reinforcement (30 mm pitch) in the pilaster units were used instead of the closed ties used in Wall 6. The wall was subjected to an axial compressive axial load of 160 kN which, with the addition to its self weight, resulted in an axial compressive stress of 0.89 MPa at the wall base. The hysteresis loops for Wall 7 were presented in Fig. 3.47.

3.8.2 General observations

Before yielding, the wall was cycled in displacement control to reach target lateral load resistances based on the predicted yield resistance of the wall of about 175 kN. The loading scheme was similar to that of Wall 6. No cracks were observed during the loading cycles before yielding.

At yielding of the outermost reinforcement, horizontal cracks were observed over almost all of the bed joints in the first storey. Some diagonal cracks were also observed in the first storey between the fifth and the tenth courses above the foundation. No cracks were observed in the second storey at this displacement level. During the loading cycle corresponding to 10 mm ($2\times\Delta_y$), the diagonal cracks extended to the second course above the foundation at the first storey. In the following loading cycle corresponding to 20 mm ($4\times\Delta_y$), diagonal cracks were observed over the entire height of the first storey, as shown in Fig. 3.48 (a). Diagonal cracks over the lower six courses in the second storey were also observed during this loading cycle, as shown in Fig. 3.48 (b).

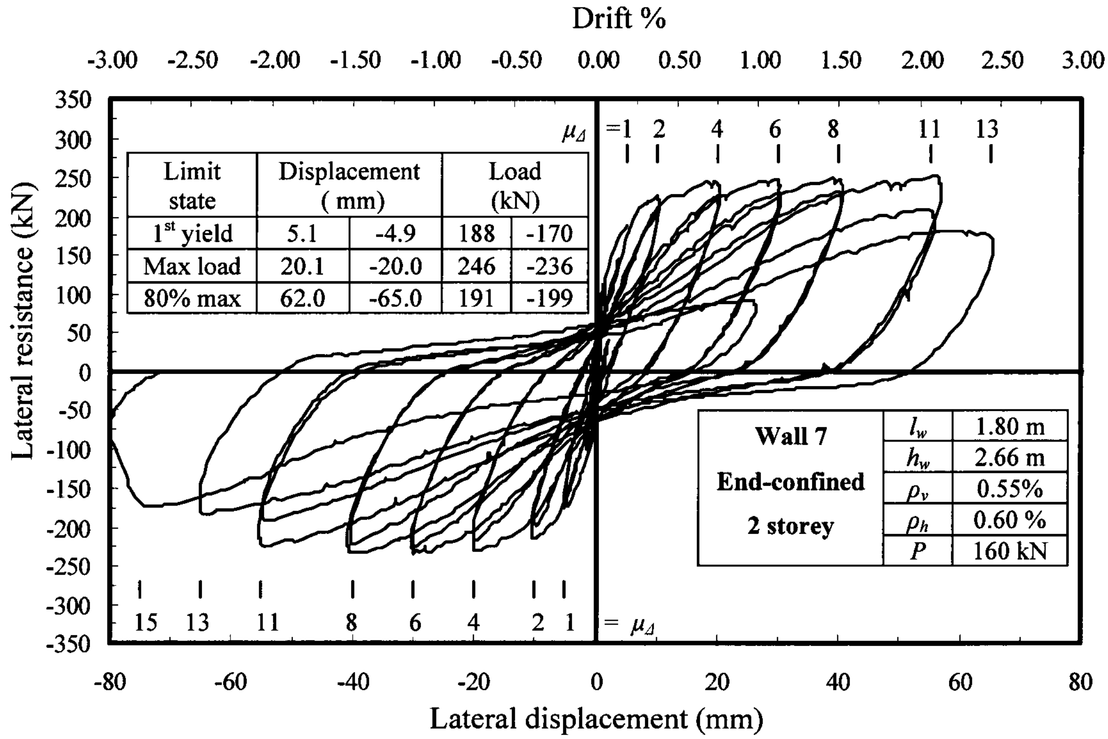

Fig. 3.47: Hysteresis loops (Wall 7)

To limit the number of loading cycles beyond yielding to reduce the possibility of fatigue failure of the reinforcement as seen in previous walls, the wall was cycled with increment of $2\times\Delta_y$, similar to Wall 6. During the loading cycle at 30 mm displacement ($6\times\Delta_y$), no new cracks were observed. However, slight propagation of diagonal cracks and widening of horizontal cracks were observed. During the loading cycle at 40 mm ($8\times\Delta_y$), vertical cracks in the right toe and inclined cracks in the left toe were observed, as shown in Fig. 3.49. Inclined cracks at the second course above the foundation and in the second storey and widening of the horizontal cracks were also observed as well as a vertical crack in the slab at the first storey.

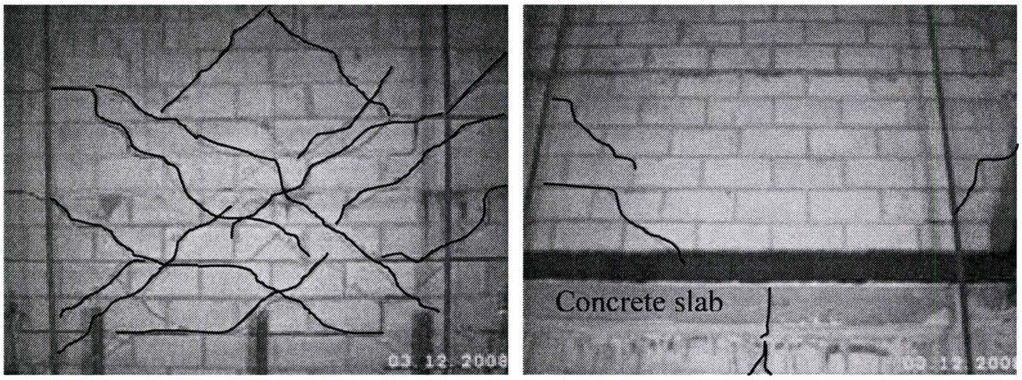

a) First storey b) Second storey

Fig. 3.48: Cracks at $4{\times}\Delta_y$ (Wall 7)

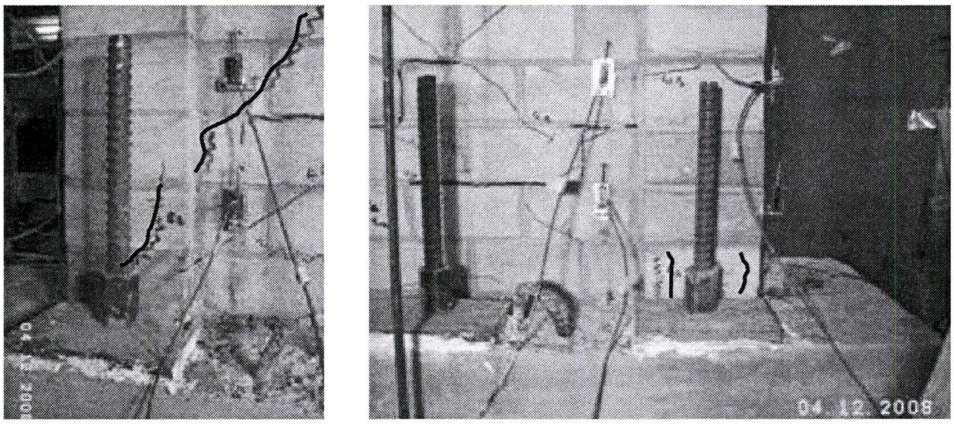

a) Left toe b) Right toe

Fig. 3.49: Vertical and inclined cracks at both toes at $8{\times}\Delta_y$ (Wall 7)

During the first loading cycle at 55 mm displacement ($11{\times}\Delta_y$), vertical cracks at the right toe up to the fourth course above the foundation and inclined cracks at the left toe up to the third course above the foundation were observed, as shown in Fig. 3.50. Spalling of the right toe up to the fourth course occurred during the unloading cycle and the grout column in the pilaster unit was visible and intact, as shown in Fig. 3.51 (a). Significant widening of the inclined cracks at the left toe was observed during the unloading cycle, as shown in Fig. 3.51 (b). During the second loading cycle, spalling of all face shells of the pilaster units up to the fourth course and crushing of the grout column above the foundation at the right end of the wall and crushing of the left toe occurred, as shown in Fig. 3.52.

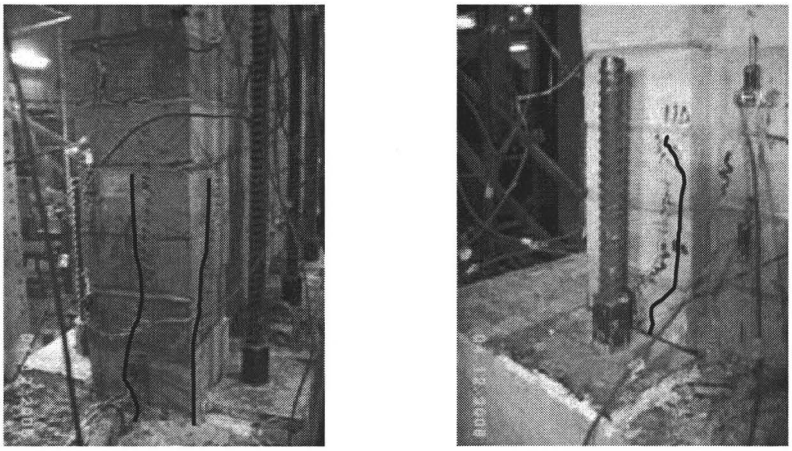

a) Right toe b) Left toe

Fig. 3.50: Toe cracking during loading at $11\times\Delta_y$ (Wall 7)

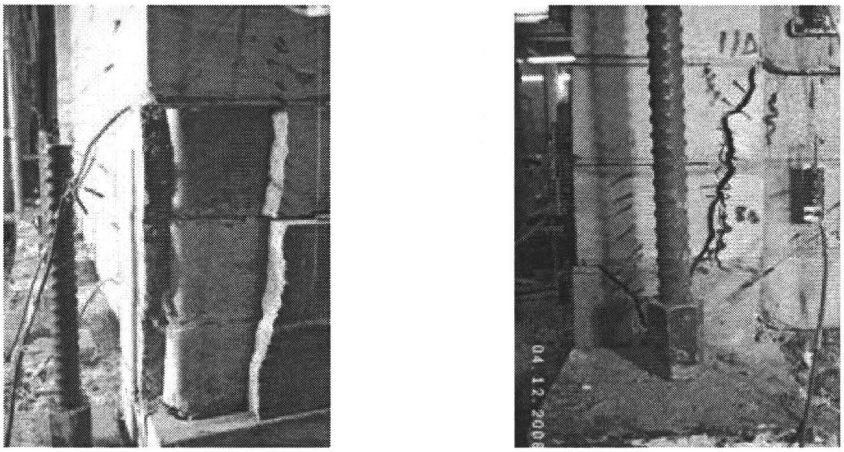

a) Right toe b) Left toe

Fig. 3.51: Spalling and cracking during the unloading cycles at $11\times\Delta_y$ (Wall 7)

When the wall was displaced to 65 mm ($13\times\Delta_y$), the spiral broke at mid-height of the first course in the right toe. Buckling of the outermost bars and crumbling of the unconfined grout outside the spiral were observed, as shown in Fig. 3.53 (a). The spalling of the blocks and the unconfined grout outside the spiral reinforcement only occurred up to the second course above the foundation at the left toe, as shown in Fig. 3.53 (b). Bulging of the face shells along the web of the wall was observed at the left end of the wall adjacent to the boundary element, as shown in Fig. 3.53 (c). During the second loading cycle to 65 mm displacement, the outermost bars at the right end of the wall bent and the wall bent laterally in the out-of-plane direction. Loading in the (+) ve direction during this cycle was stopped at about 25 mm to avoid severely damaging the wall as had happened with Wall 6. The wall was then monotonically loaded in the (–) ve direction until failure occurred at about 75 mm top lateral displacement ($15\times\Delta_y$). The loss of lateral load resistance was associated with crushing of the confined grout within the spiral reinforcement at the left end of the wall and buckling of the reinforcement leading to lateral (out-of-plane) displacement of the wall.

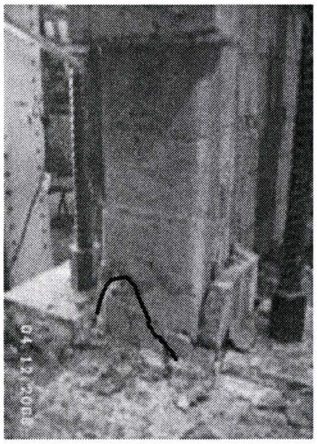

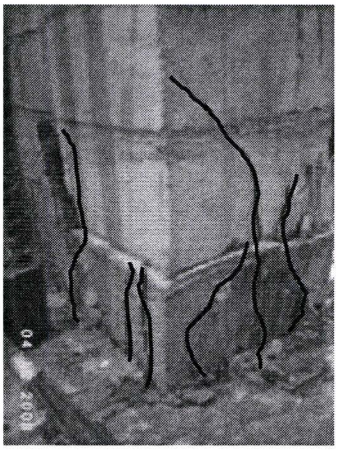

a) Spalling at right toe b) Crushing of left toe

Fig. 3.52: Damage during the second loading cycle at $11\times\Delta_y$ (Wall 7)

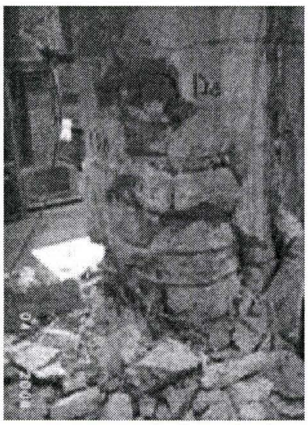

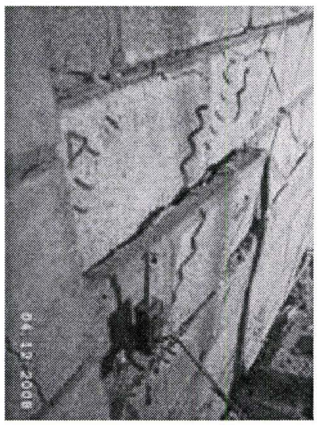

a) Broken spiral at right toe b) Spalling at left toe c) Bulging of face shells

Fig. 3.53: Damage at both ends of the wall at $13\times\Delta_y$ (Wall 7)

3.8.3 Load-displacement response

The hysteresis loops for Wall 7, shown in Fig. 3.39, indicate a symmetric response for loading in both directions. The slopes of the loops decreased gradually with increases in lateral top displacement indicating loss of stiffness similar to previous walls. The wall response was almost linear elastic, characterized by thin hysteresis loops generating low energy dissipation, up to the first yield of the outermost reinforcement at the base of the wall. At higher displacement levels, larger loops generated higher amounts of energy dissipation due to increases in plastic deformation.

The wall maintained almost the same capacity (within 5% less) when subjected to the second loading cycle at 30 mm displacement ($6\times\Delta_y$) in the (+) ve direction of loading at about 230 kN. In the (–) ve direction of loading, the wall maintained its capacity until reaching about 233 kN, corresponding to a top displacement of 40 mm ($8\times\Delta_y$). However, cycling the wall to higher displacement levels resulted in lateral resistance differences of more than 5% between the two cycles, as shown in Fig. 3.54.

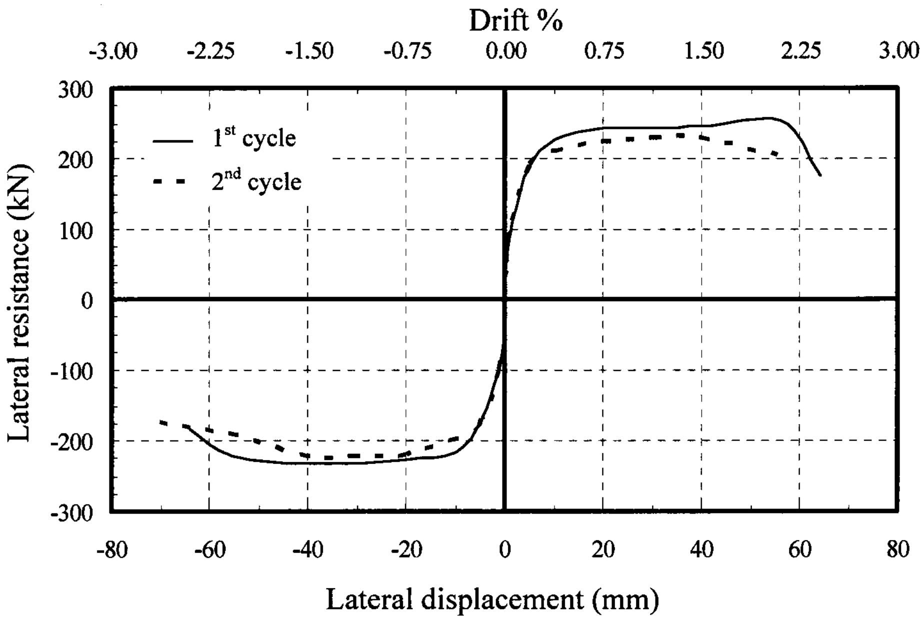

Fig. 3.54:Envelopes of load-displacement relationship (Wall 7)

Wall 7 reached a maximum lateral load capacity of 246 kN at 20.1 mm top lateral displacement ($4\times\Delta_y$) during loading in the (+) ve direction. The wall did not loose any significant amount of its lateral load capacity up to the first cycle at 55 mm top lateral displacement ($11\times\Delta_y$) but lost about 16% of its capacity during the second loading cycle at this displacement. The significant loss in strength coincided with breaking of the spiral reinforcement at the first course above the foundation followed by the spalling of the face shells and crumbling of the unconfined grout in the boundary element.

During loading in the (-) ve direction, Wall 7 reached a maximum lateral load capacity of 236 kN at 20.0 mm top lateral displacement ($4\times\Delta_y$). The wall did not loose any significant amount of its lateral load capacity up to the first cycle at 55 mm top lateral displacement ($11\times\Delta_y$) but lost about 17% of its capacity during the second loading cycle. During the loading cycle corresponding to $13\times\Delta_y$ top lateral displacement, the wall had lost about 26% of its maximum lateral load capacity but maintained the same lateral resistance up to $15\times\Delta_y$. The significant loss in strength occurred after the lateral displacement of the wall due to buckling of the reinforcement at the other end of the wall.

3.9 Lateral load capacity

One of the objectives during the specimen design phase was that the walls within each of the two phases would have approximately the same lateral load capacity. This was an important criterion to be able to determine the effect of the proposed wall end configuration on the overall response when rectangular walls were replaced with flanged and end-confined walls subjected to the same axial load.

The predicted and experimentally measured yield strengths, Q_y, and ultimate flexural strength, Q_u, were listed in Table 3.1 for all of the walls. Predictions of strength were done including compression reinforcement, even though design codes recommend ignoring compression reinforcement unless it is adequately tied. Shedid el al. (2008) demonstrated that including the compression reinforcement in predicting the capacity of reinforced masonry shear walls provide much better agreement with the experimental results compared to predictions ignoring the contribution of the compression reinforcement.

Table 3.1: Summary of predicted and measured strengths

Wall	Yield strength, Q_y (kN)				Ultimate strength, Q_u (kN)			
	Predicted		Measured		Predicted		Measured	
	CSA S304.1 (2004)	MSJC code (2008)	(+) ve	(-) ve	CSA S304.1 (2004)	MSJC code (2008)	(+) ve	(-) ve
W1	95	98	101	110	170	169	177	180
W2	122	123	121	123	163	162	151	154
W3	123	124	110	106	165	164	152	147
W4	142	147	160	162	254	253	265	267
W5	182	183	185	183	244	242	245	239
W6	183	184	173	169	246	246	241	234
W7	183	184	188	170	246	246	246	236

Using beam analysis with strain proportional to distance from the neutral axis, these predictions were carried out twice, once using CSA S304.1 (2004) and then again using the MSJC code (2008) without member or material resistance factors applied. There were three principal differences in these analyses. In CSA S304.1, the equivalent rectangular stress block uses a stress of $0.85 f'_m$ whereas $0.80 f'_m$ is used in the MSJC code. Both use a depth of rectangular stress block equal to 80% of the distance to the neutral axis. In CSA S304.1, the limiting extreme fibre compressive strain is 0.003 compared to 0.0025 in the MSJC code. Finally, in the CSA S304.1 predictions, the compressive strength of 16.4 MPa was taken directly from tests of 4-block high prisms. Since, in the MSJC code, the compressive strength of masonry is designated as corresponding to prisms with a height to thickness ratio of 2.0, the 16.4 MPa strength was adjusted to 18.8 using the MSJC height adjustment factor of 1.15.

Each experimental result in Table 3.1 can be compared to predicted values using both the Canadian (CSA, 2004) and American (MSJC, 2008) design codes. Despite the higher masonry compressive strength (18.8 MPa vs. 16.4 MPa) and higher modulus of elasticity (900×18.8 vs. 850×16.4) for the MSJC code, the yield and strength predictions were very similar and closely predicted the measured values. The measured yield strengths of the walls (average for both loading directions) were, on average, 1% higher than the predicted strengths using either code (*c.o.v.* = 9%).

Regarding the ultimate strength predictions, despite significant differences in the masonry compressive strength, height of equivalent rectangular stress block, and limiting compression strain, the Canadian and American predictions were very similar. The measured ultimate strengths of the walls (average for both directions of loading) were, on average, 2% higher than the predictions using either code (*c.o.v.* = 5%). In general, the test results indicate that the use of beam theory for flexural strength predictions is accurate for flanged and end-confined reinforced concrete block shear walls as well as for rectangular walls.

3.10 Wall ductility

In the following section, a summary of the test results and comparisons between the test specimens were provided to highlight the effects of adding flanges and boundary elements on the seismic performance of reinforced masonry shear walls. In addition, the effect of the aspect ratio of the wall on performance was discussed. The measured displacements and the corresponding displacement ductilites were used to assess the potential impact on seismic design.

3.10.1 Displacement characteristics

The measured lateral displacements for all walls at Δ_y (the onset of yield of the outermost bar), Δ_u (at maximum load), and $\Delta_{0.80u}$ (i.e., at 20% strength degradation in the post-peak stage) were listed in Table 3.2. Values at 1% drift were used in subsequent calculations.

Table 3.2: Summary of measured displacements and displacement ductilities

Wall	Direction	Displacements (mm)			Displacement ductility, [μ_Δ]						
					At Maximum load		At 1% drift		At 20% strength degradation		
		Δ_y *	Δ_u	$\Delta_{0.80u}$	$\mu_{\Delta u}$	% drift	$\mu_{\Delta 1\%}$	$\mu^{ep}_{\Delta 1\%}$	$\mu_{\Delta 0.8u}$	% drift	$\mu^{ep}_{\Delta 0.8u}$
W1	(+) ve	8.5	25.1	45.0	3.0	0.63	4.7	2.7	5.3	1.13	3.0
	(-) ve		25.3	48.0	3.0	0.63		2.9	5.6	1.20	3.5
W2	(+) ve	10.5	31.5	70.0	3.0	0.79	3.8	3.0	6.7	1.75	5.3
	(-) ve		31.5	68.0	3.0	0.79		3.0	6.5	1.70	5.2
W3	(+) ve	9.2	36.0	93.0	3.9	0.90	4.3	3.1	10.1	2.33	7.3
	(-) ve		36.1	95.0	3.9	0.90		3.1	10.3	2.38	7.4
W4	(+) ve	3.5	14.0	25.0	4.0	0.53	7.6	4.6	7.1	0.94	4.3
	(-) ve		12.5	30.0	3.6	0.47		4.7	8.6	1.13	5.3
W5	(+) ve	5.0	14.9	42.0	3.0	0.56	5.3	4.0	8.4	1.58	6.3
	(-) ve		25.1	45.0	5.0	0.94		4.1	9.0	1.69	6.9
W6	(+) ve	4.0	24.1	52.0	6.0	0.91	6.7	4.8	13.0	1.95	9.3
	(-) ve		24.0	57.0	6.0	0.90		4.8	14.3	2.14	10.3
W7	(+) ve	5.0	20.1	62.0	4.0	0.76	5.3	4.2	12.4	2.33	9.7
	(-) ve		20.0	65.0	4.0	0.75		3.8	13.0	2.44	9.4

* Values based on the first onset of yielding recorded in the outermost bar

The measured displacements at first yield, Δ_y, for the walls in each phase did not differ significantly. However, at maximum load and at 20% strength degradation large differences were observed for the walls in both Phases I and II as shown in Figs. 3.55 (a) and (b), respectively. The yield displacements ranged between 0.21% to 0.26% drift for the 3 storey walls of Phase I and between 0.13% and 0.18% drift for the 2 storey walls of Phase II. Displacements at maximum load ranged from 0.63% to 0.90% drift for the Phase I test walls with the lowest and highest values corresponding to the rectangular wall (W1) and end-confined wall (W3), respectively. For the Phase II walls, the drift range was from 0.53% for the rectangular wall (W4) to 0.95% for the end-confined wall (W6). For both aspect ratios tested (2.2 and 1.5), displacements at 20% strength degradation were, on average, about 1.0%, 1.5%, and 2.2% drift corresponding to the rectangular, flanged, and end-confined walls, respectively.

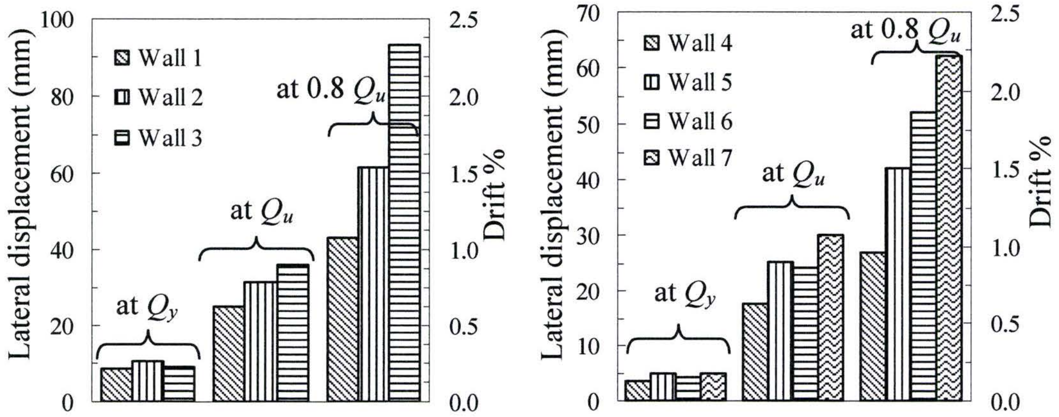

a) 3-storey walls (Phase I) b) 2-storey walls (Phase II)

Fig. 3.55: Effect of end configuration on wall displacements

The envelopes of load-displacement relationships for the test specimens in Phases I and II were presented in Fig. 3.56. The major ductility enhancement achieved by adding a flange or a boundary element to a rectangular wall is obvious. It can also be seen from the figures that the stiffnesses of the walls up to yielding were almost the same in each phase. When a *force-based* design approach is adopted, the seismic elastic design force for a building is based on the stiffness of the lateral load resisting elements. Having all of the walls with almost the same stiffness, implies that the individual design forces should be the same for all walls.

One of the study objectives was to investigate the enhanced seismic performance of a building when typical rectangular walls were simply replaced by flanged or end-confined walls when subjected to the same axial load with the same overall length and lateral force capacity. These conditions were achieved through the fact that the walls in each phase were subjected to the same axial load (representing a common tributary floor area) and by wall design for the same overall capacity (for all walls in each phase) by altering the amount of steel and flange/boundary element dimensions. Finally, the fact that all of the walls (in each phase) had almost the same elastic stiffness meant that the calculated elastic base shear would not be affected by substitution of other walls (since the building period would remain unaffected).

The displacement capabilities of walls were significantly enhanced when the boundary elements were added to the ends of the walls. In addition, increases of about 50% and 100% beyond the drift capabilities of the rectangular walls were achieved by the flanged and end-confined walls, respectively, at 20% strength degradation.

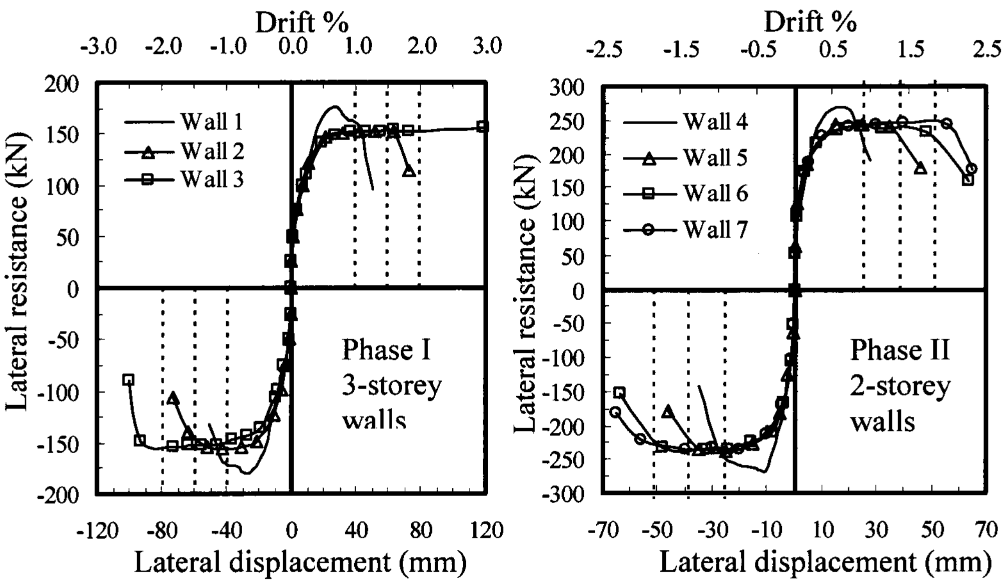

a) Walls in Phase I b) Walls in Phase II

Fig. 3.56: Test specimen load-displacement relationships

3.10.2 Displacement ductility

The actual measured wall displacement ductility, μ_Δ, was defined as the ratio between the measured top displacement at a specified limit and the measured displacement at the onset of yield of the outermost vertical bar. I The measured displacement ductility values $\mu_{\Delta u}$, $\mu_{\Delta 1\%}$, and $\mu_{\Delta 0.8u}$ at ultimate load, 1% drift, and 20% strength degradation, respectively, were listed in Table 3.2. The 1% drift level is used in the Canadian code to identify an acceptable displacement limit, whereas, the 20% degradation limit is commonly used by researchers as a reasonable limit for satisfactory performance (Priestley et al. 1996; Priestley at al. 2007). The NBCC (2005) also specifies 1% drift as the displacement limit for *post-disaster buildings*, required to be fully-operational after earthquake events, without any significant strength degradation.

The above displacement ductility values at maximum load ranged between 3.0 and 3.9 and between 5.3 and 10.3 at 20% strength degradation for the 3 storey rectangular (W1) and end-confined (W3) walls, respectively. However, for the 2 storey rectangular (W4) and end-confined (W6) walls, the ranges of these values increased to 3.6 and 6.0 at ultimate load and to 7.1 and 14.3 at 20% strength degradation, respectively. The significant enhancement of ductility at 20% strength degradation of the proposed end-confined walls compared to the rectangular walls was obvious from the test results. The actual ductility of the proposed end-confined walls was nearly double the ductility of the corresponding rectangular wall. The end-confined walls had almost the same lateral load capacity and only slightly more than half of the amount of vertical reinforcement. Flanged walls also showed an enhancement in ductility capabilities compared to the rectangular walls with about 15% increase achieved based on the unaltered data.

There are several discussions in the literature regarding the appropriate definition of displacement ductility for behaviours that are not *ideally* elastic-plastic (Park and Paulay 1975; Shing et al. 1989a; Paulay and Priestley 1992; Priestley et al. 1996; Tomazevic 1998), but, as highlighted by Priestley (2000), and Priestley et al. (2007), there is no general consensus or a unified definition for the yield and the ultimate displacements. However, several researchers have proposed equivalent elastic-perfectly plastic systems to evaluate the displacement ductility from experimentally measured results. They have used different methods to define an *equivalent system*.

The definition proposed by Tomazevic (1998) was based on equating the area under the measured and the idealized equivalent curves for a selected ultimate condition for the wall and an initial secant stiffness at the first *major crack*. Adopting the above definition, Shedid el al. (2010) demonstrated that for flexure controlled capacities of reinforced masonry shear walls, the idealized wall capacities based on the equal area approach at 1% drift and at 20% strength degradation were, on average, 97% of the measured capacities. Therefore, for simplicity, the equivalent wall capacity in the post yield branch, Q_{in}, in the elastic-plastic idealization has been taken equal to the measured capacities of the wall, Q_u, for an idealized plastic evaluation of displacement ductility, $\mu^{ep}{}_{\Delta}$. This small approximation was not expected to significantly influence the idealized displacement ductility values and provided conservative (i.e., underestimate) ductility values. A more detailed discussion related to the idealized representation of the load-displacement relationships and the idealized displacement ductility was presented later in Section 4.4.

For the above evaluation, the idealized yield displacement was calculated as the measured yield displacement times the ratio of the maximum capacity to the measured yield strength of the wall as presented in Table 3.1. The idealized displacement ductility values listed in Table 3.2 were also presented in Fig. 3.57 for displacement limits corresponding to 1% drift and 20% strength degradation. The ductility values calculated at 1% drift were similar in each test phase for the walls tested in that phase. This is mainly due to the measured yield displacement being quite similar within each test phase. However, the ductility values calculated at 20% strength degradation reflect the benefits of using boundary elements such as flanges and end-confined regions. The elastic-plastic idealized ductilities at 20% strength degradation for the flanged and end-confined walls were at least 50% and 100% higher than the ductilities for the rectangular walls. This result indicates a significant effect on seismic performance that should influence the magnitude of the design seismic response modification factor to be discussed in Chapter 5.

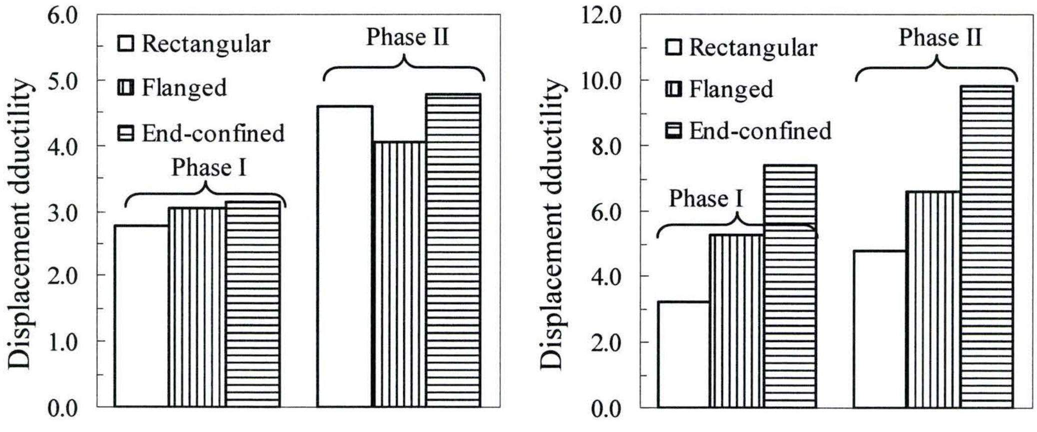

a) at 1% drift b) at 20% strength degradation

Fig. 3.57: Idealized displacement ductility capacities for the test walls

3.10.3 Effect of wall aspect ratio

Another objective of this research was to investigate the effect of different aspect ratios on the responses of the walls. Each type of wall in Phase I had the same cross section properties and was subjected to the same axial compressive load as its corresponding type in Phase II. The only difference was the 3.99 m height of the walls in Phase I versus the 2.66 m wall height in Phase II.

To investigate the effect of different wall heights, the load-displacement relationships for the walls were normalized to the height using drift ratios. To exclude the effect of different lateral load wall capacities, the lateral load capacity on the vertical axis of the load–displacement relationships was normalized to the maximum measured capacity. The normalized "back-bone" curves for the test walls were presented in Fig. 3.58 for each type of wall. It can be seen that the normalized responses of the 2 and 3 storey walls were almost identical. This finding indicates that the cross section properties may significantly influence the response of the wall regardless of the height. As discussed further in Chapter 5, this may also show that plastic hinge length is not influenced much by wall height and may be influenced by the length of the wall.

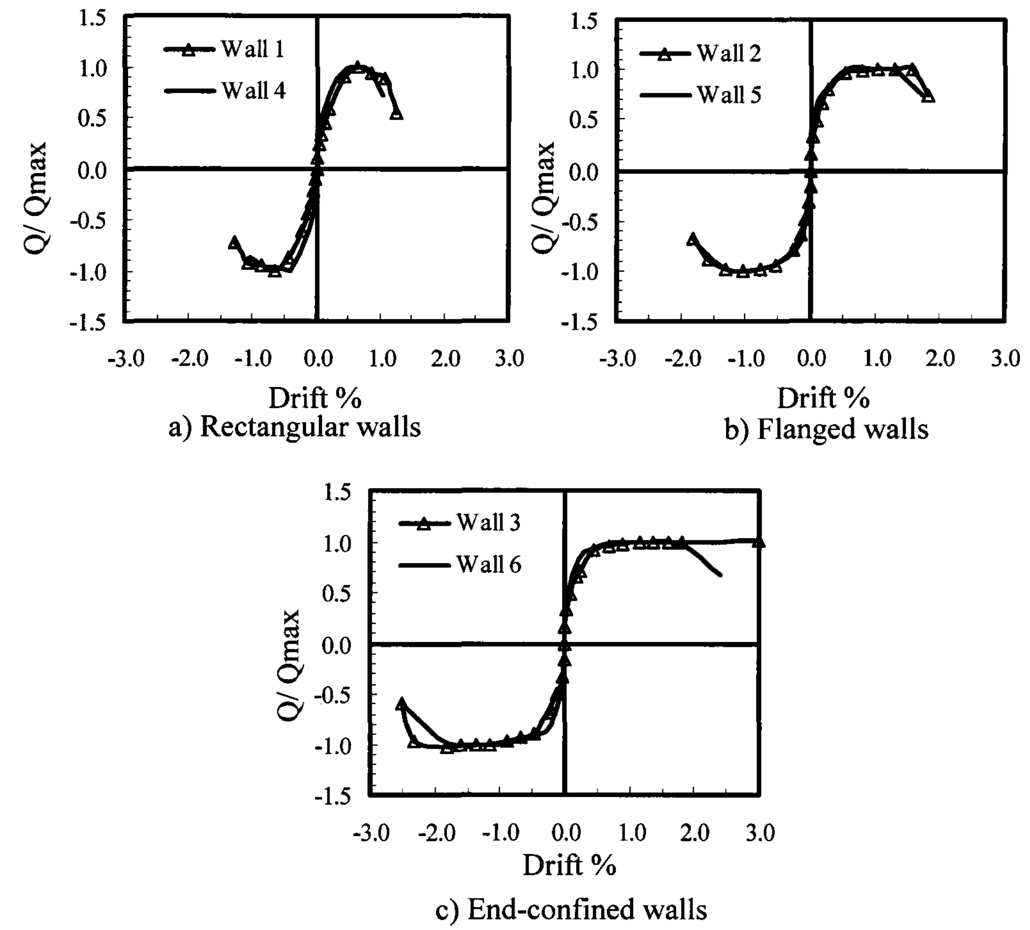

Fig. 3.58: Normalized load-displacement relationship for the test specimens

3.11 Summary and conclusions

Seven reinforced masonry shear walls were tested under displacement controlled quasi-static cyclic loading. The test specimens included rectangular, flanged, and end-confined reinforced masonry shear walls having aspect ratios of 2.2 and 1.5. The hysteresis loops for cyclic loading of the test walls indicated symmetric responses for loading in both directions and showed losses of stiffness with increasing lateral top displacement. The wall responses were almost linear elastic up to first yield of the outermost reinforcement at the bases of the walls characterized by thin hysteresis loops generating low energy dissipation. At higher displacement levels, the observed larger loops generated higher amounts of energy dissipation with increases in plastic deformations.

The walls maintained almost the same capacity when subjected to the second loading cycle at the same target displacement level until reaching displacements of several times the yield displacement. These displacements were much higher for the end-confined walls compared to the rectangular walls. This indicates that damage in the end-confined walls was significantly less than in the rectangular walls until very large displacements were reached.

The use of beam theory and inclusion of the effect of the vertical compression reinforcement in strength calculation for the tested half scale rectangular, flanged and end-confined reinforced masonry shear wall result in accurate strength predictions as was similarly observed for full scale reinforced masonry shear walls (Shedid 2006). Strength predictions for reinforced masonry shear walls failing in flexure using both the American and Canadian codes agreed closely with the experimental results.

The wall tests showed that a significant enhancement in ultimate displacements and ductility was attained, when rectangular walls were replaced by flanged or end-confined walls having the same flexural capacity, elastic stiffness, and axial load. For the aspect ratios of 2.2 and 1.5, displacements at 20% strength degradation occurred at about 1.0%, 1.5%, and 2.2% drift corresponding to the rectangular, flanged, and end-confined walls, respectively. The idealized ductilities for the proposed flanged and end-confined masonry shear walls were, respectively, at least 50% and 100% higher than those of the rectangular walls having the same properties.

Based on the normalized load-displacement relationships for the 2 and 3 storey walls, the results indicate that the cross section properties significantly influenced the response of the wall regardless of the height. This may indicate that the plastic hinge length, used to calculate plastic deformations, is influenced more by wall length than the height of the wall.

The substantially improved performances of the flanged and end-confined walls were achieved through the addition of one block at each end of the wall. This cost would be much more than offset by the elimination of 8 of the 19 vertical reinforcing bars used in the rectangular wall. It is suggested that these end geometries can be added to masonry construction with minimal impact on architectural or construction practices.

Unlike the common perception that reinforced masonry shear walls are not ductile, the reported test results have demonstrated the high ductility and energy dissipation potential of reinforced masonry. This behaviour was characterized by obvious ductility with little strength degradation within usable drift levels.

Chapter Four

Analysis of Test Results

CHAPTER 4
ANALYSIS OF TEST RESULTS

4.1 Introduction

Analysis of the test results presented in Chapter 3 was the main focus of this chapter. The goal was to extract quantitative information by analysing and comparing these test results and identifying the effects of different test parameters on wall behaviour. This intent was to provide a step forward towards a better understanding of the flexural response of reinforced concrete-block shear walls. A better understanding of the wall responses will lead to more realistic predictions of the seismic performance parameters for such walls, as will be discussed in Chapter 5 and in Appendix A. This information would then be used in the evaluation of building design parameters.

The seismic performance of shear walls is affected by some basic wall characteristics such as the wall stiffness, deformation, ductility, and energy dissipation. Flexural and shear deformations, evaluations of displacement ductility and energy dissipation characteristics, and documentation of the trends for stiffness degradation for the test walls were presented in this chapter.

Measured compressive strains in the masonry at ultimate load were presented in Sections 4.2 for the test walls and compared with the ultimate strains specified in CSA S304.1 (2004) and the MSJC code (2008). The curvatures calculated from the strain measurements at both ends of the walls were presented in Section 4.3 and compared with theoretical values predicted using the above codes.

The measured curvature profiles and the deflection profiles over the wall heights as well as the recorded strains along the outermost bars were utilized in Section 4.4 to quantify the extent of the plasticity regions, L_p. The flexure deformations were quantified in Section 4.5 using the measured curvature profiles over the wall heights. The displacement ductilities were then discussed in Section 4.6 followed in Section 4.7 by comparisons between the measured and predicted stiffnesses for the test walls. Energy dissipation and hystersesis damping calculation were presented in Sections 4.8 and 4.9. Summary and conclusions completed this chapter.

4.2 Wall strains

For each wall, average strains over segments along the wall height were calculated based on measurements from the vertical displacement potentiometers attached at the wall ends. The calculated average masonry compressive strains based on potentiometer measurements for the lower 50 mm and 150 mm of the wall heights (mid-height of the first and second courses, respectively) were presented in Fig. 4.1 for all of the walls.

Due to spalling of the face shells at the wall toes and the eventual detachment of the potentiometer anchors, these displacement measurements were discontinued at later stages of testing. Therefore, strains at 20% strength degradation are not available. Average maximum measured masonry compressive strains over the lower 50 mm and 150 mm were reported in Table 4.1. In general, the compressive strains in masonry at ultimate load, over the first 50 mm above the bases of the walls were, on average, about 11.5×10^{-3} mm/mm and approximately 4 times the maximum compressive strains of 2.5×10^{-3} mm/mm and 3.0×10^{-3} mm/mm, specified in the MSJC code (2008) and in CSA S304.1 (CSA 2004), respectively. Even when the masonry strains were averaged over the lower 150 mm at ultimate load, the 5.2×10^{-3} mm/mm average value was still about double the above specified values.

It can be seen from Fig. 4.1 that strains higher than 15×10^{-3} mm/mm were recorded prior to any strength degradation for most of the walls. Therefore, the values of maximum compressive strain are very conservative in both codes. Although use of the low code values may not alter the predicted wall strength, it does significantly affect the calculated curvatures and displacements at ultimate load.

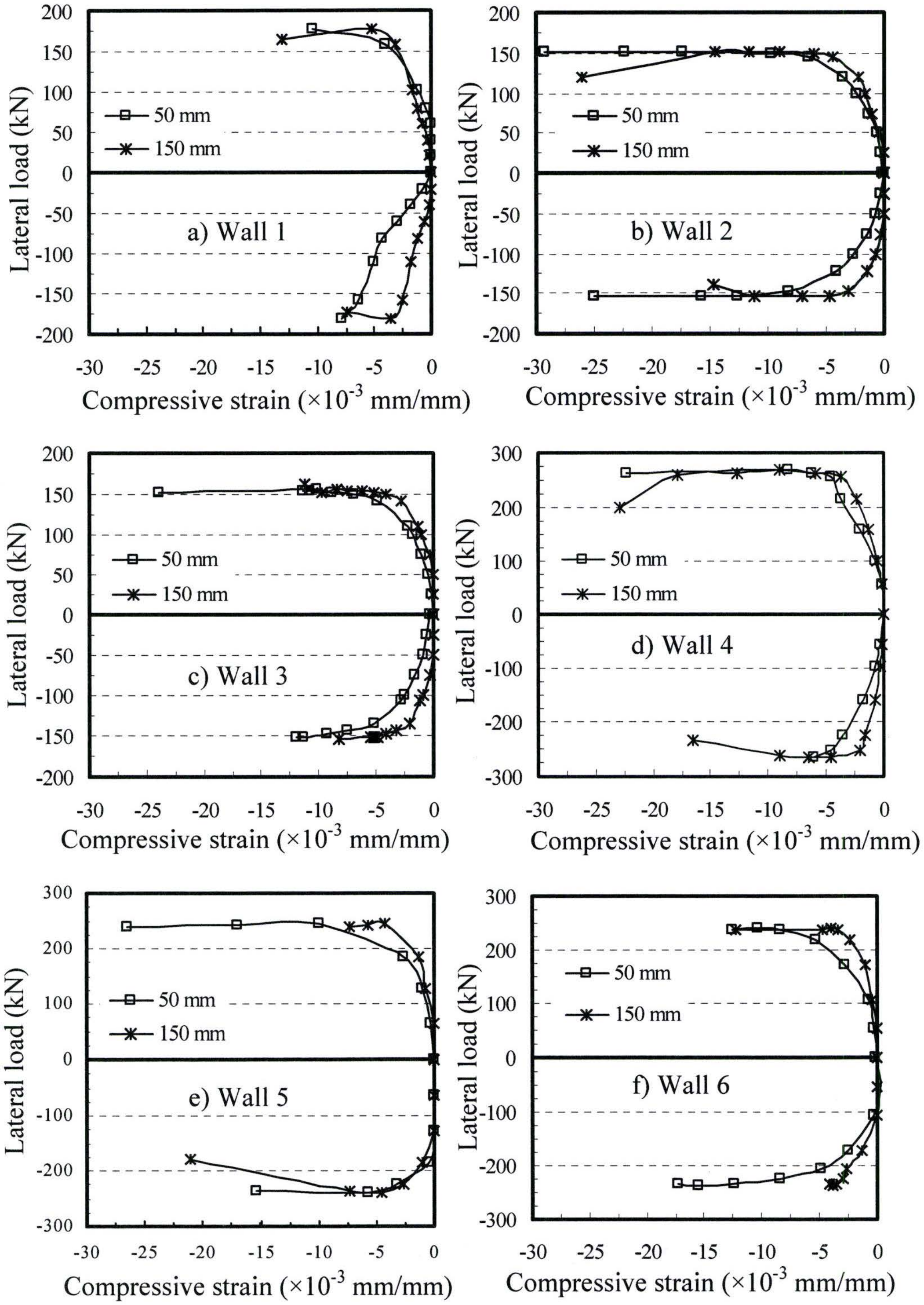

Fig. 4.1: Average masonry strains over the lower 50 and 150 mm of Walls

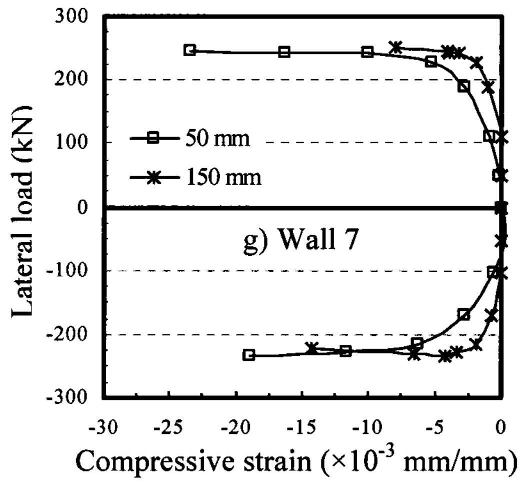

Fig. 4.1: (cont.)

Table 4.1: Average compressive strains over the lower 50 and 150 mm of wall heights

Strain location		Maximum masonry strains ($\times10^{-3}$ mm/mm)						
		W1	W2	W3	W4	W5	W6	W7
Over 50 mm	(+)ve	10.4	9.7	10.8	8.3	10.3	10.4	16.3
	(-)ve	7.9	12.7	11.4	6.1	5.7	15.5	18.9
Over 150 mm	(+)ve	5.2	6.2	6.2	5.0	4.3	4.0	3.9
	(-)ve	3.5	4.6	4.8	4.6	4.5	4.1	4.2

4.3 Wall curvatures

The theoretical values for curvatures at the base of the wall at the onset of yield of the outermost tension reinforcement, $\varphi_{y,th}$, and at ultimate load, $\varphi_{u,th}$, were calculated twice based on predicted flexural strains using beam theory and the provisions of the Canadian and American codes. These values were presented in Table 4.2, along with the theoretical curvature ductility values, $\mu_{\varphi,th}= \varphi_{u,th} / \varphi_{y,th}$.

Curvature predictions using CSA S304.1, on average, exceeded the predictions obtained using the MSJC code by about 6% and 14% at first yield and at ultimate load, respectively. These differences are attributed to the differences between the values of the modulus of elasticity, the ultimate strain, and the height of the equivalent rectangular stress block for masonry.

Table 4.2: Theoretical and measured wall curvature and curvature ductility

Wall	W1	W2	W3	W4	W5	W6	W7
Theoretical curvature values at yield and ultimate (CSA S304.1- 2004)							
$\varphi_{y,th}$ ($\times 10^{-6}$ rad/mm)	1.92	1.84	1.85	1.91	1.83	1.84	1.84
$\varphi_{u,th}$ ($\times 10^{-6}$ rad/mm)	5.60	14.81	14.51	5.62	15.05	14.60	14.60
$\mu_{\varphi,th} = (\varphi_{u,th} / \varphi_{y,th})$	2.92	8.06	7.80	2.94	8.06	7.80	7.80
Theoretical curvature values at yield and ultimate (MSJC code- 2008)							
$\varphi_{y,th}$ ($\times 10^{-6}$ rad/mm)	1.88	1.79	1.81	1.88	1.79	1.80	1.80
$\varphi_{u,th}$ ($\times 10^{-6}$ rad/mm)	4.84	13.40	12.53	4.86	13.59	12.65	12.65
$\mu_{\varphi,th} = (\varphi_{u,th} / \varphi_{y,th})$	2.58	7.61	6.93	2.59	7.61	6.93	6.93
Experimental curvatures values (Average over 50 mm from both directions of loading)							
$\varphi_{y,ex}$ ($\times 10^{-6}$ rad/mm)	4.50	6.23	5.00	4.10	4.20	5.40	5.90
$\varphi_{u,,ex}$ ($\times 10^{-6}$ rad/mm)	15.38	22.90	22.80	13.65	29.00	38.70	30.80
$\varphi_{1\%,}$ ($\times 10^{-6}$ rad/mm)	--*	34.30	29.65	--*	39.10	38.70	41.00
$\mu_{\varphi u,ex} = (\varphi_{u,ex} / \varphi_{y,ex})$	3.42	3.68	4.56	3.33	6.90	7.17	5.22
$\mu_{\varphi,1\%} = (\varphi_{1\%} / \varphi_{y,ex})$	N.A.	5.51	5.93	N.A.	9.31	7.17	6.95
Experimental curvatures values (Average over 150 mm from both directions of loading)							
$\varphi_{y,ex}$ ($\times 10^{-6}$ rad/mm)	1.80	2.63	1.91	1.62	2.01	2.14	2.20
$\varphi_{u,,ex}$ ($\times 10^{-6}$ rad/mm)	7.77	11.83	12.49	9.79	15.44	14.08	10.61
$\varphi_{1\%,}$ ($\times 10^{-6}$ rad/mm)	--*	16.31	14.63	--*	18.98	14.08	14.05
$\mu_{\varphi u,ex} = (\varphi_{u,ex} / \varphi_{y,ex})$	4.32	4.51	6.54	6.06	7.70	6.59	4.85
$\mu_{\varphi,1\%} = (\varphi_{1\%} / \varphi_{y,ex})$	N.A.	6.21	7.66	N.A.	9.46	6.59	6.38

* Measurement not available due to spalling of the face shells

Similar to the study of maximum strains in Section 4.2, the average curvatures were calculated from measured strains over the lower 50 mm (up to the midheight of the first course) and the lower 150 mm (up to the midheight of the second course) of the wall. These curvature values were shown in Table 4.2 for the onset of yielding of the outermost tension reinforcement, for ultimate load and for 1% drift. The values were averaged for both directions of loading. The corresponding curvature ductility values were also calculated.

Average curvatures over the wall height were determined based on average strain profiles at different levels over the wall height. For the 3-storey walls tested in Phase I, 11 vertically-mounted displacement potentiometers at each wall end were used to calculate the average curvature over 11 segments along the wall height. For the 2-storey walls tested in Phase II, 9 potentiometers were used, (refer to Section 2.8). A representation of a typical strain profile for a wall cross section and illustration of curvatures calculated over gauge length and wall deformation due to these curvatures were shown in Fig. 4.2. The average curvature, φ_i, for a gauge length, $h_{gauge(i)}$, along the wall height was calculated using Eq. (4.1).

$$\varphi_i = \frac{\Delta_{Ti} / h_{gauge(i)} + \Delta_{Ci} / h_{gauge(i)}}{l_w} = \left(\Delta_{Ti} + \Delta_{Ci}\right) / \left(h_{gauge(i)} \times l_w\right) \qquad \text{Eq. 4.1}$$

where, as shown in Fig. 4.2 (a):

$\varphi_i =$ Average curvature over a given segment along the wall height;

$\Delta_{Ci} =$ Net measured compression displacement at the compression end of the wall over a height $h_{gauge(i)}$;

$\Delta_{Ti} =$ Net elongation measurement at the tension end of the wall over a height $h_{gauge(i)}$; and

$h_{gauge(i)} =$ Segment height corresponding to the measured Δ_{Ci} and Δ_{Ti} values.

Average experimental curvatures over segments of the wall heights were presented in Fig. 4.3 for all the test walls and for both directions of loading. The calculated average curvatures over the first storey were significantly higher than those over the second and third storeys.

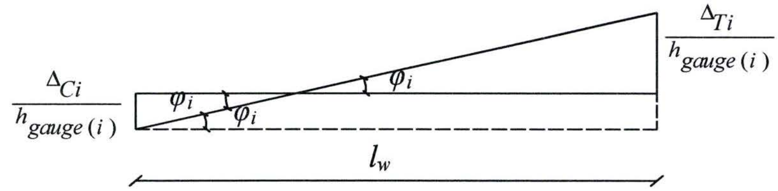

a) Strain profile used to calculate curvature

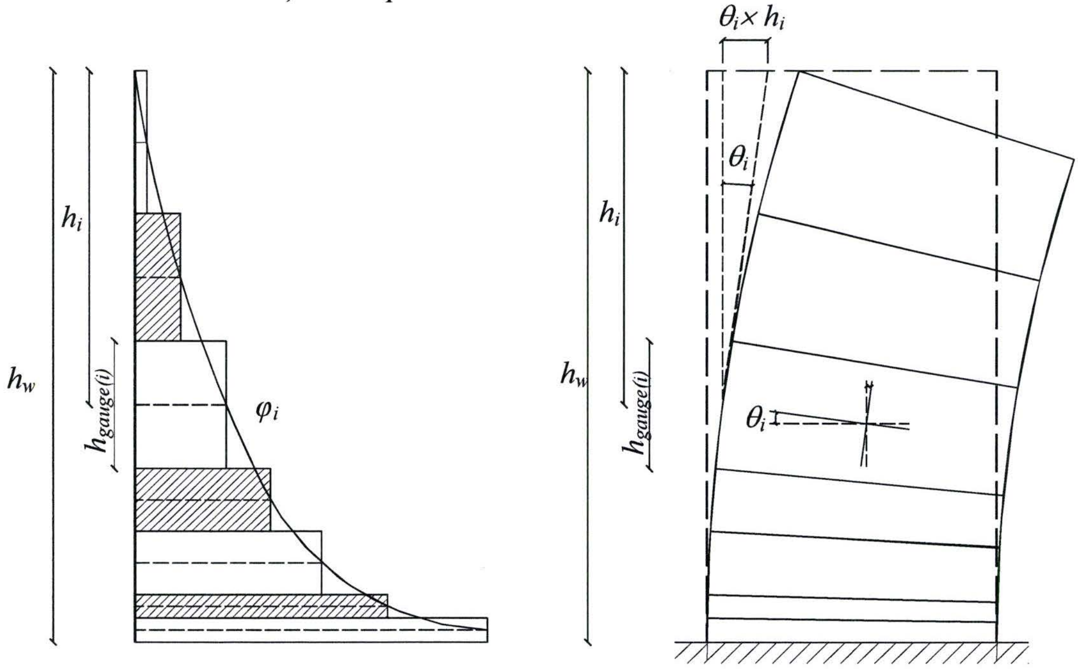

(b) Curvature profile over the wall height (c) Wall flexural deformation

Fig. 4.2: Strain and curvature profiles

The average measured curvatures (for both directions of loading) at yield, $\varphi_{y,ex}$, for the rectangular and flanged walls were, respectively, $0.0031/l_w=1.7\times10^{-6}$ rad/mm and $0.0042/l_w=2.3\times10^{-6}$ rad/mm, over the lower 150 mm of the walls [The individual values were 1.8×10^{-6} and 1.62×10^{-6} for the rectangular walls (W1 and W4) and 2.63×10^{-6} and 2.01×10^{-6} for the flanged walls (W2 and W5).] Similarly, at ultimate load, the average measured curvatures, $\varphi_{u,ex}$, for the rectangular and flanged walls were, respectively, $0.0158/l_w=8.8\times10^{-6}$ rad/mm based on individual values of 7.77×10^{-6} and 9.79×10^{-6} for walls W1 and W4 and $0.0245/l_w=13.6\times10^{-6}$ rad/mm based on individual values of 11.8×10^{-6} and 15.4×10^{-6} for walls W2 and

W5. The curvatures based on the measured vertical strain averaged over the lower 50 mm of the wall were, on average, 2.3 times (*c.o.v.* = 17%) the values based on strains averaged over the lower 150 mm of the wall.

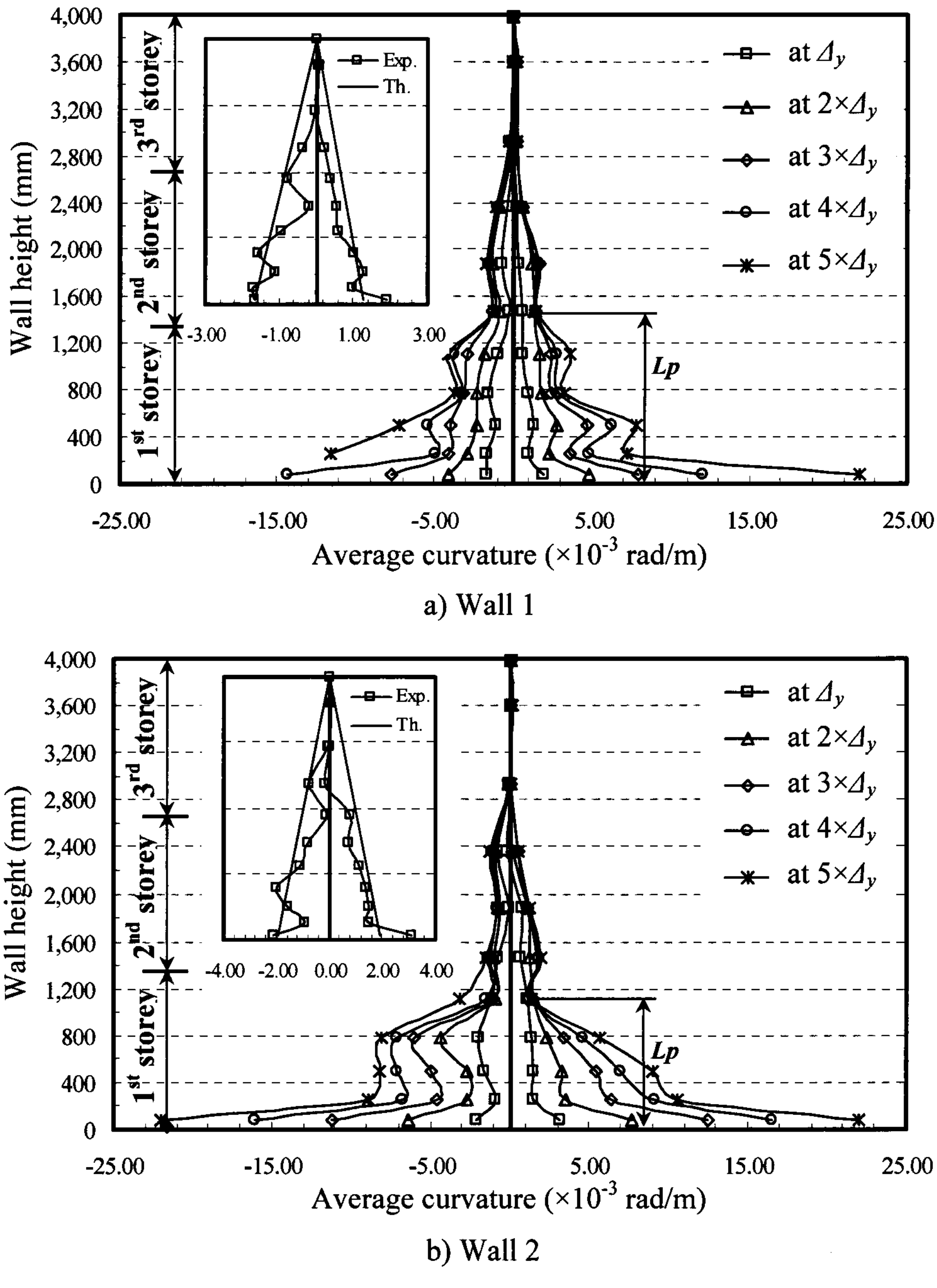

a) Wall 1

b) Wall 2

Fig. 4.3: Curvature profiles over the wall heights

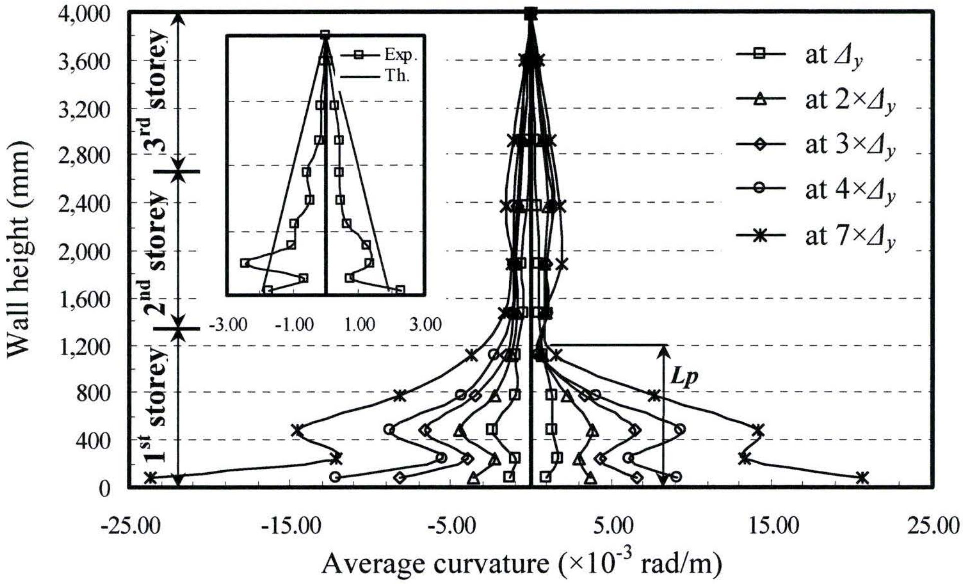

c) Wall 3

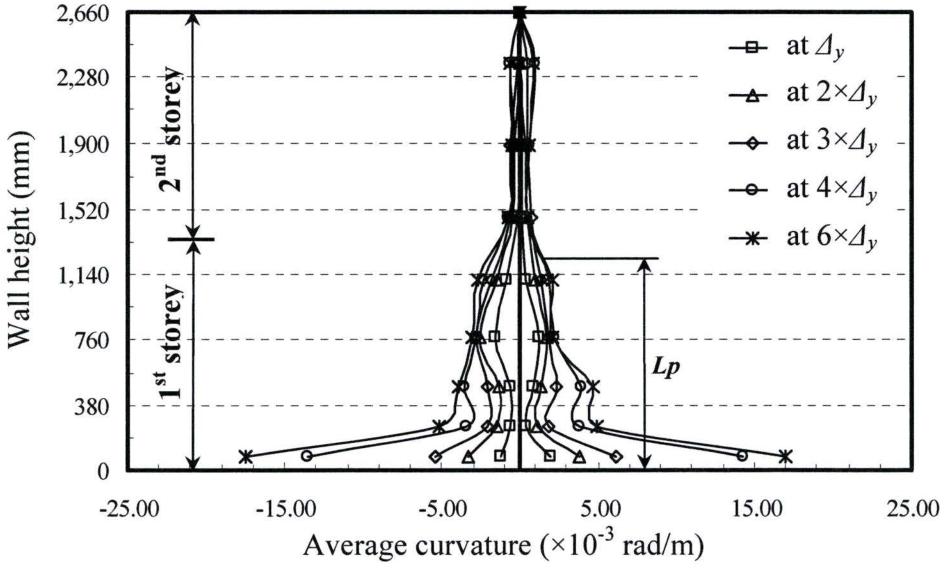

d) Wall 4

Fig. 4.3: (cont.)

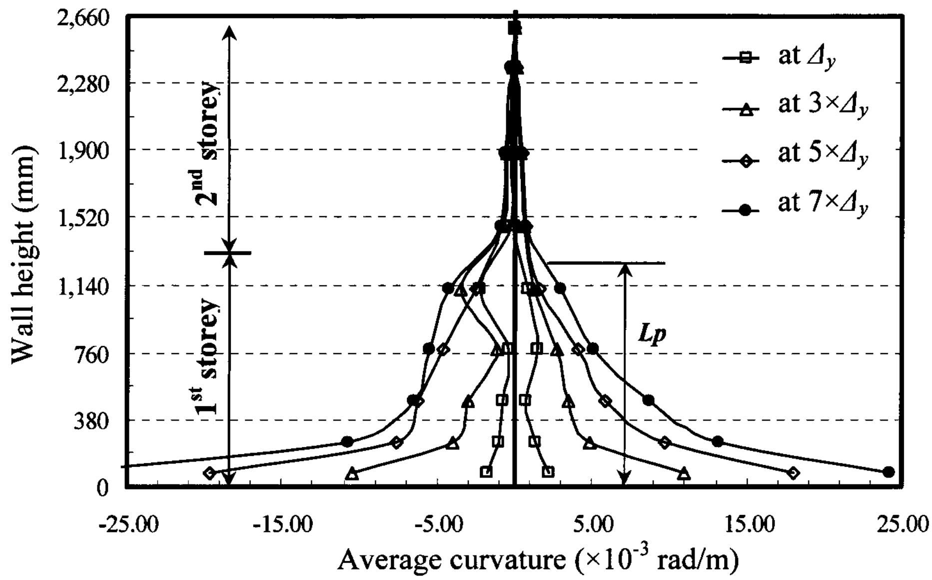

e) Wall 5

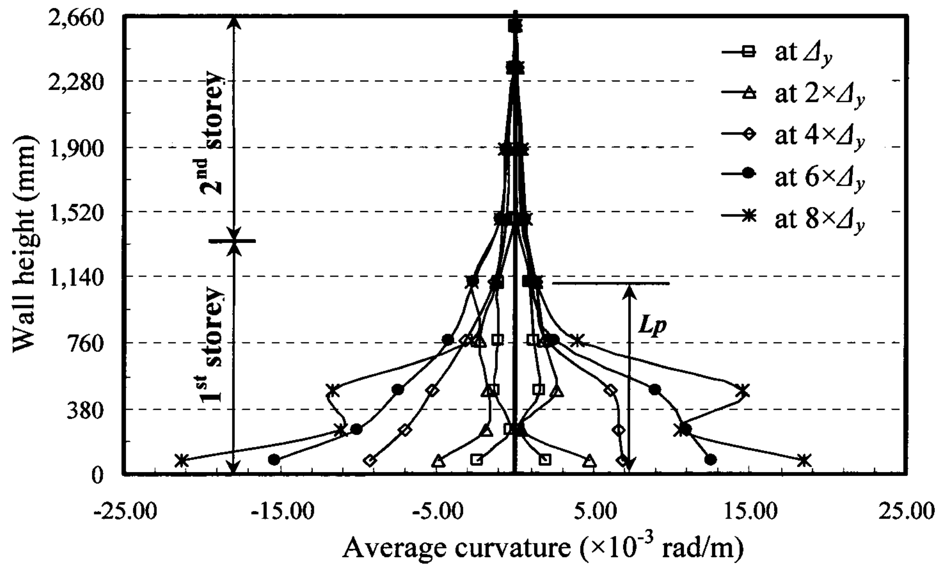

f) Wall 6

Fig. 4.3: (cont.)

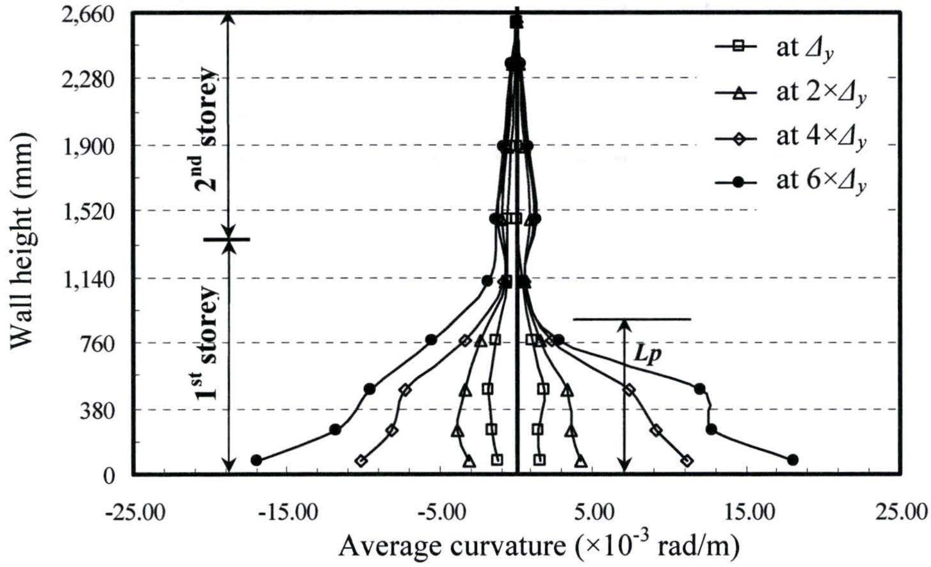

g) Wall 7

Fig. 4.3: (cont.)

On average, the theoretical curvature predictions at first yield overestimated the experimental results (averaged over the lower 150 mm) by 12% and 10% for the rectangular walls using CSA S304.1 and the MSJC code, respectively. On the other hand, the theoretical curvatures for both the flanged and end-confined walls at first yield underestimated the experimental results (averaged over the lower 150 mm) by 14% and 16%, on average, using CSA S304.1 and the MSJC code, respectively.

At ultimate load, the theoretical curvatures for the rectangular walls underestimated the experimental results (averaged over the lower 150 mm) by 36% and 44% using CSA S304.1 and the MSJC code, respectively. For both the flanged and end-confined walls, the theoretical curvatures, on average, slightly underestimated the test results by 4% and 1% using CSA S304.1 and the MSJC code, respectively. Therefore, it could be concluded that theoretical predictions of curvatures using both codes for the flanged and end-confined walls were more representative of the experimental results than those for the rectangular walls.

The average measured curvatures at first yield, $\varphi_{y,ex}$, were fairly similar for all walls with an average of about 2.0×10^{-6} rad/mm (*c.o.v.* = 15%). This resulted in almost the same yield displacement for walls within each testing phase. However, the curvatures measured at ultimate load for the flanged and end-confined walls were, on average, 56% higher (*c.o.v.* = 7%) than measured curvatures for the rectangular walls. It can be seen that the use of flanges and boundary elements significantly increased the curvatures at ultimate load which contributed to the increased top displacements for the flanged and end-confined walls compared to the rectangular walls. Even beyond ultimate load, with the increased curvatures, the flanged and end-confined walls reached drift levels of 1.5% and 2.2% at 20% strength degradation, respectively, compared to less than 1% drift attained by the rectangular walls.

Based on the averaged curvature values listed in Table 4.2 for each wall type, the average measured curvature ductility values at ultimate load, $\mu_{\varphi u,ex}$, were 4.9, 6.1, and 6.0, for the rectangular, flanged, and end-confined walls, respectively. An increase of about 24% and 22% in the curvature ductility at ultimate load was calculated for the flanged and end-confined walls, respectively, compared to the rectangular walls. The average measured curvature ductility values at 1% drift, $\mu_{\varphi 1\%}$, were about 28% and 14% higher than the corresponding values, $\mu_{\varphi u,ex}$, at ultimate load for the flanged and end-confined walls, respectively. The large increases in curvature for the flanged walls at 1% drift were attributed to the correspondingly greater damage compared to that of the end-confined walls. The higher curvatures exhibited by the flanged and end-confined walls were the main source of the increased displacements and displacement ductilities at ultimate load.

4.4 Extent of plasticity

The extent of plasticity was estimated from the average curvature profiles over the wall heights. The extent of plasticity, L_p, identified in Fig. 4.3, was defined as the highest point above the foundation to which the yield curvature extended; it is not to be confused with equivalent plastic hinge length, l_p. For almost all walls, high curvature values were recorded only over the first storey for the 3-storey walls in Phase I and the 2-storey walls in Phase II. Curvatures above the first storey tended to be almost linear indicating that most of the inelastic deformations took place within the first storey.

Plastic curvature zone heights were listed in Table 4.3 as L_p^C, (the superscript C refers to **C**urvature-based). Over these heights, extensive cracking was expected to occur. [This may require special detailing for reinforcement to, for example, increase shear reinforcement and to avoid splicing of the flexural reinforcement.] This parameter is particularly important as reliance on the masonry to fully contribute to the wall shear capacity could be an unconservative assumption due to the presence of such cracks.

The heights above the wall base where the deflection data began to exhibit nearly linear profiles were identified, as shown in Fig 4.4. Approximate values were chosen for Walls W2 and W3 as the kink or transition from curved to linear deflection profiles was not clear for these walls. The point where the kink occurred could be considered as the mid-height of the deflection-based estimate of the plasticity zone about which the wall rotates. The extent of plasticity zone heights, L_p^D, (the superscript D refers to **D**eflection-based) estimated from the experimental deflection measurements were listed in Table 4.3.

Table 4.3: Height of plasticity zones

Plasticity zone	Wall						
	W1	W2	W3	W4	W5	W6	W7
L_p^C (mm)	1,400	1,100	1,200	1,200	1,300	1,100	950
L_p^D (mm)	1,300	1,200	1,200	1,300	1,300	1,300	1,300
L_p / l_w (%)	75	64	67	69	72	67	63

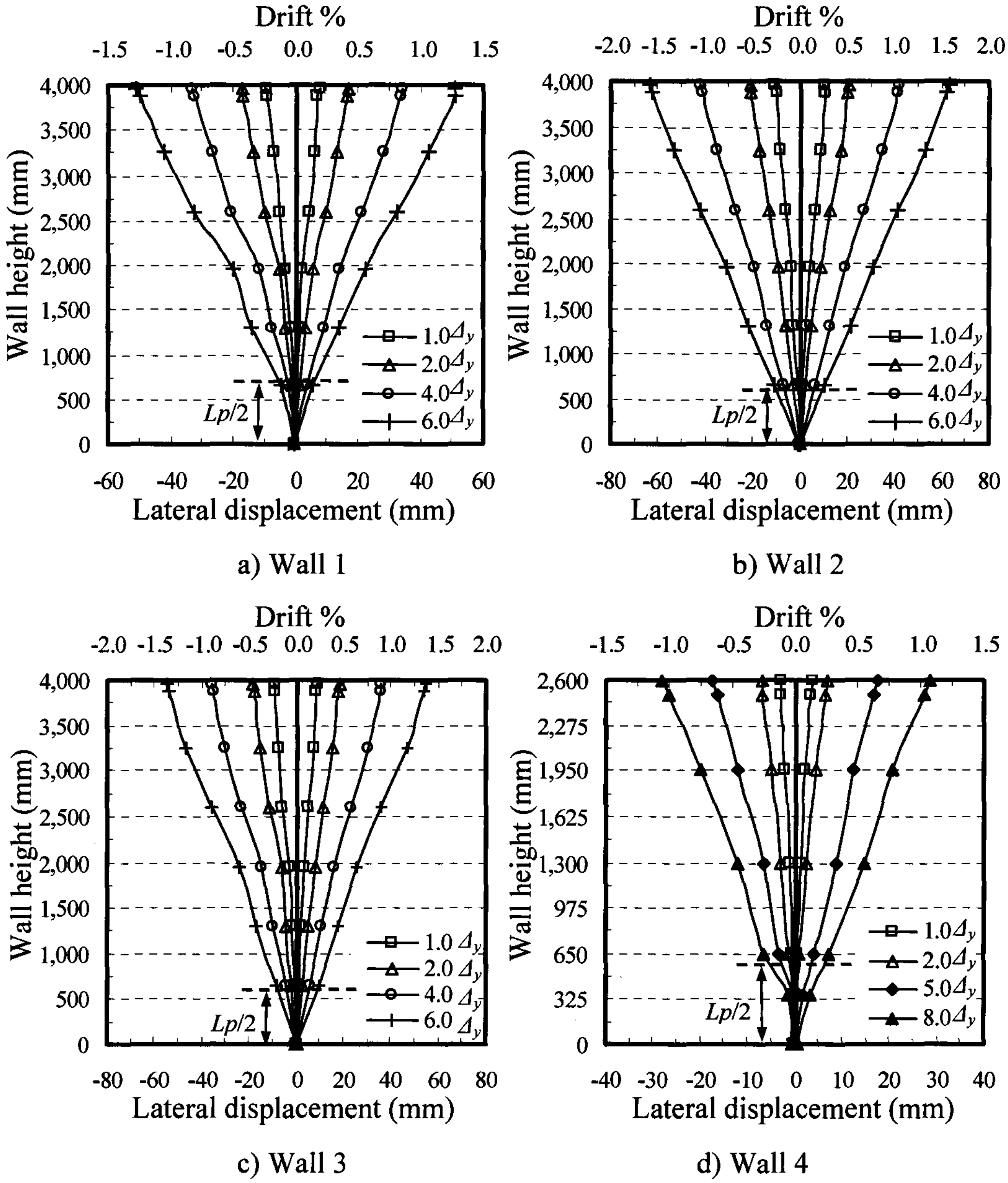

Fig. 4.4: Deflection profiles over the wall heights

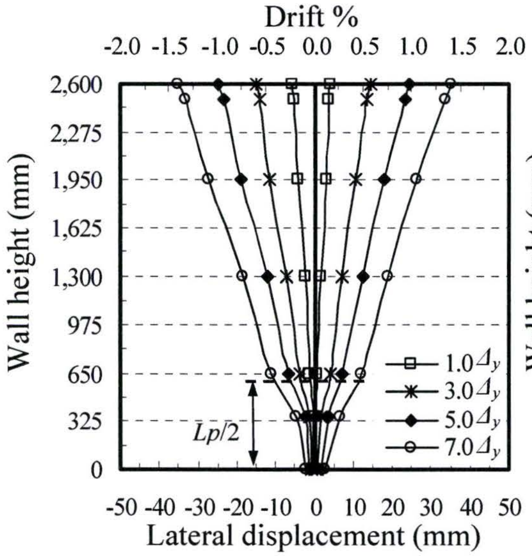

e) Wall 5

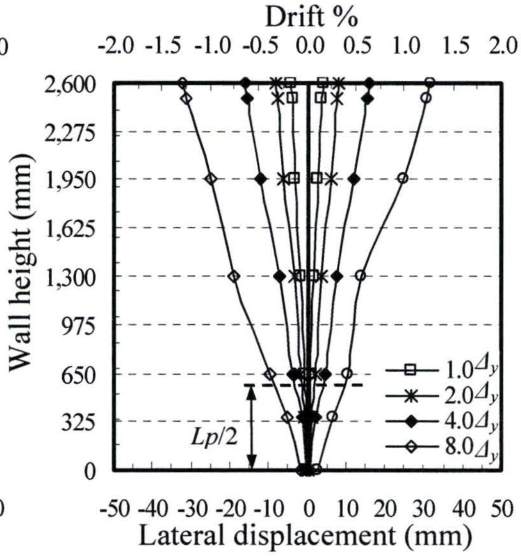

f) Wall 6

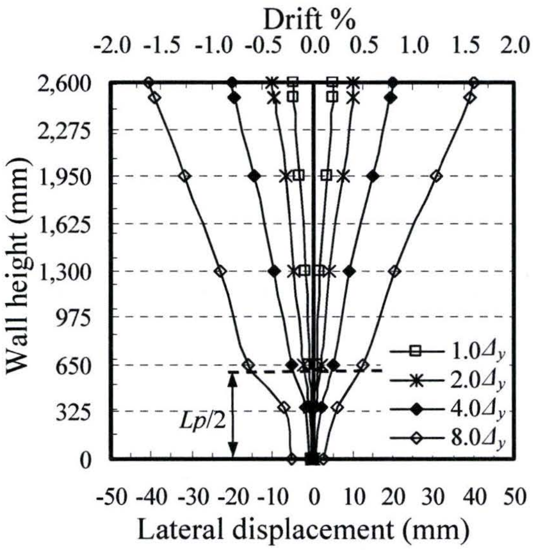

g) Wall 7

Fig. 4.4: (cont.)

Strain gauge readings on the outermost bars were used as a third measure to verify the height of the plasticity zone. At ultimate load for all walls, the measured strains on the outermost bars indicated that yielding extended well beyond the + 800 mm level above the wall base, as presented in Table 4.4. The table also showed that yielding of the bars extended to a distance of less than 200 mm inside the concrete foundation for all the walls. This indicated that the extent of plasticity inside the base for the test walls, which is expected to contribute to the lateral displacement of the wall as suggested by Paulay and Priestley (1992), was much less than within the wall itself.

Table 4.4: Strain gauge measurements on outermost bar at ultimate load

Wall	Strain in the vertical reinforcement ($\times\varepsilon_y$)							
	At (-200) mm		At (0) mm (interface)		At (+ 400) mm		At (+ 800) mm	
	Left	Right	Left	Right	Left	Right	Left	Right
W1	0.08	0.16	3.84	4.16	3.32	2.84	1.64	1.68
W2	0.08	0.07	4.12	5.20	5.24	5.36	2.72	3.04
W3	0.04	---*	4.64	6.24	5.00	6.28	4.72	5.48
W4	0.16	0.23	4.12	3.16	3.56	2.28	1.40	1.15
W5	0.15	0.18	4.80	4.00	5.04	3.32	2.64	1.93
W6	0.20	0.24	4.80	6.80	4.40	4.00	3.33	2.80
W7	0.08	0.08	3.60	3.20	2.32	1.92	1.21	1.11

* Unreliable readings due to wiring problem or damage during construction

As was shown in Table 4.3, the test results indicated that for all of the walls, the average height of the plasticity zone, L_p, (defined as the average of L_p^C and L_p^D) varied between 63% and 75% of the wall length, l_w, which is about the height of the first storey in the half scale test walls. This finding indicated that, for simplicity, special detailing requirements should be considered for the vertical and horizontal reinforcement for a height up to at least 75% of the wall length.

4.5 Wall displacements

The total measured displacements for all walls, at the onset of yield of the outermost reinforcing bar, Δ_y, and at ultimate load, Δ_u, were listed in Tables 4.5 and 4.6, respectively. These deflections consisted of three main components, namely: sliding (slip between the wall and the foundation), Δ_{sl}, flexural, Δ_f, and shear, Δ_s. Displacements due to sliding (base slip) were directly measured using the horizontal potentiometers attached at the base level. Quantification of the component of deflection due to flexural and shear deformations in the wall is the focus of the following discussion with the very small slip values removed.

Table 4.5: Summary of predicted and measured displacements at first yield

Lateral displacements		W1	W2	W3	W4	W5	W6	W7
Δ_y (mm) *(measured)*	(+)ve	8.0	10.8	9.0	3.6	4.4	4.1	5.1
	(-)ve	9.0	10.3	9.4	3.4	5.6	3.9	4.9
$\Delta_{f,y}$ (mm) *(calculated)*	(+)ve	5.8	8.4	6.5	2.4	3.2	2.9	3.2
	(-)ve	7.1	7.9	7.1	2.6	3.8	2.8	3.7
Δ_{sl} (mm) *(measured)*	(+)ve	0.0	0.3	0.1	0.0	0.2	0.0	0.1
	(-)ve	0.0	0.2	0.1	0.0	0.1	0.0	0.1
Avg. $[\Delta_{f,y}/(\Delta_y-\Delta_{sl})]$ %		76%	79%	75%	72%	73%	71%	71%
$\Delta_{f,Ay}$ (mm) *(predicted)**		10.0	9.2	9.5	4.4	4.1	4.2	4.2
$\Delta_{f,Cy}$ (mm) *(predicted)**		10.2	9.7	9.8	4.5	4.3	4.4	4.4
Δ_{sy} (mm) = $(\Delta_y - \Delta_{f,y} - \Delta_{sl})$	(+)ve	2.2	2.1	2.4	1.2	1.0	1.2	1.8
	(-)ve	1.9	2.2	2.2	0.8	1.7	1.1	1.1
Avg. $[\Delta_{sy}/(\Delta_y-\Delta_{sl})]$ %		24%	21%	25%	28%	27%	29%	29%

* $\Delta_{f,Ay}$ and $\Delta_{f,Cy}$ refer to flexural displacement predicted at yield using the MSJC code and CSA S304.1, respectively.

4.5.1 Flexural displacements

The flexure displacements at yield, $\Delta_{f,y}$, and at ultimate, $\Delta_{f,u}$, were calculated from the experimentally-obtained curvature profiles over the wall heights, presented in Fig. 4.3. The product of the average curvature, φ_i, and the corresponding segment length, $h_{gauge(i)}$, gives the average segment rotation, θ_i, considered to act at the centre of each segment. This relationship can be written as:

$\theta_i = \varphi_i \times h_{gauge(i)} = \left(\Delta_{Ti} + \Delta_{Ci}\right)/l_w$ Eq. 4.2

The summation of the product of each segment rotations, θ_i, and the distances from the center of the segment to the top of the wall, h_i, for all segments, gives the total flexure displacements at the top of each wall (as shown in Fig. 4.2), using the following equation.

$\Delta_{fE} = \sum_{i=1}^{n} \theta_i h_i = \sum_{i=1}^{n} \varphi_i h_{gauge(i)} h_i$ Eq. 4.3

Table 4.6: Summary of predicted and measured displacements at ultimate load

Lateral displacements		W1	W2	W3	W4	W5	W6	W7
Δ_u (mm) *(measured)*	(+)ve	25.1	31.5	36.0	14.0	14.9	24.1	20.1
	(-)ve	25.3	31.5	36.1	12.5	25.1	24.0	20.0
$\Delta_{f,u}$ (mm) *(calculated)*	(+)ve	20.4	25.2	27.2	9.8	11.0	17.6	15.3
	(-)ve	21.0	24.4	29.8	9.1	19.1	19.2	14.9
Δ_{sl} (mm) *(measured)*	(+)ve	0.0	0.9	0.3	0.2	0.7	1.3	0.6
	(-)ve	0.0	1.0	0.7	0.2	1.3	0.8	0.5
(Avg.) $[\Delta_{f,u}/(\Delta_u-\Delta_{sl})]$ %		82%	81%	80%	72%	80%	80%	77%
$\Delta_{f,Au}$ (mm) *(predicted)* *		26.5	74.0	69.9	13.9	41.0	38.7	38.7
$\Delta_{f,Cu}$ (mm) *(predicted)* *		19.0	43.3	42.1	10.0	25.3	24.5	24.5
Δ_{su} (mm) = $(\Delta_u - \Delta_{f,u} - \Delta_{sl})$	(+)ve	4.7	5.4	8.5	4.0	3.0	5.2	4.2
	(-)ve	4.3	6.1	5.6	3.2	4.7	4.0	4.6
(Avg.) $[\Delta_{su}/(\Delta_u-\Delta_{sl})]$ %		18%	19%	20%	28%	20%	20%	23%

* $\Delta_{f,Ay}$ and $\Delta_{f,Cy}$ refer to flexural displacement predicted at yield using the MSJC code and CSA S304.1, respectively.

The flexure displacements calculated using Eq. 4.2 for first yield of the reinforcement, $\Delta_{f,y}$, and Eq. 4.3 for ultimate load, $\Delta_{f,u}$, were presented in Table 4.5 and 4.6, respectively, for both directions of loading. It can be seen from the tables that the average flexure displacements at yield and ultimate conditions for the 3-storey walls comprised about 76% and 80%, respectively, of the top wall displacements. Slightly lower contributions from flexure displacement of about

72% and 74% of the top wall displacement were calculated for the 2-storey walls corresponding to yield and ultimate conditions, respectively. In this regard, compared to the 3-storey walls the larger contribution of shear deformations for the 2-storey walls was expected due to the 50% increase in shear force. Contributions of flexure, shear, and sliding displacements to the total top wall deflections were presented in Fig. 4.5 for all of the walls.

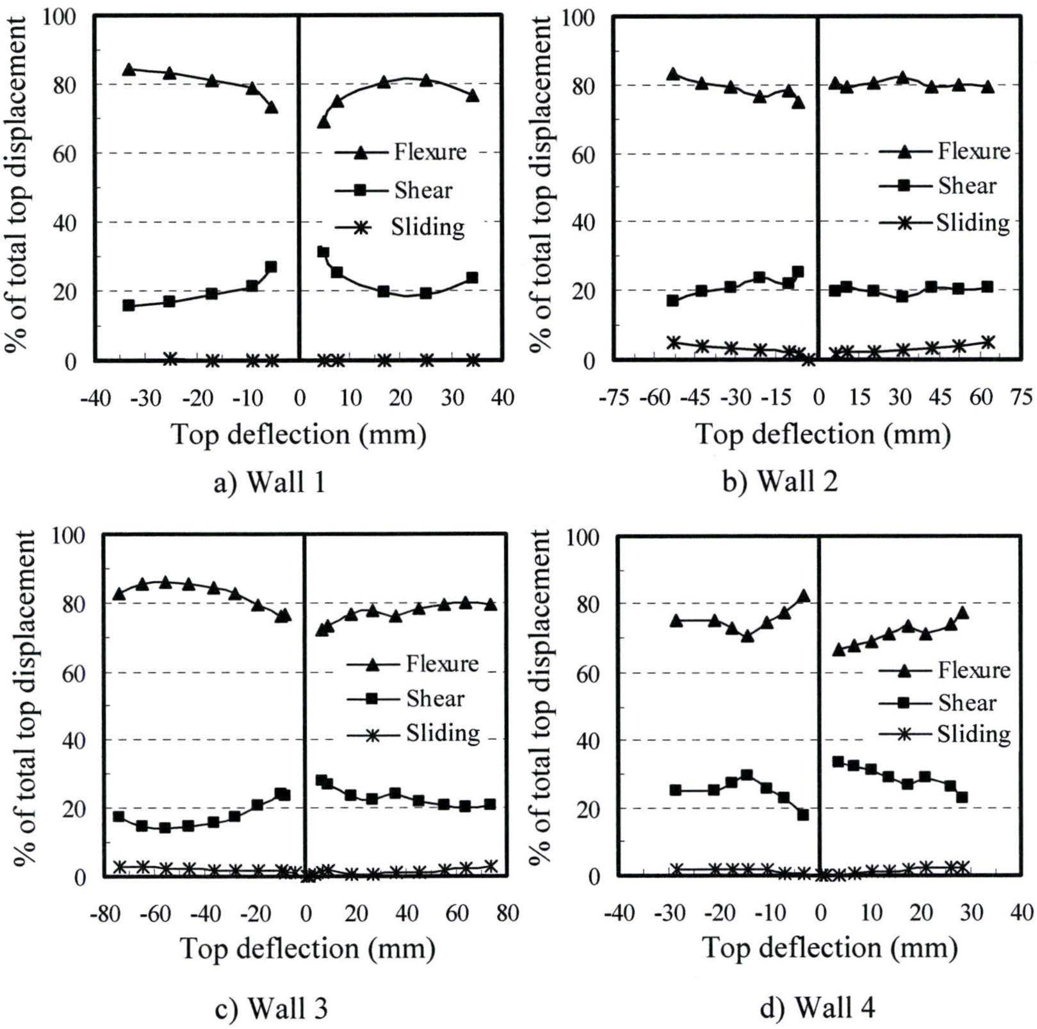

Fig. 4.5: Flexural, shear, and sliding displacements for the test walls

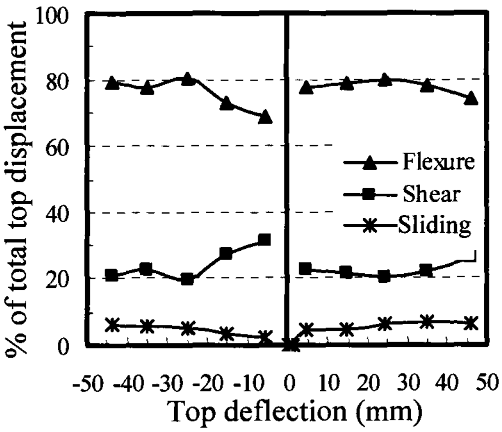

e) Wall 5

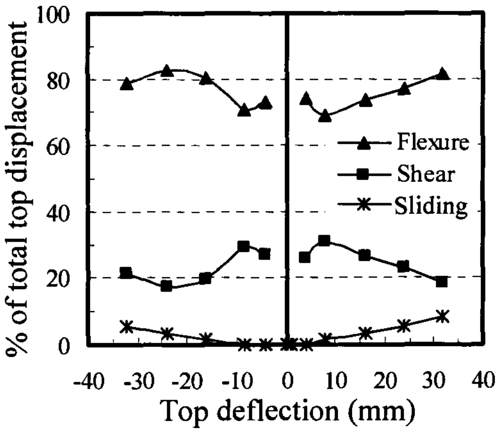

f) Wall 6

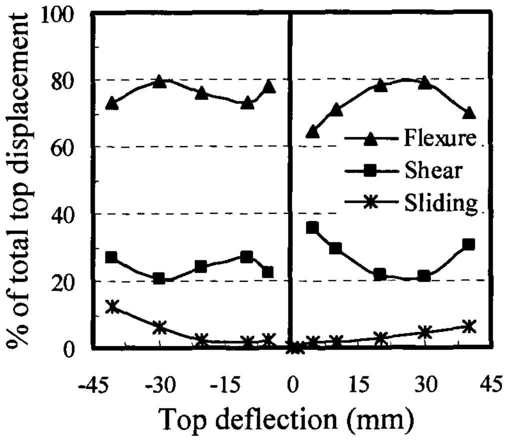

g) Wall 7

Fig. 4.5: (cont.)

The theoretical flexural displacements at yield, $\Delta_{y,\,th}$, and at ultimate load, $\Delta_{u,\,th}$, for a cantilever wall can be estimated assuming an elastic-plastic moment-curvature relationship (Paulay and Priestley 1992) as follows:

$$\Delta_{y,\,th} = \varphi_y \; \frac{h_w^2}{3} \qquad \text{Eq. 4.4}$$

$$\Delta_{u,\,th} = \Delta_{y,\,th} + (\varphi_u - \varphi_y)\; l_p\; (h_w - 0.5\; l_p) \qquad \text{Eq. 4.5}$$

where:

h_w = Wall height;

l_p = Equivalent plastic hinge length;

$\Delta_{y,\,th}$ = Flexural displacement at the onset of yielding of the outermost bar;

$\Delta_{u,\,th}$ = Flexural displacement at maximum masonry compressive strain;

φ_y = Curvatures at the wall base at the onset of yield; and

φ_u = Curvatures at the wall base at maximum masonry compressive strain.

The theoretical flexure displacements, presented in Tables 4.5 and 4.6, were calculated using the theoretical strain profiles (curvatures) at the onset of yielding and at ultimate load. This was achieved by setting the ultimate masonry compressive strain, ε_u, to 0.0025 and assuming an equivalent plastic hinge length, l_p, equal to the wall length, l_w, and to one half of the wall length, $0.5l_w$, following the guidelines of the MSJC code (2008), and CSA S304.1 (2004), respectively. Separate specific properties of the stress block based on the MSJC code and CSA S304.1, including different f'_m values, were used for displacement predictions.

The displacements $\Delta_{f,Ay}$ and $\Delta_{f,Cy}$, in Table 4.5, are the theoretical flexural displacements for the walls calculated at the onset of yield of the outermost reinforcing bar, using Eq. (4.4), following the requirements of the MSJC code (American) and CSA S304.1 (Canadian), respectively. The predicted ultimate flexural displacements $\Delta_{f,Au}$ and $\Delta_{f,Cu}$, in Table 4.6, corresponded to 0.0025 masonry compressive strain and, again, followed the requirements of the MSJC code and CSA S304.1, respectively, using Eq. 4.5.

The theoretical flexure displacements at first yield using both codes were similar but both were higher than the corresponding measured displacements. The predicted displacements were calculated assuming the same wall cross section over the entire height (i.e., ignoring the presence of the RC slabs) and assuming that all cross sections along the entire height of the wall being were cracked (i.e., assuming a constant slope of the *M/EI* or, curvature φ, relationship at yield). The inserts in Figs. 4.3 (a), (b), and (c) showed the experimentally and theoretically determined curvature profiles at yield used for deflection predictions. It can be seen that the experimental curvatures over the wall heights were lower than the theoretical values which is the main cause for the discrepancies between the theoretical and experimental yield displacement values.

For the rectangular walls, the theoretical displacement at ultimate load using the MSJC code was 28% higher than the calculated displacement from experimental results for the 3-storey wall (W1) and 47% higher for the 2-storey wall (W4). On the other hand, following CSA S304.1, better predictions for the flexure displacement of the rectangular walls W1 (within 8%) and W4 (within 6%) were calculated for the 3-storey and 2-storey walls, respectively. The differences between the two predictions were mainly attributed to the use of the previously discussed different plastic hinge values, l_p, to determine the theoretical displacement.

For the flanged and end-confined walls, the theoretical displacements calculated at ultimate load, using the MSJC code significantly overestimated the experimental results (by 100% to 200%). Similarly, but to a lesser extent, the displacement predictions at ultimate load calculated using CSA S304.1 overestimated the experimental results (by 35% to 80%). These overestimations indicated that the current l_p values in CSA S304.1 were suitable for rectangular walls but lower values should be determined for flanged and end-confined walls. On the other hand, the current values of l_p in the MSJC code significantly overestimated all of the test results.

4.5.2 Shear displacements

The amount of displacement attributed to shear deformations at first yield, Δ_{sy}, and at ultimate load, Δ_{su}, were calculated from Tables 4.5 and 4.6 by subtracting the flexural and sliding displacements at first yield and at ultimate load from the corresponding total top displacements Δ_y and Δ_u, respectively. Higher sliding displacements were recorded for the flanged walls compared to the end-confined walls and almost no sliding displacements were recorded for the rectangular walls. Walls in Phase II (2-storey with aspect ratio of 1.5) experienced more sliding than the walls in Phase I (3-storey with aspect ratio of 2.2) at ultimate load and in the post-peak region. The reason is obvious since the shear load is 50% higher in the case of the 2-storey walls. Also, it was noted that the flanged and end-confined walls experienced more sliding than the corresponding rectangular walls. This can be explained by considering that the flanged and end-confined walls had less vertical reinforcement and that a large portion of this reinforcement was in the end zones subjected to damage at high displacements. Therefore, these walls had less clamping action to create shear-friction resistance to sliding.

It can be seen from the tables that the shear displacements for the 3-storey walls were, on average, 23% and 19% of the total top displacements at Δ_y and Δ_u, respectively. Slightly higher contributions from shear of about 28% and 22% of the total top lateral displacement were calculated for the 2-storey walls corresponding to yield and ultimate conditions, respectively. These values were consistent with the results from full scale RM wall tests with aspect ratio of 2.0 reported by Shedid et al. (2009).

A theoretical shear displacement, Δ_s, for a cantilever wall with a height, h_w, subjected to a top load, Q, can be calculated by:

$$\Delta_s = \left(k \times \frac{Q \times h_w}{G_m \times A_e} \right) \qquad \text{Eq. 4.6}$$

where:

A_e = Effective shear area of the member (web area);

G_m = Shear modulus (= 0.4 E_m for Poisson's ratio = 0.25 (Drysdale and Hamid 2008), and $E_m = 850 \times f'_m$ (following the Canadian code); and

k = Shear shape factor (taken equal to 1.2 for all walls*).

Using the experimentally determined shear displacement, the effective shear area, A_e, in Eq. 4.6, was calculated using the selected constant value of the shear modulus, G_m, considering elastic behaviour. For ease of reference, the values of the effective shear area at the onset of yielding, A_{ey}, and at ultimate load, A_{eu}, were reported in Table 4.7 as a ratio of the web area of the walls cross sections. The effective shear areas for shear displacement calculation for the 3-storey walls

* This approach was selected to simplify comparison and can be justified based on the relatively small area of the flanges and boundary elements compared to the overall area of the wall

(aspect ratios of 2.2) were estimated to be, on average, 28% and 16% of the web area of the wall at first yield of the outermost reinforcing bars and at ultimate load, respectively. Similarly, the effective shear areas for the 2-storey walls (aspect ratios of 1.5) were, on average, 52% and 22% of the web area of the wall at first yield of the outermost reinforcing bars and at ultimate load, respectively. The effective shear areas estimated for the 2-storey were, on average, 1.9 and 1.4 times the effective shear areas for the 3-storey walls at yield and ultimate, respectively.

Based on these results, it can be seen that by using Eq. 4.6 and having the values of k, G_m, and the product of Q and h_w almost the same for the 3-storey and 2-stroey walls (having the same cross section), the effective shear areas will be directly related to the values of the shear displacements. Therefore, for design purposes, it is more convenient to determine the flexure displacement and amplify it by 20-30% for walls with aspect ratio of 2.2 and by 30-40% for walls with aspect ratio of 1.5 to account for shear displacement.

Table 4.7: Shear displacement and effective shear area ratios

Walls		W1	W2	W3	W4	W5	W6	W7
Δ_{sy} (mm)	(+)ve	2.2	2.1	2.4	1.2	1.0	1.2	1.8
	(-)ve	1.9	2.2	2.2	0.8	1.7	1.1	1.1
Q_y (kN)	(+)ve	101	121	110	160	185	173	188
	(-)ve	110	123	106	162	183	169	170
(Avg.) A_{ey} / A_{web} (%)		28%	30%	25%	59%	52%	53%	46%
Δ_{su} (mm)	(+)ve	4.7	5.4	8.5	4.0	3.0	5.2	4.2
	(-)ve	4.3	6.1	5.6	3.2	4.7	4.0	4.6
Q_u (kN)	(+)ve	177	151	152	265	245	241	246
	(-)ve	180	154	147	267	239	234	236
(Avg.) A_{eu} / A_{web} (%)		21%	14%	12%	26%	23%	19%	19%

4.6 Displacement ductility

Ductility is a measure of a wall's ability to deform beyond initial yielding of the flexural reinforcement. The displacement ductility, μ_{Δ}, is defined herein as the ratio of the measured top displacements at a specific displacement level beyond yielding, Δ_i, to displacement at the onset of yielding of the outermost vertical bar, Δ_y. Idealizations of the load-displacement relationships were conducted based on the approach explained in Section 3.10.2 (Tomazevic 1998). As such, the idealized displacement ductility, $\mu^{ep}{}_{\Delta 0.8u}$, was defined as the ratio between the measured top displacements at 20% degradation in strength, $\Delta_{0.8u}$, and the idealized yield displacement, $\Delta^{ep}{}_y$, as shown in Fig. 4.6. These values were presented in Table 4.8.

Idealized displacement ductility values corresponding to ultimate load, $\mu^{ep}{}_{\Delta u}$, and to 1% drift, $\mu^{ep}{}_{\Delta 1\%}$, were also calculated using the idealizations shown in Fig. 4.6. In addition, the measured displacement ductility values at ultimate load ($\mu_{\Delta u} = \Delta_u / \Delta_y$), at 1% drift ($\mu_{\Delta 1\%} = \Delta_{1\%} / \Delta_y$), and at 20% degradation in strength ($\mu_{\Delta 0.8u} = \Delta_{0.8u} / \Delta_y$), were listed in Table 4.8 for all of the walls. Also, theoretical displacement ductility at ultimate load based on the MSJC code ($\mu_{\Delta,\,Ath} = \Delta_{f,\,Au} / \Delta_{f,\,Ay}$) and CSA S304.1 ($\mu_{\Delta,\,C\,th} = \Delta_{f,\,Cu} / \Delta_{f,\,Cy}$) were included in the same table.

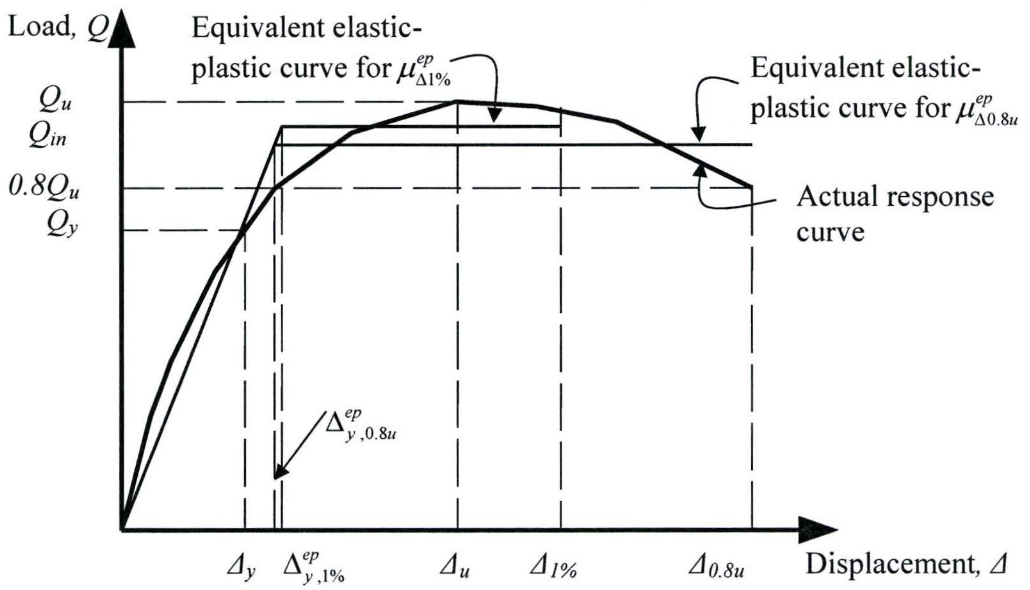

Fig. 4.6: Idealizations of the actual load-displacement relationships (Tomazevic 1998)

Table 4.8: Predicted, actual and idealized wall displacement ductilities

Wall	Theoretical $\mu_{\Delta,\ th}$		Test results									
	MSJC code (2008)	CSA S304.1 (2004)	Loading direction	Measured μ_Δ			Idealized load-displacement relationship					
							At Q_u		At 1% drift		At 0.8 Q_u	
				$\mu_{\Delta u}$	$\mu_{\Delta 1\%}$	$\mu_{\Delta 0.8u}$	$\mu_{\Delta u}^{ep}$	Q_{in}/Q_u	$\mu^{ep}_{\Delta 1\%}$	Q_{in}/Q_u	$\mu^{ep}_{\Delta 0.8u}$	Q_{in}/Q_u
W1	2.7	1.9	(+)	3.1	5.0	5.4	1.9	0.92	3.0	0.93	3.3	0.92
			(-)	2.8	4.4	4.9	1.8	0.94	2.9	0.95	3.2	0.93
W2	8.0	4.5	(+)	2.9	3.7	5.7	2.3	1.00	2.9	1.00	4.6	0.99
			(-)	3.1	3.9	6.0	2.4	1.00	3.1	1.00	5.0	0.97
W3	7.4	4.3	(+)	4.0	4.4	10.4	2.9	0.97	3.3	0.98	7.8	0.95
			(-)	3.8	4.3	9.7	2.8	0.95	3.1	0.96	6.9	0.98
W4	3.1	2.2	(+)	4.0	7.2	7.6	2.5	0.93	4.5	0.96	4.7	0.95
			(-)	3.6	7.6	8.4	2.4	0.93	4.9	0.94	5.3	0.94
W5	10.0	5.9	(+)	3.3	5.9	8.9	2.6	0.98	4.6	0.98	7.1	0.95
			(-)	4.5	4.6	6.9	3.6	0.96	3.7	0.96	5.6	0.95
W6	9.2	5.6	(+)	5.9	6.3	11.8	4.4	0.96	4.7	0.97	9.0	0.94
			(-)	6.2	6.7	15.0	4.7	0.95	5.1	0.96	11.4	0.95
W7	9.2	5.6	(+)	3.9	5.1	10.8	3.1	0.98	4.0	0.97	8.4	0.99
			(-)	4.1	5.3	11.3	3.1	0.97	4.0	0.97	8.6	0.96

It can be determined from Table 4.8 that the idealized displacement ductility values at ultimate load, 1% drift, and at 20% strength degradation performance levels were, on average, 28% (*c.o.v.*= 10%) less (average the ratio of μ^{ep}/μ at the three performance levels) than the measured displacement ductility values (Δ/Δ_y in Fig. 4.6). The inelastic capacities, Q_{in}, determined using the elastic-plastic idealization at the three performance levels (Δ_u, $\Delta_{1\%}$, and $\Delta_{0.8u}$) were, on average, 96% of the measured wall capacities, Q_u, (*c.o.v.*= 2%). Therefore, the approximation that Q_{in} equals Q_u to determine the idealized displacement ductility values in Section 3.10.2 was somewhat conservative but adequate. This also showed that the half scale rectangular, flanged, and end-confined reinforced masonry walls tested in this study have the same characteristics as the rectangular full scale RM walls tests reported by Shedid et al. (2010), with respect to the idealized bilinear elastic-plastic load-displacement relationships.

The theoretical displacement ductilities calculated using the MSJC code and CSA S304.1, as presented in Table 4.8, were basically the ratios of the predicted ultimate and yield flexural displacements previously presented in Tables 4.5 and 4.6. As determined from Table 4.8, the theoretical displacement ductilities for all test walls, based on the MSJC code, significantly overestimated the idealized displacement ductilities at ultimate load, $\mu^{ep}{}_{\Delta u}$. On the other hand, the theoretical displacement ductilities based on CSA S304.1 were in a relatively better agreement with the experimental values especially for the rectangular walls. This better agreement was mainly attributed to the assumption of a smaller equivalent plastic hinge length in CSA S304.1 (2004) compared to the MSJC code (2008).

4.7 Stiffness

To assess the variation in wall stiffness with increased loading and top displacement, the secant stiffness, defined as the ratio between the lateral resistance and the corresponding top lateral wall displacement, was used. The average measured values of wall stiffnesses obtained from both loading directions at yielding of the vertical reinforcement (commonly used in seismic design) and at ultimate load were listed in Table 4.9.

The initial gross stiffnesses for all walls, presented in Table 4.9, were calculated based on flexure and shear deformations using Eq. 4.7. The gross stiffnesses of the walls were calculated using the transformed moment of inertia, I_g, and the gross masonry area of the section, A_g. Constant section properties were assumed over the wall height.

$$K = 1/\left(\frac{h_w^3}{3\,E_m\,I} + k\,\frac{h_w}{G_m\,A}\right) \qquad \text{Eq. 4. 7}$$

where: E_m = $850f'_m$ (According to CSA S304.1, 2004)

G_m = $0.4\ E_m$ (Drysdale and Hamid 2008)

k = Shear shape factor (1.2 for all walls)

Table 4.9: Wall stiffnesses

Condition \ Walls		W1	W2	W3	W4	W5	W6	W7
Initial gross[1] (kN/mm)		28	39	38	80	104	102	102
Measured (kN/mm)	First yield[2] (% of Gross)	13 (46)	12 (31)	12 (32)	48 (60)	43 (41)	42 (41)	36 (35)
	Ultimate load (% of Gross)	7 (25)	5 (13)	4 (11)	18 (23)	10 (10)	10 (10)	11 (11)
Measured (%Gross)	At 0.1% Drift	60	46	49	63	52	66	61
	At 0.5% Drift	27	21	19	22	16	22	17
	At 1.0% Drift	14	9	10	9	8	8	9
	At 1.5% Drift	N.A.	6	7	N.A.	6	6	6

[1] I_g and A_g were the calculated uncracked section properties used to calculate stiffness

[2] Stiffness corresponding to first yield of vertical reinforcement

The stiffness variations with increased top wall displacements were presented in Figs. 4.7 (a) and (b) for the walls tested in Phases I and II, respectively. The trend of stiffness degradation for all walls were similar and showed significant decreases with increased top deflection. The experimentally-determined secant stiffnesses for the test walls were subsequently normalized with respect to the corresponding initial gross stiffnesses. The normalized wall stiffnesses in both loading directions were presented with respect to the top wall displacement and drift levels in Figs. 4.8 (a) and (b) and with respect to multiples of yield displacement in Figs. 4.8 (c) and (d) for walls in Phases I and II, respectively. The figures show similar trends of stiffness degradation for all of the test walls. The stiffnesses for all walls degraded rapidly to about 60% of the gross stiffness at about 0.10% drift.

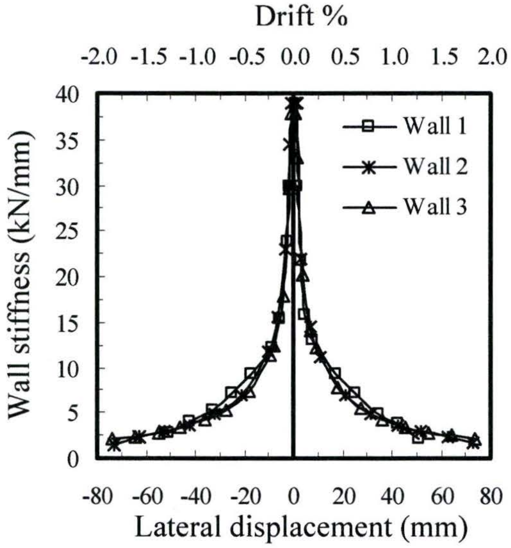

a) Walls in Phase I

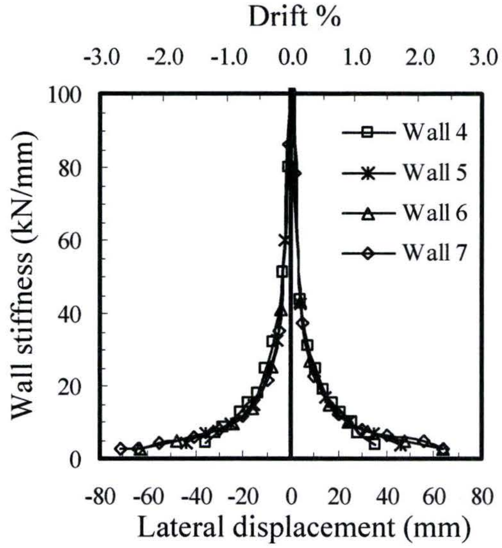

b) Walls in Phase II

Fig. 4.7: Stiffness with increased top wall displacement

Values of the normalized stiffness at drift levels of 0.1%, 0.5%, 1.0% and 1.5%, which can be used in performance based design, were also given in Table 4.9. It can be seen from the table that reasonable approximations of the test wall stiffnesses at 0.5%, 1.0%, and 1.5% drift would be, on average, 21%, 9%, and 6% of the wall stiffnesses calculated using transformed gross section properties. The experimental results indicated that the secant stiffnesses at first yield, which are of interest during the design process, were 46% and 60% of the gross stiffness for the 3-storey (W1) and 2-storey (W4) rectangular walls, respectively. The average secant stiffnesses at first yield were 32% and 39% of the gross stiffness for the 3-storey (W2 and W3) and the 2-storey (W5, W6, and W7) flanged and end-confined walls, respectively.

The stiffnesses of the rectangular walls decreased to about 20% of the gross stiffness at $4\times\Delta_y$ and $6\times\Delta_y$ for the 3-storey and 2-storey walls, respectively. For the 3-storey (W2 and W3) and the 2-storey (W5, W6, and W7) flanged and end-confined walls, the stiffness decreased to about 11% of the gross stiffness at $4\times\Delta_y$ and $6\times\Delta_y$ displacement, respectively. This indicates that the decreases in stiffnesses for the flanged and end-confined walls were more significant than for the corresponding rectangular walls. Therefore, and as was shown in Fig. 4.7, although the stiffnesses values for the flanged and end-confined walls were higher than the corresponding values of the rectangular walls at initial stages of loading, all values became almost equal at fairly low post-yield displacement levels.

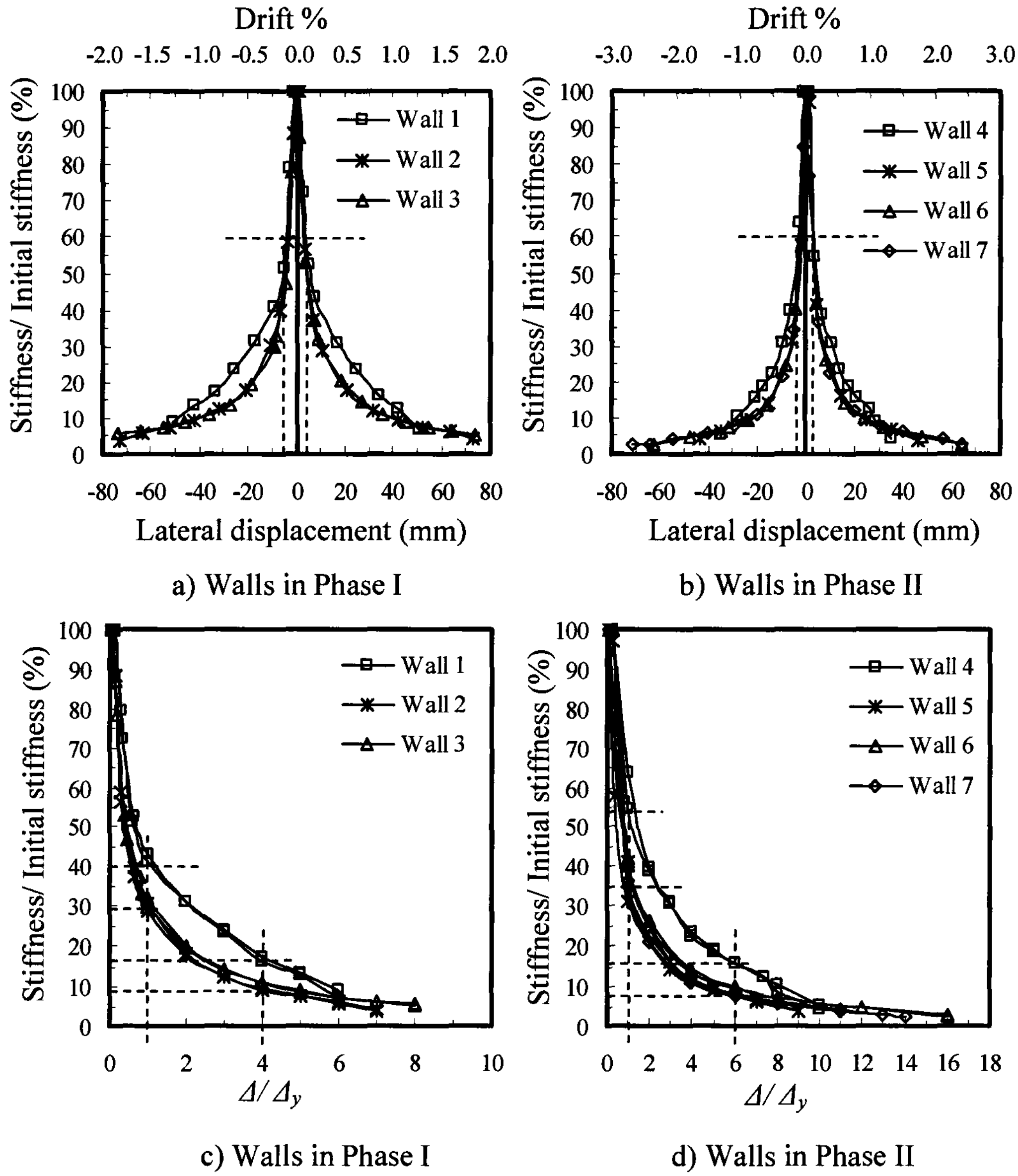

a) Walls in Phase I

b) Walls in Phase II

c) Walls in Phase I

d) Walls in Phase II

Fig. 4.8: Normalized wall stiffness

4.8 Energy dissipation

Energy dissipation, E_d, through hysteresis damping is an important aspect in seismic design since it reduces the amplitude of the seismic response and, thereby, reduces the ductility and strength demands on the structure.

Given that the displacement histories were not identical for all walls (each wall was cycled at multiples of its initial yield displacement), comparing the energy dissipated with respect to a single hysteresis loop at a particular drift level cannot be used as a basis for comparison between the test walls. Previous research (Sinha et al. 1964; Jamison 1997) showed that the envelope of the load-displacement hysteresis loops is relatively insensitive to the imposed displacement increments and to the number of cycles. Therefore, the energy dissipation, E_d, has been represented, as suggested by Hose and Seible (1999), by the area enclosed within the force-displacement curve at each displacement level. This is the horizontally-hatched area shown in Fig. 4.9. The vertically-hatched region in the same figure represents the elastic strain energy, E_s, stored in an equivalent linear elastic system.

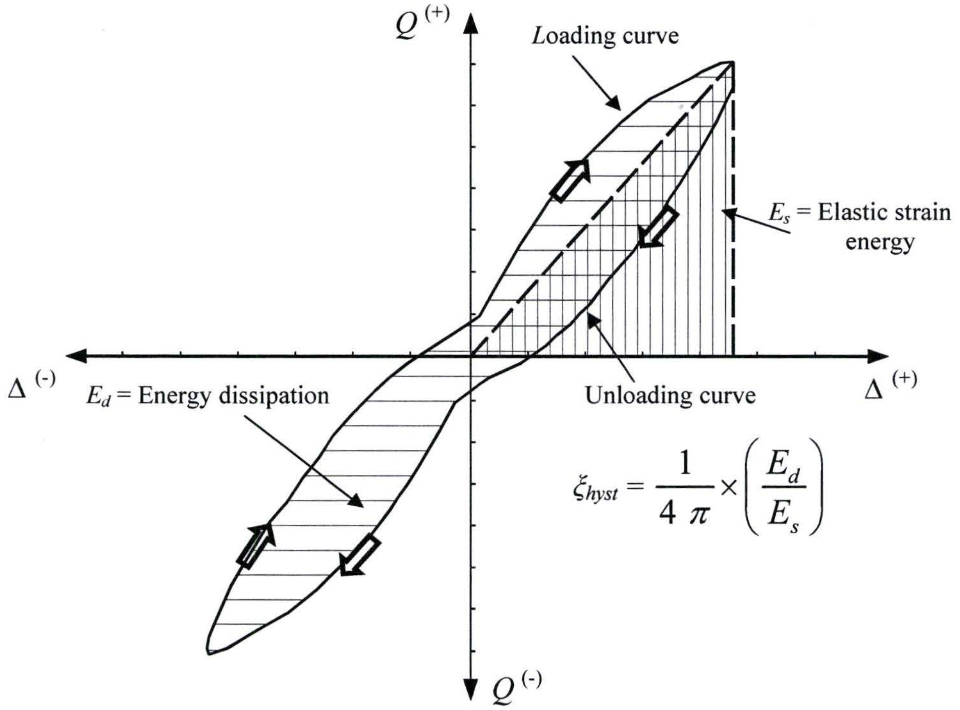

Fig. 4.9: Calculation of energy dissipation

The energy dissipation at different displacement levels of all the walls were presented in Fig. 4.10. The figure showed that, as expected for low pre-yield displacement levels, the energy dissipation was very low. For higher displacement levels, the energy dissipation increased significantly. Similar increases in energy dissipation were calculated for the 3-storey and the 2-storey walls.

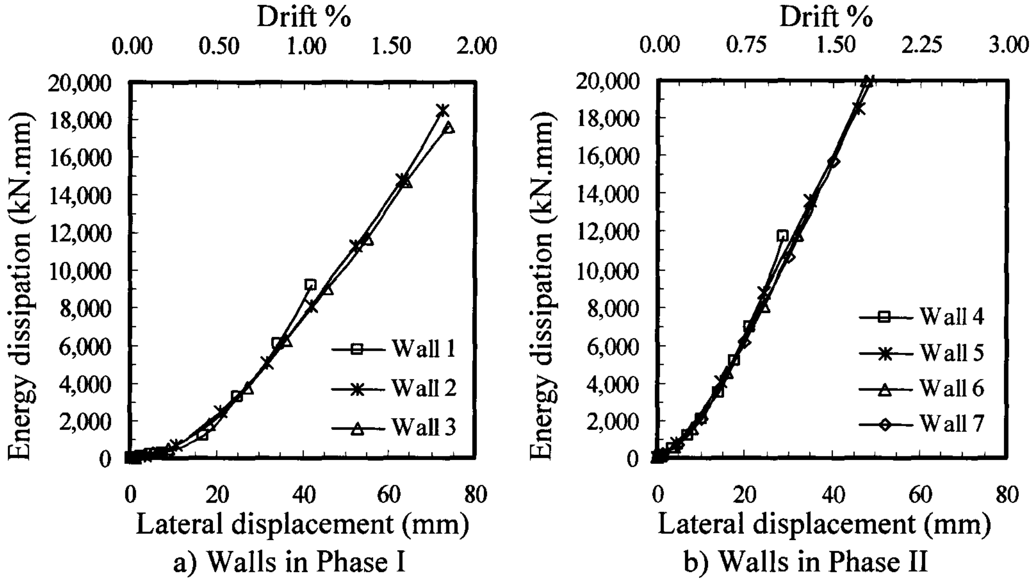

Fig. 4.10: Variation of energy dissipation with increased wall displacements

The normalized energy dissipation values, $E_{d.N}$, for the walls at different displacement levels, defined as the ratio between the energy dissipation at a certain post-yield displacement level and the calculated energy dissipation at the onset of yielding were plotted in Figs. 4.11 (a) and (b) versus the ratio of the post-yield displacement to the yield displacement. The energy dissipation was normalized for individual walls to monitor the trend of increase of energy dissipation after yielding and to eliminate the effects of differences in wall capacity and displacement. The figures showed almost linear increases in the normalized energy dissipation values with respect to the ratio of the wall post-yield to yield displacements. The normalized energy dissipation values at $2\times\Delta_y$ and $5\times\Delta_y$, respectively, were equal to or greater than 3.5 and 17 for the 3-storey walls (Phase I). The normalized energy dissipation values at $2\times\Delta_y$ and $5\times\Delta_y$ were about 2.5 and 10 for the 2-storey walls (Phase II). The increases in energy dissipation with increased wall ductility and drift levels affected the hysteresis damping as discussed in the following section.

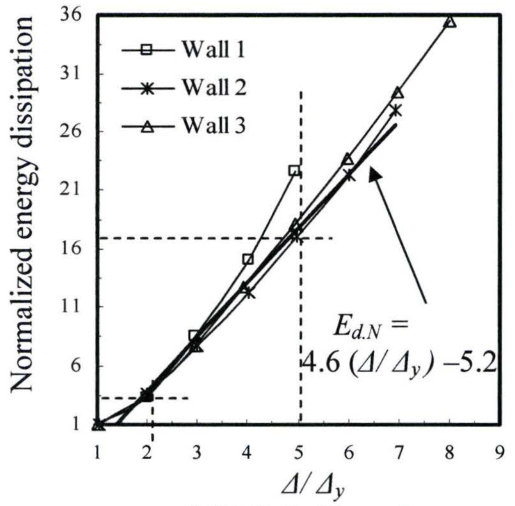

a) Walls in Phase I

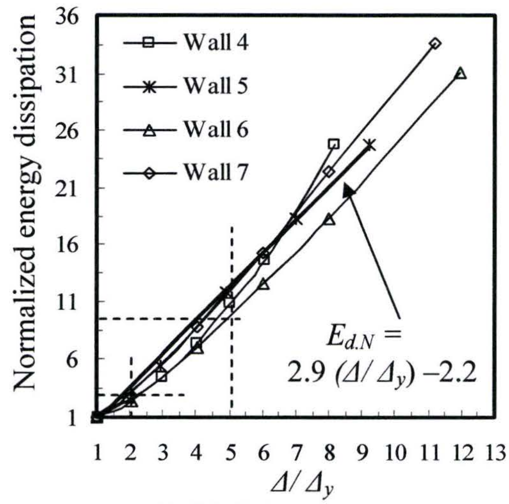

b) Walls in Phase II

Fig. 4.11: Normalized energy dissipation corresponding to multiples of Δ_y

4.9 Hysteresis damping

Hysteresis damping, ξ_{hyst}, can be quantified based on an equal area approach (Hose and Seible, 1999, and Chopra, 2000) that represents the same amount of energy loss per loading cycle. The relationship between the dissipated energy, E_d, the stored strain energy, E_s, and the hysteresis damping, ξ_{hyst}, [see Fig. 4.9] is given by:

$$\xi_{hyst} = \frac{1}{4\,\pi} \times \left(\frac{E_d}{E_s} \right) \qquad \text{Eq. 4. 8}$$

The hysteresis damping, ξ_{hyst}, was plotted against the lateral displacement (and the drift) in Figs. 4.12 (a) and (b) and against the ratio of the post-yield to the yield displacements in Figs. 4.13 (a) and (b) for all the test walls. Increasing ξ_{hyst} values with increased lateral displacements were indicated. Although damping is generally specified for a structure rather than for an element (wall), the trend of increased damping with increased ductility of individual walls gives an indication of the overall response of RM structures which are typically constructed with similar walls connected by rigid diaphragms.

The average hysteresis damping calculated at 0.3% drift and 1% drift for the 3-storey walls (Phase I) was about 6% and 19%, respectively, and about 12% and 22%, respectively, for the 2-storey walls (Phase II). It has been commonly assumed that reinforced masonry structures have an *overall damping* ratio (which also includes elastic damping) ranging between 7% and 10% of critical damping (Paulay and Priestley 1992; Drysdale and Hamid 2005). This current research indicates that RM shear wall building can be expected to experience higher levels of damping after the onset of yielding compared to the currently-accepted levels. This higher damping has the effect of significantly reducing the seismic demand.

As shown in Fig. 4.13, the hysteresis damping alone at the onset of yield (μ_Δ= 1.0) varied between 6% and 8% for the 3-storey walls (Phase I), and between 12% and 14% for the 2-storey walls (Phase II). The hysteresis damping increased to a minimum of 20% and 17% at 5×Δ_y for the 3-storey and 2-storey walls, respectively.

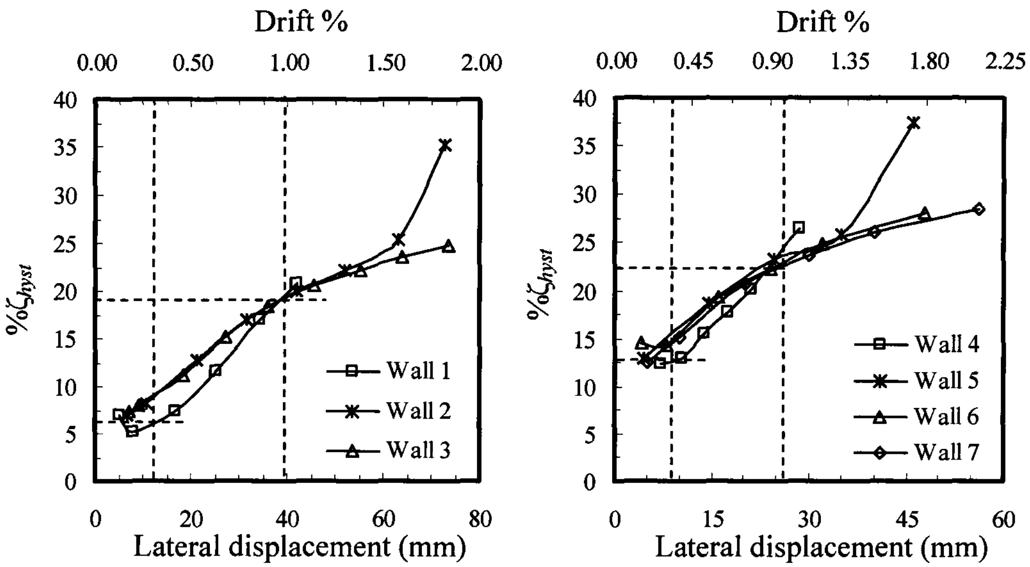

a) Walls in Phase I b) Walls in Phase II

Fig. 4.12: Hysteresis damping versus lateral displacement

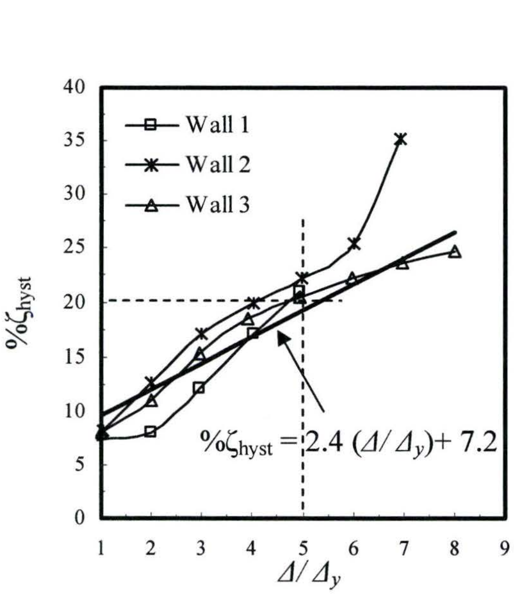

a) Walls in Phase I

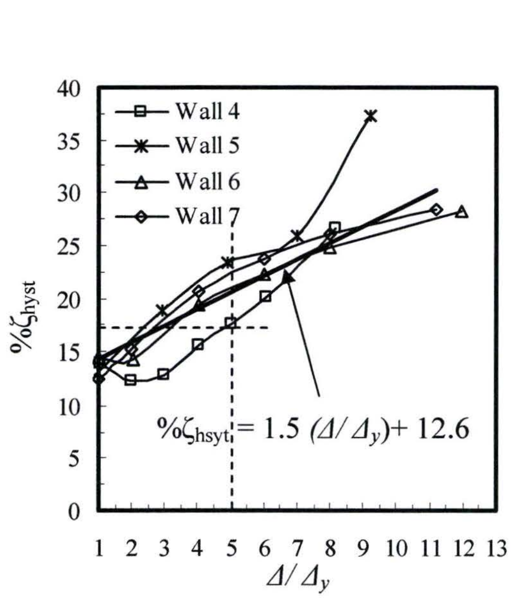

b) Walls in Phase II

Fig. 4.13: Hysteresis damping corresponding to multiples of Δ_y

The increases of the hysteresis damping with increased displacements indicated that different values of damping ratio may be assigned to structures under different design limit states. Structures designed for *Collapse Prevention* can be assigned a higher damping ratio as they are expected to exhibit high inelastic deformation and damage. Alternatively, structures designed for the *Fully-Operational* limit state, or for the *Serviceability* limit state would be assigned lower damping values since lower levels of deformations and cracking are expected. Such an approach would optimize the design for different performance levels by associating expected damage with the specific damping ratios resulting from this damage.

4.10 Summary and conclusion

This chapter contained detailed analyses of results from the experimental program and focused on evaluating the ductile performance of flexural RM shear walls with various end configurations. Measured compressive strain and curvature values at ultimate load were discussed. The extent of the plasticity region, L_p, was determined. The relative contributions of flexural and shear deformations to overall lateral wall displacement, the amount of energy dissipated by hysteretic damping and ductility, and the stiffness and strength degradation of the walls were presented.

The compressive strains in masonry at ultimate load, over the lower 50 mm of the wall (11.5×10^{-3} mm/mm, on average) were found to be approximately 4 times the maximum compressive strains of 2.5×10^{-3} mm/mm and 3.0×10^{-3} mm/mm, specified in the MSJC code (2008) and in CSA S304.1 (CSA 2004), respectively. On the other hand, the masonry strains averaged over the lower 150 mm at ultimate load (5.2×10^{-3} mm/mm, on average) were approximately double these specified values. Although the observed increases in the compressive strain had a minimal effect on wall strength, these increases significantly affected wall curvatures and, consequently, lateral displacements.

The curvatures predicted using CSA S304.1, on average, overestimated the experimental results by about 12% at first yield for the rectangular walls and underestimated those for the flanged and end-confined walls by about 14%. On the other hand, at ultimate load, the theoretical curvatures, on average, underestimated the experimental results by 36% for the rectangular walls and by 4% for the flanged and end-confined walls.

The test results indicated that for all walls (rectangular, flanged, and end-confined with aspect ratios of 1.5 and 2.2), the average height of the plasticity zone, L_p, varied between 63% and 75% of the wall length, l_w. This indicated that special detailing should be considered for the vertical and horizontal reinforcement within a height above the base equal to at least 75% of the wall length.

Higher sliding displacements were recorded for the flanged walls compared to the end-confined walls and almost no sliding displacements were recorded for the rectangular walls. This was attributed to the reduction of the vertical reinforcement, which also served as dowels, from 19 to 11 bars at the interface between the wall and the foundation. Having the majority of the vertical reinforcement in the damage regions at the ends of the flanged and end-confined walls also added to increases in this small amount of displacement. Walls with aspect ratio of 1.5 experienced more sliding than the walls with aspect ratio of 2.2 at displacements corresponding to and beyond ultimate loads. This was attributed to the increased lateral force applied to the 2-storey walls compared to the 3-storey walls.

The shear displacements for the walls with aspect ratio of 2.2 were, on average, 23% and 19% of the total top lateral displacements (minus sliding) at yield and ultimate conditions, respectively. Slightly higher contributions from shear of about 28% and 22% of the total top lateral displacement (minus sliding) were determined for the walls with aspect ratio of 1.5 corresponding to Δ_y and Δ_u, respectively.

Idealized displacement ductility values at ultimate load, 1% drift, and at 20% strength degradation were, on average, 28% less than the actual displacement ductility values calculated using Δ_y. The inelastic capacities for the elastic-plastic idealization at the aforementioned three performance levels were, on average, 96% of the measured wall capacities. Therefore, in the bilinear idealization of the actual load-displacement relationship for RM shear walls, assuming the wall's inelastic capacity, Q_{in}, equalled to the actual capacity, Q_u, of the wall was a conservative but reasonable approximation.

The stiffnesses for all walls degraded rapidly to less than 60% of the initial gross stiffnesses at low displacement levels equal to about 0.1% drift. Reasonable values for the test wall stiffnesses at 0.5%, 1.0%, and 1.5% drift can be assumed to be approximately 20%, 9%, and 6% of the wall stiffnesses calculated using uncracked (gross) transformed section properties.

The relationships between the normalized energy dissipation at first yield and the ratios of the post-yield displacements to the yield displacement were almost linear. The energy dissipation values calculated at $5\times\Delta_y$ were more than 10 times larger than the values at Δ_y. The hysteresis damping calculated at 0.3% drift and 1% drift for the 3-storey walls (Phase I) was at least 6% and 19%, respectively. Higher values were calculated for the 2-storey walls (Phase II).

The information reported in this study is expected to provide a better understanding of the behaviour of RM shear walls under seismic loads. This facilitated development of the proposals for more rational code design provisions presented in Chapter 5. Before proceeding with such analyses of the multi-storey half scale walls tested in this study, the behaviour of the full scale RM shear wall, previously tested by Shedid (2006) without RC floor slabs, were analysed and presented in Appendix A. This research was an important step where quantification of the seismic performance parameters for the full scale walls would eliminate complications associated with interpreting the test results of the walls reported in the current study. The information was placed in an appendix to avoid confusion with the current experimental study.

Chapter Five

Seismic Performance Parameter for The Proposed Wall categories

CHAPTER 5
SEISMIC PERFORMANCE PARAMETERS FOR THE PROPOSED WALL CATEGORIES

5.1 Introduction

In Appendix A, seismic performance parameters were investigated for the full scale concrete block shear walls tested previously by Shedid (2006). This chapter contained analyses of the same seismic performance parameters for the half scale concrete-block shear walls tested in this study. Based on the methods of obtaining the measured and the theoretical curvatures and curvature ductility values presented in Section 4.3 and the idealized displacement ductility values presented in Section 4.6, the equivalent plastic hinge lengths, l_p, required for wall deflection predictions were determined in Section 5.2 for the test walls.

Force-based seismic design provisions include reduction factors to reduce the design forces to lower values than those based on assumed linear elastic responses for structures. In NBC 2005, seismic force modification factors include a ductility-related force modification factor, R_d, and an overstrength-related force modification factor, R_o. Although seismic force modification factors are assigned to building systems, the hypothesis followed in Sections 5.3 to 5.6 is that the response of individual wall would be representative of the overall building response. This is particularly relevant to masonry construction as it is common to construct mid-rise masonry structures using equally-spaced identical walls. Therefore, neglecting possible coupling between walls, it can be expected that the response of individual walls can, to a great extent, represent the response of the building in terms of the overall load-displacement relationship where the load is appropriately scaled-down. Idealized bilinear load-displacement relationships were used in Section 5.3 to calculate the R_d values for individual walls. This analysis will provide evidence of what is possible for systems of walls. Similarly, R_o values also were determined in Section 5.3.

The current Canadian standard (CSA S304.1-2004) provides general seismic force modification factors for concrete-block shear walls. Although it may be that the use of rectangular walls was anticipated, no separate provisions for flanged and end-confined concrete-block shear walls exist, so they currently fall into the general category. However, the concrete design standard CSA A23.3 (2005) does include provisions to determine the R_d values for reinforced concrete flanged walls and walls with boundary elements. Calculation of representative R_d values for flanged and end-confined masonry walls following the Canadian concrete standard were presented in Section 5.4.

Similar to the approach adopted by the Canadian code, the American codes, such as the ASCE-7 (2008), define an overall seismic force-reduction factor, R, and a deflection amplification factor, C_d, to determine the design seismic forces and the corresponding displacements. However, ASCE-7 (2008) requires a dynamic analysis to determine the seismic reduction factors. To evaluate this approach, an analytical model was developed for the test walls (not for whole buildings) and ground motions were selected. Then nonlinear time history analyses were conducted and R and C_d values were determined in Section 5.5.

Although most seismic design codes currently follow the force-based design method which mainly relies on the initial elastic characteristics of the structure, *displacement-based* design methods have been developed to mitigate some deficiencies in the current design method. The post-yield performance characteristic of the walls, including stiffness reduction and its effect on period increase were presented in Section 5.6 corresponding to drift and ductility demand. (Such information is essential when displacement-based design approaches are adopted.) The main findings and the chapter conclusions were presented in Section 5.7.

5.2 Equivalent plastic hinge length

Using the evaluated curvature and displacement ductility values, the equivalent plastic hinge length, l_p, for each wall was calculated by rearranging Eq. A.1, as discussed in Section A.6. As previously explained, an idealized bilinear load displacement relationship was used to calculate the l_p values. The displacement at the top of the wall at ultimate load, Δ_u, was used as the maximum displacements in the idealization approach. In order to idealize the nonlinear load-displacement relationship into an elastic-plastic relationship for the walls, the *idealized* yield displacement, Δ_y^{ep}, and yield curvature, ϕ_y^{ep}, were used (refer to Section A.6). The idealized displacement ductility, $\mu_{\Delta u}^{ep}$, was used instead of the actual values calculated directly from the test results. All of the values used in the calculation of the equivalent plastic hinge lengths, l_p, were presented in Table 5.1.

Table 5.1: Calculation of equivalent plastic hinge length

Walls		W1[1]	W2[2]	W3[3]	W4[1]	W5[2]	W6[3]	W7[3]
$\mu_{\Delta u}^{ep}$	(+)ve	1.9	2.3	2.9	2.5	2.6	4.4	3.1
	(-)ve	1.8	2.4	2.8	2.4	3.6	4.7	3.1
Calculation based on theoretical curvatures								
$\mu_{\varphi,th}$		2.9	8.1	7.8	2.9	8.1	7.8	7.8
l_p (mm)	(+)ve	683	254	392	807	209	488	290
	(-)ve	600	274	370	743	350	537	290
	$\%l_w$	36%	16%	21%	43%	16%	28%	16%
Calculation based on curvatures at ultimate load								
$\mu_{\varphi u}$	(+)ve	4.1	4.0	6.2	5.4	4.8	6.5	4.9
	(-)ve	4.6	5.3	7.0	5.6	11.6	6.7	4.8
$\mu_{\varphi u}^{ep}$	(+)ve	2.5	3.2	4.5	3.4	3.8	4.9	3.9
	(-)ve	2.9	4.1	5.2	3.8	9.3	5.1	3.7
l_p (mm)	(+)ve	893	900	814	635	580	952	760
	(-)ve	600	662	626	494	294	995	829
	$\%l_w$	41%	43%	40%	31%	24%	54%	44%

[1] Rectangular wall [2] Flanged wall [3] End-confined wall

Using the theoretical curvatures, the equivalent plastic hinge lengths, presented in Table 5.1, were, on average, 640 mm, 254 mm, and 381 mm for the 3-storey rectangular, flanged and end-confined walls, respectively, corresponding to the idealized displacement ductility values. For the 2-storey linear, flanged and end-confined walls, the corresponding average l_p values were 770 mm, 279 mm, and 401 mm, respectively.

The idealized displacement ductility values at ultimate load, $\mu^{ep}_{\Delta u}$, of the end-confined and flanged walls were higher than those of the rectangular walls. However, the required equivalent plastic hinge lengths, l_p, were not longer as a result of their significantly higher theoretical curvature ductility values. The l_p values for the rectangular walls (when the theoretical curvature ductility values were used) were, on average, 39% of the wall length. The average l_p values for the flanged and the end-confined walls (based on the theoretical curvatures) were 16% and 21% of the wall length, respectively.

Using the experimental curvatures, the average equivalent plastic hinge lengths, also presented in Table 5.1, were 746 mm, 781 mm, and 720 mm for the 3-storey rectangular (W1), flanged (W2) and end-confined (W3) walls, respectively, based on the idealized displacement ductility values. For the 2-storey rectangular (W4), flanged (W5) and end-confined (W6 and W7) walls, the corresponding average l_p values were 565 mm, 437 mm, 885 mm, respectively. The average l_p value for the rectangular walls (W1 and W4) was 36% of the wall length (based on the experimental curvature ductility values). The average l_p values for the flanged (W2 and W5) and the end-confined (W3, W6, and W7) walls were 34% and 46% of the wall length, respectively (based on the experimental curvatures).

As can be seen from the table and the reported l_p values for all walls, it is difficult to draw general conclusion when numbers are used at face value, without engineering judgement. This is due to the fact that each wall had its own measured yield displacement, where only 1 mm change (about 4% of the displacement at ultimate load) could result in differences of about 25% in the idealized displacement ductility values. Therefore, minimal differences in wall displacements at yield significantly affected the idealized displacement ductility values used to determine l_p of the walls. In addition, and as presented for walls W6 and W7 (which can be considered to be reasonable similar walls), the ratio of calculated displacement ductility values was 1.47 and this resulted in ratios for l_p values of 1.81 and 1.23 calculated using the theoretical and measured curvature ductilities, respectively. These factors led to difficulty in interpretation of the values given in Table 5.1.

To establish a common basis for comparison and provide useful information that can be used by designers for more realistic predictions of ultimate displacement and displacement ductility values, simple and practical idealizations of the walls were conducted. The load-displacement relationship was idealized using simple information that can be determined by designers. This approach also made use of the recommended values for stiffness at first yield of the walls, presented in Table 4.9. It should be noted that all walls were originally designed to resist the same ultimate load. Moreover, the stiffnesses at first yield for the walls in each phase were found to be almost the same. Therefore, a single idealized yield displacement value was determined for all walls tested in each test phase to facilitate comparison between the walls in each phase.

The average measured ultimate lateral loads, Q_u, for the walls in Phases I and II were 160 kN (*c.o.v.* = 9%) and 245 kN (*c.o.v.* = 5%), respectively, and the average yield stiffnesses, k_e, were 12 kN/mm (*c.o.v.* = 4%) and 43 kN/mm (*c.o.v.* = 11%), respectively. Using these values, the calculated idealized yield displacements for walls in Phases I and II were 13.0 mm (= 160/12) and 5.8 mm (= 245/43), respectively.

This approach of using the elastic stiffness and ultimate load can be very convenient in design offices. The measured capacities of the walls shown in Fig. 5.1 were normalized by dividing the capacity at any displacement level by the ultimate wall capacity (ratio of Q to Q_u) to facilitate comparison. The idealized displacement ductility values corresponding to ultimate load, $\mu^I_{\Delta u}$, 1% drift, $\mu^I_{\Delta 1\%}$, and 20% strength degradation, $\mu^I_{\Delta 0.8u}$, were presented in Table 5.2 based on the proposed approach. The theoretical curvature ductility values were also presented along with the corresponding l_p values for each displacement limit in Table 5.2.

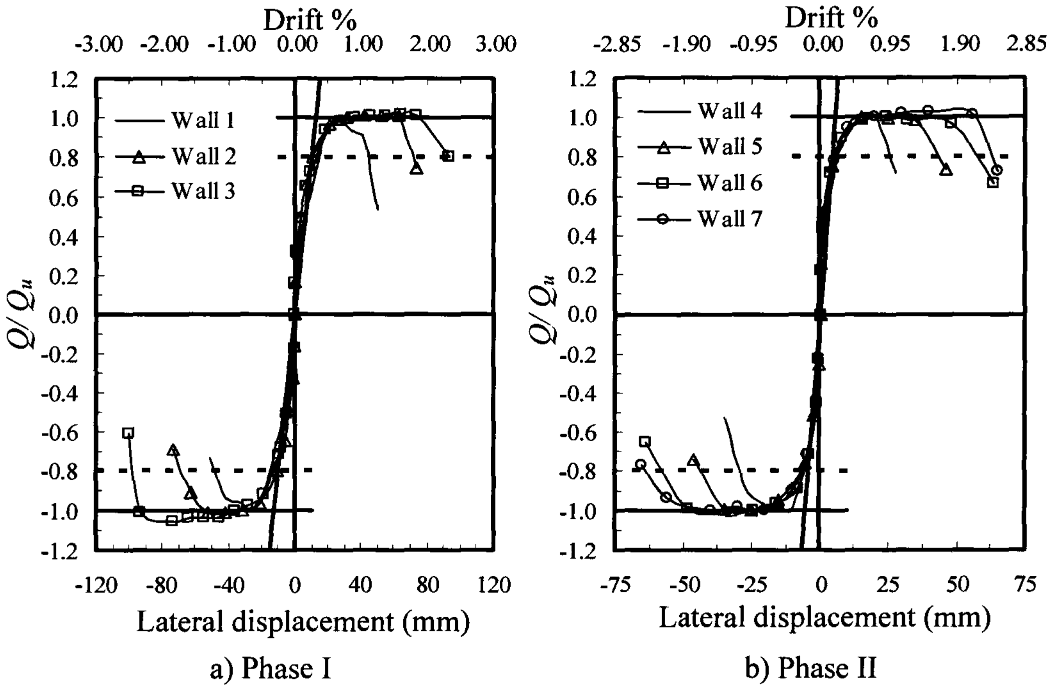

Fig. 5.1: Proposed idealization for the test walls

The l_p values expressed as a percentage of wall length and calculated using theoretical curvature ductility values given in Table 5.1, were plotted against the corresponding displacement ductility in Fig. 5.2. The calculated average l_p values for the test walls corresponding to the idealized displacement ductilities at ultimate load and 20% strength degradation were indicated in Fig. 5.2.

Using the proposed idealization, the l_p values listed in Table 5.2 at ultimate load for the 3-storey rectangular, flanged and end-confined walls were, on average, 41%, 15%, and 20% of the wall length, respectively. The corresponding average l_p values for the 2-storey rectangular, flanged and end-confined walls were 39%, 18%, and 25% of the wall length, respectively. Unlike the values presented in Table 5.1, the calculated l_p values at ultimate load for the 2 and 3-storey walls having the same cross-section were almost the same. This suggests that the l_p values were more related to wall length and less influenced by wall height which is consistent with the observations by Priestley et al. (1996) regarding l_p values of reinforced concrete columns with the same cross section but different heights.

Larger l_p values were found for the displacements at 1% drift and at 20% strength degradation (Table 5.2) compared to those found at ultimate conditions. For design purposes, these values would better predict the displacement of the walls corresponding to different performance levels using the easily predicted theoretical curvature ductility values.

Table 5.2: Equivalent plastic hinge lengths based on the proposed idealization

Walls	W1		W2		W3		W4		W5		W6		W7	
	(+)ve	(-)ve	(+)ve	(-)ve	(+)ve	(-)ve	(+)ve	(-)ve	(+)ve	(-)ve	(+)ve	(-)ve	(+)ve	(-)ve
Δ_y (mm)	13.0	13.0	13.0	13.0	13.0	13.0	5.8	5.8	5.8	5.8	5.8	5.8	5.8	5.8
Δ_u (mm)	25.1	25.3	31.5	31.5	36.0	36.1	14.0	12.5	14.6	25.1	24.1	24.0	20.1	20.0
$\Delta_{0.8u}$ (mm)	45.0	48.0	70.0	68.0	93.0	95.0	27.0	28.0	42.0	45.0	52.0	57.0	62.0	65.0
$\mu_{\varphi, th}$	2.9	2.9	8.1	8.1	7.8	7.8	2.9	2.9	8.1	8.1	7.8	7.8	7.8	7.8
Calculation corresponding to ultimate load														
$\mu^I_{\Delta u}$	1.9	1.9	2.4	2.4	2.8	2.8	2.4	2.2	2.5	4.3	4.2	4.1	3.5	3.4
l_p (mm)	717	734	278	278	363	366	769	611	198	458	450	447	344	340
l_p ($\%l_w$)	40	41	15	15	20	20	43	34	11	25	25	25	19	19
Calculation corresponding to 1% drift														
$\mu^I_{\Delta 1\%}$	3.1	3.1	3.1	3.1	3.1	3.1	4.6	4.6	4.6	4.6	4.6	4.6	4.6	4.6
l_p (mm)	1,935	1,920	414	414	431	431	---*	---*	497	497	519	519	519	519
l_p ($\%l_w$)	108	107	23	23	24	24	---*	---*	28	28	29	29	29	29
Calculation corresponding to 20% strength degradation														
$\mu^I_{\Delta 0.8u}$	3.5	3.7	5.4	5.2	7.2	7.3	4.7	4.8	7.2	7.8	9.0	9.8	10.7	11.2
l_p (mm)	2,500	3,052	937	900	1,479	1,530	---*	---*	955	1,060	1,416	1,680	2,065	2,642
l_p ($\%l_w$)	139	170	52	50	82	85	---*	---*	53	59	79	93	115	147

* l_p could not be established corresponding to 1% drift and 20% strength degradation as a results of using the theoretical curvature ductilities in combination with the experimental displacement ductilities.

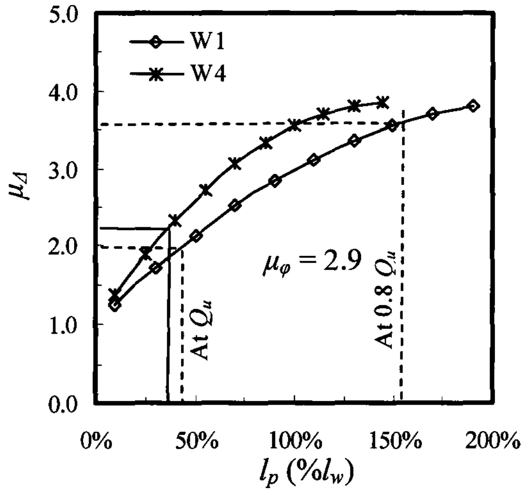

a) Rectangular walls (W1 and W4)

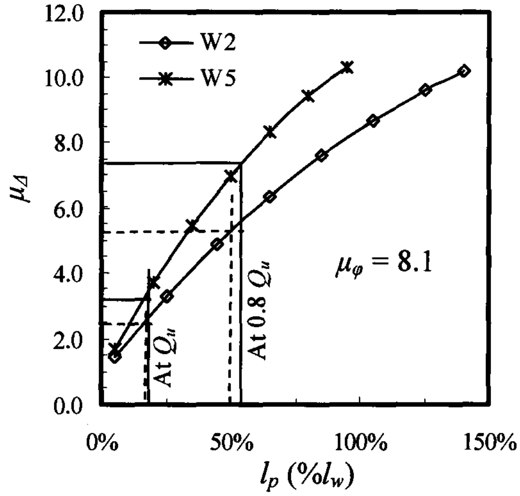

b) Flanged walls (W2 and W5)

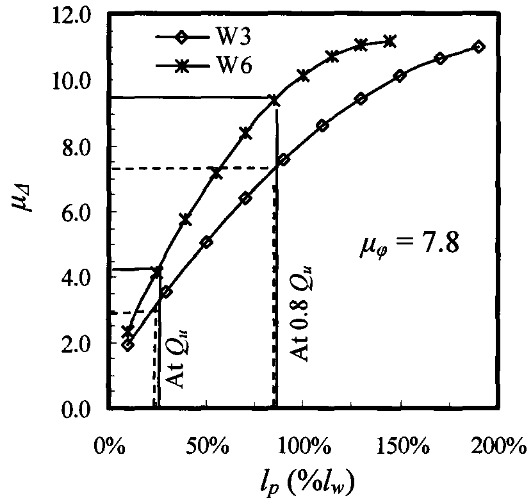

c) End-confined walls (W3 and W6)

Fig. 5.2: Equivalent plastic hinge length at different displacement levels

5.3 Seismic reduction factors based on the Canadian code

To account for the actual material resistance, overdesign, ductility and energy dissipation in actual structures, seismic response modification factors are used in force-based design codes (such as the current American and Canadian codes) to reduce the seismic force from that which would have developed if the structure had remained elastic.

Most force-based design codes use the equal displacement approach to determine the relationship between R_d and the displacement ductility for structural systems (Priestley el al. 2007). To obtain a reasonable indication of system performance, the idealizations discussed in Section A.7 for individual walls were used as the basis for determining the seismic force modification factors. As discussed in Section 4.6 and presented in Fig. 4.6, the actual load displacement relationship of the wall can be idealized by an elastic-plastic relationship having an initial stiffness evaluated as the measured lateral resistance at first yield, Q_y, divided by the corresponding lateral displacement, Δ_y. The ultimate load used in this calculation was set equal to the idealized plastic resistance, Q_{in}, of the wall. In this regard, displacements corresponding to 20% strength degradation are commonly considered as an acceptable ultimate performance level (Priestley el al. 1996; Priestley el al. 2007; ATC-63, 2008).

As discussed earlier in Section 4.6, Q_{in} was found to be about 96% of Q_u. Therefore, for simplicity and convenience in design, Q_{in} was taken equal to Q_u in the following calculations. Also, since use of face values of the test results may lead to misleading or confusing results, a single idealized yield displacement value was adopted for all walls tested in each phase as was discussed in Section 5.2.

From the above discussion, the R_d value (used for ductility) was defined as the ratio between the elastic lateral load, Q_e, corresponding to the lateral displacement, Δ_e, and the idealized wall capacity, Q_u, based on test walls. By similar triangles (refer to Fig. A.7), R_d is equal to $\mu^I_{\Delta 0.8u}$ (presented in the bottom part of Table 5.2). The R_o value (used for overstrength) was defined as the ratio between the wall capacity, Q_u, and the design capacity, Q_d, amplified by 5% assuming conservative overdesign (commonly taken between 5% and 10%).

The design lateral load capacities, Q_d, of the walls were calculated based on the guidelines of the CSA S304.1 (2004). The design lateral load capacities were presented in Table 5.3 and were used to determine the R_o factor. As explained in Section A.7, the design capacities were calculated using material resistance factors for masonry and steel and neglecting the contribution of compression reinforcement in strength calculation following the Canadian standard. The average compressive block strength was 27 MPa [specific strength = 27×(1-1.64×*c.o.v.*% of 0.10 minimum) = 22.5 MPa], however the strength specified by the supplier was 15 MPa. [This value has been typical for cases when the specified block strength was 15 MPa (Chahine 1989).] Therefore, to determine Q_d, the masonry compressive strength, f'_m, was taken equal to 7.5 MPa as listed in CSA S304.1 corresponding to grout filled hollow 15 MPa block.

Table 5.3: Seismic response modification factors

Wall	Design capacity		Experimental results		Force modification factors		
	$Q_d^{(1)}$ (kN)	$Q_d^{(2)}$ (kN)	Q_y (kN)	Q_u (kN)	R_d	$R_o = 1.05\times Q_u/Q_d^{(1)}$	$R_d\times R_o$
W1	61	93	101	177	3.5	3.0	10.7
			110	180	3.7	3.1	11.5
W2	81	97	121	151	5.4	2.0	10.6
			123	154	5.2	2.0	10.4
W3	80	99	110	152	7.2	2.0	14.4
			106	147	7.3	1.9	14.1
W4	91	140	160	265	4.7	3.1	14.4
			162	267	4.8	3.1	14.8
W5	122	146	185	245	7.2	2.1	15.2
			183	239	7.8	2.1	16.0
W6	119	149	173	241	9.0	2.1	19.1
			169	234	9.8	2.1	20.2
W7	119	149	188	240	10.7	2.1	22.7
			170	236	11.2	2.1	23.3

(1) Compression reinforcement not included in design strength calculation
(2) Compression reinforcement included in design strength calculation

Although 400 MPa steel strength was specified, the delivered steel for all walls had about 497 MPa yield strength based on the tensile tests conducted. However, in the calculation of the design strengths, the yield strength of the reinforcing bars was taken equal 447 MPa instead of 400 MPa (as commonly steel yield strength is about 50 MPa higher than specified). The calculated design strengths using the above approach were listed in Table 5.3 and for comparison purposes, design strengths calculated including the contribution of compression reinforcement were also listed. The experimental results for yield and ultimate strengths, along with the ductility related force modification factor, R_d (=$\mu^I_{\Delta 0.8u}$, reproduced from Table 5.2), the calculated overstrength related force modification factor, R_o, and the product of $R_d \times R_o$ were also presented in Table 5.3.

As can be seen, the average values of R_d (corresponding to 20% strength degradation) were 3.6, 5.3, and 7.3 for the 3-storey rectangular, flanged, and end-confined walls, respectively. For the 2-storey rectangular, flanged, and end-confined walls, the average R_d values were 4.8, 7.5, and 10.3, respectively. Although, the R_d values for the rectangular walls were quite high compared to usual perceptions for normal reinforced masonry construction, it is note worthy that the R_d values for the flanged and end-confined walls were much higher. The R_d values for the flanged and end-confined walls were, respectively, at least 1.5 and 2.0 times those corresponding to the rectangular walls. Such increases in the R_d values significantly reduce the seismic demand on masonry buildings. This means that the competitiveness of RM construction can be significantly improved as the design loads are inversely proportional to R_d. Additionally, even at the same capacity, the required amount of vertical reinforcement in the flanged and the end-confined walls was only 58% of the amount used in the rectangular walls. Thus, there are additional savings in steel material and placement costs resulting from adopting the proposed wall configurations.

Average values of R_o calculated for the test walls were 2.34 (*c.o.v.*= 21%) based on the design capacities calculated following the Canadian code. When compression reinforcement was included in strength calculation, average values of R_o were 1.76 (*c.o.v.*= 9%).

The average overall response modification factors, $R_d \times R_o$, calculated for the walls were 11.1, 10.5, and 14.2 for the 3-storey rectangular, flanged, and end-confined walls, respectively, and 14.6, 15.6, and 21.3 for the 2-storey rectangular, flanged, and end-confined walls, respectively, based on evaluating the wall design capacity in accordance with CSA S304.1 (2004). When compression reinforcement were included in the design strengths, the average overall response modification factors, $R_d \times R_o$, were 7.3, 8.8, and 11.5 for the 3-storey rectangular, flanged, and end-confined walls, respectively, and 9.5, 13.1, and 17.0 for the 2-storey rectangular, flanged, and end-confined walls, respectively.

The average overall response modification factors for the flanged and end-confined walls (when compression reinforcement was included in the design strengths) were 30% and 72% higher than those for the rectangular walls. Provided that the corresponding displacements are acceptable, this means that the flanged and the end-confined walls could be designed for 77% (1/1.30) and 58% (1/1.72) of the load that the rectangular wall would be designed for.

5.4 Qualification of the proposed wall categories to higher R_d values using the concrete code provisions

The Canadian concrete design code [CSA A23.3 (2005)] specifies ductile walls as walls with a ductility-related force modification factor, R_d, equal to at least 3.5. Several requirements must be satisfied to be able to use such values, including limitations on aspect ratio and dimension of the walls, as well as on the ratios, detailing and distributions of reinforcement. These requirements are stipulated to prevent possible wall instability in potential plastic hinge zones, congestion and buckling of the reinforcement, premature yielding of the bars, and, in general, to ensure adequate wall rotational capabilities within the plastic hinge zone. Specifically, the inelastic rotational capacity of the wall, θ_{ic}, should be greater than the inelastic rotational demand of the wall, θ_{id}. In addition, θ_{ic} and θ_{id} should meet the requirement that:

$$\theta_{ic} > \theta_{id} \qquad \text{Eq. 5.1}$$

$$\theta_{id} = \frac{\left(\Delta_F R_o R_d - \Delta_F \gamma_w\right)}{\left(h_w - l_w / 2\right)} \geq 0.004 \qquad \text{Eq. 5.2}$$

$$\theta_{ic} = \left(\frac{\varepsilon_{cu} l_w}{2c} - 0.002\right) \leq 0.025 \qquad \text{Eq. 5.3}$$

where:

$\Delta_F R_o R_d$ = Design displacement ($R_d R_o$= 3.5×1.6), CSA A23.3 (2005);

γ_w = Wall overstrength factor equal to the ratio of the load corresponding to nominal moment resistance of the wall to the factored load on the wall;

Δ_F = Deflection of the top of the wall due to factored loads;

$\Delta_F \gamma_w$ = Elastic portion of the displacement (γ_w = 1.6), CSA A23.3 (2005);

ε_{cu} = Ultimate concrete compressive strain; and

c = Depth of the compression zone.

Given that the stress-strain relationship of grouted masonry is similar to that of concrete (Drysdale and Hamid 2008), the above equations can be used directly after replacing the ultimate concrete compressive strain (0.0035) with the ultimate masonry compressive strain (0.003) as specified in the CSA S304.1 (2004).

The flanged and end-confined walls satisfy most of the dimension and reinforcing requirements specified in CSA A23.3 (Cl.21.6). However, CSA A23.3 (2005) stipulates that the wall should be detailed for plastic hinges over a height equal at least 1.5 times the wall length to prevent shear failure resulting from diagonal cracks that can extend over a height approximately equal to the wall length and to prevent premature yielding of the vertical bars. Although this latter requirement was not satisfied in the tested flanged and end-confined walls, shear failure and premature steel yielding were not observed. In addition, the flanged walls did not satisfy one of the dimension limitations in CSA A23.3 (2005) to prevent instability of the wall in the potential plastic hinge zone. Again, neither instability nor out-of-plane buckling at the ends of the walls were observed until significant strength degradation occurred well beyond the 20% strength degradation limit. CSA A23.3 also stipulates the need for at least 4 bars at the ends of the wall to allow for effective tying of the vertical bars in the potential plastic hinge zone to prevent buckling of the bars. Although this requirement was not satisfied in the flanged walls, buckling of the bars was not observed until significant strength degradation and damage of the flange had occurred. Therefore, based on the observed failure modes and the high levels of ductility of the flanged and end-confined walls, it appears that not meeting all of the requirements stipulated in CSA A23.3 (2005) did not affect the wall behaviour.

Inelastic rotational demand and capacity were calculated to investigate the possibility of qualifying the test walls for the R_d value of 3.5 specified in the concrete code. The calculated inelastic rotational demands and capacities for the flanged and end-confined walls were presented in Table 5.4 along with the values for the neutral axis depth, c. These were calculated using the actual material strengths for masonry and steel, material resistance factors, and included the effect of compression reinforcement in strength calculation.

CSA A23.3 (2005) defines walls with aspect ratio less than 2.0 as being squat walls and limits the maximum R_d value to 2.0 on the basis that such walls are more likely to develop an inelastic shear failure mechanism. However, since shear failures were not observed and ductile flexural responses dominated wall behaviour, the other requirements to qualify for the R_d value assigned for ductile reinforced concrete walls were applied for all the test walls (aspect ratios of 2.2 and 1.5) as shear failures was not observed and ductile flexural response dominated wall behaviour. The inelastic rotational capacities, $\theta_{ic,}$, of the flanged and end-confined walls were greater than or equal to 0.0067, as shown in Table 5.4, which is greater than the minimum specified inelastic rotational demand, θ_{id}, of 0.004 specified in CSA A23.3 (2005). This indicates that the test walls were capable of providing high ductility, which qualifies them for at least the specified $R_d = 3.5$ value.

Table 5.4: CSA A23.3 (2005) ductility requirement applied to the test walls

	W2	W3	W5	W6	W7
c (mm)	312	289	312	289	289
θ_{ic} (rad)	0.0067	0.0073	0.0067	0.0073	0.0073
Q (kN)	130	129	194	192	192
Δ_F (mm)	4.9	5.0	2.7	2.7	2.7
$\Delta_F R_d R_o$ (mm)	27.6	27.9	14.9	14.9	14.9
$\Delta_F \gamma_w$ (mm)	7.9	8.0	4.2	4.3	4.3
θ_{id} (rad)	0.0064	0.0064	0.0060	0.0061	0.0061
Δ_y (mm)	10.5	9.2	5.0	4.0	5.0
Δ_u (mm)	31.0	36.0	20.0	24.0	20.0

In order to determine θ_{id}, the elastic displacement must be determined in accordance with CSA A23.3 (2005). The displacements due to factored loads, Δ_f, were computed using Eq. 5.4 by adopting the approximations of the effective wall stiffness and shear areas also given in CSA A23.3 (2005).

$$\Delta_F = Q\left(\frac{h_w^3}{3\,E_m\,I_e} + k\,\frac{h_w}{G_m\,A_e}\right) \qquad \text{Eq. 5.4}$$

where: E_m $= 850 f'_m$;

G_m $= 0.4\,E_m$;

k = Shear shape factor (taken equal to 1.2 for all walls);

I_e $= (0.6 + \sigma/f'_m)\,I_g$;

A_e $= (0.6 + \sigma/f'_m)\,A_g$;

σ = Axial compressive stress on the wall;

Q = Design lateral wall capacity (calculated based on actual material strengths and material resistance factors for masonry and steel).

The inelastic rotational demands, θ_{id}, on the walls were then calculated based on the calculated elastic and design displacements where it can be seen from the table that they were lower than the inelastic rotational capacities, θ_{ic}, of the walls. This indicates that the flanged and end-confined concrete-block shear walls developed high ductility capacities similar to those of ductile reinforced concrete shear walls specified in the A23.3 (2005), even though the test walls did not satisfy some of the restrictions related to geometry and reinforcing. As presented in Table 5.4, the calculated elastic displacements, $\Delta_F\ \gamma_w$, were, on average, 12% (*c.o.v.* =13%) less than the experimental displacements at first yield, Δ_y, and the design displacements, $\Delta_F\ R_dR_o$, were, on average, 25% (*c.o.v.*=13%) less than the experimental displacements at ultimate load, Δ_u. Based on this discussion, higher seismic force modification factors than for ductile walls in CSA A23.3 (2005) can be justified for the flanged and end-confined masonry walls similar to the tested walls.

5.5 Seismic reduction factors based on the American code

The overall seismic force-reduction factor, R, and the deflection amplification factor, C_d, discussed in this chapter were based on the American code approach, as presented by Uang (1991) and ATC-63 (2008). In ASCE 7 (2008), the R factor is the ratio of the force level that would be developed in a linear elastic system for design earthquake ground motion versus the design base shear and the C_d factor is used to estimate the maximum inelastic displacement by amplifying the elastic displacement, Δ_d, induced by the design seismic forces, as shown in Fig. 5.3.

The R value, as shown in Fig. 5.3, was taken as the ratio of the lateral force, Q_e, that would have developed in the seismic force-resisting system if the system remained entirely elastic under the *design* earthquake ground motions versus the design lateral force or base shear, Q_d, assuming inelastic system behaviour. The design lateral force, Q_d, is taken equal to 0.6 Q_u as suggested by ATC-63 (2008) to ensure that the system is essentially linear elastic at that stage. This assumption is also consistent with the definition proposed by Uang (1991) indicating that Q_d is the level beyond which the behaviour of the system deviates significantly from the elastic response. The ratio between the ultimate load, Q_u, and the design load Q_d, in the American code is defined by the factor Ω as shown in the figure.

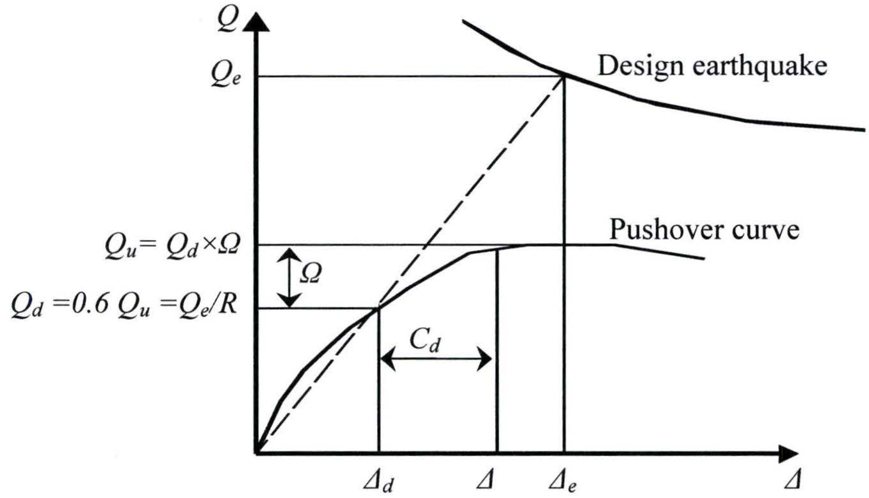

Fig. 5.3: Definition of force reduction, deflection amplification, and overstrength factors (ATC-63, 2008)

ATC-63 (2008) also defines an overall seismic force-reduction factor of 1.5 R when the *maximum considered* earthquake, expected to result in small probability of collapse, is used instead of the design earthquake. This 1.5 factor accounts for the ASCE-7 (2008) definition of design earthquake motions as being two-thirds of the maximum considered earthquake ground motion. To determine the displacement Δ attained by the inelastic system when subjected to ground motion, ASCE-7 (2008) requires that a dynamic analysis be performed for the seismic force resisting system.

5.5.1 Analytical model

In this study, the nonlinear analysis program IDARC-5 (2002) was selected to evaluate the performance of the test walls. The test results were modeled using a trilinear idealization of the experimentally-determined moment-curvature relationships at the base of the walls as required for IDARC-5 input. This user-input trilinear relationship was selected, as opposed to the bilinear relationship commonly used for beams and lightly stressed members, as it better represented the experimental moment-curvature relationship for the test walls subjected to axial loads. The properties of the segments required to define the trilinear (M-φ) relationship in IDARC-5 were shown in Fig. 5.4. In the figure, M is the bending moment at the base of the wall and φ is the corresponding curvature. The subscripts (1 to 3) associated with M and φ values represent the end of each stage of the trilinear relationship used in modeling. The ratio of M_1 and φ_1 is EI_1, where, E is the modulus of elasticity of masonry, and I_1 is the transformed moment of inertia of the gross wall cross section. The ultimate curvature, φ_{max}, is the curvature value existing just prior to any significant loss in strength and was taken from the experimental M-φ relationships.

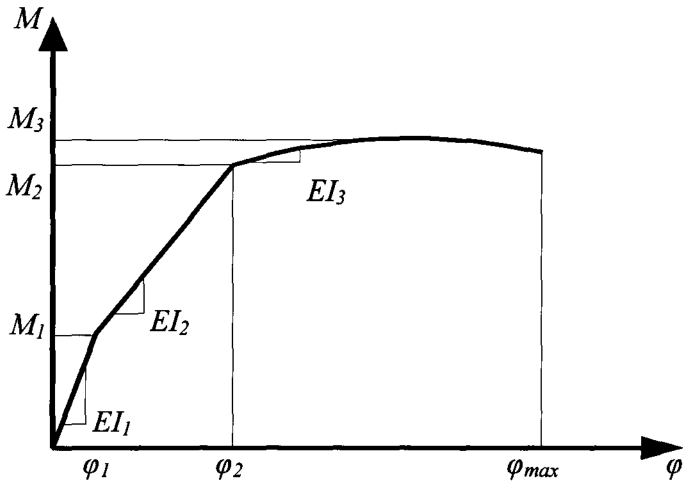

Fig. 5.4: Trilinear envelope used for modelling wall elements in IDARC-5

The values used to define the wall properties were listed in Table 5.5. For ease of reference, the selected values for M_1 (initiation of significant cracking) and M_2 (start of the post-yield stage for the wall) were given as percentages of M_3 (the ultimate moment capacity of the wall cross section). The EI_2 and EI_3 values were reported as percentages of EI_1 (based on gross transformed cross section properties of the walls).

Table 5.5: Wall properties used in the analytical model

Wall	EI_1 (N.mm^2)	M_1 (% M_3)	M_2 (% M_3)	M_3 (kN.m)	EI_2 (%EI_1)	EI_3 (%EI_1)	φ_{max} (rad/mm)
W1	5.64E+11	33.5%	88.1%	700	18.3%	4.0	1.72E-05
W2	5.89E+11	31.2%	77.4%	608	24.0%	4.5	2.35E-05
W3	5.87E+11	46.5%	87.3%	600	12.4%	2.0	4.70E-05
W4	5.64E+11	33.2%	80.0%	705	18.3%	3.0	2.29E-05
W5	5.89E+11	29.6%	73.5%	644	24.0%	3.4	3.53E-05
W6	5.87E+11	44.1%	83.3%	630	12.4%	2.0	4.70E-05

To simulate the nonlinear behaviours of the walls, nonlinear pushover analyses were conducted. In IDARC-5, user-input hysteresis parameters related to ductility, *HBD*, and to strength degradation, *HBE*, were calibrated for each type of wall to replicate the nonlinear portion of the load-displacement relationships beyond ultimate load. The calibration of these factors was based on reaching an ultimate capacity and a displacement at 20% strength degradation less than 5% different than the corresponding experimental values for each wall. The hysteresis parameters used in the analytical model were listed in Table 5.6, and the experimental envelope of the load-displacement relationships for all walls and the corresponding pushover curves were presented in Fig. 5.5. Almost no differences in the experimental load-displacement relationships were observed between walls W6 and W7, therefore, only wall W6 was discussed in this chapter.

Table 5.6: Hysteresis parameters used in the analytical model

Wall	HBE	HBD	HC	HS
W1 and W4[(1)]	0.01	0.30	0.8	0.6
W2 and W5[(2)]	0.01	0.40	1.0	0.6
W3 and W6[(3)]	0.01	0.42	1.0	0.6

[(1)] Rectangular walls [(2)] Flanged walls [(3)] End-confined walls

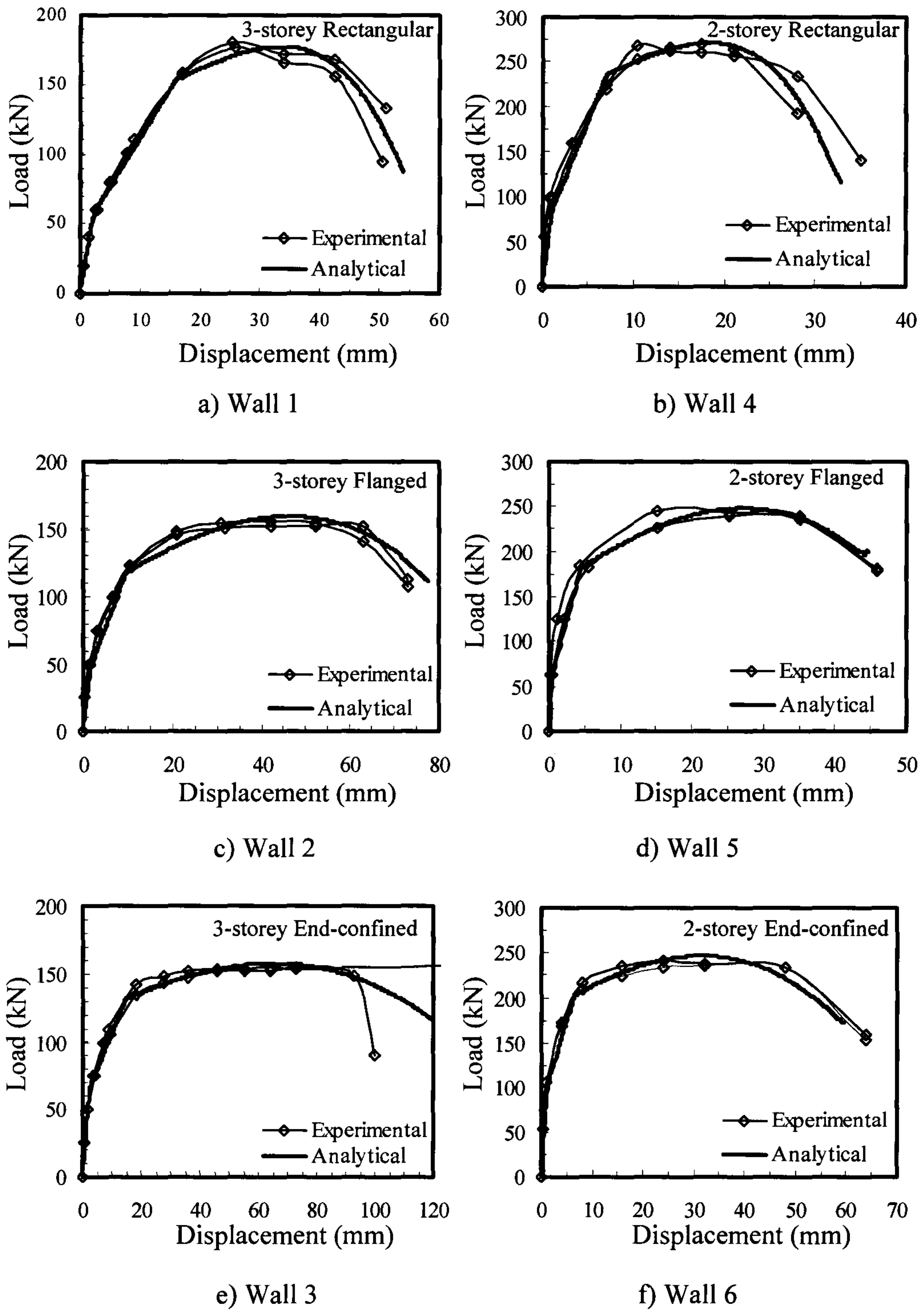

Fig. 5.5: Experimental and analytical load-displacement relationships

Quasi-static analyses were then conducted for all walls to calibrate the user-input slip parameter, *HS*, and the stiffness degradation parameter, *HC*, to capture pinching of the hysteresis loops and to define the slope of the loading and the unloading branches. The calibration of the parameters *HC* and *HS* was initially based on the hysteresis loop at ultimate load. This was followed by refinement of these values to generate, as much as possible, the same hysteresis loops as the experimental results for the regions between $2\times\Delta_y$ and at least $5\times\Delta_y$ for walls in Phase I and to at least $7\times\Delta_y$ for walls in Phase II. As illustrated in Fig. 5.6 for Wall 2, these ranges covered almost the entire portion of the load-displacement curve prior to any loss of wall strength.

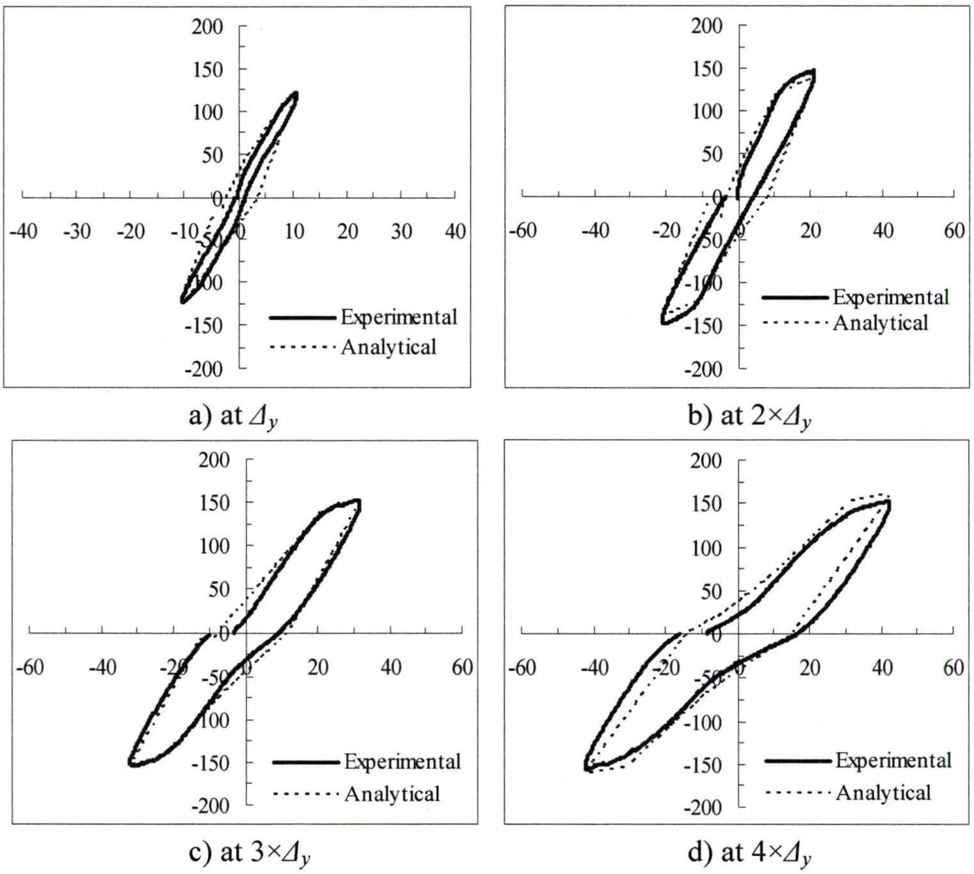

Fig. 5.6: Sample experimental and analytical hysteresis loops (Wall 2)

The experimental hysteresis loops for all walls and the corresponding loops from the quasi-static analysis were reproduced in Fig. 5.7. The unloading stiffness was not accurately represented at very low and at very high displacement levels which was attributed to the simplified definition of the stiffness degradation parameter, *HC,* in the software. For all walls, once strength degradation began, the slope of the unloading stiffness significantly deviated from the trend followed in previous cycles. However, this was expected to have minor effects as the pushover curves were matched only up to 20% strength degradation as the limit of interest in hysteresis behaviour. HBE and HBD parameters were explained earlier in this section.

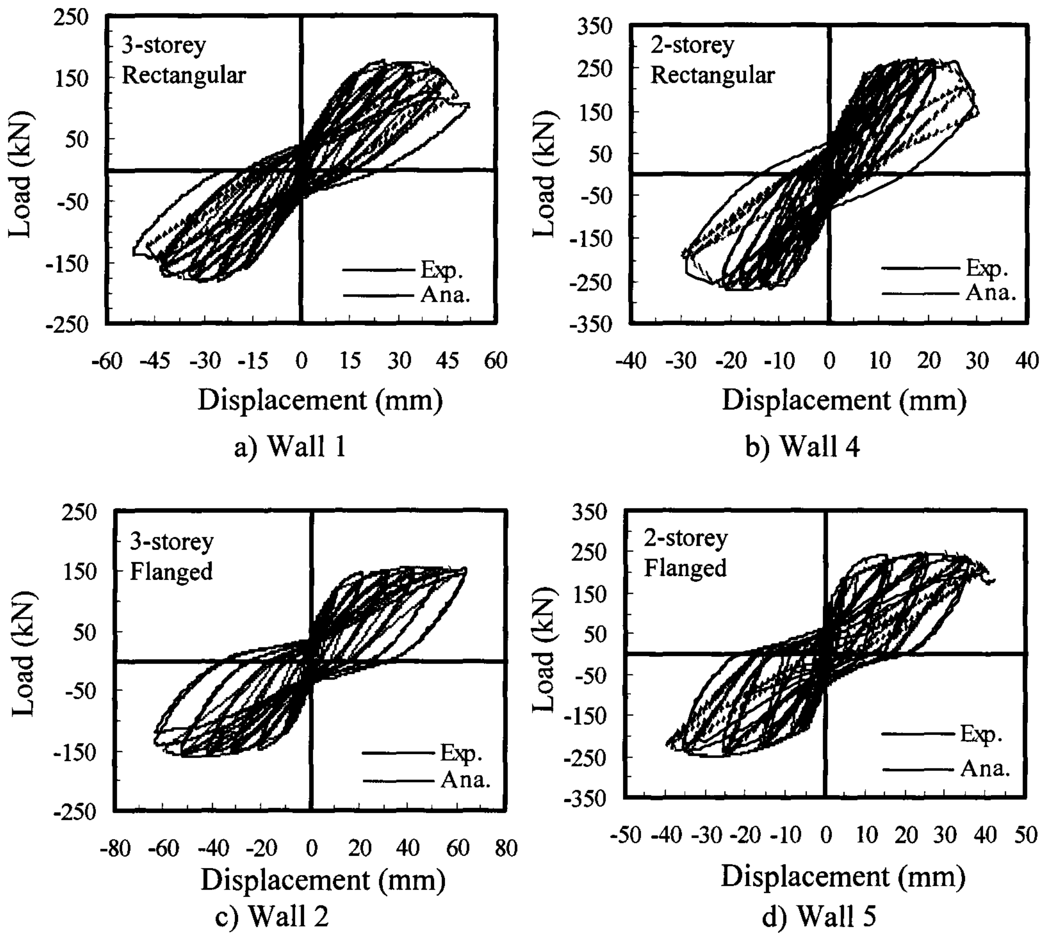

Fig. 5.7: Experimental and analytical hysteresis loop

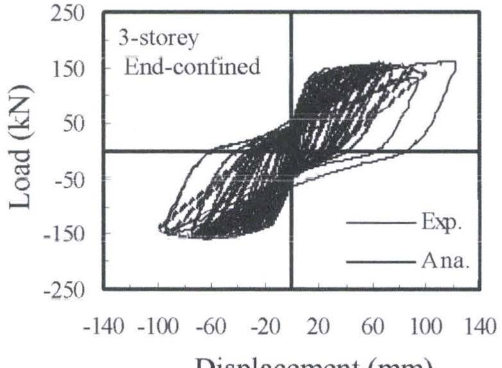

e) Wall 3

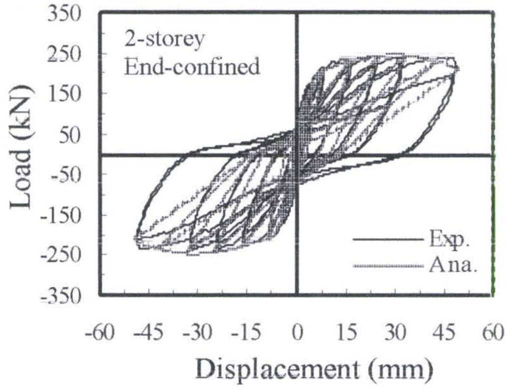

f) Wall 6

Fig. 5.7: (cont.)

5.5.2 Ground motion selection

A series of earthquakes with low, medium, and high frequencies (based on different acceleration versus velocity ratios, a/v) was selected for the nonlinear dynamic analyses. The properties of the selected ground motions were summarized in Table 5.7 with the response spectrum for the selected ground motions presented in Fig. 5.8.

Table 5.7: Properties of ground motions (adopted from PEER 2006)

Record	Earthquake	Site	Date	PGA[(1)] (g)	PGV[(2)] (*m/sec*)	PGA/PGV g/(*m/sec*)
1	Loma Prieta	Apeel Crystal-Spr Res	Oct- 18, 1989	0.104	0.18	0.57
2	Imperial Valley	El-Centro	Oct- 15, 1979	0.143	0.17	0.81
3	Northridge	Playa Del Rey	Jan- 17, 1994	0.136	0.19	0.73
4	San Fernando	La Hollywood Stor Lot	Feb- 09, 1994	0.174	0.15	1.17
5	Kern County	TAFT Lincoln School	Jul- 21, 1952	0.178	0.18	1.02
6	Imperial Valley	El-Centro	May- 19, 1940	0.313	0.30	1.05
7	Lytle Creek	Wrightwood	Sept- 12, 1970	0.200	0.11	1.90
8	Parkfield	Cholame	Jun- 28, 1966	0.442	0.25	1.79
9	San Francisco	Golden Gate	March-22, 1944	0.112	0.05	2.43
10	Imperial Valley	Bonds Corner	Oct- 15, 1979	0.775	0.46	1.69

[(1)] Peak ground acceleration [(2)] Peak ground velocity

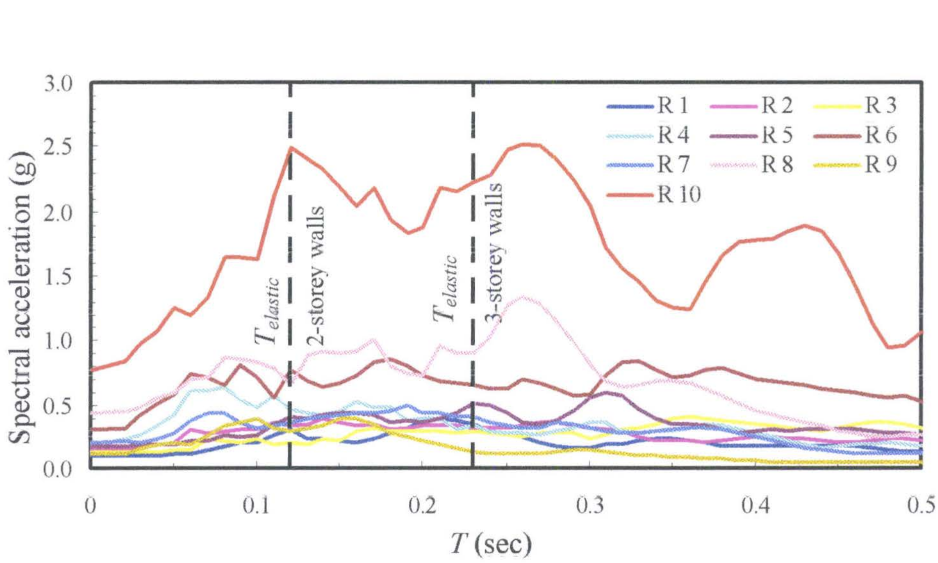

Fig. 5.8: Scaled response spectrum of the selected ground motions

The time scales for the ground motions were scaled by a factor of ($1/\sqrt{2}$) to account for the use of half scale construction in the experimental program. The time step, *dt*, selected for dynamic analysis was taken equal to one tenth of the input wave time interval, Δt, for each record (i.e., $dt = \Delta t/10$). A sensitivity analysis was conducted on the selection of the time step and one half, *dt* /2, and one fifth, *dt* /5, of the selected time step were also used in analyses to confirm the results.

5.5.3 R and C_d factors for the test walls

Each wall was subjected to the selected earthquake records with incrementally increases (scaling) of the PGA until the failure criterion was met and the maximum inelastic displacement, $\Delta_{0.8u}$, was reached. The failure criterion in this study was considered to have occurred when a wall reached the top displacement corresponding to 20% strength degradation. The damage of the wall at this performance level had minimal impact on the lateral behaviour as demonstrated by the bilinear idealization of the nonlinear load-displacement relationships at 20% degradation as discussed in Section 4.6. This implies that the amount of damage at this deformation level is not considered to be even close to that which would be acceptable under the effects of the maximum considered earthquake [expected to result in a small probability of collapse as specified in the ATC-63 (2008)]. Therefore, the definition of the seismic reduction factors corresponding to the design earthquake was used for the test walls.

All of the test walls were subjected to a constant axial load, P, of 160 kN applied at the top of the all. This load was considered to represent the mass in the dynamic analysis. Although distribution of the top mass to the floor levels of the 3-storey and the 2-storey walls would have been more representative for dynamic analysis, this would have resulted in lower axial stresses over the upper storeys which was not the case for the test walls. Lower axial stresses over the upper storeys would have involved using different M-φ relationship for each storey and resulted in increased wall displacements and, therefore, changes in the load-displacement characteristics of the walls. Since such data was not available as a result of the top loading only test setup, a single mass was placed at the top of the wall and the wall was analysed as a single-degree-of-freedom system.

For every scaled record that resulted in wall failure, an elastic system with the same period as the wall's elastic period was subjected to the same scaled record to determine the resulting elastic load, Q_e. Then, calculations were conducted of $R = Q_e/Q_d$ and $C_d = \Delta_{0.8u} / \Delta_d$, respectively, to determine the response modification factor and the deflection amplification factor (refer to Fig. 5.3) corresponding to each record.

The wall design capacity Q_d [= 0.6 Q_u, as stipulated in ATC 63 (2008)] and the corresponding displacement Δ_d [$=Q_d / k_e$] were presented in Table 5.8, along with the average yield stiffnesses, k_e [refer to Section 5.2], and the corresponding elastic periods T_d [= $2\pi\sqrt{m / k_e}$, where m is the ratio of the axial load on the walls (160 kN), P, and the gravitational acceleration, g]. The ultimate wall capacities and top wall displacements at 20% degradations were also presented in Table 5.8 along with the corresponding C_d values.

Table 5.8: Properties of the test walls used for dynamic analysis

Wall	Q_d (kN)	Δ_d (mm)	k_e (kN/mm)	T_d (sec)	Q_u* (kN)	$\Delta_{0.8u}$** (mm)	$C_d = \Delta_{0.8u}/\Delta_d$
W1	107	8.9	12	0.23	179	45	5.1
W2	91	7.6	12	0.23	152	68	8.9
W3	89	7.5	12	0.23	149	93	12.4
W4	160	3.7	43	0.12	267	27	7.3
W5	145	3.4	43	0.12	242	42	12.4
W6	144	3.3	43	0.12	237	52	15.8

* Average values from both directions of loading (refer to Table 5.3)

** Lower values for both directions of loading (refer to Table 5.2)

The calculated C_d value (5.1) for the 3-storey rectangular wall (W1) was higher than that of the *special reinforced masonry* shear walls (3.5) but was consistent with that for *special reinforced concrete* shear walls (5.0) designated in ASCE-7 (2008). The C_d values for the flanged and end-confined walls were at least 70% and 110% higher than those of the rectangular walls, having similar elastic stiffness and almost the same ultimate capacity. Higher values were calculated for the 2-storey walls. Better predictions of the actual wall displacement can be achieved using more representative C_d values which govern not only the design of structural elements in buildings but also non-structural components.

The results of the dynamic analyses were presented in Tables 5.9 to 5.14 for walls W1 to W6, respectively. For each record, the peak ground acceleration corresponding to the actual record, *PGA*, was listed along with the maximum peak ground acceleration of the amplified record, PGA_{max}, needed to reach the failure criterion for the walls. The elastic load, Q_e, and the calculated R values were also presented for all walls corresponding to each earthquake record. The modified Thompson technique (Wheeler and Ganji 1996), used for rejecting questionable data points, was used to determine the average values of R. In the tables, 2 columns of R values were presented; the first includes all of the data points whereas the second column showed only the data point(s) used to calculate the average values.

Table 5.9: Results of dynamic analysis of Wall 1 (3-storey rectangular)

Record	*PGA* (g)	PGA_{max} (g)	Q_e (kN)	$R = Q_e/Q_y$	
1	0.104	1.33	711	6.6	*NI*
2	0.143	1.29	468	4.4	4.4
3	0.136	1.03	347	3.3	*NI*
4	0.174	1.55	477	4.4	4.4
5	0.178	1.15	522	4.9	4.9
6	0.313	1.19	403	3.8	*NI*
7	0.200	1.68	546	5.1	5.1
8	0.442	1.40	460	4.3	4.3
9	0.112	2.90	554	5.2	5.2
10	0.775	1.13	520	4.8	4.8
			Average	4.7	**4.7**
			c.o.v. %	19	7

NI = Not included

Table 5.10: Results of dynamic analysis of Wall 2 (3-storey flanged)

Record	*PGA* (g)	PGA_{max} (g)	Q_e (kN)	$R = Q_e/Q_y$	
1	0.104	1.37	733	8.0	8.0
2	0.143	1.44	522	5.7	5.7
3	0.136	1.03	347	3.8	3.8
4	0.174	1.82	560	6.1	6.1
5	0.178	1.32	600	6.6	6.6
6	0.313	1.29	437	4.8	4.8
7	0.200	2.12	689	7.6	7.6
8	0.442	2.54	834	9.1	9.1
9	0.112	4.79	914	10.0	*NI*
10	0.775	1.19	548	6.0	6.0
			Average	6.8	**6.4**
			c.o.v. %	29	17

NI = Not included

Table 5.11: Results of dynamic analysis of Wall 3 (3-storey end-confined)

Record	*PGA* (g)	PGA_{max} (g)	Q_e (kN)	$R = Q_e/Q_y$	
1	0.104	1.54	823	9.2	9.2
2	0.143	1.80	652	7.3	7.3
3	0.136	1.20	405	4.5	4.5
4	0.174	2.50	770	8.6	8.6
5	0.178	1.75	795	8.9	8.9
6	0.313	1.75	593	6.6	6.6
7	0.200	3.65	1187	13.3	13.3
8	0.442	4.59	1508	16.9	*NI*
9	0.112	5.59	1067	11.9	11.9
10	0.775	1.85	852	9.5	9.5
			Average	9.7	**8.9**
			c.o.v. %	37	19

NI = Not included

Table 5.12: Results of dynamic analysis of Wall 4 (2-storey rectangular)

Record	*PGA* (g)	PGA_{max} (g)	Q_e (kN)	$R = Q_e/Q_y$	
1	0.104	1.65	773	4.8	4.8
2	0.143	1.99	742	4.6	4.6
3	0.136	1.91	462	2.9	2.9
4	0.174	1.51	642	4.0	4.0
5	0.178	1.63	591	3.7	3.7
6	0.313	1.94	758	4.7	4.7
7	0.200	1.93	565	3.5	3.5
8	0.442	2.00	471	2.9	2.9
9	0.112	2.35	995	6.2	*NI*
10	0.775	1.45	745	4.6	4.6
			Average	4.2	**4.0**
			c.o.v. %	24	19

NI = Not included

Table 5.13: Results of dynamic analysis of Wall 5 (2-storey flanged)

Record	PGA (g)	PGA_{max} (g)	Q_e (kN)	$R = Q_e/Q_y$	
1	0.104	1.52	544	4.9	4.9
2	0.143	1.76	692	4.5	4.5
3	0.136	1.61	372	2.7	*NI*
4	0.174	1.85	742	5.4	5.4
5	0.178	1.69	590	4.2	4.2
6	0.313	1.83	642	4.9	4.9
7	0.200	1.96	614	4.0	4.0
8	0.442	2.10	671	3.4	3.4
9	0.112	3.10	1443	9.0	*NI*
10	0.775	1.49	737	5.3	5.3
			Average	4.8	**4.6**
			c.o.v. %	35	15

NI = Not included

Table 5.14: Results of dynamic analysis of Wall 6 (2-storey end-confined)

Record	PGA (g)	PGA_{max} (g)	Q_e (kN)	$R = Q_e/Q_y$	
1	0.104	1.85	866	6.0	6.0
2	0.143	2.01	749	5.2	5.2
3	0.136	1.80	436	3.0	*NI*
4	0.174	2.35	999	6.9	6.9
5	0.178	1.85	671	4.7	4.7
6	0.313	1.98	774	5.4	5.4
7	0.200	2.27	665	4.6	4.6
8	0.442	2.34	551	3.8	3.8
9	0.112	3.32	1,406	9.8	*NI*
10	0.775	1.70	873	6.1	6.1
			Average	5.5	**5.3**
			c.o.v. %	33	17

NI = Not included

The average calculated R value for the 3-storey rectangular wall (W1), having an elastic period of 0.23 sec, was 4.7 which was close to the R = 5.0 in ASCE-7

(2008) specified for *special reinforced masonry* shear wall designation. The average R values for the 3-storey flanged and end-confined walls were, respectively, 36% and 90% higher than that of the 3-storey rectangular wall, having similar elastic stiffness and almost the same ultimate capacity. For the 2-storey walls, the R values were lower than those of the 3-storey walls, and, for the rectangular wall, the 4.0 value was lower than the 5.0 values specified in ASCE 7 (2008). The differences between the results for the 3 and 2-storey walls may be attributed to the lower elastic period (and higher elastic stiffness) of the 2-storey walls.

5.6 Period variation under cyclic loading

When a force-based seismic design approach is used, structural response is mainly characterized in terms of the elastic stiffness corresponding to first yielding. Then the seismic force is modified using appropriate seismic force modification factors. Although this approach attempts to keep the seismic risk for a given structure below an acceptable limit, it does not result in uniform risk (Priestley el al. 2007). An alternative approach is to adopt a displacement-based seismic design approach which characterizes the structural response by a secant stiffness, K_i, at any displacement level and uses a specific equivalent damping value corresponding to the energy absorbed during inelastic response (Priestley 2000). The secant stiffness, K_i, at a particular displacement is defined as the ratio between the corresponding lateral wall resistance and that displacement. For a given level of ductility demand, the effective period of the structure, T_i, at this displacement level can be determined from a set of design displacement spectra. Using an equivalent single-degree-of-freedom (SDOF) oscillator to represent the structure, the stiffness, K_i, required to calculate the design force, can be calculated as follows:

$$T_i = 2\pi\sqrt{\frac{m}{K_i}} \qquad \text{Eq. 5.5}$$

where: m = the equivalent mass of the SDOF system.

The normalized period ratio, T_{norm}, defined as the ratio between the periods at a specific drift level and the initial period is given by:

$$T_{norm} = \frac{T_i}{T_{initial}} \qquad \text{Eq. 5.6}$$

where: $T_{initial}$ = the period corresponding to the initial stiffness.

The mass of the structure and, subsequently, the mass of the equivalent SDOF system remains unaffected by damage. On the other hand, damage results in reduced stiffness and, thus, the normalized period will be proportional to the square root of the ratio between the initial stiffness and the secant stiffness at a specific drift level. Substituting Eq. 5.5 in Eq. 5.6, T_{norm}, can be calculated for a certain drift level, by:

$$T_{norm} = \sqrt{\frac{K_{Gross}}{K_i}} \qquad \text{Eq. 5.7}$$

where: K_{Gross} = the wall stiffness calculated using gross transformed section properties.

To assess the wall's stiffness variation with loading, the normalized stiffness (K_i / K_{Gross}) defined as the ratio between the secant stiffness at any displacement level and the gross stiffness was plotted against the drift levels in Fig. 5.9 and against multiples of yield displacement in Fig. 5.10 for all the walls.

As discussed in Section 5.1, in a masonry construction, it not uncommon to have many equally-spaced identical walls as the predominant structure. Therefore, neglecting possible coupling between walls, it can be expected that the response of individual walls can, to a great extent, represent the response of the building in terms of the overall load-displacement relationship where the load is appropriately scaled-down. This also means that the dynamic characteristics of the building would be similar to those of the wall as the ratio of the mass to wall stiffness remains constant. The observed significant reduction in individual wall stiffness with increased loading is expected to result in a similar building behaviour resulting in an overall increase of the building period.

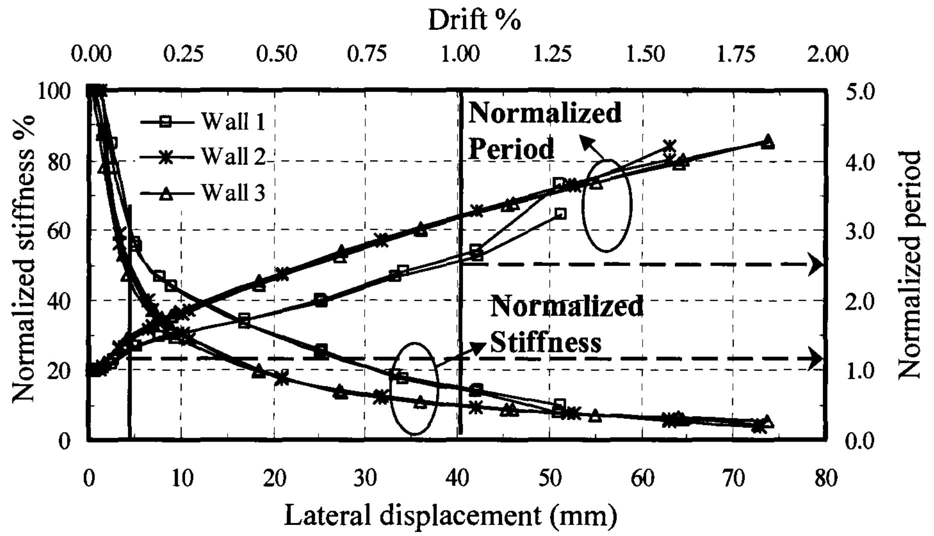

a) Phase I, 3-storey walls

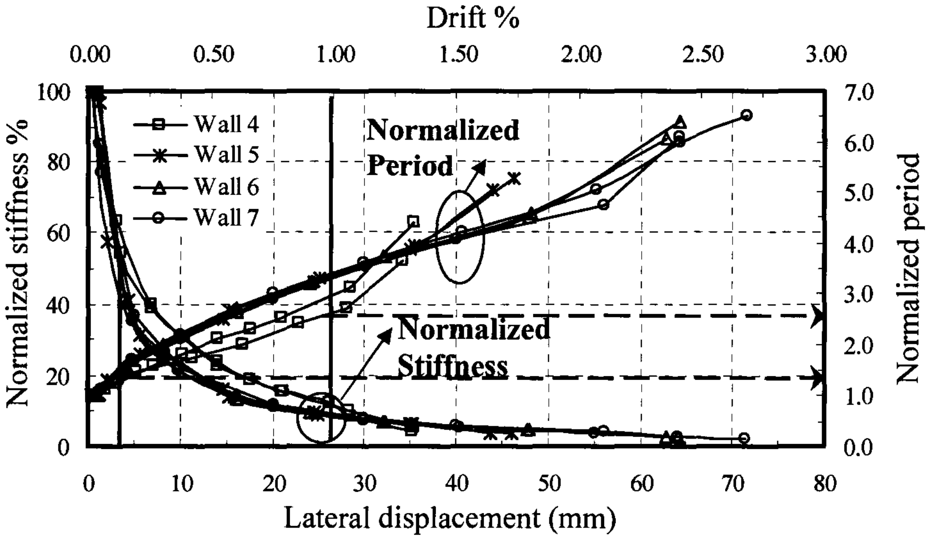

b) Phase II, 2-storey walls

Fig. 5.9: Normalized stiffness and period versus top wall displacements for cyclic loading in both directions

It can be seen from Fig. 5.9 (a) and (b) that the periods at 0.1% drift for all walls were at least 1.2 times the initial periods (see the vertical lines in Fig. 5.9 (a) and (b) at 0.1% drift). This corresponded to decreases in stiffness of about 40% of the initial wall stiffnesses. For the rectangular wall, the periods at 1% drift were at least 2.5 times the initial periods (see the vertical lines in Fig. 5.9 (a) and (b) at 1% drift) and corresponded to decreases in stiffness of at least 85% of the initial stiffnesses of the walls. For the flanged and end-confined wall types, the corresponding increases in period were at least 3 times the initial periods. As shown, the increase in period was significant when large stiffness degradation occurred. Such changes dramatically alter the building seismic demand.

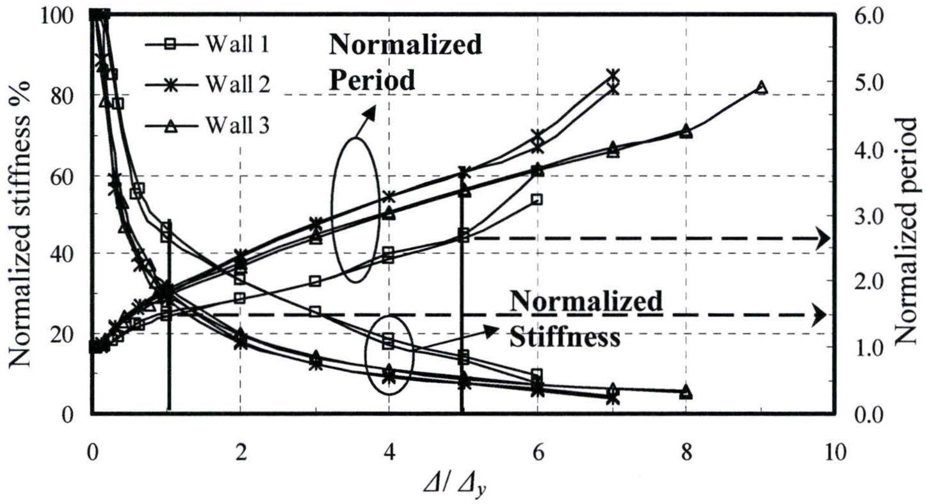

a) Phase I, 3-storey walls

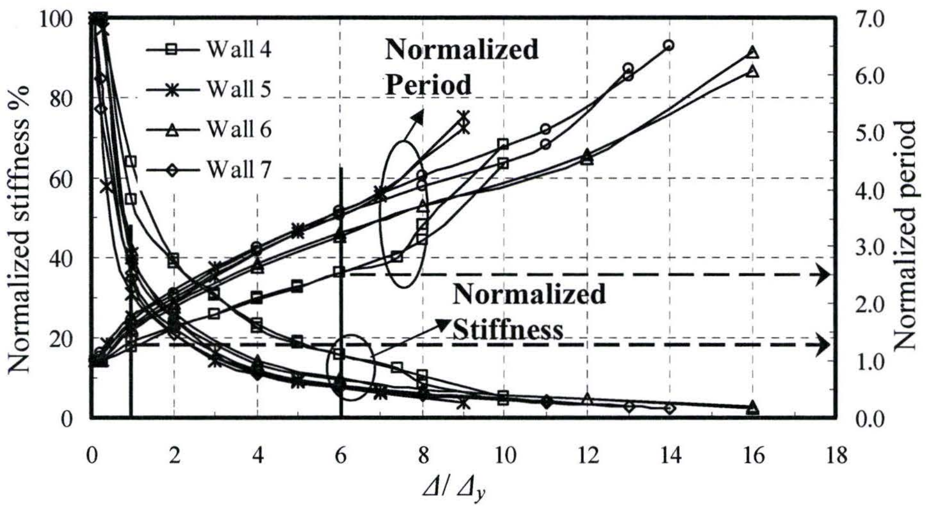

b) Phase II, 2-storey walls

Fig. 5.10: Normalized stiffness and period versus multiples of Δ_y

Relationships between stiffness, period, and multiples of yield displacements were plotted in Fig. 5.10 (a) for the 3-storey walls (Phase I) where it can be seen that the period at first yield was about 1.5 times the initial period for the rectangular wall compared to about 2.0 times the initial period for the flanged and end-confined walls. The period calculated at $5\times\Delta_y$, corresponding to almost no strength degradation for the rectangular wall (W1) in Phase I, (T_{norm} = 2.6) was about 1.7 times that at first yield (T_{norm} = 1.5). Larger increases in the normalized periods were calculated for the flanged and end-confined walls compared to those for the rectangular wall at the same displacement ductility levels.

As shown in Fig. 5.10 (b), for the 2-storey walls (Phase II), the period at first yield was about 1.4 times the initial period for the rectangular wall compared to about 1.8 times the initial period for the flanged and end-confined walls. Period calculated at $6\times\Delta_y$, corresponding to almost no strength degradation for the rectangular wall (W4) in Phase II (T_{norm} = 2.5) was about 1.8 times the period at first yield (T_{norm} = 1.4). Again, larger increases in the normalized periods were calculated for the flanged and end-confined walls compared to those for the rectangular wall at the same displacement ductility level. Such increases in period are expected to significantly reduce the seismic demand, assuming that the trend of changes in wall stiffness represents the trend of stiffness changes for the whole masonry building.

5.7 Summary and conclusions

The seismic performance parameters for the half scale concrete-block shear walls tested in this study have been calculated and discussed in this chapter. The parameters included equivalent plastic hinge length, l_p, required in wall deflection predictions, ductility-related force modification factor, R_d, and overstrength-related force modification factor, R_o. The provisions for ductile reinforced concrete shear walls in CSA A23.3 (2005) were utilized to calculate ductilities for the very similar reinforced masonry shear walls. Also, the seismic force-reduction factor, R, and the deflection amplification factor, C_d, defined in ASCE-7 (2008) were determined for the test walls. Modeling of the test walls was conducted using the nonlinear dynamic analysis software IDARC-5 (2002). A user-input trilinear idealization of the moment-curvature relationship at the base of the wall was used for modeling and calibration of the hysteresis parameters in IDARC-5 was performed to generate the nonlinear load-displacement relationships and the hysteresis loops for the test walls. Nonlinear dynamic analyses were conducted by subjecting the analytical model generated in IDARC-5 to a series of 10 earthquake records representing low, medium, and high frequencies. The post-yield performance characteristic of the walls, including stiffness reduction and its effect on period increase were presented corresponding to drift and ductility demand.

It was found that equivalent plastic hinge lengths, l_p, for the 2-storey and 3-storey walls having the same configuration were almost the same. The values for l_p based on theoretical curvatures and the attained idealized displacement ductilities at ultimate load for the rectangular, flanged and end-confined walls were 40%, 15%, and 19% of the wall length, respectively. Higher values were calculated for displacement ductilities corresponding to 1% drift and 20% strength degradation.

The test results and the accompanying analyses showed that rectangular concrete block shear walls were ductile, and that adding flanges or boundary elements at the wall ends resulted in even higher ductilities. The R_d values for the flanged and end-confined walls were, respectively, at least 1.5 and 2.0 times those corresponding to the rectangular walls. The average value of R_o calculated for the test walls was 2.34 based on the design capacities calculated using CSA S304.1.

The overall response modification factors, $R_d \times R_o$, were at least, 7.3 and 9.5 for the 3-storey and 2-storey rectangular walls, respectively, following the Canadian code. The overall response modification factors, $R_d \times R_o$, calculated for the flanged and end-confined walls were, respectively 30% and 72% higher than those for the rectangular walls.

The inelastic rotational capacities of the flanged and end-confined walls were much greater than the minimum specified inelastic rotational demands stipulated in CSA A23.3 (2005) for ductile reinforced concrete shear walls. This indicates that the test walls were capable of providing high ductility, which should qualify the walls constructed with flanges and boundary elements to an R_d value of at least 3.5 similar to their RC counterparts.

The analytical results showed that the R value calculated for the 3-storey rectangular wall was close to 5.0 which was consistent with the value in ASCE-7 (2008). The R values for the 3-storey flanged and end-confined walls were 6.4 and 8.9, respectively. The R values for the 2-storey walls were lower than those of the 3-storey walls.

The results showed that C_d value of the 3-storey rectangular wall was about 45% higher than the 3.5 value given by ASCE-7 (2008) for special reinforced masonry shear walls and even satisfied the 5.0 value specified for special reinforced concrete shear walls. Significantly higher C_d values of at least 9 and 12 were calculated for the flanged and end-confined walls, respectively. Higher values were calculated for the 2-storey walls compared to the 3-storey walls.

Relationships between stiffness, period, and multiples of yield displacements were presented. The periods at first yield were about 1.5 times the initial period for the 3-storey rectangular wall compared to at least 2.0 times the initial period for the 3-storey flanged and end-confined walls. For the 3-storey walls, periods at $5\times\Delta_y$, corresponding to almost no strength degradation, were at least 1.7 times those at first yield. Slightly higher periods (1.8 times those at first yield) were calculated for the 2-storey walls tested in this study. Such period increases are expected to significantly reduce the seismic demand. In this discussion, it is assumed that the trend for changing stiffnesses of the walls would be similar to the trend for changing stiffnesses for the entire masonry building.

Chapter Six

Summary and Conclusions

CHAPTER 6
SUMMARY and CONCLUSIONS

6.1 Summary

The results for displacement-controlled cyclic loading tests on seven reinforced concrete-block shear walls with aspect ratios of 1.5 or 2.2 (2- or 3-storey high) were reported and analyzed. The experimental program was designed to evaluate the flexural response of rectangular reinforced concrete block shear walls and to compare that response to responses of walls with flanges and confined ends. The test matrix was selected to investigate the influence of attaching flanges or end confining elements to rectangular walls on the ultimate curvatures, stability of the compression zone, wall ductility, and failure mode. All of the test walls were subjected to fully-reversed displacement-controlled quasi-static cyclic loading and were cycled up to 50% degradation in strength in order to obtain information on post-peak behaviour.

Detailed descriptions of the experimental program and the wall test matrix used in this study were presented. Also, material properties, specimen design and construction, reinforcement detailing, description of the test setup and instrumentation, and predicted capacities and displacements were presented.

Observations pertaining to cracking and the progress of damage during the tests were described. The hysteresis loops for the walls were presented and the load-displacement responses of the walls were discussed. Bilinear idealizations of the load-displacement envelopes were carried out and displacement ductilities based on this elastic-plastic idealization were calculated.

Quantitative information was extracted by analysing and comparing the test results and the effects of different test parameters on wall behaviour, ductility, and post-peak retention of strength were discussed. Also, seismic performance parameters such as stiffness, deflection, ductility, and energy dissipation were determined at different loading stages of the test walls. The individual contributions of the flexural and the shear deformation to the total wall displacements were determined.

The measured compressive strains in the masonry at ultimate load were presented for the test walls and compared with the ultimate strains specified in CSA S304.1 and the MSJC code. Also, the extent of plasticity and equivalent plastic hinge length were calculated for the test walls. Ductility-related, R_d, and overstrength-related, R_o, seismic response modification factors following the provisions of the NBCC (2005) were determined for the half scale test walls tested in this study and for full scale RM shear walls tested earlier by Shedid (2006).

The overall seismic force-reduction factor, R, and the deflection amplification factor, C_d, defined in ASCE-7 (2008) were determined for the test walls. The test results were modeled using a trilinear idealization of the experimentally determined moment-curvature relationships at the base of the walls as required for dynamic analysis using IDARC-5. Pushover and quasi-static analysis were conducted to determine hysteresis parameters to capture the load-displacement envelopes and the hysteresis behaviours of the test walls. The nonlinear dynamic analyses were conducted by subjecting the analytical model generated in IDARC-5 to a series of 10 earthquake ground motions representing low, medium, and high frequencies to determine R and C_d values.

6.2 Conclusions

The following conclusions were drawn from the research reported in the preceding chapters:

1. The addition of flanges and end-confined elements to reinforced masonry shear walls can be easily achieved in construction. Also, these modifications can be easily incorporated in current codes.
2. The test results showed that along with a saving of more than 40% in the total amount of vertical reinforcement, significant enhancements in ultimate drifts and ductilities were attained by the flanged and end-confined walls designed to resist the same ultimate loads as the rectangular walls.

3. The idealized ductilities of the flanged and end-confined masonry walls at 20% strength degradation were at least 50% and 100% larger than those for the rectangular wall counterparts having the same overall length and subjected to the same axial load. This indicates that the use of flanged and end-confined walls would be very beneficial in achieving reductions in seismic design load.
4. For both aspect ratios tested (h_w/l_w =2.2 and 1.5), the drifts at 20% strength degradation were about 1.0%, 1.5%, and 2.2% corresponding to the rectangular, flanged, and end-confined walls, respectively. This clearly highlights the benefit of the proposed alternative construction strategies especially for *Important buildings* that, based on the NBCC (2005), have a drift limit of 1.5% and may require some minor repair after earthquake event.
5. Based on normalized load-displacement relationships of the 2- and 3-storey walls, the test results indicated that the cross section dimensions significantly influence the response of the wall with relatively little dependence on the wall height. This confirms that plastic hinge length, which is needed to determine the level of plastic deformations, was consistently a function of the wall length and was less influenced by the height of the wall.
6. The shear displacements for the walls with aspect ratio of 2.2 ranged between 20-30% for both aspect ratios considered with only minor variations attributed to different end configurations. It is suggested that such shear displacements should be accounted for in the predictions of the overall wall displacement.
7. Using bilinear idealizations of the nonlinear load-displacement relationships for the test walls, the idealized displacement ductility values at maximum load, at 1% drift, and at 20% strength degradation were about 28% less than their corresponding measured displacement ductility values. The idealized inelastic capacities at these three performance levels were, on average, 96% of the measured wall capacities. Therefore, a reasonable and simplifying approximation is to assume that the idealized wall capacity is equal to the actual wall capacity.

8. The stiffnesses for all walls degraded rapidly to less than 60% of the initial stiffness at low displacement levels equal to about 0.1% drift for all walls. Reasonable estimates for the test wall stiffnesses at 0.5%, 1.0%, and 1.5% drift can be taken to be around 30%, 15%, and 5% of the calculated wall stiffnesses using uncracked transformed section properties.
9. The relationships between the normalized energy dissipation at first yield and the ratio of the post-yield displacement to the yield displacement were almost linear. Differences between the rectangular, flanged, and end-confined walls were relatively insignificant.
10. The compressive strains in masonry at maximum load, over the lower 50 mm of the wall were approximately 4 times the specified maximum compressive strains in the MSJC code (2008) and in CSA S304.1 (CSA 2004). This indicated that theoretical curvatures at the bases of the walls significantly underestimated actual curvatures at ultimate loads.
11. Ductility modification factors calculated for the flanged and end-confined walls were, respectively, at least 1.5 and 2.0 times those corresponding to the rectangular walls. Although, the test results showed that rectangular concrete block shear walls were ductile, the proposed modifications to the wall ends, either by attaching a flange or forming a boundary element, resulted in significantly increased wall ductilities. These results should allow higher reduction factor to be used for rectangular walls and even higher values for the flanged and end-confined walls.
12. The inelastic rotational capacities of the flanged and end-confined walls were greater than the minimum specified inelastic rotational demands as specified in the Canadian concrete design standard (CSA A23.3-05) for ductile reinforced concrete shear walls. This demonstrates that the flanged and end-confined reinforced masonry walls should qualify for an R_d value of at least 3.5.
13. Relationships between stiffnesses, periods, and multiples of yield displacements were investigated. The periods at first yield were about 1.5 times the initial

period for the 3-storey rectangular wall compared to at least 2 times the initial periods for the 3-storey flanged and end-confined walls. For the 3-storey walls, periods at $5 \times \Delta_y$, corresponding to almost no strength degradation, were at least 1.7 times those at first yield. Similar increases were found for the 2-storey walls. Such increases in period are expected to significantly reduce the seismic demand, assuming that the trend of changes in wall stiffness represents the trend of stiffness changes for the entire masonry building.

14. The analytical results showed that the *R* value calculated for the 3-storey rectangular wall was close to 5.0 which was consistent with the value in ASCE-7 (2008). The *R* values for the 3-storey flanged and end-confined walls were 6.4 and 8.9, respectively. The *R* values for the 2-storey walls were lower than those of the 3-storey walls. This difference might be attributed to the lower elastic period (and higher elastic stiffness) of the 2-storey walls.

6.3 Future work

The research presented in this thesis included experimental testing of RM shear walls with different end configurations and different aspect ratios. Detailed analyses of the experimental results and calculated seismic design parameters for rectangular, flanged and end-confined RM shear walls were provided for use by researchers, practicing engineers, and code committees. However, this is not the end of this challenging and interesting research topic. Several issues remain unresolved and may require further investigation. This section attempts to address possible extensions to the research to enlarge the database related to the seismic performance of RM shear walls.

Testing of walls with higher aspect ratio and having the same cross-section properties as the ones tested in this study could be conducted to verify that the load-displacement relationship of walls with the same cross sectional properties can be normalized for different wall heights. This may result in relying on section properties to develop normalized load-displacement relationships for taller walls that cannot be easily tested experimentally.

Testing of flanged and end-confined walls subjected to lower and higher axial stress could be conducted to determine the effect of axial load on the overall wall response. The results could then be compared with previous tests on rectangular walls with various axial loads.

Walls with larger flanges and boundary elements could be tested to investigate the effect of their size on the overall wall response. Therefore, recommendations on the minimum flange width to achieve high ductility could be given.

Walls having boundary element in the lower stories and flanges or even rectangular cross sections in the upper stories could be tested to investigate the wall response. This may achieve a significant amount of saving in construction costs and still provides the benefit of the boundary element in the highly stressed plastic hinge regions at the base of the wall.

Using the experimental data for walls subjected to different axial compressive stresses, multi degree of freedom idealizations of the walls could be conducted, as opposed to the single degree of freedom idealizations in this study. This could result in more representative dynamic analyses which could also be extended to investigate the system response to ground motion as opposed to component response.

System testing in addition to component (wall) evaluation could be conducted to investigate the effects of wall interaction and diaphragm action. This would facilitate comparison between wall responses in a system to responses of individual walls. Conclusions based on both wall performances will determine the accuracy of superposition of individual wall responses to characterize the system response. In addition, a seismic force modification factor can then be calculated for systems rather than for components.

This study along with the future work are expected to draw a road map for further research to facilitate better understanding and provide more realistic methods to predict the seismic performance of masonry shear wall construction.

REFERENCES

American Society of Civil Engineers (ASCE 2008), *"Minimum design loads for buildings and other structures."* ASCE-7, American Society of Civil Engineers, Reston, Virginia, USA.

American Society for Testing and Material (ASTM 2006), *"Standard test method for compressive strength of masonry prisms."* ASTM-C1314, West Conshohocken, PA.

American Society for Testing and Material (ASTM 2007), *"Standard specification for deformed, plain, low carbon, chromium, steel bars for concrete reinforcement."* ASTM-A1035/ A103 M, West Conshohocken, PA.

American Society for Testing and Material (ASTM 2008), *"Standard test method for compressive strength of hydraulic cement mortar (using 50 mm cube specimen) ."* ASTM-C109, West Conshohocken, PA.

ATC (2008), *"Quantification of building seismic performance factors."* ATC-63 Project report – 90% draft, Applied Technology Council, Redwood City, California.

Bae S., Mieses A., and Bayrak O. (2005), *"Inelastic buckling of reinforcing bars."* ASCE J. Struct. Eng.(131)2, 314-321.

Brunner, J., and Shing, P. (1996), *"Shear strength of reinforced masonry walls."* Masonry Society Journal, Vol. 14, No.1.

Canadian Standards Association (2004), *"CSA A165: CSA Standards on concrete masonry units."* CSA, Mississauga, ON, Canada.

Canadian Standards Association (2004), *"CSA S304.1-04: Design of masonry structures."* CSA, Mississauga, ON, Canada.

Canadian Standards Association (2005), *"CSA A23.3-05: Design of reinforced concrete structures."* CSA, Mississauga, ON, Canada.

Chahine, G. (1989), *"Behaviour characteristics of face shell mortared block masonry under axial compression."* M. Eng. Thesis, Department of Civil Engineering, McMaster University, Ontario, Canada.

Chopra, A. (2000), *"Dynamics of structures: Theory and application to earthquake engineering."* (2nd edition), Prentice Hall, Upper Saddle River, N.J.

Drysdale, R., and Hamid, A. (2005), *"Masonry structures- behaviour and design."* First Canadian Edition, Canada Masonry Design Ccentre, Mississauga, ON.

Drysdale, R., and Hamid, A. (2008), *"Masonry structures: behavior and design."* 3rd Ed., The Masonry Society, Boulder, Colorado.

Elghadamsi, F., and Mohraz, B. (1987), *"Inelastic earthquake spectra."* Earthquake Engineering and Structural Dynamics, Vol. 15, pp. 91-104.

Federal Emergency Management Agency (FEMA 1997), *"Commentary on the NHREP guidelines for the seismic rehabilitation of buildings."* FEMA 273/274, Washington, D.C.

Federal Emergency Management Agency (FEMA 2004), *"NEHRP Recommended Provisions for Seismic Regulations for New Buildings and Other Structures."* FEMA 450-1/2003 Edition, Part 1: Provisions, Federal Emergency Management Agency, Washington, D.C.

Halucha, J. (2002), *"In-plane behaviour of reinforced concrete masonry panels."* M.A.Sc. Thesis, Department of Civil Engineering, McMaster University, Ontario, Canada.

Harries, K (2004), *"Discussion of seismic force modification factors for the proposed 2005 edition of the National Building Code of Canada."* Canadian Journal of Civil Engineering, Vol. 31, 393-394.

Hose, Y. and Seible, F. (1999), *"Performance evaluation database for concrete bridge components, and systems under simulated seismic loads."* PEER report 1999/11, Pacific Earthquake Engineering Research Center, College of Engineering, University of California, Berkley, U.S.A.

International Building Code (IBC 2008), International Code Council, Falls Church, Va.

Ibrahim, K., and Suter, G. (1999), *"Ductility of concrete masonry shear walls subjected to cyclic loading."* 8th North American Masonry Conference, June 6-9, USA.

Idarc-5 (2002) Valles, R.E., Reinhorn, A.M., Kunnath, S.K., Li, C. and Madan, A., *"IDARC Version 5.0."* National Center for Earthquake Engineering Research, Buffalo, NY.

Jamison, J. (1997), *"Monotonic and cyclic performance of structurally insulated panel shear walls."* Master Thesis, Department of Civil Engineering, Virginia Polytechnic Institute and State University, Blacksburg, VA, US

King, J. (1946), *"The effect of lateral reinforcement in reinforced concrete columns."* ASCE J. Struct. Eng., (24)7, 355–38

Lam, S., Wu, B., Wong, Y., Wang, Z., Liu, Z., and Li, C. (2003), *"Drift Capacity of Rectangular Reinforced Concrete Columns with Low Lateral Confinement and High-Axial Load."*ASCE J. Struct. Eng., (129)6, 733-742.

Lefas I., Kotsovos M., Ambraseys N. (1990), *"Behaviour of reinforced concrete structural walls: strength, deformation characteristics, and failure mechanisms."* ACI Struct. J., (87)1, 23-31.

Long, L. (2006), *"Behaviour of half-scale reinforced concrete masonry shear walls."* M.A.Sc. Thesis, Department of Civil Engineering, McMaster University, Ontario, Canada.

Miller, S., El Dakhakhni, W., and Drysdale, R. (2005), *"Experimental evaluation of the shear capacity of reinforced masonry shear walls."* 10th Canadian Masonry Symposium, Banff, Alberta, Canada.

Miranda, E. (1993), *"Site dependent strength reduction factors."* ASCE J. Struct. Eng., (119)12, 3503-3519.

Mitchell, D., Tremblay, R., Karacabeyli, E., Paultre, P., Saatcioglu, M., and Anderson, D. (2003), *"Seismic force modification factors for the proposed 2005 edition of the National Building Code of Canada."* Can. J. Civ. Eng. 30: 308-327

Masonry Standards Joint Committee (MSJC 2008), *"Building code requirements for Masonry Structures."* TMS 402/ASCE 5/ACI 530, American Concrete Institute, American Society of Civil Engineers, and The Masonry Society, Detroit, New York, and Boulder.

Nassar, A., and Krawinkler, H. (1991), *"Seismic demands for SDOF and MDOF systems."* Report No. 95, The John A. Blume Earthquake Engineering center, Stanford University, Stanford, California.

NBCC (2005), National Building Code of Canada, Institute for Research in Construction, National Research Council of Canada, Ottawa, ON.

Newmark, N., and Hall, W. (1973), *"Seismic evaluation and upgrading of existing buildings."* Report No. 46, Building practices for disaster mitigation, National bureau of standards, U.S. Department of Commerce, pp. 209-236.

Orakcal O., Wallace J. (2006), *"Flexural modeling of reinforced concrete walls-experimental verification."* ACI Journal, (103)2, 196-206.

Ozcebe, G., and Saatcioglu, M. (1987), *"Confinement for concrete columns for seismic loading."* ACI Journal, (84)4, 308-315.

Pacific Earthquake Engineering Research Center (PEER-2006), *"Strong motion database."* PEER, Univ. of California at Berkley, Berkley, Calif., (http://peer.berkley.edu/smcat/).

Park, R. and Paulay, T. (1975), *"Reinforced concrete structures."* John Wiley and Sons, Inc., New York.

Paulay, T. (1980), *"Earthquake-resisting shear walls- New Zealand Design Trends."* ACI Structural Journal, (77)3, 144-152.

Paulay, T. and Priestley, M. (1992), *"Seismic design of reinforced concrete and masonry buildings."* John Wiley and Sons, New York.

Paulay, T., and Priestley, M., (1993), *"Stability of ductile structural walls."* ACI Structural Journal, (90)4, 385-392.

Paulay, T., Priestley, M., and Synge, A. (1982), *"Ductility in earthquake resisting squat shear walls."* ACI Structural Journal, (79)4, 257-269.

Priestley M. and Elder D. (1983), *"Stress-Strain curves for unconfined and confined concrete masonry."* Proceedings ACI Journal, (80)3, 192-201.

Priestley, M. (1986), *"Seismic design of concrete masonry shear walls."* ACI Structural Journal, (83)1, 58-68.

Priestley, M., and Limin, H. (1990), *"Seismic Response of T-Section Masonry Shear Walls."* Masonry Society Journal, (9)1, 10-19.

Priestley, M., and Park, R. (1987), *"Strength and ductility of concrete bridge columns under seismic loading."* ACI Journal, (84)1, 61-76.

Priestley, M. (1977), *"Seismic resistance of reinforced concrete masonry shear walls with high steel percentages."* Bull. New Zealand Nat. Soc. Earthquake Engineering., 10(1).

Priestley, M. (2000), *"Performance based seismic design."* Proceedings 12th World Conference Earthquake Engineering, Auckland, New Zealand.

Priestley, M., Seible, F., and Calvi, G. (1996), *"Seismic design and retrofit of bridges."* John Wiley and Sons, Inc., New York, N.Y.

Priestley, N., Calvi, G., and Kowalsky, M., (2007), *"Displacement-Based Seismic Design of Structures."* IUSS Press, Pavia, Italy.

Riddell, R., and Newmark, N. (1979), *"Statistical analysis of the response of nonlinear systems subjected to earthquakes."* Structural research series No. 468, Department of Civil Engineering, University of Illinois, Urbana.

Riddell, R., Hidalgo, P., and Cruz, E. (1989), *"Response modification factors for earthquake resistant design of short period structures."* Eq. Spectra, (15)3, 571-590.

Saatcioglu, M. (1991), *"Deformability of reinforced concrete columns."* Earthquake resistant concrete structures-Inelastic response and design, ACI (SP-127)10, 421–452.

Sakai, K., and Sheikh, S. A. (1989), *"What do we know about confinement in reinforced concrete columns? (A critical review of previous work and code provisions) ."* ACI Structural. J., (86)2, 192–207.

Scott, B., Park, R., and Priestley, M. (1982), *"Stress-strain Behaviour of Concrete Confined by Overlapping Hoops at Low and High Strain Rates."* ACI Journal Proceedings, (79)1, 13-27.

Seible, F., Hegemier, G., Priestley, M., Kingsley, G., Igarashi, A., and Kurkchubasche A. (1993), *"Preliminary results from the TCCMAR 5- storey full scale reinforced masonry research building test."* Masonry Society Journal, (12)1, 53-60.

Shedid, M. (2006), *"Ductility of reinforced concrete masonry shear walls."* M.A.Sc. Thesis, Department of Civil Engineering, McMaster University, Ontario, Canada.

Shedid, M., Drysdale, R., and El-Dakhakhni, W., (2008), *"Behavior of Fully Grouted Reinforced Concrete Masonry Shear Walls Failing in Flexure: Experimental Results."* ASCE J. Struct. Eng. (134)11, 1754-1767.

Shedid, M., El-Dakhakhni, W., and Drysdale, R., (2009), *"Inelastic Behavior of Reinforced Concrete Masonry Shear Walls: Analysis."* Engineering Structures, (31) 9, 2032-2044.

Shedid, M., El-Dakhakhni, W., and Drysdale, R., (2010), *"Seismic Performance Parameters of Reinforced Concrete-Block Shear Wall Construction."* ASCE J. Constructed Facilities (24)1, DOI: 10.1061(ASCE) CF.19435509.0000061.

Shing, P., Noland, J., Klamerus, E., and Spaeh., H. (1989a), *"Inelastic behavior of concrete masonry shear walls."* ASCE J. Struct. Eng., (115)9, 2204-2225.

Shing, P., Noland, J., Spaeh, H., and Klamerus, E. (1989b), *"Inelastic behaviour of masonry wall panels under in-plane cyclic loads."* 4th North American Masonry Conference, Los Angles, California.

Sinha, B., Gerstle, K., and Tulin, L. (1964), *"Stress-strain behaviour for concrete under cyclic loading."* Journal ACI, (61)2, 195-211.

Sittipunt C., Wood S., Lukkunaprasit P., and Pattararattanakul P. (2001), *"Cyclic behavior of reinforced concrete structural walls with diagonal web reinforcement."* ACI Journal, (98)4, 554-562.

Sveinsson, B., McNiven, H., and Sucuoglu, H. (1985), *"Cyclic loading tests of masonry single piers, Vol. 4 – Additional tests with height to width ratio of 1."* Report No. UCB/EERC-85/15, Earthquake Eng. Res., Ctr., Univ. of California, Berkeley, California.

Thomsen, J., and Wallace, J. (2004), *"Displacement-based design of slender reinforced concrete structural walls- Experimental verification."* ASCE J. Struct. Eng., (130)7, 618-630.

Tomazevic, M. (1998), *"Earthquake-Resistant Design of Masonry Buildings."* Imperial College Press, London, UK.

Uang C. (1991), *"Establishing R (or R_w) and C_d Factors for building seismic provisions."* ASCE J. Struct. Eng., (117)1, 19-28.

Vidic, T., Fajfar, P., and Fischinger, M. (1992), *"A procedure for determining consistent inelastic design spectra."* Proceeding workshop on nonlinear seismic analysis of RC structures, Bled, Slovenia.

Voon, K., and Ingham, J. (2004), *"Shear strength of concrete masonry walls."* 7th Australasian Masonry Conference, pp. 102-112.

Voon, K., and Ingham, J. (2006), *"Experimental in-plane shear strength investigation of reinforced concrete masonry walls."* ASCE J. Strut. Eng., (132)3, 400-408.

Wehbe, N., Saiidi, M., and Sanders, D. (1999), *"Seismic performance of rectangular columns with moderate confinement."* ACI Journal, (96)2, 248-258.

Wheeler, A., and, Ganji, A. (1996), *"Introduction to Engineering Experimentation"* Published by Prentice Hall Inc., New Jersey, USA.

Appendix A

Seismic Performance Parameters for Full Scale Shear Walls

APPENDIX A
SEISMIC PERFORMANCE PARAMETERS FOR FULL SCALE SHEAR WALLS

A.1 Introduction

The focus of this appendix was to analyze previously reported test results (Shedid 2006) to evaluate equivalent plastic hinge lengths for full scale concrete block shear walls and to extract related seismic performance parameters. The cyclic tests of the full scale walls formed the initial phase of the long term research program on seismic behaviour of reinforced masonry shear walls at McMaster University. Further analyses of these previously published results provided useful background before proceeding with similar analyses of the half scale masonry shear walls tested in the current study. The results also helped to confirm the validity of directly applying the results of half scale tests to full scale behaviour. The performance parameters studied in this appendix were the equivalent plastic hinge length and the response modification factors related to ductility and overstrength.

Inelastic curvature at the base of a shear wall is the main source of plastic deformation for flexurally-dominated behaviour. Reasonable estimation of the equivalent plastic hinge length and realistic values for inelastic curvatures at the base of the wall are required for accurate predictions of top wall displacement. For the full scale walls, measured compressive strains close to the base of the wall at ultimate load were significantly higher than the strains specified in the current Canadian and the American codes. Although these higher strains may not alter the wall predicted strengths, they significantly affect the curvatures at the base of the walls and, consequently, the ultimate displacements.

A brief description of the earlier experimental shear wall study (Shedid 2006) was reported as a background to the above analyses and the envelopes of the hysteresis loops from the cyclic tests were reproduced. Also, calculations of displacement ductility for the test walls were presented. The measured compressive and tensile strains close to the base of the wall, the average curvatures and curvature ductility values evaluated close to the base were documented. This data was then synthesized to calculate seismic force modification factors defined in the Canadian code.

A.2 Experimental Program

Six fully-grouted 1.8 m long × 3.6 m high reinforced concrete block shear walls were constructed using 20 cm normal weight hollow concrete blocks. They were tested under displacement-controlled cyclic loading simulating earthquake effects (Shedid 2006). All walls were cycled to about 50% post-peak degradation in strength in order to obtain information about the post-peak behaviour, ductility, and stiffness degradation. The previously reported (Shedid et al 2009) test setup and instrumentation scheme are presented in Fig. A.1.

The reinforcement ratios, number of bars, and level of applied axial compressive stress for the test walls were given in Table A.1. The flexural and shear reinforcement ratios, ρ_v and ρ_h, respectively, were the areas of the reinforcing steel divided by the gross areas of the horizontal and vertical masonry cross sections, respectively. All walls were designed to exhibit ductile flexural failure by providing sufficient horizontal reinforcement to prevent shear failure. As shown in the envelopes of the hysteresis curves in Fig. A.2, all walls displayed reasonably symmetric responses in both directions of loading until toe crushing began and marked the maximum lateral capacity.

Table A.1: Wall reinforcement details and axial compressive stresses

Wall	1	2	3	4	5	6
$\rho_v^{(1)}$ (%)	0.29	0.78	0.73	1.31	1.31	1.31
$\rho_h^{(1)}$ (%)	0.08	0.13	0.13	0.26	0.26	0.26
Compressive stress (MPa)	0	0	0	0	0.75	1.50

$^{(1)}\rho_v$ = vertical reinforcement, ρ_h = horizontal reinforcement

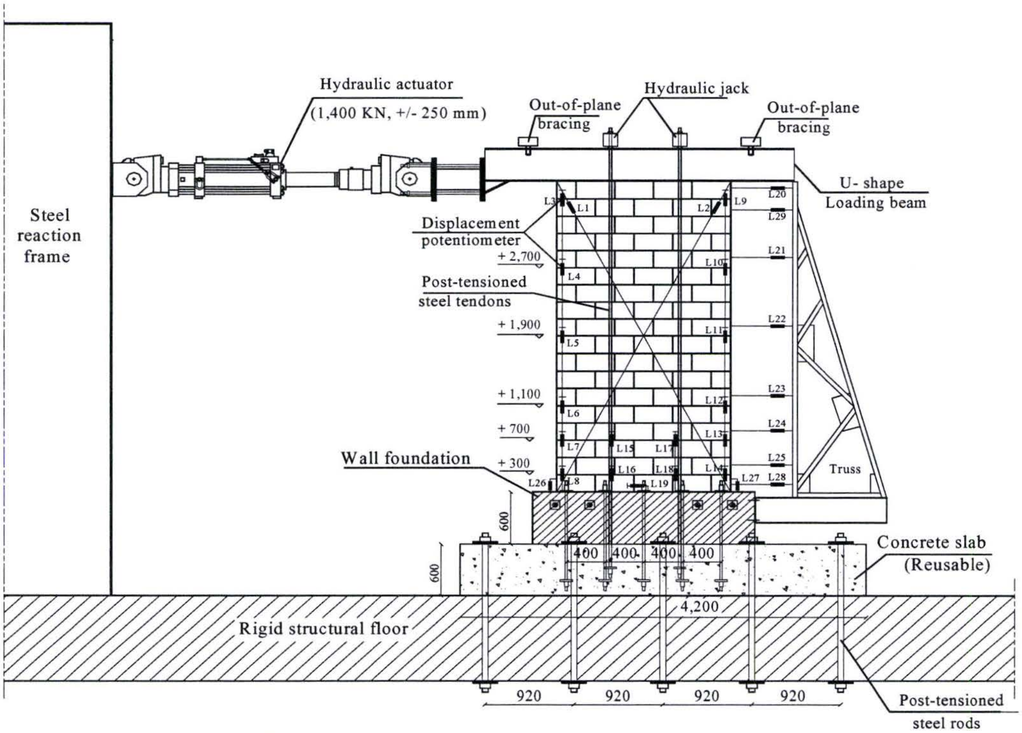

Fig. A.1: Test setup and instrumentation (Shedid et al. 2009)

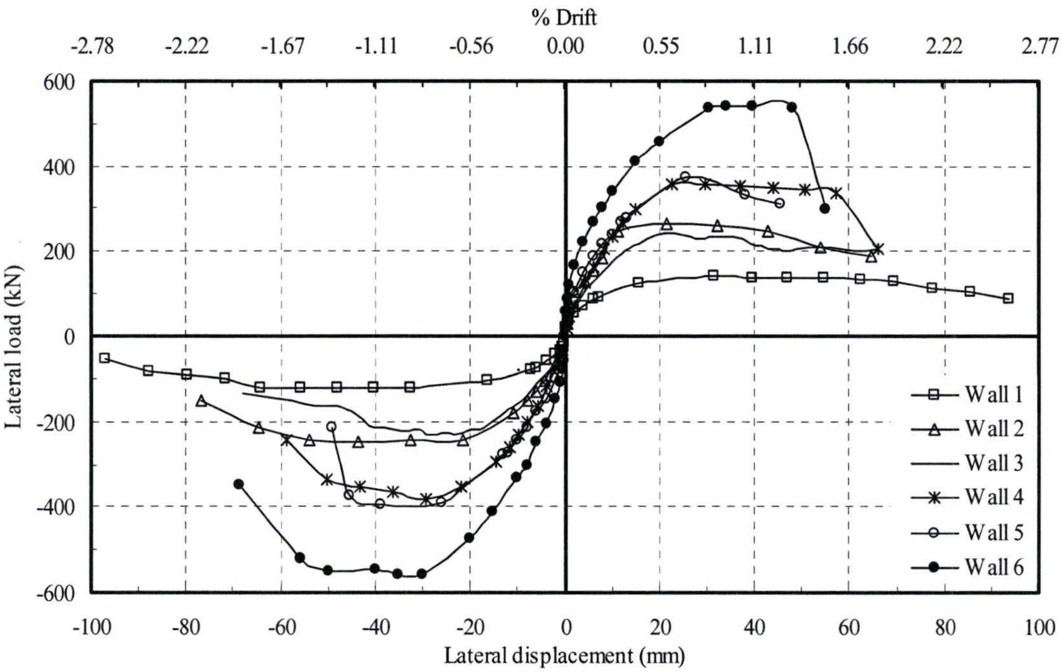

Fig. A.2: Envelopes of the load-displacement relationships for the test walls (Shedid et al. 2010)

A.3 Wall Displacement and Displacement Ductility

Ductility is a measure of the ability of a wall to deform beyond initial yielding of the flexural reinforcement. The measured top wall displacements, at the onset of yield of the outermost reinforcing bar, Δ_y, at ultimate load, Δ_u, and at 20% strength degradation, $\Delta_{0.80u}$, (i.e., at 80% of the ultimate load in the post-peak stage) were reported in Table A.2. The relationships between the theoretical flexural displacement ductilities, μ_Δ, and curvature ductilities, μ_φ, for different values of plastic hinge lengths were presented in Fig. A.3 using the following equation for walls with aspect ratio of 2.0:

$$\mu_\Delta = 1 + 3(\mu_\varphi - 1)\frac{l_p}{h_w}\left(1 - 0.5 \times \frac{l_p}{h_w}\right) \qquad \text{Eq. A.1}$$

where:

h_w = Wall height;

l_p = Equivalent plastic hinge length;

μ_Δ = Theoretical displacement ductility (Δ_u / Δ_y); and

μ_φ = Theoretical curvature ductility (φ_u / φ_y).

Measured displacement ductility, μ_Δ, is defined herein as the ratio between the measured top displacement at a specified limit and the measured displacement at the onset of yielding of the outermost vertical reinforcing bar. This definition of displacement ductility is simply based on the measured displacement values without idealization of the load-displacement relationship. The measured displacement ductility values $\mu_{\Delta u}$, $\mu_{\Delta 1\%}$, and $\mu_{\Delta 0.8u}$ at ultimate load, 1% drift, and 20% strength degradation, respectively, were listed in Table A.2.

There are several discussions in the literature regarding the appropriate definition of displacement ductility for behaviours that are not *ideally* elastic-plastic as discussed in Section 3.10.2 and as indicated by Priestley (2000), there is no general consensus or a unified definition for the yield and the ultimate displacements. In order to establish a common basis for comparisons between the walls, the definition proposed by Tomazevic (1998), presented in Fig. 4.6, has been adopted in this study to generate an idealized elastic-plastic response. This method is based on equating the area under the measured and the idealized curves for a selected post-yield wall displacement and an initial stiffness equivalent to the secant stiffness at the first *major crack* (taken at the onset of yield).

Table A.2: Summary of wall displacements and displacement ductilities

Wall	Direction	Measured displacements (mm)			Displacement ductility, [μ_Δ]					
					At Ultimate load		At 1% drift		At 20% strength degradation	
		Δ_y [(1)]	Δ_u	$\Delta_{0.80u}$	$\mu_{\Delta u}$	% drift	$\mu_{\Delta 1\%}$	$\mu^{ep}_{\Delta 1\%}$	$\mu_{\Delta 0.8u}$	$\mu^{ep}_{\Delta 0.8u}$
1	+ ve	7.0	31.6	77.5	4.5	0.88	5.14	3.56	11.07	7.70
	- ve		32.4	79.7	4.6	0.90		3.56	11.39	7.78
2	+ ve	11.1	32.9	64.7	2.9	0.91	3.24	2.33	5.83	4.32
	- ve		33.2	64.6	2.9	0.92		2.48	5.82	4.52
3	+ ve	11.3	24.2	46.7	2.1	0.67	3.19	2.35	4.13	3.22
	- ve		29.2	44.0	2.5	0.81		2.24	3.89	2.80
4	+ ve	14.8	29.8	61.6	2.0	0.83	2.43	2.00	4.16	3.50
	- ve		29.1	54.5	1.9	0.81		1.89	3.68	3.00
5	+ ve	16.2	25.3	45.4	1.5	0.70	2.22	1.69	2.80	2.32
	- ve		33.2	47.1	2.0	0.92		1.63	2.91	2.24
6	+ ve	16.9	29.9	51.6	1.7	0.83	2.13	1.44	3.05	2.26
	- ve		34.2	62.2	2.0	0.95		1.40	3.68	2.79

(1) Values based on the onset of yielding recorded in the outermost reinforcement

Using the method described above, the idealized elastic-plastic values of $\mu^{ep}_{\Delta 1\%}$, and $\mu^{ep}_{\Delta 0.8u}$, listed in Table A.2, were calculated for 1% drift, and 20% strength degradation conditions, respectively. The wall capacities based on the idealized approaches at 1% drift and at 20% strength degradation were, on average, 97% (*c.o.v.* = 2.1%) of the measured capacities. The average equivalent elastic-plastic displacement ductility values $\mu^{ep}_{\Delta 1\%}$, and $\mu^{ep}_{\Delta 0.8u}$ were, respectively, 27% and 24% (*c.o.v.* = 6.9% for both) lower, respectively, than the corresponding non-idealized calculated displacement ductility values, $\mu_{\Delta 1\%}$, and $\mu_{\Delta 0.8u}$.

Plastic displacements and displacement ductilities were significantly influenced by the levels of strains and curvatures generated at the wall bases especially within plastic hinge zones. The strains and the curvatures measured close to the wall bases at different loading stages were discussed in the following sections.

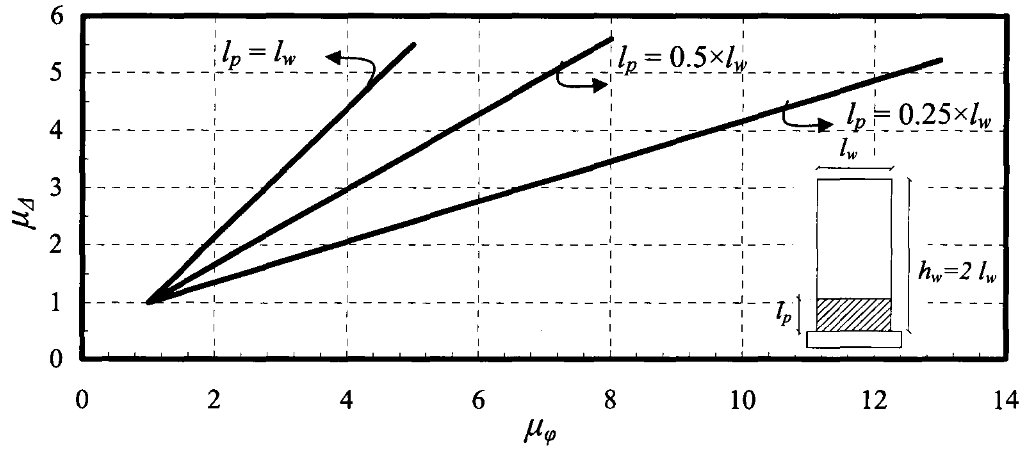

Fig. A.3: Relationship between μ_Δ and μ_φ for various plastic hinge lengths

A.4 Wall Strains

Average strain profiles over seven segments along the wall height were calculated based on measurements using vertical displacement potentiometers attached at the wall ends. The calculated average masonry compressive strains based on potentiometer measurements for the 100 mm and 300 mm wall heights above the foundation were presented in Fig. A.4 for all of the test walls. Due to spalling of the face shells at the wall toes and detachment of the displacement potentiometer anchors, these displacement measurements were discontinued at late stages of testing. Therefore, strains and curvatures at 20% strength degradation were not available.

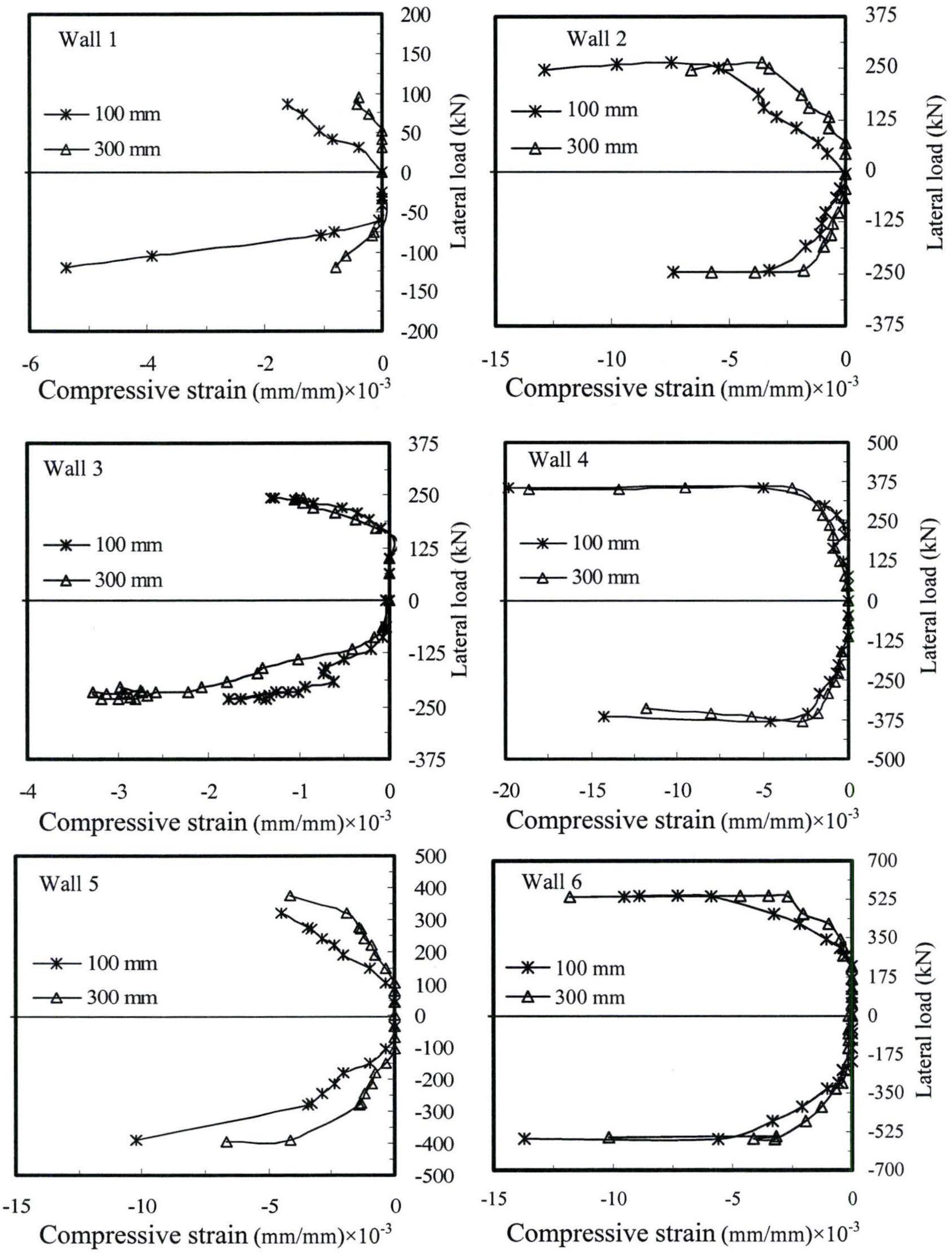

Fig. A.4: Masonry compressive strain over the lower 100 mm and 300 mm of the test walls

In general, it can be seen that the maximum compressive strains in the masonry, over the first 100 mm above the base of the wall were very much higher than the maximum average compressive strains of 2.5×10^{-3} mm/mm and 3.0×10^{-3} mm/mm, specified in the MSJC code (2008) and in CSA S304.1 (CSA 2004), respectively. As shown for all walls, except Walls 1 and 3, the maximum masonry strains averaged over the first 300 mm above the base were also significantly higher than the above specified values. For Walls 1 and 3 with bars in every other cell and not subjected to an axial compressive stress, the recorded compressive strains were significantly lower than for Walls 2 and 4 with bars in every cell and for Walls 5 and 6 which were tested under accompanying axial compressive stress. Even though Walls 1 and 3 attained similar or higher displacements and ductilities, strain readings were terminated at relatively low displacements.

A.5 Wall Curvatures

The theoretical values for curvatures at the base of the wall at the onset of yielding of the outermost tension reinforcement, $\varphi_{y,th,}$ and at ultimate load, $\varphi_{u,th}$, were calculated based on flexural strains and beam theory using code values for ε_u and Em but actual strengths of material and excluding material resistance factors. These were presented in Table A.3, along with the theoretical curvature ductilities.

Experimental values for curvatures over the wall height were calculated from the measured strains at the wall ends using the recorded displacements of the vertical potentiometers located at both ends of the walls. An average curvature, φ_i, over a certain gauge length, $h_{gauge(i)}$, along the wall height (see Fig. A.5 (a)) was calculated as explained in Section 4.3.

Relationships between measured average curvatures over short heights at the base of the wall and the corresponding moment at the base of the wall were presented in Figs. A.6 (a) and (b), respectively, for heights of +100 mm and +300 mm above the base. The figures showed that, for all walls, the curvatures at ultimate load were significantly higher than the curvatures at the onset of yielding of the outermost reinforcement, where a distinct change in the slope of the moment-curvature relationships occurred. Experimental values for average curvatures over the lower 100 mm of the wall at the onset of yield of the outermost tension reinforcement, $\varphi_{y,ex}$, at ultimate load, $\varphi_{u,ex}$, and at 1% drift, $\varphi_{1\%}$, were presented in Table A.3 along with the corresponding curvature ductility values, $\mu_{\varphi u,ex}= \varphi_{u,ex}/ \varphi_{y,ex}$, and $\mu_{\varphi 1\%}= \varphi_{1\%}/ \varphi_{y,ex}$. Experimental values for average curvatures over the lower 300 mm of the wall at the onset of yield of the outermost tension reinforcement, at ultimate load, and at 1% drift were also presented in Table A.3 along with the corresponding curvature ductility.

Table A.3: Theoretical and measured wall curvature and curvature ductilities

Wall	1	2	3	4	5	6
Theoretical curvature values at yield and ultimate						
$\varphi_{y,th}$ ($\times 10^{-6}$ rad/mm)	1.78	1.95	1.94	2.07	2.16	3.00
$\varphi_{u,th}$ ($\times 10^{-6}$ rad/mm)	12.17	6.04	6.72	4.74	4.26	3.71
$\mu_{\varphi,th}= (\varphi_{u,th} / \varphi_{y,th})$	6.84	3.09	3.47	2.29	1.97	1.24
Experimental values based on curvatures averaged over the lower 100 mm of the wall						
$\varphi_{y,ex}$ ($\times 10^{-6}$ rad/mm)	2.43	2.80	2.90	2.34	--(1)	2.29
$\varphi_{u,,ex}$ ($\times 10^{-6}$ rad/mm)	23.40	13.59	13.36	19.70	--(1)	12.40
$\varphi_{1\%}$ ($\times 10^{-6}$ rad/mm)	25.40	22.32	20.83	25.10	--(1)	20.21
$\mu_{\varphi u,ex}= (\varphi_{u,ex} / \varphi_{y,ex})$	9.63	4.85	4.61	8.42	--(1)	5.41
$\mu_{\varphi,1\%} = (\varphi_{1\%} / \varphi_{y,ex})$	10.45	7.99	7.18	10.75	--(1)	8.83
Experimental values based on curvatures averaged over the lower 300 mm of the wall						
$\varphi_{y,ex}$ ($\times 10^{-6}$ rad/mm)	1.20	1.61	1.74	1.64	1.72	1.84
$\varphi_{u,,ex}$ ($\times 10^{-6}$ rad/mm)	9.64	8.43	6.01	6.84	--(1)	4.67
$\varphi_{1\%}$ ($\times 10^{-6}$ rad/mm)	10.57	9.83	9.94	13.20	--(1)	7.52
$\mu_{\varphi u,ex}= (\varphi_{u,ex} / \varphi_{y,ex})$	8.03	5.24	3.45	4.17	--(1)	2.54
$\mu_{\varphi,1\%} = (\varphi_{1\%} / \varphi_{y,ex})$	8.81	6.11	5.71	8.07	--(1)	4.08

(1) Measurement not available for Wall 5 due to loss of potentiometers

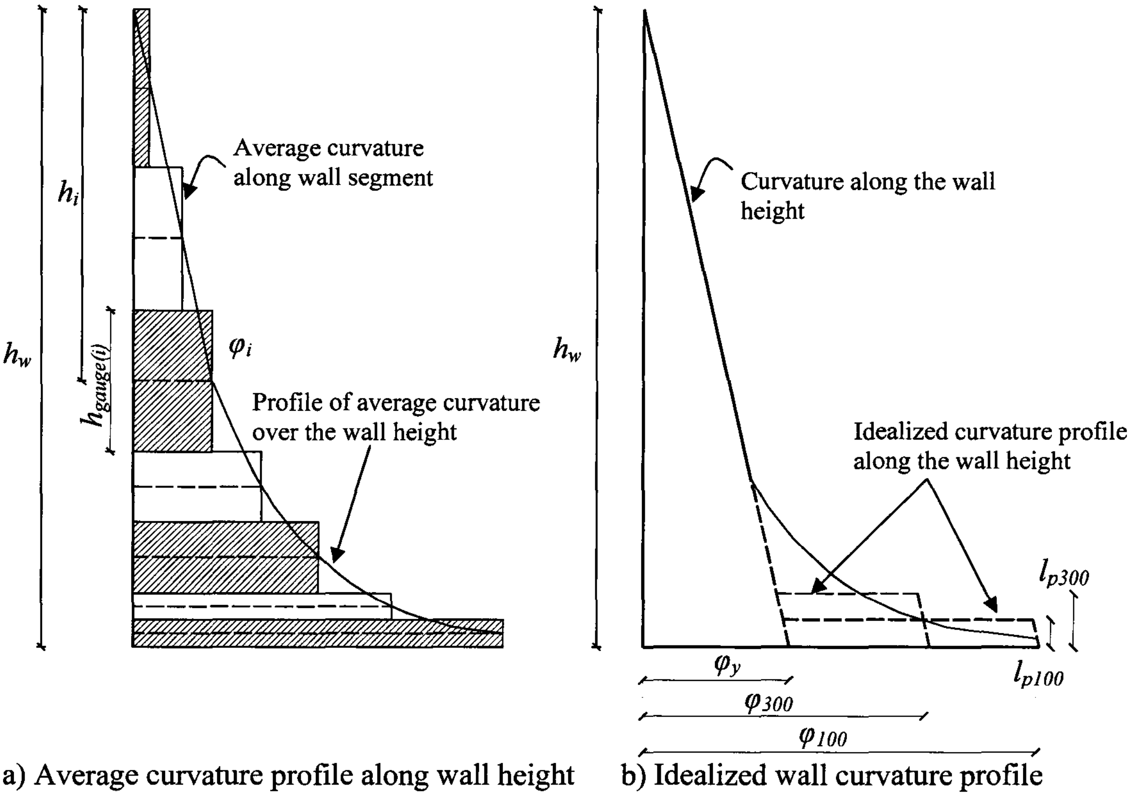

Fig. A.5: Average and idealized wall curvature

The measured average curvatures at yield, $\varphi_{y,ex}$, varied between 0.0023 rad/m and 0.0029 rad/m, over the lower 100 mm of the wall (corresponding to about $0.004/l_w$ and $0.005/l_w$) as indicated in Table A.3. At ultimate conditions, the curvatures, $\varphi_{u,ex}$, varied between 0.012 rad/m and 0.023 rad/m (corresponding to about $0.022/l_w$ and $0.042/l_w$), whereas, at 1% drift, the curvatures, $\varphi_{1\%}$, varied between 0.020 rad/m and 0.025 rad/m for all walls (corresponding to about $0.036/l_w$ and $0.045/l_w$). Based on these measured curvature values, the curvature ductility at ultimate, $\mu_{\varphi u,ex}$, varied between 4.6 and 9.6, and the curvature ductility at 1% drift, $\mu_{\varphi 1\%,}$, varied between 7.2 and 10.7.

Alternatively, when averaged over the lower 300 mm of the wall, the experimental curvature and curvature ductility values, presented in Table A.3, were significantly lower than curvature and curvature ductility values averaged over the lower 100 mm of the wall, which clearly showed that most of the deformation took place over the lower course of a wall. Both curvature ductilities were well in excess of the theoretical values.

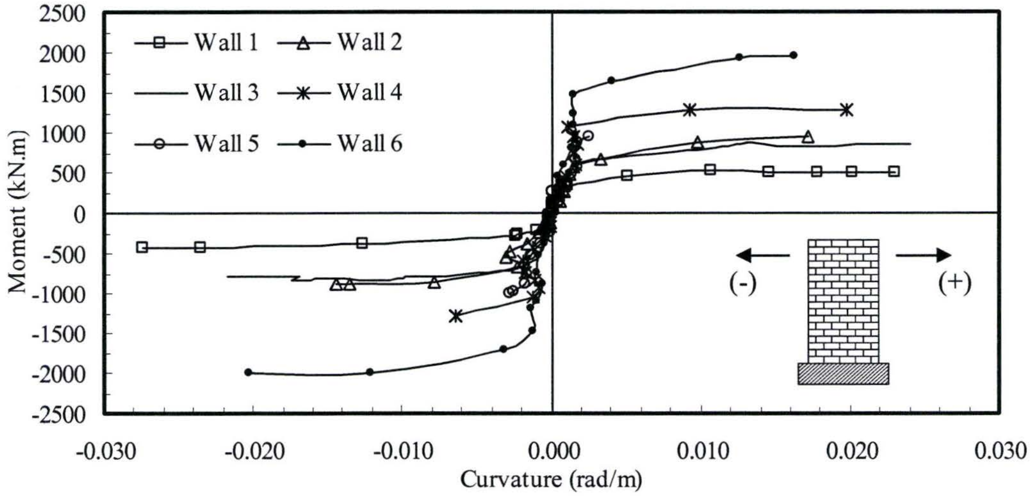

a) Average curvature based on displacement measurements over the lower 100 mm

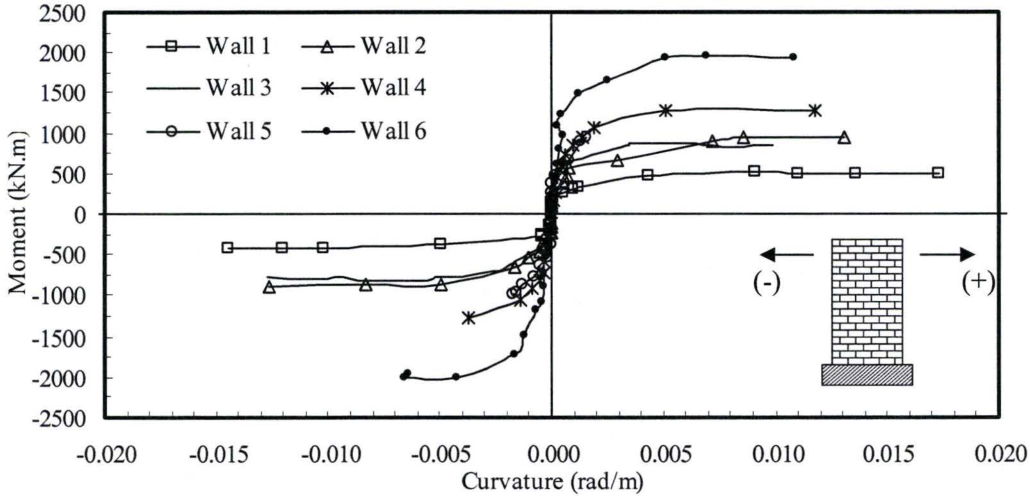

b) Average curvature based on displacement measurements over the lower 300 mm

Fig. A.6: Moment-curvature relationships of the test walls (Shedid et al. 2010)

As can be inferred from Table A.3, there was a significant discrepancy between curvature ductilities calculated at different stages of loading. (Because strains were not available, the highest curvature ductilities at 20% degradation of capacity were not shown). Clearly, the experimental results indicated that reinforced masonry shear walls were capable of developing significantly higher curvatures than those theoretically predicted. This discrepancy between observed and theoretical had a major impact on developing design parameters including determining equivalent plastic hinge lengths as discussed in the following section.

A.6 Equivalent Plastic Hinge Length

Using the experimentally determined curvatures and displacement ductilities listed in Tables A.3 and A.2, respectively, the equivalent plastic hinge lengths, l_p, for the test walls were calculated by rearranging Eq. A.1. The equivalent plastic hinge length, l_p, was defined as the length within the plastic region of the wall height used to predict the plastic wall displacements assuming constant plastic curvature. The idealized bilinear load displacement relationship suggested by Tomazevic (1998), based on equal areas, was used to calculate the l_p values. In order to establish a common basis for comparison, the top displacement at 1% drift, $\Delta_{1\%}$, was used as the maximum displacement in the idealized approach.

Replacement of the nonlinear load-displacement relationship with the idealized elastic-plastic relationship for the walls as shown in Fig. 4.6, means that the *idealized* yield displacement, Δ_y^{ep}, should be used. Consequently, as suggested by Hose and Seible (1999), a different yield curvature value, corresponding to the idealized yield displacement of the elastic-plastic load-displacement relationship, referred to as the idealized yield curvature, ϕ_y^{ep}, should also be used. Based on this discussion, the μ_Δ and μ_φ in Eq. A.1 were to be replaced by the idealized displacement ductility, $\mu_{\Delta 1\%}^{ep}$ ($=\Delta_{1\%}$ / Δ_y^{ep}), and the idealized curvature ductility, μ_ϕ^{ep} ($\varphi_{1\%} / \phi_y^{ep}$), in order to determine the equivalent plastic hinge length, l_p, from the experimental results.

Using the 1% drift limit, calculated equivalent plastic hinge lengths were presented in Table A.4. As shown in the table, for these test walls with an aspect ratio of h_w/l_w = 2.0 the l_p values required to reach a displacement ductility corresponding to a top displacement of 1% drift, varied between about 6% to 29% of the wall length, l_w, using the average curvature over the bottom 100 mm. This corresponded to curvature ductilities, μ_φ^{ep}, calculated for the idealized relationships, which varied between 5.3 to 8.9. The results showed that larger flexural reinforcement ratios corresponded to reduced equivalent plastic hinge lengths, as can be concluded by comparing the results of Walls 1, 2, 3, and 4. Based on the results for Walls 4, and 6, the level of axial compressive stress on the wall had a less significant effect on l_p.

Table A.4: Calculated equivalent plastic hinge length, l_p, for 1% drift

Wall	1	2	3	4	5	6
Idealized displacements and displacement ductilities						
Δ_y (mm)	7.01	11.10	11.30	14.81	16.22	16.91
Δ_y^{ep} (1) (mm)	10.10	15.41	15.22	17.90	21.21	24.91
$\mu_{\Delta 1\%}^{ep} = (\Delta_{1\%} / \Delta_y^{ep})$	3.56	2.33	2.35	2.00	1.69	1.44
Calculations based on curvatures averaged over the lower 100 mm of the wall						
φ_y^{ep} ($\times 10^{-6}$ rad/mm)	3.50	3.88	3.91	2.82	--(1)	3.37
$\mu_\varphi^{ep} = (\varphi_{1\%} / \varphi_y^{ep})$	7.25	5.75	5.33	8.89	--(1)	5.99
l_{p100} *(mm)*	530	352	395	155	--(1)	107
(l_{p100} / l_w) (%)	29(%)	20(%)	22(%)	9 (%)	--(1)	6 (%)
Calculations based on curvatures averaged over the lower 300 mm of the wall						
φ_y^{ep} ($\times 10^{-6}$ rad/mm)	1.73	2.24	2.34	1.98	2.25	2.71
$\mu_\varphi^{ep} = (\varphi_{1\%} / \varphi_y^{ep})$	6.11	4.40	4.24	6.68	--(1)	2.77
l_{p300} *(mm)*	661	505	540	217	--(1)	311
(l_{p300} / l_w) (%)	37(%)	28(%)	30(%)	12(%)	--(1)	17(%)

(1) Measurement not available for Wall 5 due to loss of potentiometers

Larger l_p values of between 12% and 37% of l_w would be required if the average curvatures at 1% drift over the bottom 300 mm of the walls (corresponding to μ_{φ}^{ep} varying between 2.8 to 6.7) were used instead of the values over the bottom 100 mm of the wall. Calculation of plastic hinge length based on the average curvature over the lower 300 mm of the wall (see Fig. A.5 (b) and Table A.4) might be reasonable and more compatible with previous assumptions of 0.5 l_w in CSA S304.1 (2004). The plastic hinge lengths were much lower when based on the average curvature over the lower 100 mm of the wall.

Using the theoretical values for curvature ductility, $\mu_{\varphi,th}$, for the test walls and the idealized displacement ductility at 1% drift, $\mu_{\Delta 1\%}^{ep}$, the required equivalent plastic hinge length, l_p, varied between 32% to 61% of l_w for all walls, except for Wall 6 where the theoretical curvature ductility was less than the measured displacement ductility. Based on using the theoretical curvatures, it seems reasonable that different values of l_p would result from using different displacement limits.

A.7 Seismic Force Modification Factor

Although force modification factors were intended for buildings, they are calculated here from wall behaviour as a conservative assessment of these factors. With redundancies, coupling, and redistribution of forces, buildings are expected to produce larger values for both ductility, R_d, and overstrength, R_o, response modification factors. To account for ductility and energy dissipation in actual structures, seismic response modification factors are used in force-based design codes (such as the current Canadian code) to reduce the seismic forces that would have to be designed for if the structure remained elastic. Although these factors are intended for building systems rather than individual element, the response of individual walls is assumed, as discussed in Section 5.1, to represent the response of the building in terms of the overall load-displacement relationship where the load is appropriately scaled-down.

Most force-based design codes use the equal displacement approach to determine the relationship between the ductility modification factor, R_d, and the displacement ductility (Priestley el al. 2007). In this regard, as discussed in Section 4.6, it seems appropriate that the idealized load-displacement curve based on equal energy should be used. However, since it was shown that in this idealization the idealized yield load, Q_{in}, only differed from the measured ultimate load, Q_u, by a few percent (refer to Section A.3), it was decided to use the more simple idealization presented by Mitchell et al. (2003) and the ultimate displacements, $\Delta_{0.8u}$, recommended of Priestley et al. (1996) as the basis to determine the seismic force modification factor. This approach is shown in Fig. A.7 where the elastic part of the idealization passes through the measured yield load, Q_y, and yield displacement, Δ_y, and extends up to the ultimate load, Q_u, and the corresponding displacement, $\Delta^{ep}= \Delta_y\ (Q_u/Q_y)$. The plastic part of the idealization is the constant load part extending to the chosen limiting condition shown as corresponding to the displacement, $\Delta_{0.80u}$, in the post-peak region at 0.8 Q_u. As discussed in Section 4.6, the idealized displacement ductility at 20% strength degradation, $\mu^{ep}_{\Delta 0.8u}$, can be defined as the ratio of $\Delta_{0.80u} / \Delta^{ep}$.

The ductility related force modification factor for a structure, R_d, is defined as the ratio between the elastic lateral load, Q_e, shown in Fig. A.7 corresponding to a lateral displacement demand, $\Delta_e= \Delta_{0.80u}$, to the ultimate wall capacity, Q_u. By similar triangles, R_d should be equal to $\mu^{ep}_{\Delta 0.8u}$. The R_o value (used for overstrength in NBCC 2005) was defined as the ratio between the ultimate wall capacity, Q_u, and the design capacity, Q_d, as is illustrated in Fig. A.7. The overstrength force modification factor can be due to rounding of sizes and dimensions, difference between nominal and factored resistance, ratio of actual yield to minimum specified yield of reinforcement, strength enhancement of the steel at large deformations due to strain hardening, and development of sequential plastic hinges in redundant structures (Harries 2004). The R_o value (used for overstrength) was defined as the ratio between the ultimate wall capacity, Q_u, and the design capacity, Q_d, amplified by 5% assuming conservative overdesign (commonly taken between 5% and 10%).

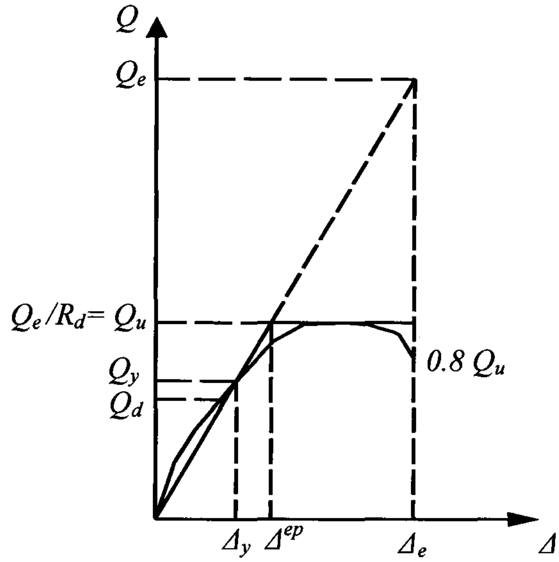

Fig. A.7: Actual and idealized load-displacement relationships for the test walls used for response modification factor calculation

The design capacities, Q_d, were calculated using material resistance factors for masonry and steel following the Canadian standard and the effect of the compression reinforcement was ignored. The average compressive strength of the concrete blocks used was 25 MPa [specific strength = 25×(1-1.64×*c.o.v.*% = 20.9 MPa, where the minimum 10% *c.o.v.* is used]. However, since the strength specified by the supplier was 15 MPa, for the calculation of the design strength of the walls, masonry compressive strength, f'_m, was taken equal to 7.5 MPa (The supplied overstrength of the block is typically lower (Chahine 1989) than usually supplied). Although 400 MPa steel yield strength was specified by the supplier, the delivered steel for all walls had about 490 MPa strength except for Wall 6 where the strength was about 600 MPa, based on the conducted tensile tests. To avoid an unrepresentative calculation, the strength of the reinforcing bars was taken equal 440 MPa as steel yield strength is commonly 40 to 60 MPa higher than specified.

At the 20% strength degradation commonly considered to be an acceptable ultimate performance level (Priestley el al. 1996; Priestley el al. 2007; and ATC-63, 2008), the average drift level for the test walls was 1.62%. Again, to be conservative in the calculation of the R_d values (given in Table A.5), the displacement demand, Δ_e, presented in Fig. A.7, was taken equal to the displacement corresponding to 1.3% drift. This represents the lowest test value at 20% strength degradation from all of the test walls. The measured wall resistance at the onset of yielding of the outermost vertical bar, Q_y, and at ultimate load, Q_u, for all walls were reported in Table A.5 for both the (+) ve and (-) ve directions of cyclic loading. For ease of reference, all values required to calculate the R_d and R_o force modification factors were presented in Table A.5.

Table A.5: Seismic force modification factor

Wall	Design capacity	Experimental results				Idealized displacement Δ_{ep} (mm)	Force modification factors		
	Q_d (kN)	Q_y (kN)	Q_u (kN)	Δ_y (mm)	Δ_u (mm)		R_d	R_o=1.05 $\times Q_u / Q_y$	$R_d \times R_o$
1	77	95	143	7.0	46.8 mm (1.3% drift)	10.5	4.4	2.0	8.7
		-84	-122			10.1	4.6	1.7	7.7
2	134	185	265	11.1		15.9	2.9	2.1	6.1
		-182	-246			15.0	3.1	1.9	6.0
3	135	174	242	11.3		15.7	3.0	1.9	5.6
		-190	-235			13.9	3.3	1.8	6.1
4	163	296	360	14.8		18.0	2.6	2.3	6.0
		-292	-380			19.2	2.4	2.4	5.9
5	140	311	377	16.2		19.6	2.4	2.8	6.7
		-316	-407			20.8	2.2	3.1	6.8
6[(1)]	114	450	541	16.9		20.3	2.3	5.0	11.5
		-455	-558			20.7	2.3	5.1	11.6

[(1)] Reinforcement in Wall 6 had strength of about 600 MPa.

Values of R_d ranging from 2.2 to 4.6 were calculated for the test walls corresponding to drift levels of 1.3% with the upper values corresponding to lightly reinforced walls not subjected to axial compressive stress and the lower values corresponding to heavily reinforced - heavily loaded walls. Values of R_o calculated for the test walls, except for Wall 6, which was not considered to be representative of actual construction, averaged 2.2 (*c.o.v.*= 20%) based on the design capacities calculated following the CSA S304.1. (Complications in analyzing and discussing the results for Wall 6 subjected to 10% f'_m compressive stress, were reported by Shedid (2006). Therefore, the R_o results and the product ($R_d \times R_o$) for this wall were not considered.) The overall response modification factor, $R_d \times R_o$, calculated for the walls varied between 5.6 and 8.7 with lower values corresponding to heavily reinforced - heavily loaded walls and higher values for lightly-reinforced walls with no axial compressive stress.

A.8 Conclusions

This appendix contained analyses of previously reported test results for six full scale reinforced concrete masonry shear walls tested to failure under reversed cyclic lateral loading (Shedid 2006). The aim of the analyses was to determine seismic performance parameters for full scale RM shear walls.

The average masonry compressive strain measured over the lower 100 mm (mid height of the first course) were much larger than the ultimate strains specified in the MSJC code (2008) and in CSA S304.1 (2004).

At ultimate conditions, the curvatures measured over the bottom 100 mm of the wall varied between $0.022/l_w$ and $0.042/l_w$, which were about double the corresponding theoretical values. At 1% drift, the curvatures, $\varphi_{1\%}$, varied between $0.036/l_w$ and $0.045/l_w$, with the lower values corresponding to heavily-reinforced walls subjected to axial compression and the upper values corresponding to lightly-reinforced walls with no axial compression. The much higher than predicted measured strains and curvatures at ultimate load did not affect the predicted strengths of the walls. However, they significantly influence the experimentally determined curvature ductility values and, consequently, wall displacements and displacement ductility values.

The curvature ductility varied between 4.6 and 9.6 at ultimate load, and between 7.2 and 10.7 at 1% drift, based on the average masonry strain over the lower 100 mm of the wall height. Alternatively, based on the average masonry strain over the lower 300 mm, the curvature ductility varied between 2.5 and 8.0 at ultimate load, and between 4.1 and 8.8 at 1% drift. For both cases, the calculated curvature ductility values were significantly higher than the theoretical values which ranged from 1.2 to 6.8.

The calculated equivalent plastic hinge lengths varied between 12% and 37% of the wall length based on the measured curvatures over the bottom 300 mm of the wall. Based on these findings, it is suggested that plastic hinge length should be related to the wall dimensions and reinforcement but further investigations should be conducted to develop a more rational method of determining equivalent plastic hinge length.

Values of the ductility-related seismic response modification factor, R_d, ranged from 2.2 to 4.6 corresponding to drift a level of 1.3%. Values of the seismic response modification factor due to overstrength, R_o, for the test walls were, on average, 2.2 based on evaluating the wall design capacity following the CSA S304.1. The product of reduction factors calculated for the test walls varied between 5.6 and 8.7.

Similar investigations to those reported in this appendix have been conducted in Chapter 5 to determine seismic performance parameters for the half scale masonry walls reported in Chapter 3.